GaN ON ZnO: A NEW APPROACH TO SOLID STATE LIGHTING

A Dissertation
Presented to
The Academic Faculty

By

Nola Shin-Yih Li

In Partial Fulfillment
Of the Requirements for the Degree
Doctor of Philosophy in Electrical and Computer Engineering

Georgia Institute of Technology

May 2009

GaN ON ZnO: A NEW APPROACH TO SOLID STATE LIGHTING

Approved by:

Dr. Christopher Summers, Advisor
School of Materials Science and Engineering
School of Electrical and Computer Engineering
Georgia Institute of Technology

Dr. Miroslav Begovic
School of Electrical and Computer Engineering
Georgia Institute of Technology

Dr. Gary S. May
School of Electrical and Computer Engineering
Georgia Institute of Technology

Dr. Nikolaus Dietz
Department of Physics and Astronomy
Georgia State University

Dr. Bonnie H. Ferri
School of Electrical and Computer Engineering
Georgia Institute of Technology

Date Approved: January 7, 2009

Out of the gloom shone a shining star…

my Sunshine

ACKNOWLEDGEMENTS

I would like to thank my advisors, Dr. Ian Ferguson and Dr. Christopher Summers, for their advice and support through this degree. I also want to thank the MOCVD group who have helped immensely with the project: Ali Asghar, Dr. Martin Strassburg, Dr. Adam Payne, Dr. Ming Pan, Dr. Eun-Hyun Park, Dr. June-O Song, Dr. Vincent Woods, Dr. Shen-Jie Wang, Dr. Hongbo Yu, Dr. Muhammad Jamil, Dr. Matthew Kane, Dr. Hun Kang, Dr. David Nicol, Dr. Omkar Jani, Shalini Gupta, Will Fenwick, Yong Huang, Tahir Zaidi, Andrew Melton, Tim Xu, Olivier Hamard, Jill Morris, James Bain, John Buchanan, Petko Petkov, and Peter Speirs. Thanks also go to Dr. Feng and his students who helped with characterization not available at GaTech and also John Blair who helped maintain the ALD tool. This research also could not have been possible without funding from the Department of Energy (DE-FC26-06NT42856). Special thanks go out to my parents, Mindy, and best friend(s) for their support and belief in me.

TABLE OF CONTENTS

LIST OF TABLES

LIST OF FIGURES

LIST OF EQUATIONS

LIST OF SYMBOLS AND ABBREVIATIONS

Symbol	Unit	Description
α	m^{-1}	absorption coefficient
AO		Al_2O_3
AlInGaP		Aluminum indium gallium phosphide
AlN		aluminum nitride
Al_2O_3		aluminum oxide
NH_3		ammonia
θ	degree	angle
A	m^2	area of surface
AES		atomic emission spectroscopy
AFM		atomic force microscopy
J		atomic flux
ALD		atomic layer deposition
f		atomic weight fraction
M	g/mole	atomic weight
N_o	/mole	Avogadro's number
E_g	eV	bandgap
ΔE		broadening parameter
x	%	composition
C	atoms/cm^3	concentration
CCT		correlated color temperature

ρ	g/cm^3	density
D	cm^2/sec	diffusivity
DMHy		dimethylhydrazine
DOE		department of energy
η	%	efficiency
e-beam		electron beam
ECP		emissivity correcting pyrometer
EDS		energy dispersive x-ray spectroscopy
EPD		etch pit density
EQE		external quantum efficiency
Φ	$mole \cdot m^{-2} \cdot s^{-1}$	flux
FWHM	arcsec, eV	full width at half maximum
GaN		gallium nitride
t	minutes	growth time
HAADF		high angle annular dark field
HBLEDs		High-brightness LEDs
HRXRD		high resolution x-ray diffraction
HT		high temperature
HVPE		hydride vapor-phase epitaxy
InGaN		indium gallium nitride
n		integer or refractive index of a material
φ	degree	internal reflection angle

l	meter	length
LED		light emitting diode
Ω	degree	light escape angle
LEEBI		low energy electron beam irradiation
LT		low temperature
MOCVD		metalorganic chemical vapor deposition
MBE		molecular beam epitaxy
MQW		multiple quantum well
OT		optical transmission
OMVPE		organometallic vapor phase epitaxy
PL		photoluminescence
PLD		pulse laser deposition
Raman		Raman scattering spectroscopy
RTA		rapid thermal annealing
Γ		reflection coefficient
RHEED		reflection high-energy electron diffraction
RMS		root mean square
RBS		Rutherford backscattering spectroscopy
SEM		scanning electron microscope
STEM		scanning transmission electron microscopy

SIMS		secondary ion mass spectrometry
SSL		solid state lighting
d	Å	spacing between planes in atomic lattice
SL		superlattice
T or χ	μm, nm	thickness of layer
T	%	transmission
TEM		transmission electron microscopy
TE		transverse electric modes
TM		transverse magnetic modes
TEGa		triethylgallium
TMAl		trimethylaluminum
TMGa		trimethylgallium
TMIn		trimethylindium
UHV		ultrahigh vacuum
XPS		x-ray photoelectron spectroscopy
λ	nm	wavelength
VAS		void assisted separation
YAG		yttrium aluminum garnet
AZ		$ZnAl_2O_4$
$ZnAl_2O_4$		zinc aluminum oxide
ZnO		zinc oxide

SUMMARY

The objective of the proposed research is to develop high quality GaN epitaxial growth on alternative substrates that can result in higher external quantum efficiency devices. Typical GaN growth on sapphire results in high defect materials, typically $10^{8-10}cm^{-2}$, due to a large difference in lattice mismatch and thermal expansion coefficient. Therefore, it is useful to study epitaxial growth on alternative substrates to sapphire such as ZnO which offers the possibility of lattice matched growth. High-quality metalorganic chemical vapor deposition (MOCVD) of GaN on ZnO substrate is hard to grow due to the thermal stability of ZnO, out-diffusion of Zn, and H_2 back etching into the sample.

Preliminary growths of GaN on bare ZnO substrates showed multiple cracks and peeling of the surface. A multi-buffer layer of LT-AlN/GaN was found to solve the cracking and peeling-off issues and demonstrated the first successful GaN growth on ZnO substrates. However, secondary ion mass spectrometry showed high Zn diffusion into the epilayer, which decreases the optical qualities of GaN. Therefore, InGaN was grown on bare ZnO because of the perfect lattice match with ZnO at 18% indium and low growth temperature. Good quality InGaN films were seen with the use of a low temperature (530^{o}C) GaN buffer layer. Indium composition of 17-27% increased with a decrease in growth temperatures from 720-680^{o}C. The InGaN films showed no indium droplets or phase separation. Shifts in InGaN-related photoluminescence (PL) emissions of 0.5$\pm$0.1eV may have been due to recombination involving Zn-/O-impurities due to the Zn/O diffusion from the substrate. An activation energy of 59meV was found for the InGaN epilayer, which correlated to findings in literature. A study of InGaN phase

separation demonstrated ZnO's ability to sustain a higher strain state than sapphire, and thereby incorporating higher indium concentrations into the InGaN layers without phase separation. InGaN on ZnO substrates exhibited indium content as high as 43% without phase separation compared to the same growth on sapphire with only 32%. Si doping of InGaN layers, a known inducer for phase separation, did induce phase separation on sapphire growths, but not for growths on ZnO. This higher strain state for ZnO substrates was correlated to its perfect lattice match with InGaN at 18% indium concentration. Layers grown on ZnO stayed strained past 18-20% indium content, a point where sapphire started showing signs of phase separation. This finding could lead to higher efficient green LEDs at 555nm. Transmission electron microscopy results revealed reduction of threading dislocation and perfectly matched crystals at the GaN buffer/ZnO interface showing coherent growth of GaN on ZnO. These were the first reported results of successful GaN on ZnO by MOCVD. However, Zn diffusion into the epilayer was still an issue.

Therefore, an atomic layer deposition of Al_2O_3 was grown as a transition layer prior to GaN and InGaN growth by MOCVD. Annealing studies were performed to find the best crystalline Al_2O_3 phases for MOCVD growth. X-ray and PL showed distinct GaN peaks on 20nm Al_2O_3/ZnO whereas no peaks were seen on 50nm Al_2O_3/ZnO demonstrating the first GaN films grown on Al_2O_3/ZnO. Optical transmission measurements showed that the bandgap energy of InGaN was not altered significantly when grown on annealed Al_2O_3/ZnO substrates. X-ray photoelectron spectroscopy showed a decrease in Zn diffusion into the epilayer, demonstrating that an ALD Al_2O_3 layer was a promising transition layer for GaN growth on ZnO substrates by MOCVD.

CHAPTER 1

INTRODUCTION AND HISTORY OF SOLID STATE LIGHTING

The objective of the proposed research is to develop high quality GaN epitaxial growth on alternative substrates that can result in higher external quantum efficiency devices, light emitting diodes (LEDs) specifically. The dominant method of LED growth in industry is by metalorganic chemical vapor deposition (MOCVD) on sapphire substrates. Typical GaN growth on sapphire results in high defect materials, typically $10^{8-10}cm^{-2}$, due to a large difference in lattice mismatch and thermal expansion coefficient. Therefore, it is useful to study epitaxial growth on alternative substrates to sapphire such as ZnO which offers the possibility of lattice matched growth. However, high quality MOCVD GaN growth on ZnO is difficult due to the thermal instability of the ZnO substrate, out-diffusion of Zn from the substrate, and H_2 back etching into the sample. This thesis covered three generations of GaN growth on bare ZnO solving both the cracking and peeling of the GaN epitaxial layer on ZnO. These results led to a fourth generation, where InGaN was grown on ZnO showing ZnO's potential for high indium composition without any phase separation. Findings showed the first successful GaN and InGaN growths on ZnO substrates, but also showed high Zn diffusion into the epilayers, which would in turn. Therefore, an atomic layer deposition (ALD) growth of Al_2O_3 was proposed as a transition layer before MOCVD growth of GaN or InGaN. The goal of the layer was to block Zn

diffusion, promote GaN growth, and prevent H_2 etching into the substrate. Successful growths of GaN and InGaN were reported demonstrating the first growths of GaN and InGaN on Al_2O_3/ZnO. Also, depth profiling showed a decrease in Zn diffusion into the epilayer.

1.1 Introduction

The advent of human lighting all started with fire, which brought not only warmth, safety, and cooking, but LIGHT whenever one wanted. From the very beginning the obsession with lighting took hold and whisked itself through the ages leading to the LEDs, which are the basis of the research discussed in this thesis. The area of lighting that uses LEDs is known as solid state lighting, and it has been forecasted as the next replacement for all lighting (accent lighting and general illumination). LEDs have been seen in successful applications, such as displays, traffic signals, automotive parts, backlighting, accent lighting, as well as in other applications. They have proved successful in accent and design oriented applications. However, the breakthrough for LEDs would be in general illumination. Lighting companies such as Gallium Lighting and Lithonia have produced and sold general lighting fixtures with white LEDs for use in office spaces and street lighting. However, cost is still high and many issues, as will be discussed below, hold back the acceptance of LEDs for general illumination. Such issues include standardization of LEDs specifications, binning, thermal management, and efficacy of the LEDs.

LEDs have advantages over conventional light sources, such as higher efficiency, longer life, smaller size, and enhanced controllability, among other characteristics. The

smaller size and enhanced controllability offer designers more freedom to create novel devices and fixtures while adding new functionality to lighting systems. There is also tremendous potential for energy savings with an associated reduction in green house emissions [2]. In 2005, 19% of the total global electricity used was from lighting. However, the success of solid state lighting in general illumination depends on the development of novel sources that offer additional features rather than an equivalent replacement while still being sensitive to the market requirements for lighting products. The SSL source must reach a price point where they can be competitive with conventional sources such as incandescent and fluorescent lamps. The continued adoption of SSL in general illumination will require further cost reductions in manufacturing through innovations in device fabrication techniques and material growths [3]. This thesis will cover material growth of GaN on ZnO, which allows for a lower internal defect LED, and thereby an increase in efficiency. Details will be provided in the following chapters.

1.2 Background

Fire was the first source of light and even to this day can still be seen in third world countries as the sole source of lighting. The additional use of wax created the candle as a sustainable light source that could be used in everyday households. In 1772, gas lighting was invented making controllable light available to the public. Gas lighting was followed by the invention of the light bulb, incandescent, in 1879 by Swan and Edison, and thereby providing a source of lighting that we still use to this day. The great invention of the light bulb by Edison was the screw-base lamp, which allowed for a set fixture to be built

into any building, lamp, vehicle, etc. In 1938, the fluorescent bulb was invented and has now become a potential replacement for the incandescent bulbs due to its higher efficiency and longer lifetime than incandescent. Also, LEDs were invented during this period by H.J. Round in 1907. However, the first functional LED (red) was not available to the public until 1962.

Holonyak discovered the first major breakthrough for LEDs. The idea was not new, but making the idea into a physical useful form was. Against the ideas of his fellow colleagues, Holonyak used his own method to create a mixed crystal. In an ampoule, he cooked gallium arsenide and gallium phosphide together with a metal halide, setting the standard of using an alloy compound to emit light. The addition of phosphorus to gallium arsenide increased the band gap which shifted the wavelength of the emitted light to the red region. As more and more phosphor was added, the photon production dropped below lasing capabilities, but it was enough to make the first red LED. In 1962, these first LEDs were used as indicators and replaced meters and nixie tubes in electronics and cost $260 each. Nowadays, they only cost about four cents each [4].

AlGaInP on GaAs was achieved with the development of organometallic vapor phase epitaxy (OMVPE), also known as MOCVD. This new material made possible high-brightness materials from yellow to red, and after refinement by Lumileds Lighting in the 1990s, AlInGaP LEDs obtained almost 100% internal quantum efficiency [5].

In the late 1980s Amano and Akasaki at Nagoya University used AlN to obtain p-type GaN, and the first GaN pn junction was invented. Nakamura at Nichia Chemical was also working on AlInGaN at the same time and invented the first GaN-based blue and green LEDs in the 1990s, which is now the standard for commercial GaN LEDs.

High power LEDs started with Lumileds Lighting in 1998. Advances in greater power levels, better thermal packaging, and hence more lumens, started off the revolution towards illumination for general lighting. High-brightness LEDs (HBLEDs), as of 2003, made up $1.8 billion a year, about half of the overall LED market. As of 2007, HBLEDs made up $4.6 billion in sales, growing by 9.5% from 2006 [6]. The companies advancing GaN LEDs comprise of an international mix: Philips LumiLeds, Nichia, Siemens, Honeywell, CERMET Inc., Northrop Grumman, and Fujitsu Labs Ltd. [7].

1.3 LED Device

A LED in its simplest form is a pn junction. It emits light when an electric current is applied in the forward direction of the device. Most current device structures incorporate multiple quantum wells (MQW) active regions to enhance light output, usually comprised of InGaN/GaN alternating layers. A typical device structure is comprised of a n-type GaN layer, followed by an active layer of InGaN/GaN MQWs, and then a p-type GaN layer, Figure 1.1. The desired wavelength emission can be controlled by the amount of indium doped in the MQWs. Mg and Si are the most common p-type and n-type dopants respectively. AlGaN is also used to produce shorter wavelength emitters. Commercially available LEDs are almost exclusively grown by MOCVD. Material systems include AlGaAs for red, AlInGaP for red to yellowish green, and AlGaN for green to UV. This thesis will cover InGaN growth on ZnO, which led to the discovery of higher indium incorporation without phase separation. This finding can lead to the ability to grow green LEDs at 555nm, which is an area of high interest due to green LEDs being the least efficient out of the entire visible spectrum. Current growth methods on sapphire

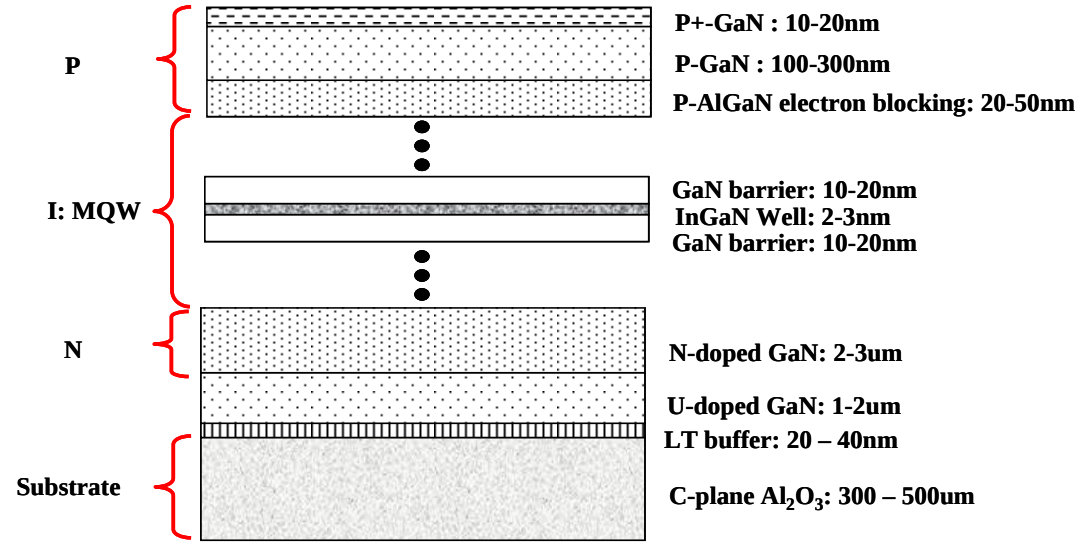

Figure 1.1: Typical growth structure of an LED.

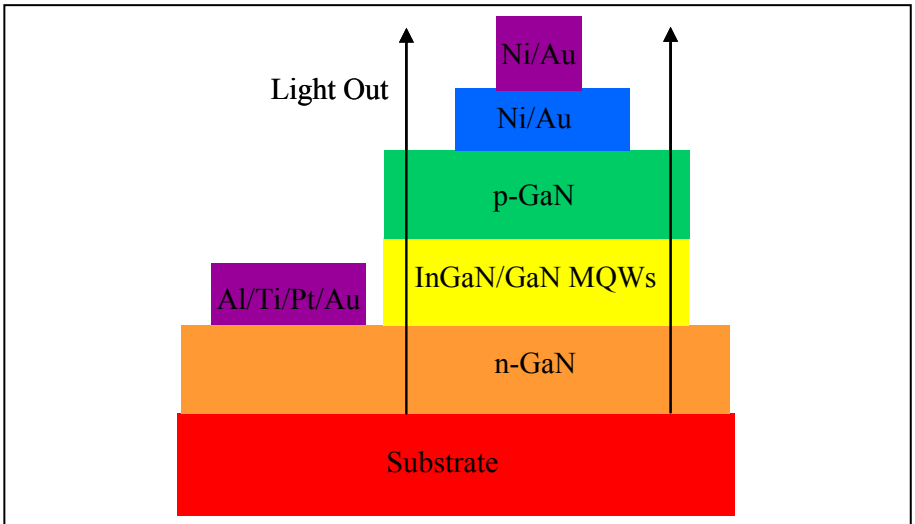

Figure 1.2: Typical device structure of an LED after fabrication.

substrates have too high of a defect density, $10^{8\text{-}10}cm^{-2}$, to allow for high indium concentrations without phase separation.

The fabrication of LEDs is much simpler than those used for microelectronics for computers. The device consists of large features and typically uses 4-5 alignment and patterning steps, Figure 1.2. More advanced chip designs involve surface roughening techniques and die shaping to improve light extraction. There is also substantial work in p-type metallization schemes to improve contact resistance and increase light output such as low resistance ohmic transparent contacts.

Phosphor development has been widespread for LED phosphor converted devices. Yttrium aluminum garnet (YAG) is the most commonly used compound. YAG absorbs photons with wavelengths in the blue part of the spectrum and has a relatively broadband emission peak at 550 nm (yellow light). White light is produced when some of the blue light is transmitted and mixed with the yellow light; however, this light is lacking in the red part of the spectrum and suffers in color rendering tasks. To compensate for this, red-emitting phosphors have been developed and incorporated with the YAG to provide higher quality white light. Another solution is to mix a certain amount of orange, yellow, green, and blue phosphors pumped with a 400 nm device to achieve the desired color [3]. White LEDs are also made by combing a red, a green, and a blue LED, also known as RGB LED. Also, HBLEDs take advantage of flip-chip fabrication techniques that extract the light through the substrate. Flip-chip designs incorporate solder bumps to attach the chip to a submount which can be used to extract heat better than thin gold wires [8]. This method is harder to fabricate, but allows for better light extraction.

1.4 Opportunities for Solid State Lighting

The United States uses one fourth of the world's energy resources with only 5% of the world's population, 8.2quads for lighting, or about 22% of the total electricity generated in the US. Most of the electricity comes from burning combustible fossil fuels (71% in 2001) and nuclear power (20% in 2001). The cost to produce this energy as well as the environmental impact all have to be taken into consideration. Much of this energy is wasted using incandescent bulbs because only 10% of the energy is given to light while the rest of it is given off as heat. The United States Department of Energy (DOE) and Optoelectronics Industry Development Association (OIDA) estimated in a 2001 report that by 2025 SSL could reduce the global electricity usage for lighting by 50%, saving 11.1 billion dollars a year. This would lead to an overall savings potential in the US alone of 16.6quads (760GW) of electrical energy, thereby eliminating 258 million metric tons of carbon emission and alleviating the need of 133 new power stations (1000MW each) [9]. However, this all depends on how fast SSL technology will advance by 2025. The wall-plug efficiency, lm/W, of LEDs needs to outperform conventional light sources such as incandescent and fluorescent lamps. The efficiency of incandescent light sources and fluorescent lighting is about 14lm/W and 60lm/W, respectively. These values will likely remain unchanged by 2025, as cost efficiency has already saturated. Current LEDs have reported just over 100lm/W, which is a great improvement of the 10-40lm/W previously reported in 2001. However, the cost of LEDs is still significantly more expensive than incandescent and fluorescents and spread over a broad range due to large differences in performance and technological capabilities of the different material systems, associated with a specific wavelength range. LEDs can achieve full market

penetration in almost all lighting applications if the efficacy of the LED can reach more than 120lm/W or a power conversion efficiency of ~50%, showing a first cost price of about 0.6dollars/klm [9].

The smaller size, longer life, and greater controllability of SSL sources enable new fixture designs unrealizable using incandescent or fluorescent bulbs. Incorporation of lighting systems into the building infrastructure could become a reality as SSL sources have lifetimes that may outlive the other technologies employed in a building. Lighting is the second largest end-use of energy in buildings. SSL sources would lead to lower maintenance cost as well as energy savings. Traffic signals and large area displays are two of the most prominent markets where colored LEDs have become very successful. One of the biggest motivators for the solid state lighting market has been the use of LEDs as backlights in mobile phones. LEDs are ideally suited for backlighting because of their small size, high efficiency, and low output requirements. They are especially useful in embedded designs where their long lifetime means they will outlive the product into which they are incorporated. In September 2004, IEE Review said that general lighting LEDs are already employed in flashes for camera phones, backlighting for laptop screens, and televisions. In addition, automotive lighting is taking advantage of LEDs where they are being used as taillights, interior illumination, dash backlighting, and starting this year in 2005, headlights. Designers have more flexibility due to the small size of the LEDs. In addition, LEDs are suited for the harsh environment of automotive lighting requirements because they do not require a glass bulb that is easily breakable. LED backlighting for television is also getting bigger with the unveiling of Sony's 40in and 46in domestic LCD televisions. With the start of Lumileds's Luxeon Lighting Network

even more new innovations are coming out as well as encouragement for further adoption of LEDs [10].

Rural areas also greatly benefit from general lighting LEDs. Places such as Nepals and Bolivia have had installation of white LEDs in their homes where once kerosene lamps used to hang. These areas did not have access to a power grid, and so, the LEDs ran off of their own solar panel supply. Each lamp required 12 white LEDs, mounted on a hand-soldered circuit board and only consumed one watt of power while producing 30 lumens; enough light to read, cook, or work [11]. Thirty lumens is about as bright as a 20W incandescent bulb. Funding only came from volunteers who in addition to paying for their own trip also paid $750 which covered the lighting of 20 homes. With the increase in more cost effective fabrication and material usage, the total cost for LEDs could go down. This would allow for rural places such in Bolivia to start buying and investing in electricity, which many of us take for granted [11].

Dynamic sources that can change their output over time are also being realized using LEDs. Applications such as wall washes and decorative lighting are markets where LEDs coupled with control circuitry are becoming widespread. Color Kinetics has developed many sources for these applications. Control is achieved easily with LEDs because they are relatively narrow band emitters compared to incandescent or fluorescent sources and have fast switching speeds. A wide color assortment including many shades of white can be realized by proper mixing, and this could be tuned as desired with a control system.

Future visions involve going beyond illumination for visual activity and venturing into psychological aspects of lighting; for example, choosing a particular lighting

distribution or color variation in retail applications. Consideration should also be given to the physiological effects of lighting that cause biological changes in a person within the environment. LEDs have high potential in playing a major role in such systems [12].

1.5 Issues in Solid State Lighting

Issues with solid state lighting exist in every level of the technology from materials to chip designs to packaging and fixtures. Problems at one level affect designs at higher levels, so proper solutions at lower levels, such as material or chip issues, could reduce the amount of setbacks at the packaging or fixture levels. For example, higher quality material could reduce resistivity and heat, affecting chip design, packaging, and ultimately the entire system.

Providing a supportable, high color-quality supply of white LEDs is the single biggest challenge facing the power LED industry even with all the acknowledged benefits of power LEDs, such as efficiency, sustainability, and durability. The variation in white color that are the result of today's manufacturing processes lead to a large number of bins around the black body locus. The primary problem with the LED/phosphor devices is the variation of the correlated color temperature (CCT) due to variations in the emission wavelength of the LED and phosphor matrix. This results in the need for extensive testing and binning to obtain products with similar characteristics for lighting applications. Moreover, another problem arises in that many of the bins are not on the Planckian black body locus making them unsuitable for general illumination. For solid state lighting to provide a competitive advantage over conventional lighting there must be greater control over the manufacturability of the product. The inefficiencies of binning

create structural vulnerability in the supply chain for the market. The only way most manufacturers can consistently produce sufficiently large quantities of the desired bins for general lighting has been to increase the volume of white LEDs manufactured and discard those that don't fit in the desired color spaces. However, this does little to address the supply chain risk and produces tremendous waste, the cost of which must be absorbed by the market.

The majority of blue, green, and ultraviolet emitters are made from some permutation of the AlInGaN material system, which lacks a readily available native substrate. Thus, devices are predominately grown on SiC or sapphire substrates which require AlN or GaN buffer layers to accommodate the lattice mismatch between the substrate and the device layers. However, devices produced this way typically contain a defect concentration, dislocations. Materials with high defect densities tend to be resistive and have lower internal quantum efficiency. Lattice-matched epitaxy on native GaN or other substrate technologies such as ZnO will likely be a solution. ZnO is a prime candidate due to its close lattice match with GaN.

UV emitters are also desired for several applications including SSL and biological sensing applications. However, in the AlGaN material system used for UV devices, increasing aluminum concentration to achieve shorter wavelengths results in a reduction of light output. High Al concentration devices show poor crystallinity as compared to GaN. Consequently, radiative recombination is reduced and the material is more resistive. New growth schemes and other novel solutions are required to solve this problem.

P-type doping of GaN has also been a major issue in device development. In 1988 Amano and Akasaki reported the first p-type GaN doped with Mg and activated with low

energy electron beam irradiation (LEEBI). Since then Mg has been the most common p-type dopant, but at room temperature only about 1% of possible acceptors are ionized. Thus, in order to achieve high hole concentrations large amounts of Mg are introduced to the GaN which causes degradation of the material. Hole concentration versus Mg doping reaches a maximum when the introduction of more Mg causes defects to occur that act as compensating donors. The crystalline quality of highly doped GaN:Mg also has higher resistivity, leading to losses and difficulty in contacting. Thermal activation around 800-900ºC has proven effective. However, it can have adverse effects on high indium concentration in InGaN causing the indium to separate into clusters. Growth with dimethylhydrazine instead of ammonia may be a solution because it does not require thermal activation of the Mg. Also, there is no need to go to high temperatures to grow which would keep indium from separating. N-vacancies in GaN are also naturally occurring and cause undoped material to be slightly n-type on the order of 10^{15} to 10^{16} cm^{-3}. Inefficiency caused by the defects can lead to resistive heating in the material when put under bias, which can also degrade the material and cause problems at the chip and packaging level [3]. For contact to the p-layer, further studies have shown an increase in the optical output power when using a nickel-oxide (NiOx)—indium-tin-oxide (ITO) bilayer transparent Ohmic contact. Previous contacts using Ni-Au did not show as good results as NiOx-ITO for high brightness LEDs [2].

1.6 Summary of History of Solid State Lighting

Lighting has come a long way since the discovery of fire. The incandescent bulb revolutionized lighting and has been around for 130 years. LEDs are on their way to be the next revolutionizing product for lighting. LEDs have proven themselves to be long

lasting, robust, and energy saving, to name a few traits. However, many challenges are still ahead before there is a widespread SSL adoption such as the improvement of internal/external quantum efficiencies and low-cost optical packaging associated with the growth of high-quality epilayer, fabrication, and development of efficient phosphors. Enhanced external quantum efficiency is currently the most research area for GaN LEDs. Extraction efficiency, and specifically single facet extraction efficiency, of over 50% for LEDs can have tremendous economical and environmental implications.

CHAPTER 2

SUBSTRATES FOR LIGHT EMITTING DIODES

Metalorganic chemical vapor deposition (MOCVD) is the primary method used by industry to grow LEDs. This method surpasses molecular beam epitaxy (MBE) due to its ease in scalability, turn around time, and flexibility. This is a great advantage for producing light emitting diodes (LED). Therefore, this project focuses on growth by MOCVD. Various substrates, such as sapphire and SiC, have been investigated and used successfully for InGaN growth and LED fabrication. However, alternative substrates are needed for further improvements to be made in the solid state lighting field.

2.1 Introduction

Progress in the growth of GaN materials has enabled the production of many new optoelectronic devices that operate at shorter wavelengths than previous materials have allowed. The main challenge in fabricating these devices has been in growing high quality GaN and GaN-based alloys on non-native substrate materials, such as sapphire and SiC, which have large mismatches in lattice constant and thermal expansion coefficient. Although the best approach is to use homoepitaxial growth on GaN substrates, current GaN substrates are still too expensive for commercial LED production. An alternate approach is to use heteroepitaxial growth techniques on a lattice matched substrate, as this can lead to a low epitaxial strain and a lower critical thickness before the

appearance of misfit dislocations. However, even the identification of latticed matched substrates in GaN is problematic. The equilibrium phase of GaN is the hexagonal wurtzite phase instead of the cubic zincblende structure, as is common in most III-V semiconductors. Thus, there are fewer substrates available simply because of the lower relative number of hexagonal compounds to cubic compounds.

Another great breakthrough for visible LEDs is the ability to alloy indium with GaN, forming a range of InGaN compounds. Current LED technology has two main material system groups: AlInGaP and InGaN. The AlInGaP system has proven to be very successful in the higher red wavelength region, while InGaN has shown to be very efficient in the lower blue wavelength range. The efficiency for both material systems falls considerably in the middle of the visible spectrum, Figure 2.1. This decrease in efficiency does not lend well for potential green LEDs or future white LEDs. One drawback for AlInGaP is that it is an indirect bandgap material system and therefore is less efficient due to its inability to emit photons by radiative recombination. The photon uses a two-step process, co-operation with a phono, to return to the valence band in order to emit the photon. In contrast, InGaN is a direct bandgap material system and is therefore naturally a more efficient light emitter. Also, AlInGaP does not have the ability to cover the entire visible region as the GaN material can, see Figure 2.2. However, in order for InGaN to extend down into the desired green region of 555nm and also achieve high efficiency, high indium concentrations must be incorporated with no phase separation of indium, formation of indium droplets, or InN formation. Obtaining high indium concentrations has proven to be difficult for growths on foreign substrates such as sapphire and SiC. However, the work performed here has shown that there is a much

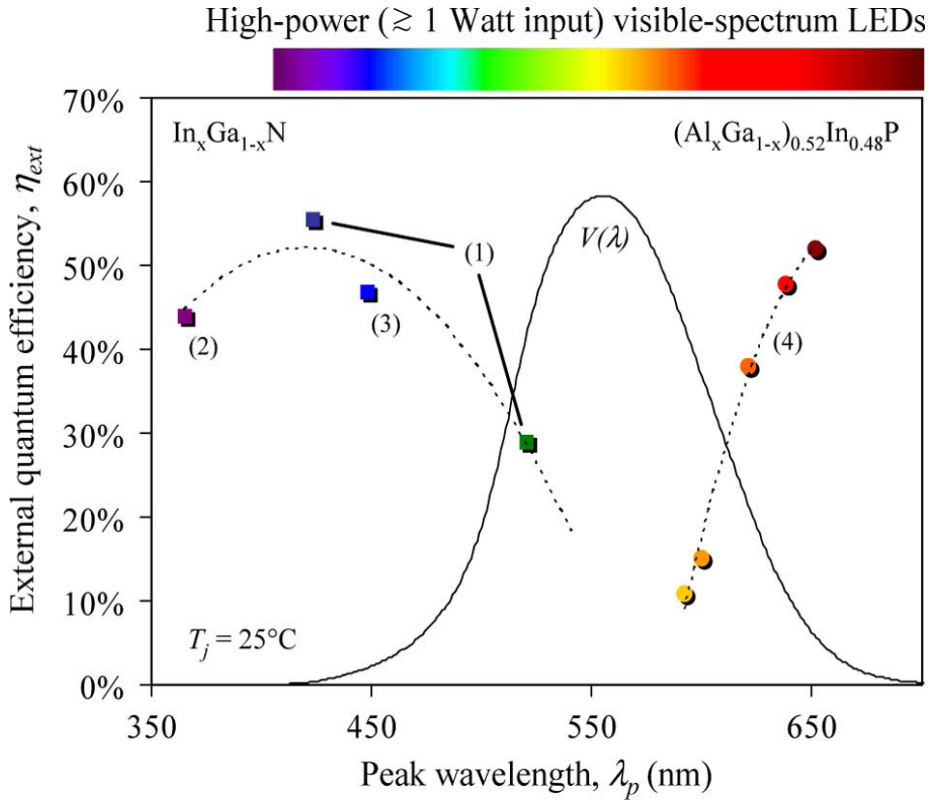

Figure 2.1: LED external quantum efficiency compared with the eye sensitivity to light. The efficiency of the LEDs drops as the eye efficiency increases to its maximum.

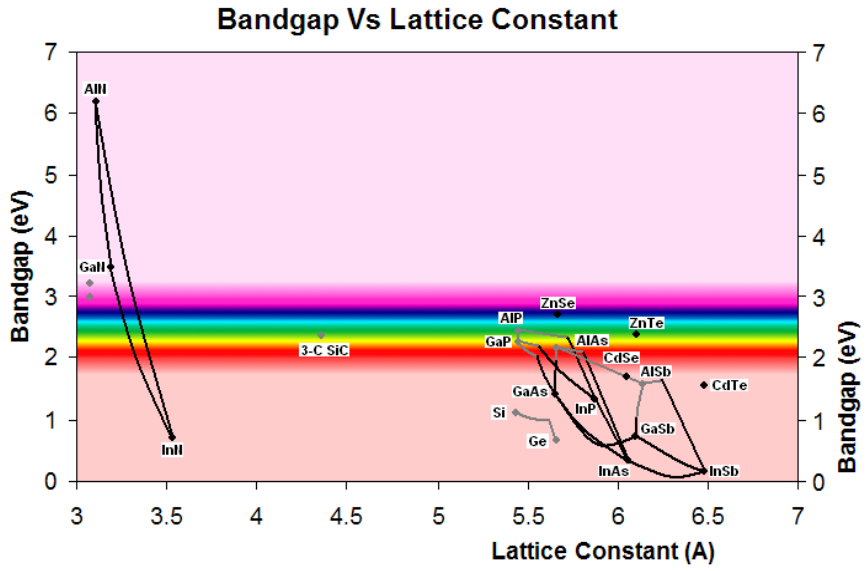

Figure 2.2: Bandgap versus lattice constant of different material systems commonly available for LEDs covering the visible range.

higher possibility of non-phase separated InGaN growth at high indium concentrations on ZnO substrates. A background overview will be discussed below on sapphire, GaN, and ZnO substrates followed by the issues involved with growing GaN on ZnO substrates.

2.2 Sapphire Substrate

Typical GaN-based LEDs are mass produced on sapphire or SiC substrates. Growth on other such substrates is not ideal, as differences in lattice constant and coefficients of thermal expansion result in high defect densities and compromised device performance. Sapphire has a 16% lattice mismatch with GaN but can be produced in large quantities and hence offers a stable material at a low cost. The large lattice mismatch and thermal expansion coefficient mismatch requires that a GaN template be grown on the sapphire first before any epilayer is grown. Details of this growth will be discussed in the following chapter. This GaN template has become a standard growth process and is available in mass production from companies such as Honeywell (now Silian), Rubicon Technology, Tokyo Denpa, and Lumilog. These companies sell standard polished sapphire substrates and/or epitaxy-ready sapphire substrates, which are sapphire substrates with the GaN template already grown. These materials help reduce production times and equipment downtime and are promised to have low defect dislocations. However, due to the large mismatches between GaN and sapphire, the defect density cannot be reduced below 10^{8}-10^{10}cm^{-2}. This high defect density severely limits the LED's efficiency, which could be greatly increased if a better substrate was available for GaN growth.

2.3 Bulk GaN Substrate

GaN substrates are the ideal substrate for GaN epilayer growth as they are the same material and hence have the same lattice match, same thermal expansion coefficient match, and would provide a direct one-to-one growth for GaN epilayer. However, it is very difficult to produce single crystals of GaN by the standard single crystal growth techniques, such as the Czochralski and Bridgeman techniques, because GaN is a refractory material with a melting temperature greater than 1800K. A successful GaN melt would have to be carried out at a pressure of > 6GPa and a temperature of 2220°C [13, 14]. This leaves hydride vapor-phase epitaxy (HVPE) and solution (solvothermal) techniques as viable options. HVPE growth is costly and dislocation generation has been a persistent problem. However, even with these faults, GaN substrates have been successfully grown by Cree, Kyma, TopGaN, and Sumitomo Electric by vapor-phase transport or epitaxial-type growths. However, wafer sizes are small and prices high. Researchers have paid up to $2400 for a 0.5 inch GaN wafer.

Cree has demonstrated production of 3 inch and 2 inch diameter GaN substrates, 330 to 400μm thick by using HVPE with dislocation densities reported as low as $3x10^6cm^{-2}$. Two different processes are used: a single-wafer approach and a cost-effective boule-based approach. The single-wafer approach utilizes HCl with molten GaN to form GaCl, which in turn reacts with NH_3 to form GaN. The growth rate is high, which enables the growth of self-supporting wafer thicknesses in a reasonable time period [15]. Kyma has demonstrated 3 inch and 4 inch diameter GaN substrates. Kyma uses a chemical vapor-phase process to grow bulk GaN material and a vapor-phase process (licensed from North Carolina State University) to provide the starting GaN template. This process, according

to Kyma, has a growth rate up to 10 times faster than any other commercialized deposition process for nitride-based materials [16]. A third player in GaN substrates production is TopGaN, who produces GaN substrates using extreme growth conditions. Their growth process includes pressures of 15,000atm and temperatures of 1600ºC. One growth can produce 20-30 crystals 10mm in diameter, exhibiting very low dislocation densities of $100cm^{-2}$. These 5μm thick GaN layers are grown on sapphire wafers and are meant for special devices and not for mass production [17].

In April of 2007, Hitachi Cable claimed they were able to remove defects from GaN substrates for 3 inch diameter wafers. They used a novel void-assisted-separation (VAS) technology. A thin GaN layer is grown on a sapphire base substrate followed by metal deposition, such as titanium, on the thin GaN layer. This structure is then heated in a gas mixture containing hydrogen where the GaN decomposes, leaving voids at the interface, which helps to lower the stress between the sapphire and GaN and thereby lowers the defect density in the subsequent GaN layer. A thicker GaN layer is then deposited by HVPE on top of the metal. The voids also enable removal of the thick GaN layer leaving a "freestanding, large-diameter GaN" wafer [18]. However, there are drawbacks to this method such as the need for sapphire substrates as well as the need to grow GaN in multiple steps. All these parameters are unnecessary in the current growth method on sapphire with a GaN template.

In March of 2007, Panasonic claimed to have made a breakthrough with a high-power 460nm emission chip grown on high-quality GaN substrates [19]. This is claimed to be the first commercial white LED on GaN substrate and has an efficiency more than 50% higher than conventional LEDs on sapphire substrates. Also, these LEDs have the

highest output in the industry with a total radiative flux of 355mW when driven at a forward current of 350mA. The external quantum efficiency (EQE) of these devices is 38% and is comparable to Lumileds's new thin-film flip-chip InGaN LEDs, which also had an EQE of 38%. Lumileds's LEDs emit at wavelengths of 440-445nm with a total radiative flux of 350mW at 350mA, increasing to nearly 900mW at a drive current of 1A. Panasonic's LEDs are being tested in a 3W power device for lighting applications, a reflector design for camera flashes, and a point source for use in compact lighting fixtures. Samples are said to be available at $4.30 per unit. If these LEDs succeed then a huge market change will occur in the LED industry.

All of the above growth methods were made in custom designed reactors. Therefore, the knowledge on mass producing GaN substrates at the quality and quantity needed by industry is still not available to the commercial market. GaN-based LEDs grown on foreign substrates are so successful that manufacturers may never transfer to GaN substrates. Standardized templates might be the solution as an alternative to the high cost of GaN substrates. Templates allow for actual LED growth times and material costs to be reduced, since all the steps up until the growth of the LED structure are removed. Reactors would require less maintenance due to the decreased deposition time of GaN and therefore lead to less reactor downtimes and longer reactor lifetimes. Standardized templates also lower issues associated with the growth of the foundation layer, which may be subject to intellectual property issues [17].

2.4 Bulk ZnO Substrate

For this study, ZnO substrates were obtained from CERMET Inc. and Tokyo Denpa for GaN growth by MOCVD. The substrates from CERMET Inc. were more readily available and hence were the main substrates used in this study.

2.4.1 CERMET Melt Growth Method

The ZnO substrates supplied from CERMET Inc were $20x20mm^2$ and $10x10mm^2$ and grown by a high quality proprietary pressurized melt growth process [20-22]. This melt growth technique produces ZnO crystals of very high quality in a much shorter time period and at a lower cost than existing techniques. The approach exploits a patented method of melting and crystallizing materials that have volatile components, or have thermodynamic instabilities, at or near the melting point of a material. A schematic of the growth apparatus is shown in Figure 2.3. The system uses an RF induction melting process. Eddy currents developed in the material result in joule heating of the system. Reaction with the crucible is prevented through water cooling. This process has several advantages over other growth techniques; issues with crucible reactivity, crystal contamination and decomposition have been minimized using a high pressure variation of the established induction melting technique. An etch pit density (EPD) as low as $10^4 cm^{-2}$ can be achieved with this method, as well as high transparency as measured by optical transmission. CERMET also has the ability for application specific doping and scalability to large diameter wafers (up to 100mm in diameter is possible), Figure 2.4. CERMET Inc. is located in Atlanta, GA and has worked closely with GaTech on a number of ZnO related projects.

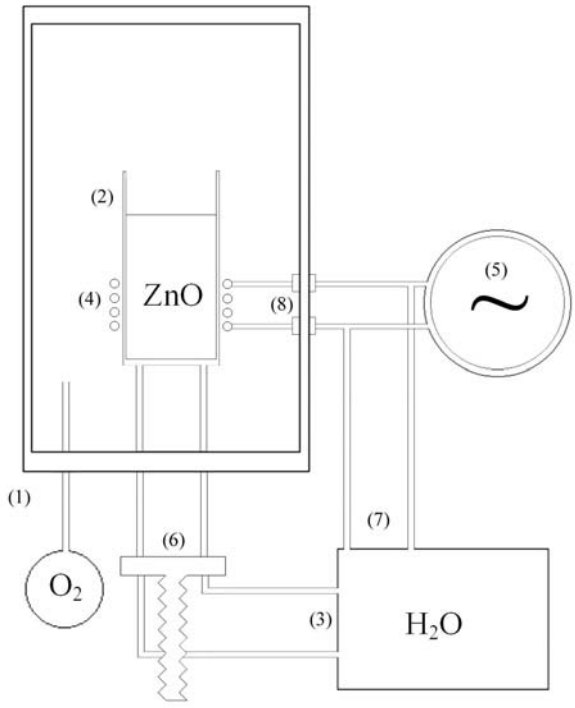

Figure 2.3: Schematic of melt growth apparatus.

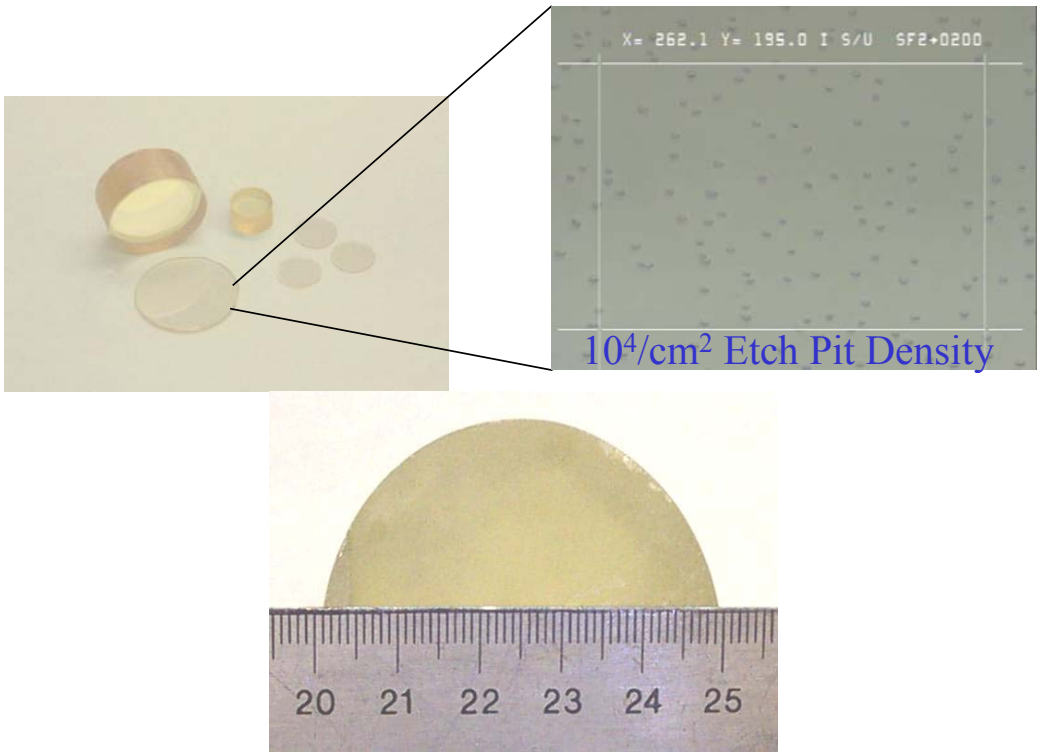

Figure 2.4: Low etch pit density, application specific doping, scalable to large diameter wafers, (up to 100 mm diameter possible).

2.4.2 Tokyo Denpa Substrates

Tokyo Denpa has successfully grown ZnO single crystals by a hydrothermal method that was transferred from synthetic quartz crystals [23]. ZnO wafers 2 inches in diameter are sliced from the grown single crystal. The substrates have a reported EPD of $<80 cm^{-2}$, high transparency, high crystallinity, high purity, and are defect free.

2.4.3 Case Study Between CERMET and Tokyo Denpa Substrates

A case study was performed between the CERMET and Tokyo Denpa substrates in order to compare substrate quality with the subsequent GaN growth by MOCVD. X-ray measurements showed a very distinct ZnO peak for an omega scan of the Tokyo Denpa substrate, whereas the CERMET substrates showed a number of peaks covering a wide range of angles, as seen in Figure 2.5. AFM surface roughness measurements of the Tokyo Denpa substrates showed a root mean square (RMS) value between 0.2-0.4nm, Figure 2.6. The CERMET ZnO substrates had a similar RMS value showing that both substrates had a flat surface for epitaxial growth. GaN was grown on both substrates to check if there was any quality difference due to the substrate. However, growth on Denpa ZnO substrates proved just as hard as on CERMET samples. X-ray features corresponding to GaN growth were not observed. Therefore, at $360 per substrate, the Tokyo Denpa substrates were not cost effective and could not be obtained in high quantity as was needed for this research.

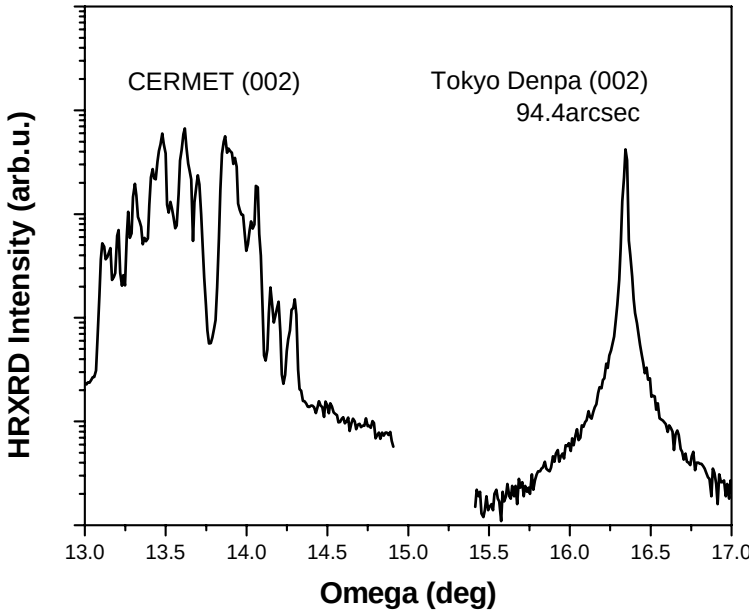

Figure 2.5: Comparison of x-ray omega scans for CERMET Inc. and Tokyo Denpa ZnO substrates.

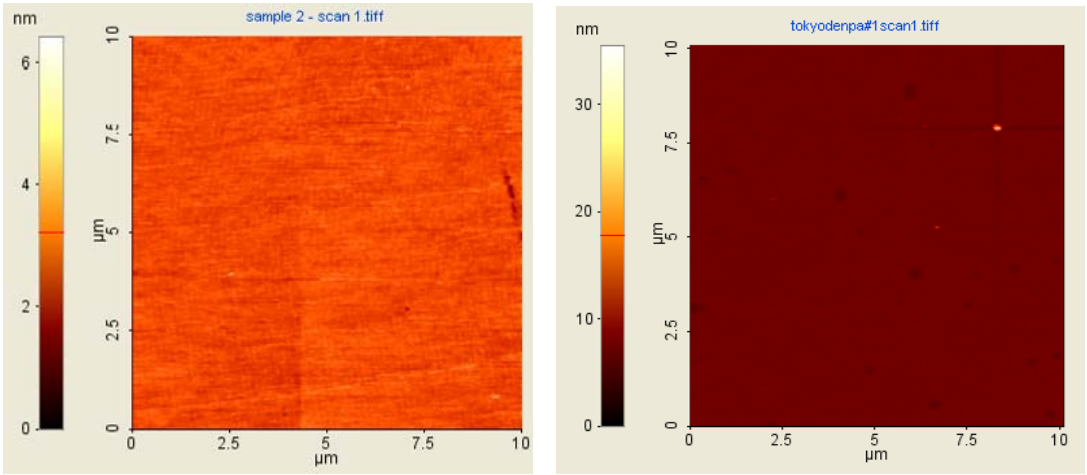

Figure 2.6: AFM of CERMET Inc. and Tokyo Denpa ZnO substrates showing similar RMS values of 0.2-0.4nm.

2.5 ZnO as a Viable Substrate for GaN and Major Challenges

2.5.1 GaN on ZnO Advantages

As a substrate, ZnO offers many advantages due to its many structural similarities to GaN. Both are wurtzite crystal structures with identical stacking order, closely matched lattice constants, and similar thermal expansion coefficients. In addition, ZnO is perfectly lattice matched to an 18% InGaN composition, a material necessary for green emission devices, Figure 2.7. Also, ZnO has high electrical conductivity; devices grown on ZnO can use backside contacts to improve current spreading. In addition, ZnO can be chemically etched leaving only a thin GaN film for better current spreading. Chemical etching saves time and cost compared to the laser lift-off process currently used for sapphire substrates. Finally, ZnO is a polar material. There are four kinds of wurtzite-structure (0002) ZnO surfaces: Zn-polar with O- or Zn-termination or O-polar with O- or Zn-termination. Zn-face (Zn-polar) ZnO, such as the ones used in this study, result in Ga-polar GaN. Ga-polar GaN growths yield better crystal quality compared with N-polar GaN.

ZnO has been investigated for use as a buffer layer and more recently as a bulk substrate material for the growth of GaN because of the many inherent advantages described above. There have been several reports of successful growth of GaN on ZnO via MBE and pulsed layer deposition (PLD). Early MBE results showed that the polarity of the GaN films grown on *c*-plane ZnO is somewhat dependant on the polarity of the substrate, with GaN grown on the O-face ZnO exhibiting better crystal quality [1, 24]. However, more recent reports have suggested that proper surface preparation and control of growth parameters can also yield good quality GaN films on the Zn face [25]. GaN

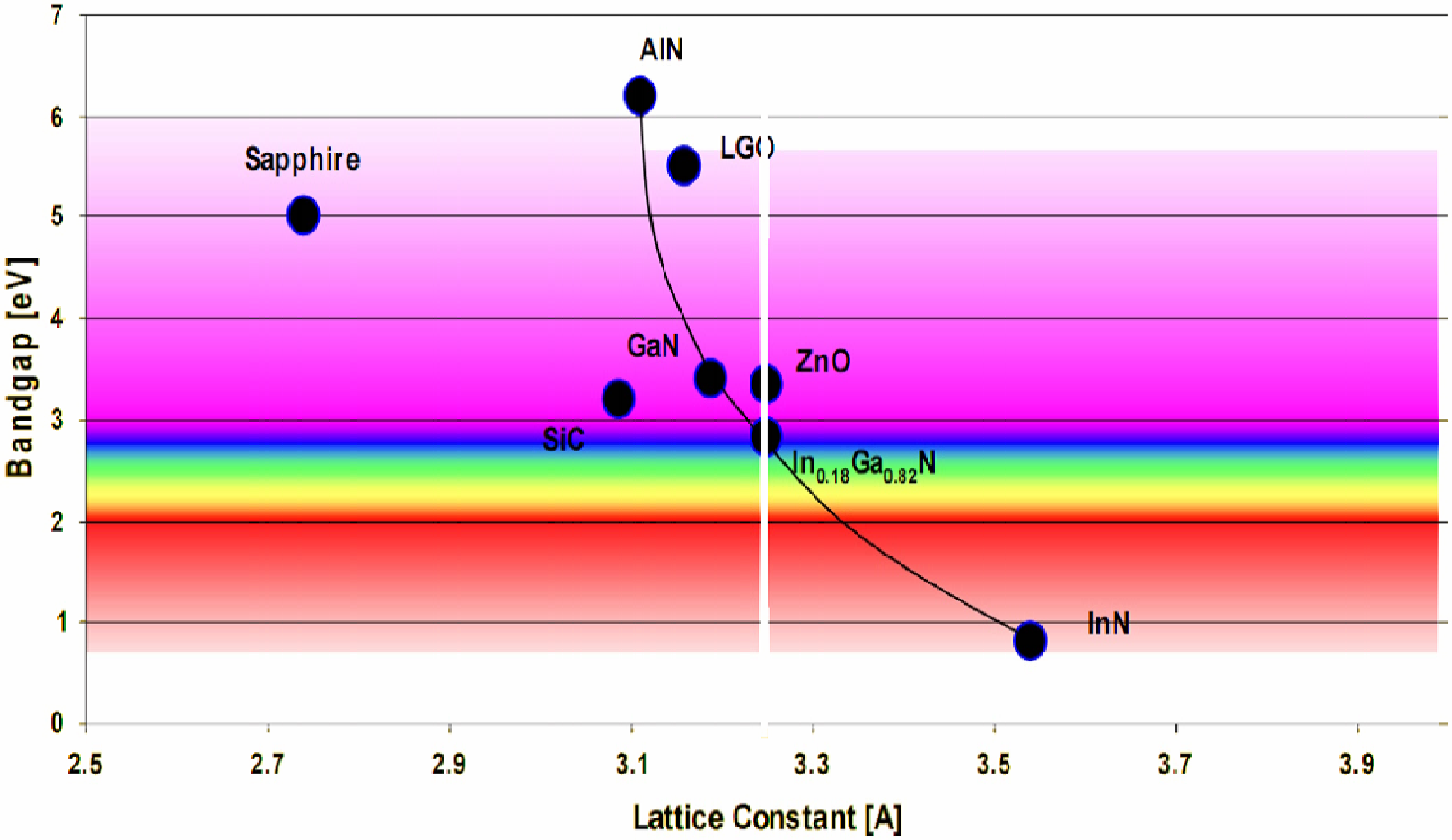

Figure 2.7: Lattice constants and bandgap energies of group III-N alloys and various substrate materials.

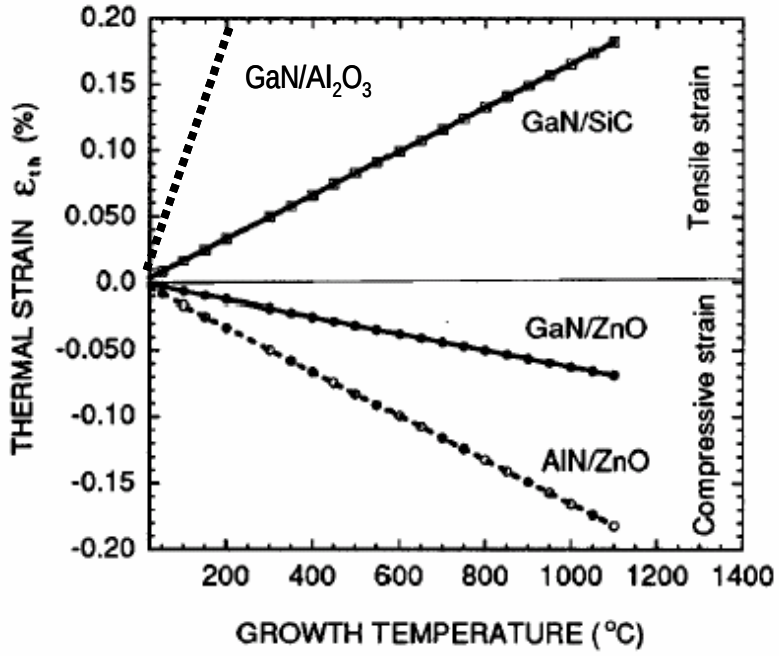

Figure 2.8: Calculations of thermal induced strain for GaN/ZnO, AlN/ZnO, and GaN/SiC [1].

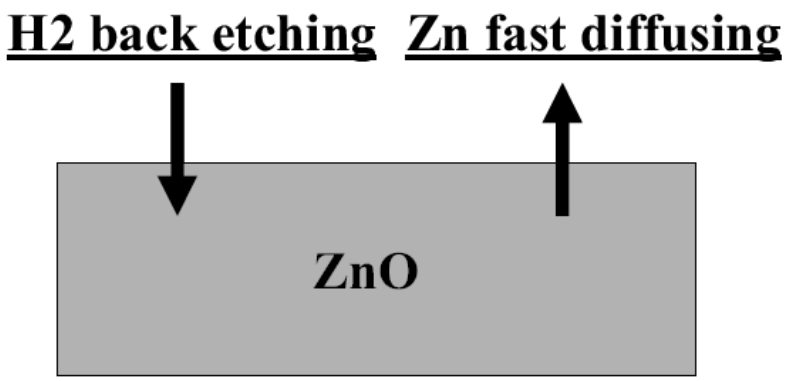

Figure 2.9: Issues related to growth of GaN by MOCVD on ZnO substrates shows H_2 back etching into substrate and Zn diffusing into epilayers, both causing poor epilayer growth of GaN.

films grown on bulk ZnO also showed reduced strain and defects density compared to films grown on sapphire, Figure 2.8 [1].

These studies show that there is a need to explore MOCVD growth of III-N on ZnO substrates because MOCVD is currently the dominant growth technology for GaN-based materials and devices. However, there are a number of obstacles that need to be addressed. These include the thermal stability of the ZnO substrate, the out-diffusion of Zn from the substrate into the epilayer, and H_2 back etching into the substrate, Figure 2.9.

2.5.2 Issues for MOCVD Growth of GaN on ZnO

In the commercial MOCVD process GaN is deposited on sapphire substrates at temperatures greater than 1000^{o}C, which makes it difficult to grow GaN on ZnO substrates. So far, only R. Paszkiewicz et al. has reported MOCVD growth of GaN on ZnO, and observed x-ray diffraction (2nd order) and photoluminescence peaks from the as grown layer [26]. However, x-ray full width at half maximum (FWHM) for GaN on ZnO, 2000arcsec, was also significantly larger than for GaN on sapphire, 180arcsec. The PL also was very weak. Poor surface preparation and high temperature growth by MOCVD can degrade the GaN film quality. ZnO also displays a much lower hardness compared to other materials at high temperature allowing it to decompose more easily than other available materials, Figure 2.10. The decomposition leads to an increase in Zn diffusion causing poor epilayer growth of GaN.

An additional problem associated with high temperature growth is H_2 back etching of the ZnO substrate. An increase in temperature increases the H_2 etching rate, thereby, damaging the substrate before the epilayers can be deposited, Figure 2.11. Ammonia (NH_3), as the N source during MOCVD GaN growth contributes H_2 to the growth. At

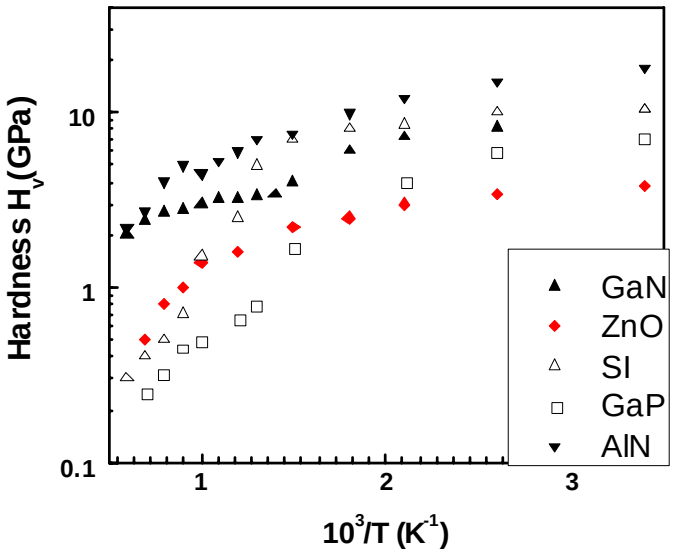

Figure 2.10: Thermal decomposition of various materials. ZnO has a much lower hardness compared to other materials at high temperature allowing it to decompose more readily than other available materials.

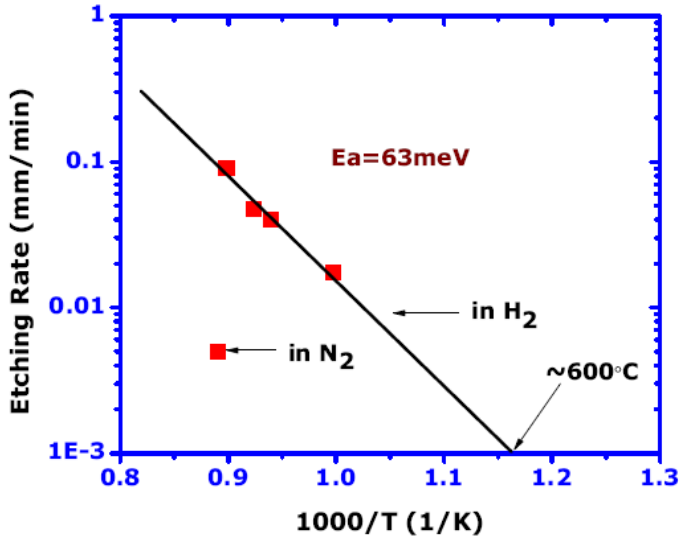

Figure 2.11: Arrhenius plot for the H_2 etching rate (mm/min) of ZnO versus temperature (1/T).

low temperatures ~500°C the contribution of H_2 is small and therefore not detrimental. However, the NH_3 cracking efficiency increases quickly as the temperature is ramped up to 600°C and higher causing excess H_2 to rapidly etch the ZnO substrate. Dimethylhydrazine (DMHy) and Tertiarybutylhydrazine (TBHy) have been investigated as H_2-free N sources with low-temperature decomposition (100% below 800°C), but both were found to cause high levels of carbon contamination making high quality GaN growth impossible [27].

Another issue is heterovalency at the GaN/ZnO interface forming intermediate phases such as Ga_2ZnO_4. This phase has been identified with poor crystalline quality and diminishes the advantage of the lattice-matched ZnO substrate [24]. Therefore, several studies used low temperature growth to solve this problem enabled by PLD and plasma-assisted MBE. Also, numerous studies have reported that high quality GaN films could be successfully grown on thermally treated Zn- and O-face ZnO substrates and are able to avoid the intermediate phase by using MBE [25, 28]. However, from SIMS measurements, T. Suzuki et al. found that the Ga_2O_3 and Zn_3N_2 phases still appeared at the GaN/ZnO interface, confirming significant interdiffusion [29]. From PLD results, the authors revealed terrace structures on the GaN surface and no interfacial layer existence under low temperature [30, 31]. Nevertheless, this intermediate layer still occurred above 540°C. As a result, PLD and MBE techniques for the growth of GaN on ZnO substrates are still limited by temperature control and growth rate.

Table 2.1: Year 1 DOE activities.

Activities
• GaN thin film growth directly on Si(001) and ZnO • Growth of buffer layers (e.g. Al_2O_3, AlN, ZnO) on Si(001) and/or ZnO using ALE technique. • GaN thin film growth on buffer layers • *Ex-situ* analysis (XRD, PL, SEM, etc.) of GaN layers. • Assess need/parameters for buffer layer

Table 2.2: Gate metrics for x-ray, PL, Hall, and SIMS.

Activities	Deliverables	Gate
X-ray Diffraction	**Photoluminescence response[1]**	**Hall Effect Characteristics[2]**
FWHM ≤ 500 arcsec (002)	FWHM ≤ 0.4 eV Intensity > 2000 Counts/ms	Carrier Concentration ≤ 2.0×10^{18} cm^{-3} Mobility > 350 $cm^2V^{-1}s^{-1}$ **SIMS Analysis** $Concentration_{Impurity} \leq 10^{18}$ cm^{-3} (Carbon, Oxygen)

2.6 Gate Metrics

This project was funded by the Department of Energy (DOE) and consequently certain gate metric parameters were set up with DOE. The activities and deliverables can be seen in Table 1. The gate metrics for this project are listed in Table 2. The metrics specify the FWHM needed for x-ray and photoluminescence, as well as the minimum conditions for Hall and SIMS.

2.7 Summary of Substrates for Light Emitting Diodes

Currently, LEDs are grown on foreign substrates such as sapphire and SiC. These substrates have proved to be very viable and have demonstrated LEDs over 100 lumens. However, foreign substrates can only allow LEDs to reach a certain efficiency due to the internal defects generated by lattice mismatch and differences in thermal expansion coefficient. Sapphire substrates also require a GaN template to be grown prior to any epitaxy growth. This growth process uses up valuable metalorganic resources, growth time, and tool lifetime. GaN substrates have been successful for some companies such as Cree and Kyma, but are still too expensive for research or commercial LED production. Therefore, ZnO substrates were proposed in this project as an alternative substrate for GaN growth. ZnO has a small lattice mismatch with GaN, only 1.8%, and has a similar thermal expansion coefficient. Also, ZnO is perfectly lattice matched to InGaN at 18% indium concentration. The defect densities present in current LED devices grown on sapphire or SiC are expected to decrease significantly just by the use of ZnO. The following chapters will show that the use of ZnO enables the incorporation of higher indium concentrations compared to the use of sapphire substrates. Higher indium

concentrations allow the LED emission wavelength to be shifted into the green region where current LED technology is least efficient. However, the growth LEDs by MOCVD proves to be difficult for growth of GaN on ZnO. The following chapters will discuss these difficulties and solutions for achieving high-quality GaN on ZnO.

CHAPTER 3

GAN GROWTH AND CHARACTERIZATION METHODS

The focus of the growth methods used in this research was metalorganic chemical vapor deposition (MOCVD) and atomic layer deposition (ALD). Annealing studies of the amorphous ALD layers were performed using an MXI furnace and used to optimize MOCVD GaN growth for higher crystal quality. A variety of characterization methods were used to study the optical and physical attributes of the samples immediately following growth for rapid assessment of material quality as well as for detailed studies of the properties of the materials. These characterization tools included high resolution x-ray diffraction (HRXRD or x-ray), room-temperature and low-temperature photoluminescence (PL), optical transmission (OT), atomic force microscopy (AFM), Raman scattering spectroscopy (Raman), atomic emission spectroscopy (AES), x-ray photoelectron spectroscopy (XPS), secondary ion mass spectrometry (SIMS), Rutherford backscattering spectroscopy (RBS), field-emission scanning electron microscope (FE-SEM), energy dispersive x-ray spectroscopy (EDS), cross-sectional high angle annular dark field (HAADF) scanning transmission electron microscopy (STEM), and high-resolution transmission electron microscopy (HRTEM).

3.1 Introduction

MOCVD is the current growth method used for light emitting diodes (LEDs) in industry. Therefore, it is highly conducive to enhance LEDs by this growth method. MBE was attempted, but did not give good results. A buffer layer technique wad developed by ALD. Samples from ALD were initially amorphous. Therefore, an annealing study was preformed on the ALD samples prior to GaN growth. A wide range of characterization methods were performed on the samples. X-ray and PL were the main characterization tools and used after every run to quickly check the optical qualities in order to optimize the following run. Additional characterization tools were used for detailed studies of the crystal quality, surface morphology, and elemental composition. Details of the growth, annealing, and characterization tools are given below.

3.2 Growth Methods

3.2.1 Metalorganic Chemical Vapor Deposition

Metalorganic chemical vapor deposition (MOCVD) is currently the leading technology for LED growth production. In a MOCVD system, a metalorganic precursor for the Group III compound is introduced into a heated reactor vessel. This metalorganic precursor is transported to the reactor via a carrier gas which bubbles through the liquid source. The group V precursor is often a hydride, such as ammonia (NH_3) in this case. Near the substrate surface, these precursors will pyrolyze, or disassociate with heat. The atomic species then adsorb onto the surface and diffuse along the surface until they assemble in the form of a crystalline compound semiconductor thin film. A schematic of the gas flow process during MOCVD growth is shown in Figure 3.1.

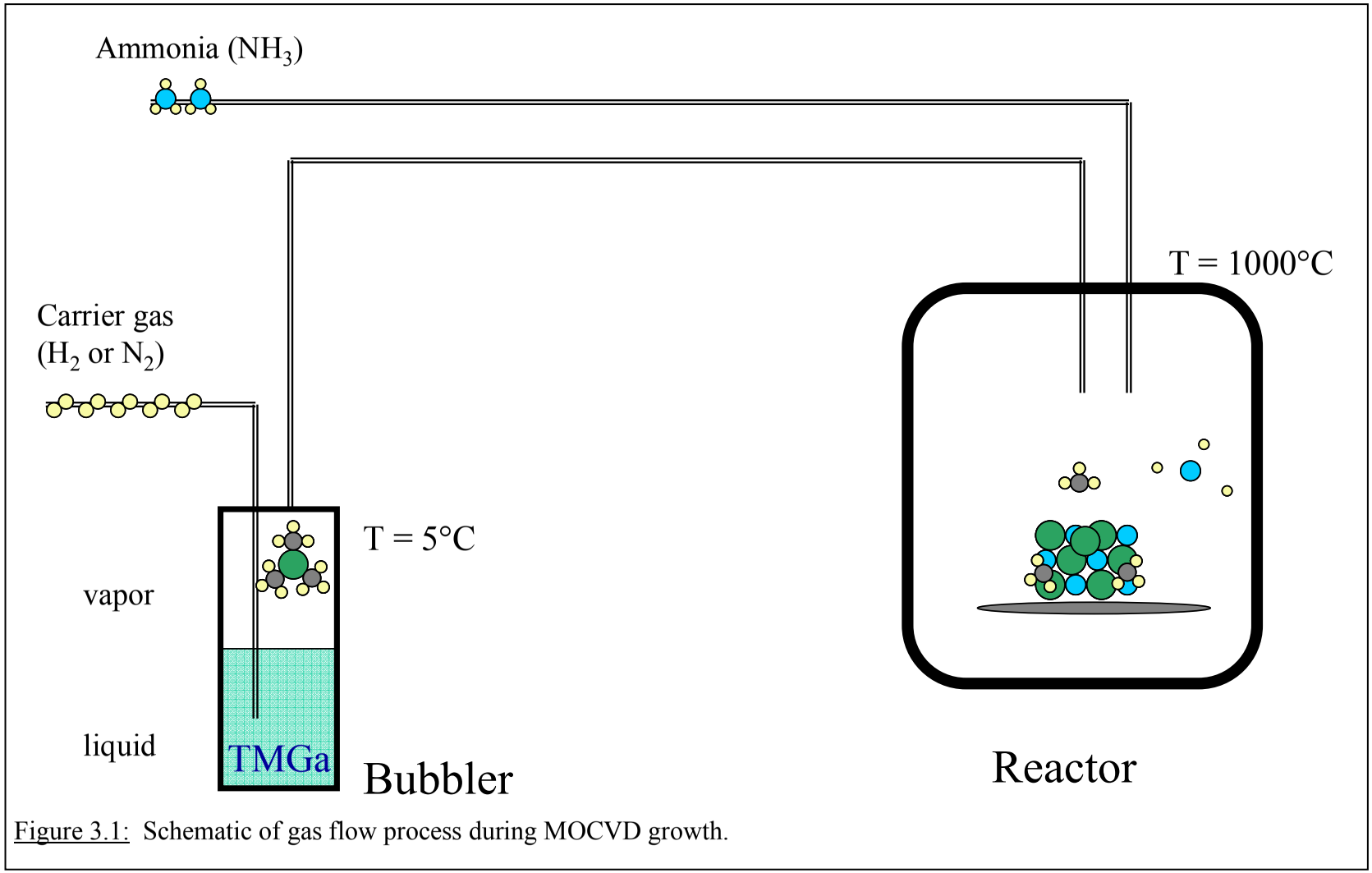

Figure 3.1: Schematic of gas flow process during MOCVD growth.

A convenient method for monitoring the growth of GaN is through *in situ* reflectance. GaN is transparent in the visible spectrum, so a light beam incident perpendicular to the sample will not be significantly absorbed. Based on differences in the refractive indices of the substrate and epilayer, reflections will occur at the interface of the materials, as well as at the epilayer-atmosphere interfaces. Because of constructive and destructive interference depending on the thickness of the film, it is possible to measure the growth of the film through the use of Fabry-Perot oscillations in the reflectance spectra. In addition, the reflectance spectrum also provides a way to monitor the various steps occurring during the growth process.

Typical GaN growths on sapphire require a GaN template due to the large lattice mismatch and thermal expansion coefficient mismatch between GaN and sapphire. An example of a typical *in-situ* reflectance curve for a GaN template on sapphire can be seen in Figure 3.2. The figure also depicts what the growth process was at each stage of the *in-situ* curve. First, the sapphire substrate is pre-treated by heating to between 1000 and 1100ºC. This helps to clean the sapphire substrate and nitride the surface. The reflectivity will increase during this time due to a change in refractive index with temperature. Then the temperature is ramped down to 550ºC to grow a nucleation layer of GaN. The temperature is then ramped back up to 1050ºC to recrystallize and recover the thin GaN layer by roughening the surface to create a single-phase layer. This 3-D growth mode forms islands, which leads to an increase in the reflectance signal. During growth, the islands coalesce, and the growth mode transforms from 3D to 2D layer-by-

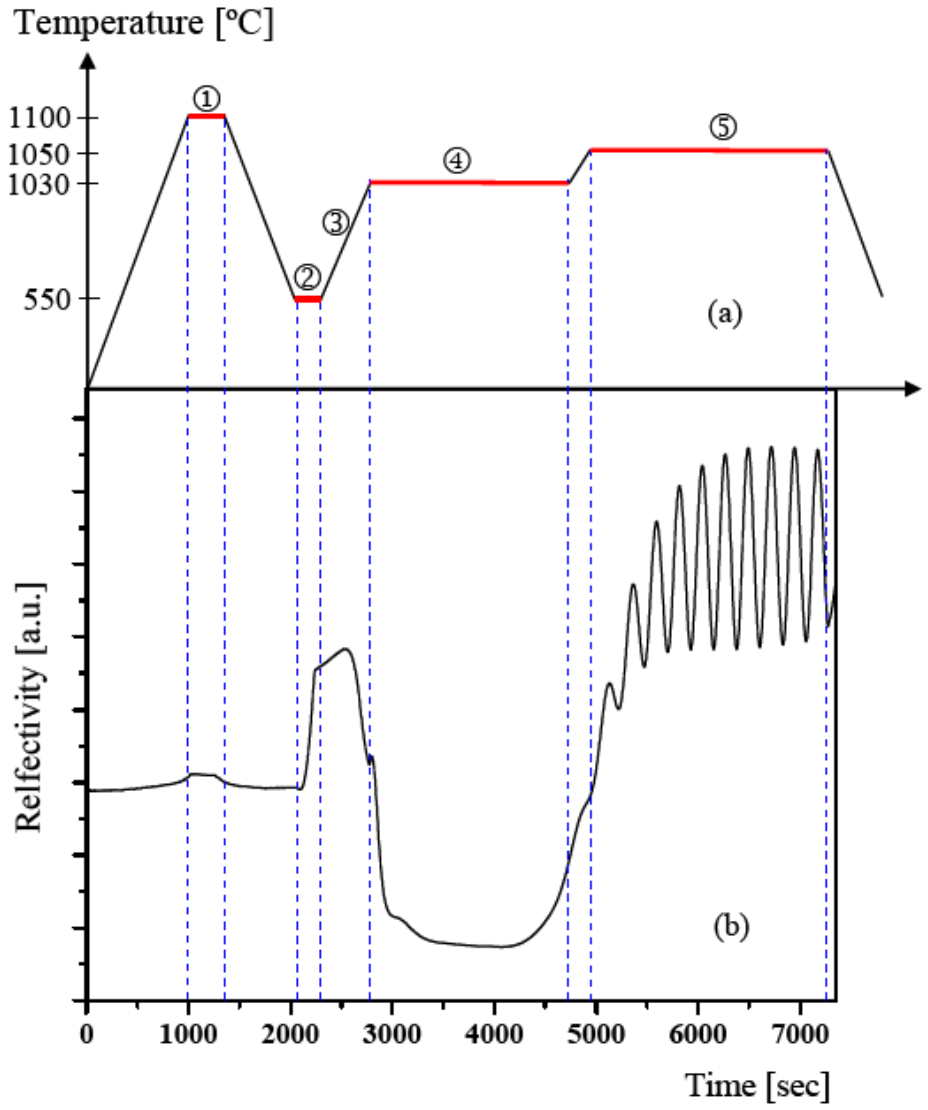

Figure 3.2: Example of temperature profile used during growth and corresponding *in-situ* reflectance curve of GaN template grown on sapphire.

layer growth. Fabry-Perot oscillations are then visible until the desired thickness is obtained of between 2-4μm, where the layer is now completely relaxed and defects are at a minimal level. The intrinsic high defect densities and thermal strain in the GaN template is shown in Figure 3.3. This 2μm thick GaN layer provides the foundation for the growth of the GaN LED structure.

Typical GaN growths on sapphire require temperatures of over 1000°C and the use of H_2 for good-quality GaN. H_2 bonds break easier than N_2 bonds and also help with Ga and N interactions. The H_2 can be supplied from the H_2 carrier gas as well as a byproduct from NH_3, which is the typical nitrogen source for GaN. However, issues arise when using these parameters for GaN growth on ZnO by MOCVD, as described in the previous chapter. Optimization of the gas flow conditions and V/III precursor ratios are also essential for growing a high-quality GaN film by MOCVD. Trimethylgallium (TMGa) was used as the metalorganic gallium source for GaN and InGaN. TMGa has a high vapor pressure, is relatively stable in liquid form, readily disassociates at high growth temperatures, and is commercially available in ultra-pure quality. Triethylgallium (TEGa) was also used as the metalorganic gallium source. TEGa has a lower carbon contribution than TMGa and is ideal for growth at lower temperatures due to its ability to decompose below 500ºC, however, it has a low vapor pressure and therefore is not as commonly used as TMGa. The nitrogen source is more problematic as there are no known organic nitrogen sources that can disassociate at a low enough temperature and crack cleanly without resulting in carbon contamination of the as-grown films. Both Dimethylhydrazine (DMHy) and Tertiarybutylhydrazine (TBHy) cuase too much carbon contamination to make them viable nitrogen sources. NH_3 is an accepted nitrogen source

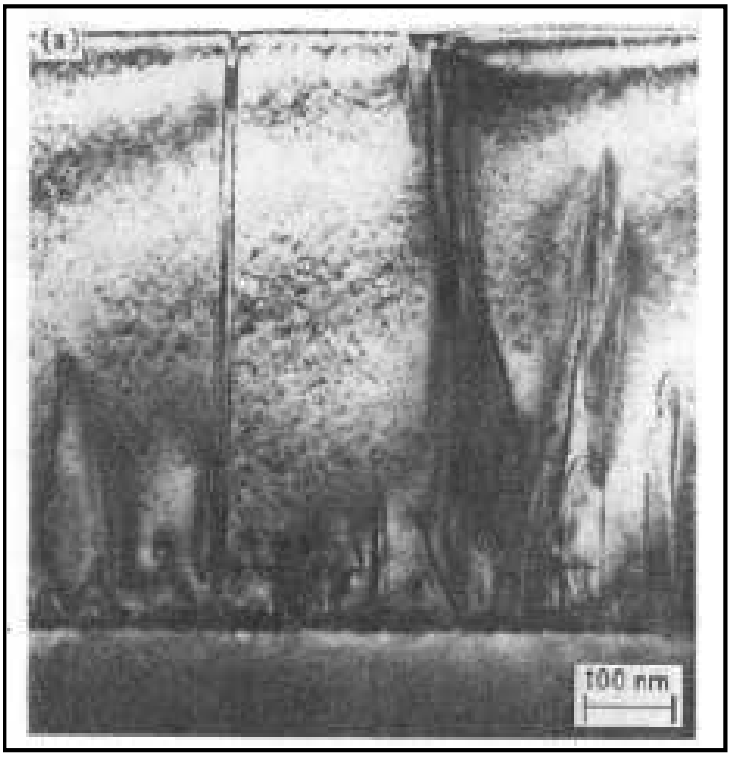

Figure 3.3: Defects inherent in a GaN template grown on sapphire substrates.

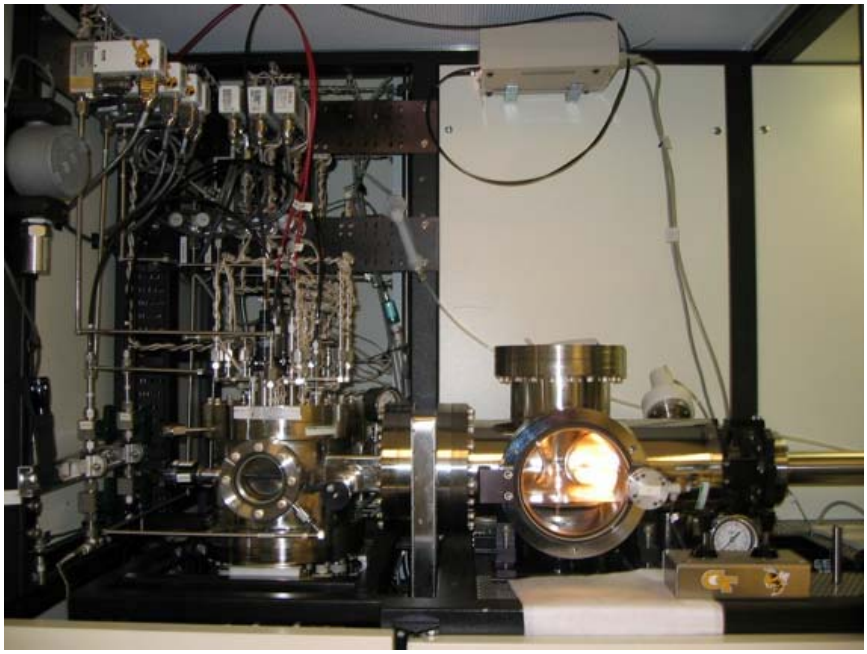

Figure 3.4: MOCVD tool used in this study.

for GaN growth on sapphire, does not contribute carbon, and undergoes pyrolysis at temperatures in excess of 800°C. However, efficient cracking of NH_3 is difficult to achieve. Therefore, the V/III ratio is typically as high as 2000-3000 to ensure that sufficient nitrogen is available to be incorporated so as to form a stoichiometric film. Due to the limited nitrogen sources available NH_3 was used as the nitrogen source in this study.

The GaN growth system at Georgia Tech used in this study is based on a commercial system but has been specially modified. A photograph of the growth tool is shown in Figure 3.4. The reactor is on the left and the load lock used to transfer the wafer carrier into the reactor is shown on the right. Two reactors, specified as the device and material chambers, are interchangeable in this MOCVD system. The device chamber is typically reserved for growths using only standard III-Nitride precursurors and dopants to decrease the likelihood of contamination by experimental materials, including ZnO. The materials chamber is used for all unknown gasses typically not seen for standard III-Nitride growths. The system is designed to accommodate growth temperatures over 1200^{o}C. Moreover, the system has been designed to be able to rapidly switch between two carrier gases, such that depending on the environment and chemistry, either nitrogen or hydrogen can be used as the carrier gas.

3.2.2 Molecular Beam Epitaxy

An alternate method for the growth of LEDs is molecular beam epitaxy (MBE). MBE is an epitaxial growth technique performed under ultrahigh vacuum (UHV). Molecular beams of reactants are produced from various sources and aimed at a substrate to deposit a film that grows epitaxially. Atomic gallium is provided by a K-cell for the

GaN source, while the N source is produced from gaseous N_2 activated by a radio frequency (RF) plasma source. This technique, also known as plasma-assisted MBE, was used in this project. The quality of the growth layers was monitored i*n situ* by use of reflection high-energy electron diffraction (RHEED). MBE growth of GaN is typically performed at a relatively low temperature of 550ºC, compared to the MOCVD temperature of greater than 1000ºC, and at much slower growth rates compared to MOCVD. MBE also allows for H_2 to be used during GaN growth on ZnO.

However, the samples grown by MBE for this project were non-uniform and showed surface pits. Photoluminescence (PL) showed broad spectrums for both GaN and InGaN on ZnO, as can be seen in Figure 3.5. Also, this method is not accepted by industry due to its need for ultra high vacuum and inability to be scaled up as easily as MOCVD. Therefore, further growth studies were continued only by MOCVD.

3.2.3 Atomic Layer Deposition

Atomic layer deposition (ALD) was used to provide a transition layer for promoting nitride growth by MOCVD. ALD is a process where single precursors are pulsed into the reactor separated alternately by purging N_2 or evacuation periods. One critical advantage of ALD over conventional deposition techniques is that film growth is surface-controlled instead of source-controlled. This method allows for a self-limited, layer-by-layer growth mode. Therefore, the film thickness is accurately controlled by the number of growth cycles alone and is largely independent of growth conditions such as temperature. Additionally, precursor fluxes do not need to be uniform across the substrate surface and only need to be large enough so that the chemisorption layer is saturated. Each cycle deposits the same amount of material, with the excess being swept away during purging

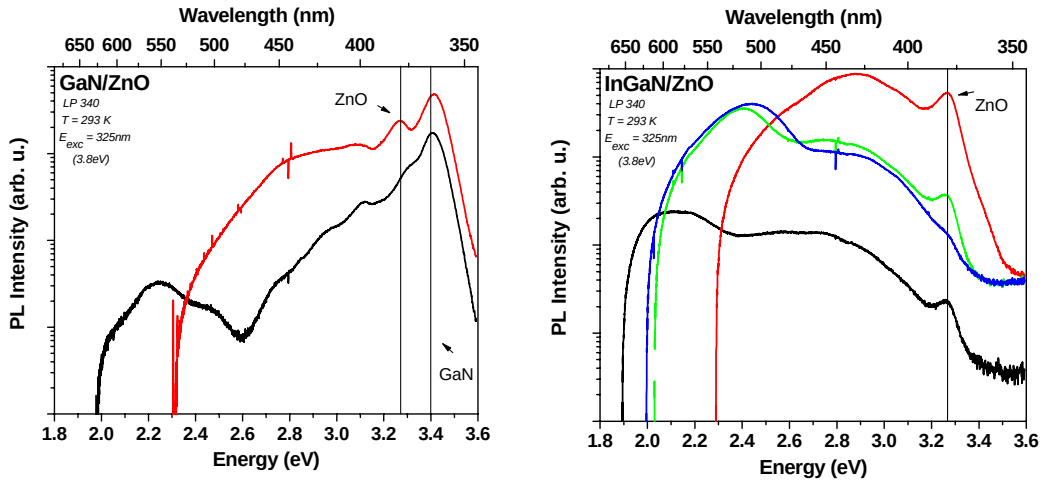

Figure 3.5: Photoluminescence of GaN and InGaN grown on ZnO by MBE.

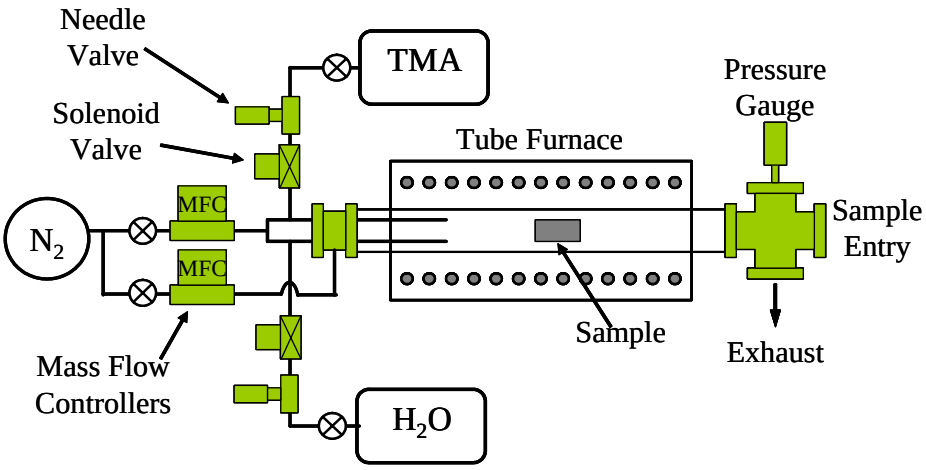

Figure 3.6: Schematic of atomic layer deposition system and picture.

[32, 33]. This method allows for smooth layer deposition with low pinhole density and good uniformity over large-area substrates. The ALD schematic and a picture of the ALD system used for Al_2O_3 deposition on ZnO substrates is shown in Figure 3.6.

3.3 Annealing of ALD Transition Layers

ALD layers are amorphous when grown and therefore annealing tests were performed to crystallize the Al_2O_3 layer for the subsequent MOCVD growth of GaN or InGaN. This process was attempted by rapid thermal annealing (RTA), *in-situ* right before nitride growth in the MOCVD reactor, *in-situ* during ALD growth, and in a conventional thermal annealing furnace. The results will be discussed in Chapter 6. Details of the annealing equipment used are described below.

3.3.1 Rapid Thermal Annealing

Rapid thermal annealing (RTA) is a process where the sample is quickly heated to a high temperature for several minutes or less. RTA is only meant for rapid annealing, such as for p-GaN activation in an LED sample. Samples must be brought down to lower temperatures slowly so that they do not break due to thermal shock. Rapid heating rates are attained by high intensity lamps or laser process. The RTA used in this study was a UVAC MILA-3000.

3.3.2 Furnace Annealing

The bulk of the annealing study was performed in a furnace because of its ability to anneal samples for long durations at high temperatures, over 1000ºC. The furnace was also used to maintain a clean environment for the annealing tests. The MOCVD chamber would allow for the same annealing process; however, it has contaminants from previous

growth runs that could become incorporated into the samples during annealing. The furnace used in this study was a MXI furnace that can reach temperatures as high as 1300ºC. A safety mechanism will shut down the furnace if the inside temperature exceeds a maximum threshold.

3.4 Characterizations

Both destructive and non-destructive measurements were used to characterize and evaluate the grown materials. The non-destructive techniques included high resolution x-ray diffraction (HRXRD or x-ray), room-temperature and low-temperature photoluminescence (PL), optical transmission (OT), atomic force microscopy (AFM), Raman scattering spectroscopy (Raman), atomic emission spectroscopy (AES), and x-ray photoelectron spectroscopy (XPS) to give information on material structure, band structure and defects, absorption features, surface morphology, crystal quality, surface composition, and depth profile. The destructive processes included secondary ion mass spectrometry (SIMS), Rutherford backscattering spectroscopy (RBS), field-emission scanning electron microscope (FE-SEM), energy dispersive x-ray spectroscopy (EDS), cross-sectional high angle annular dark field (HAADF) scanning transmission electron microscopy (STEM), and high-resolution transmission electron microscopy (HRTEM), and provides detailed information on epilayer microstructure, atomic structure, and atomic concentration of alloyed elements. A brief overview of the characterization techniques used in this study is provided below.

3.4.1 High Resolution X-ray Diffraction

High resolution x-ray diffraction (HRXRD or x-ray) is one of the fundamental studies used to characterize the structure of materials. This characterization was used after every

run for quick assessments of crystalline quality so that the subsequent runs could be adjusted and optimized accordingly. This technique uses the principle that waves – in this case an incident x-ray beam – interacting with atomic planes in a sample exhibits the phenomenon of diffraction. At certain angles of incidence, x-rays scattering off neighboring parallel planes of atoms interfere destructively or constructively, resulting in output signals of varying intensity. These constructive interferences occur when the path length difference is an integer multiple of the x-ray wavelength, or when the Bragg condition is met, as given by Equation 3.1:

$$n\lambda = 2d \sin\theta \tag{3.1}$$

An important measurement in epitaxial single-crystal thin films is the study of the planes parallel to the growth axis, known as the on-axis measurement. Additional information related to the crystalline quality and strain in the thin films can be ascertained from diffraction data through other x-ray measurements, such as rocking curves, reciprocal space maps, superlattice peaks, and x-ray reflectivity. Moreover, to examine the crystalline quality of off-axis reflections, it is important that the goniometer have a full range of motion such that it can tilt the diffraction planes of interest into a position perpendicular to the beam of the diffractometer. Studies used in this work were performed using a Philips X'pert MRD-pro 4-circle diffractometer with a monochromatized CuKalpha x-ray source, as seen in Figure 3.7. A schematic of x-ray diffraction is shown in Figure 3.8.

3.4.2 Photoluminescence

The second most important characterization technique is photoluminescence (PL). This technique gives information on band structure and, more importantly, defects within

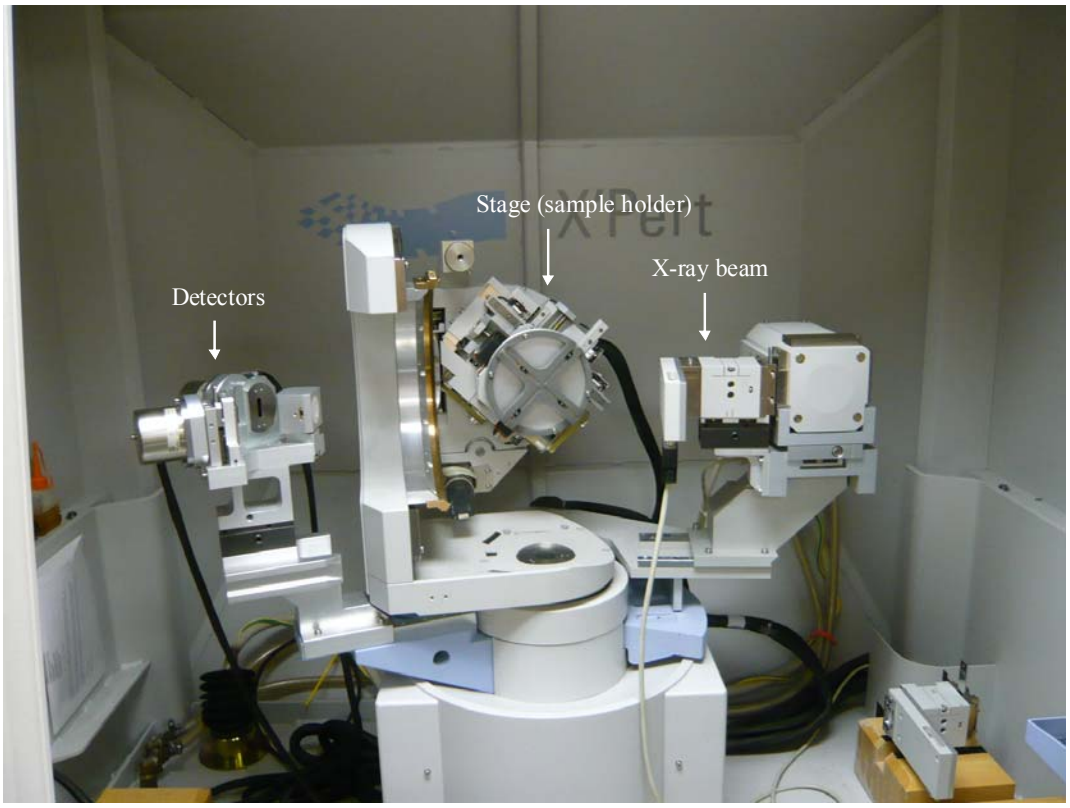

Figure 3.7: Photograph of high resolution x-ray diffraction.

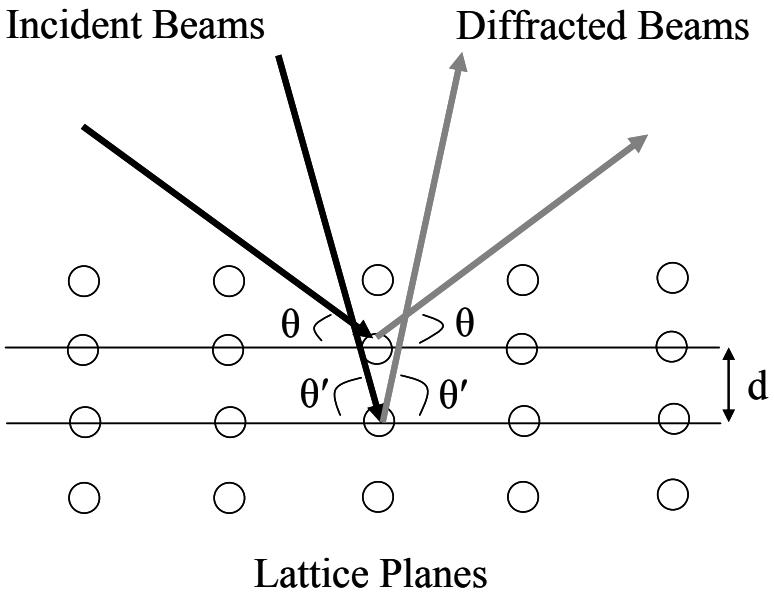

Figure 3.8: Schematic of x-ray diffractions.

the sample, therefore allowing a quick assessment of material quality for subsequent growths. In the PL method, electron-hole pairs are generated by applying an incident laser beam with photon energy greater than E_g on the surface of a sample. These electron-hole pairs will recombine, often through radiative transitions back to the ground state of the activated center. By measuring the wavelength of the emitted photon information can be derived about the band structure, donor and acceptor levels, defect types, impurities, defect densities, and optical quality of the material system. Most PL measurements were performed at room-temperature, which allowed for the study of reactions close to the operational temperatures of a LED. However, low-temperature PL measurements were also performed to temperatures as low as 10K. Low-temperature measurements allow for transitions to slow down or "freeze" in order to remove phonon assisted effects and therefore enabling the capture of emissions that might not be possible at higher temperatures. Two different PL systems were used in this study. One used a Ne-Cu 248nm laser. The emitted light was then passed through a CVI monochrometer and then detected by a Hamamatsu photomultiplier tube. The second system used a He-Cd 325nm laser as the excitation source. The emitted light was passed through a SP-2300i monochrometer and detected using a PIXIS100 CCD camera. An example of a PL system along with a cryostat for low-temperature measurements is shown in Figure 3.9 and possible optical transitions that can be observed in PL are identified in Figure 3.10.

3.4.3 Optical Transmission

Optical transmission (OT) utilizes a tunable light source that is shown through the sample and either absorbed or transmitted through the sample. Apart from reflection losses, light will be almost completely transmitted when the light source energy is less

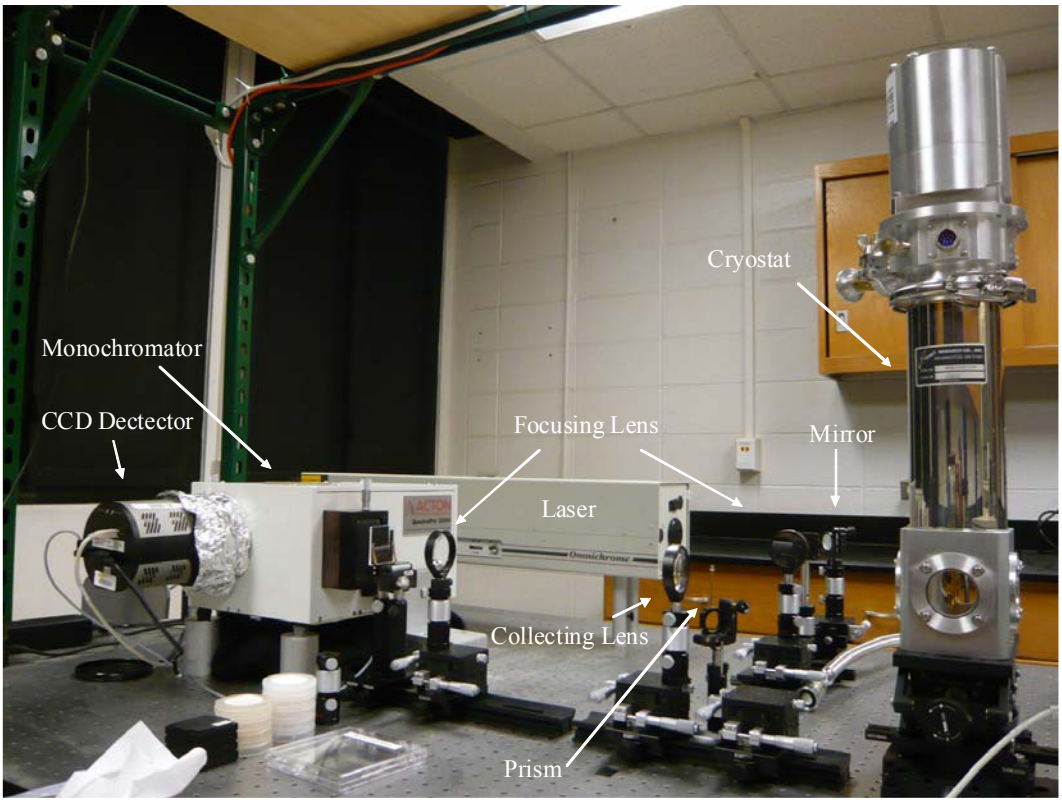

Figure 3.9: Room-temperature and low-temperature photoluminescence setup.

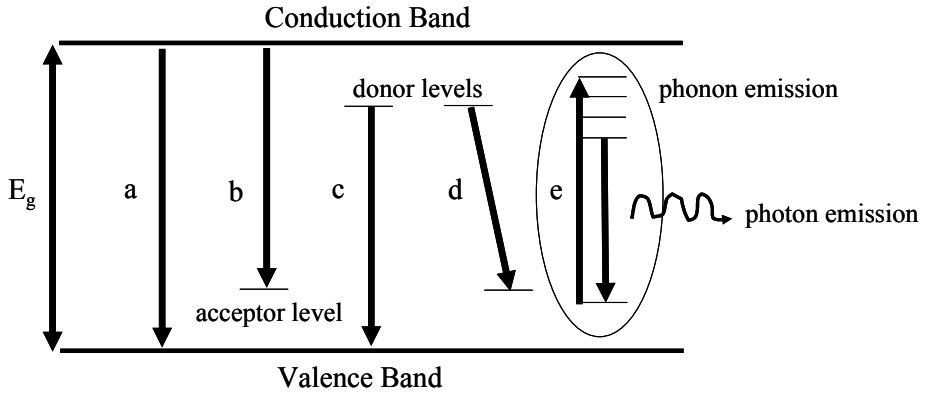

E_g = Energy gap
a = band-to-band transition
b = free electron to acceptor level
c = donor electron and free hole recombination
d = donor-acceptor transition
e = localized transition

Figure 3.10: Possible optical transitions responsible for photoluminescence.

than the bandgap of the material and almost completely absorbed when the photon energy is greater than the bandgap. This technique is useful in detecting absorption-related features that may not show up during luminescence measurements. It also provides an indication of the optical bandedge within a semiconductor material. Transmission measurements for this research used a UV-VIS white light source system.

3.4.4 Atomic Force Microscopy

Atomic force microscopy (AFM) is a technique that measures the surface morphology of films/samples at an atomic-resolution. An atomically sharp tip mounted at the end of a cantilever is scanned across the surface of the sample. A laser light is reflected off of the top of the cantilever, and the position of the reflected laser spot on a position sensitive photo detector (PSPD) can be used to precisely measure the deflection in the cantilever and thus the contours of the surface. This can be done at a constant height above the sample by two different setups. The first setup measures the force in a non-contact mode, and the second measures the deflection of the cantilever by using a fixed force. The surface morphology of the layers in this work was analyzed using an *ex-situ* experimental AFM in a PSIA XE 100 in both contact and non-contact mode. A typical 2D and 3D AFM image for GaN on ZnO and a schematic of an AFM setup are shown in Figure 3.11. The 2D and 3D images show the surface of a ZnO substrate with a surface roughness of RMS = 0.27nm.

3.4.5 Raman Scattering Spectroscopy

Raman scattering spectroscopy (Raman) is another method that can be used to study the crystal quality of a material. Its results are used to study vibrational, rotational, and other low-frequency modes in a system. Raman scattering measures the interaction of

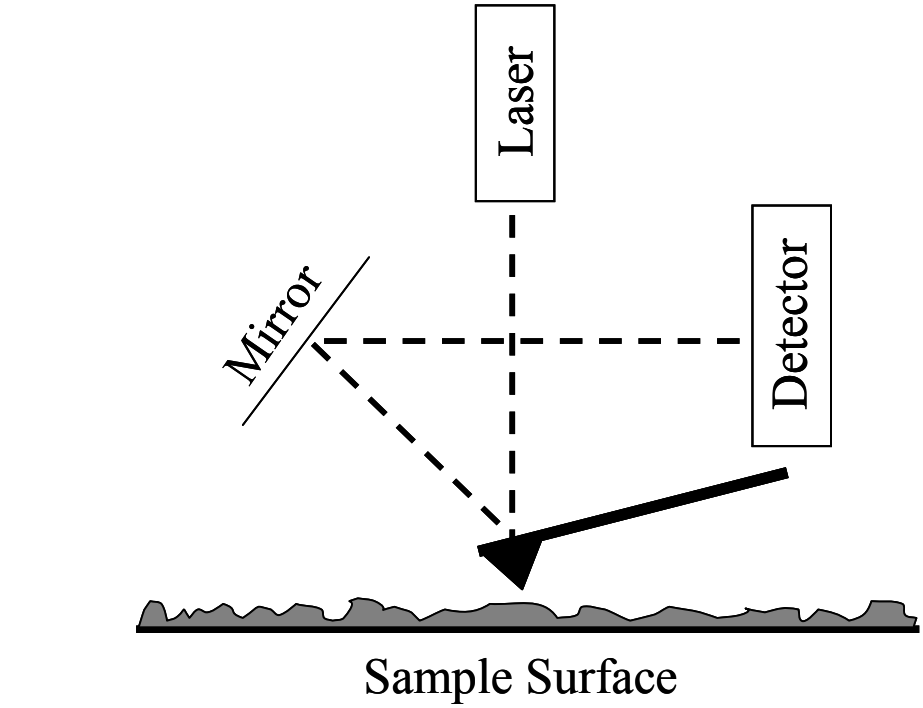

(a)

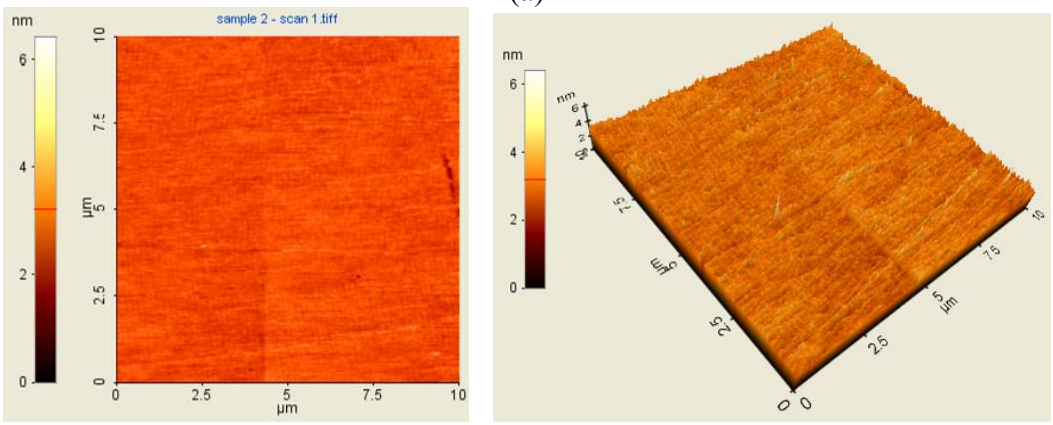

(b)

Figure 3.11: (a) Schematic and (b) typical images obtained from atomic force microscopy. The data shows a 2D and a 3D image of the surface of a ZnO substrate with a surface roughness of RMS = 0.27nm.

light via inelastic scattering from an incident laser beam off of a material. One method for inelastic scattering is to transfer this energy into lattice vibrations or phonons. The laser light interacts with phonons or other excitations in the system, resulting in the energy of the laser photons being shifted up or down. The shift in energy gives information on the phonon modes in the system. Thus, by measuring the energy transferred to or from phonons to photons, which is manifested as a Stokes or Anti-Stokes shift in the inelastically scattered light source, valuable information regarding the quality of the thin films can be obtained. These peaks are usually several orders of magnitude weaker than the laser line, which must be filtered out in order to observe the Raman signal. The variation in scattered intensity or full width at half maximum (FWHM) of scattered light can be related to and used to study crystal quality, which can be related to strain in the material. Raman spectroscopy measurements in this work were performed to determine the crystalline quality using a Renishaw micro-Raman system with a 488 nm excitation source. A schematic of Raman optical phonon modes for wurzite GaN is shown in Figure 3.12. These modes can be applied to the peaks seen for a characterized wurzite GaN layer on sapphire, 20nm Al_2O_3/ZnO, and bare ZnO, Figure 3.13.

3.4.6 X-ray Photoelectron Spectroscopy

X-ray photoelectron spectroscopy (XPS), also known as electron spectroscopy for chemical analysis (ESCA), is a quantitative technique that can measure the elemental composition of the surface of a sample. A sample is irradiated by a beam of aluminum or magnesium x-rays of ~1200-1500eV while simultaneously measuring the kinetic energy spectrum (KE) and number of electrons that escape. XPS requires ultra-high vacuum

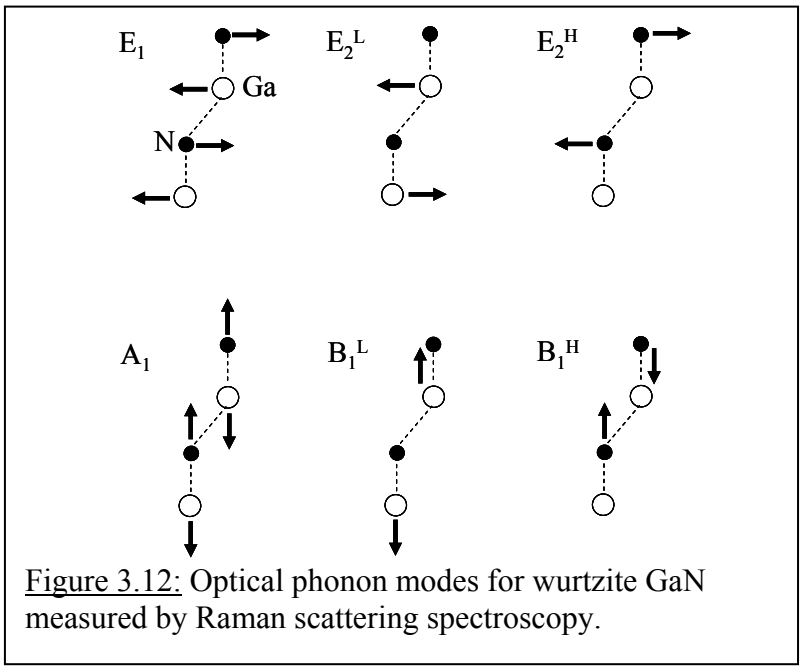

Figure 3.12: Optical phonon modes for wurtzite GaN measured by Raman scattering spectroscopy.

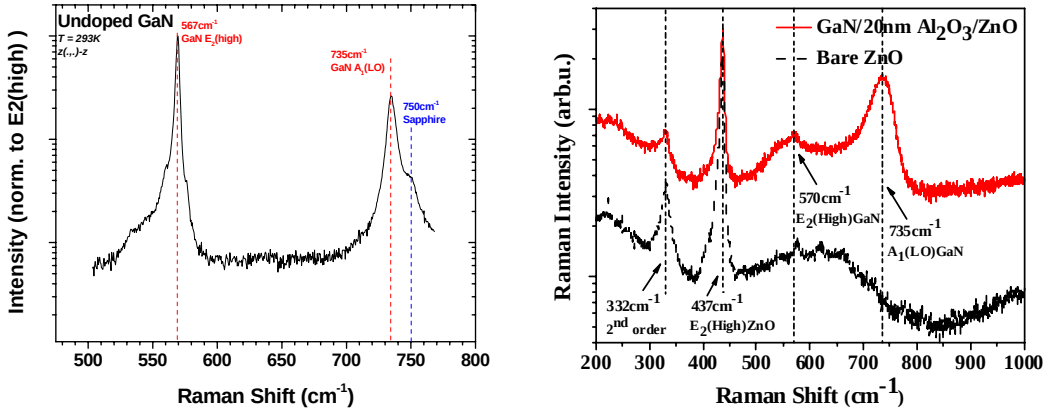

(a) (b)

Figure 3.13: Raman spectroscopy of (a) GaN on sapphire and (b) GaN on 20 nm Al_2O_3/ZnO and bare ZnO substrate.

(UHV) conditions. XPS detects all elements with an atomic number between lithium (atomic number = 3) and lawrencium (atomic number = 103), which means that hydrogen (atomic number = 1) and helium (atomic number = 2) cannot be detected. XPS is also able to measure depth profiles in a non-destructive method. However, it is less sensitive than SIMS due to the detection limit of the available standards at $10^{19\text{-}20}$atoms/cm^{-3}. The XPS system used in this study is a dual chamber Vacuum Generators ESCA/SIMSLAB.

3.4.7 Atomic Emission Spectroscopy

Atomic emission spectroscopy (AES), similar to XPS, is a quantitative technique that can measure the elemental composition of the surface of a sample. However, unlike XPS it uses electrons instead of x-ray as the incident beam. The electrons excite the atoms into excited electronic states that subsequently emit light when they return to the ground electronic state. Each element emits light at a certain wavelength, which is dispersed by a grating or prism and detected in the spectrometer. AES also has the capability to measure Auger electrons or the three-electron recombination process. Two electrons recombine and give off their energy to a neighboring electron, which is then detected by the spectrometer. AES also has the capability to measure depth profiles non-destructively. However, like XPS, it is not as sensitive as SIMS due to the detection limit of the available standards at $10^{19\text{-}20}$ atoms/cm^{-3}.

3.4.8 Secondary Ion Mass Spectrometry

Secondary ion mass spectrometry (SIMS) allows for a detailed study of the atomic concentration of different alloying elements within the lattice. This study is especially important for measuring the degree of Zn and O diffusion into the epilayer during GaN growth on ZnO by MOCVD. SIMS is a destructive method that accelerates ionized

particles towards the material to be measured. The sputtered particles are then captured via a mass spectrometer, which counts the number of particles in a given mass. A standardized sample is used for comparison to account for the differing sputter yields of each element. With these results, it is possible to measure the concentration profile of an element within the host material. This method can be very sensitive and measure concentrations of an element on the order of $10^{14\text{-}15}cm^{-3}$ depending on the particle and source ion. Most SIMS systems have both a cesium and oxygen beam as the primary ion source. For this study only the cesium beam was used due to the need to detect oxygen in all the samples. The SIMS used in this study was the IMF 6f, by Cameca (France).

3.4.9 Rutherford Backscattering Spectroscopy

Rutherford backscattering spectroscopy (RBS), also known as high-energy ion scattering (HEIS) spectrometry, was used to determine the thickness and crystalline quality of materials by measuring the backscattering of a beam of high energy ions impinging on a sample. RBS is generally used to measure the bulk composition and structure of a sample. However, special channeling of the signal can also allow for studies on the surface of the sample. A variety of surface changes can be detected by RBS. One example is the growth of epilayers on foreign substrates. The epilayers tend to either match the substrate structure they are grown on, or completely relax and change into some other structure. Such changes can include the relaxation of a GaN template layer grown on sapphire. The GaN layer is initially strained on sapphire but eventually relaxes once it reaches a certain thickness and is no longer constrained by the sapphire lattice parameters. Surface studies on this relaxation can be studied by RBS. Also, RBS can study if impurities such as Zn or O have diffused from the substrate into the GaN

epilayer. Changes in intensity or peak width can give information on these different materials. The RBS used in this study was a 5SDH-2Pelletron with a collimated 2.023MeV He^+ beam.

3.4.10 Scanning Electron Microscope

Scanning electron microscope (SEM) is a destructive process but provides detailed information on epilayer microstructure as well as cross-sectional information of the layers grown on the substrate. A thin layer of gold is deposited on the layer prior to measurement due to the need for the material to be conducting to prevent charging of the substrate. An electron beam, with an energy range of 200V-30KV, is focused on a point on the sample with a spot size of about 1-5nm. The beam rasters over a rectangular area on the sample causing energy exchange between the electron beam and the sample, which results in the emission of electrons and electromagnetic radiation. The detected secondary electrons create a 2D image. The brightness of the signal depends on the number of secondary electrons reaching the detector. SEM has the ability to image both bulk and thin film materials. The SEM used in this study was a LEO 1530 thermally-assisted field-emission (TFE) scanning electron microscope. FESEM produces clearer, less distorted images with resolution as low as 1nm, which is almost 6 times better than conventional SEM.

3.4.11 Energy Dispersive X-ray Spectroscopy

Energy dispersive x-ray spectroscopy (EDS) is a surface analysis method used to determine the elemental distribution on a surface. EDS systems can be standalone, but are more commonly connected with a SEM system, as was the case for this study. There are four primary components of the EDS setup: beam source, x-ray detector, pulse

processor, and analyzer. Charged particles from the beam source hit the sample, emitting x-rays. Analysis of the x-rays allows for a detailed study of each element in the sample due to fact that each element has a unique atomic structure.

3.4.12 Transmission Electron Microscopy

Transmission electron microscopy (TEM) is a technique where a beam of electrons is transmitted through a very thin sample, interacting with the atoms in the sample as they pass through. The interaction forms an image as the electrons pass through the sample, which is magnified and captured by a CCD camera. The sample preparation for this measurement is very time consuming as the samples have to be thin enough for electrons to pass through. Therefore, the throughput of samples is low. The two TEM measurements used in this study are high-resolution transmission electron microscopy (HRTEM) and cross-sectional high angle annular dark field (HAADF) scanning transmission electron microscopy (STEM). HRTEM utilizes high resolution imaging in order to see the individual atoms in the material. However, HRTEM relies on phase-contrast between electrons which sometimes makes it hard to interpret images without a simulation. The electron optics in a STEM focuses onto a narrow spot and then rasters over the area, thereby avoiding phase-contrast. The combination of STEM with HAADF allows for an atomic resolution image where direct correlation to the atomic number can be made.

3.5 Summary of Growth and Characterization

The main growth process investigated in this work was MOCVD, which is the industry accepted method for LED production. The use of MOCVD brings up many

issues for GaN growth on ZnO due to the high temperature requirements for GaN deposition and the need for H_2 as a catalyst during growth. A solution was developed by utilizing a transition layer technique based on ALD. The ALD layers were amorphous after growth; and therefore, an annealing study was performed in order to obtain the optimal annealing parameters for subsequent MOCVD growth of GaN. The materials were characterized by destructive and non-destructive methods in order to understand the material structure, band structure and defects, absorption features, surface morphology, crystal quality, epilayer microstructure, and atomic concentration of alloyed elements. These detailed studies provided a close analysis of the materials grown and lead to the results discussed in the following chapters.

CHAPTER 4

INITIAL GROWTH STUDIES OF GaN ON BARE ZnO SUBSTRATE

This work has demonstrated the first GaN growth on bare ZnO substrates by metalorganic chemical vapor deposition (MOCVD). Initially, MOCVD growth of GaN on ZnO brought many challenges because of Zn diffusion out of the substrate and H_2 back-etching into the substrate. These problems caused cracking in the epilayer and surface peeling while in the chamber. Various methods were attempted to resolve these issues, such as applying buffer layers of different materials, growth at different temperatures ranging from 540ºC to 950ºC, and different flow rates of the metalorganic and hydride precursor sources. Three generations are presented to show the steps leading to a uniform, crack-free, and strongly adherent (no peel-off) GaN epilayer grown on ZnO by MOCVD.

4.1 Introduction

GaN and other III-nitride materials offer superior characteristics over many other III-V materials for electronic and optoelectronic applications due to its wide energy bandgap, saturated electron velocities, and good stability at high temperature. This material system can be used to develop light emitting diodes (LEDs) to cover the whole visible color spectrum. The traditional method of GaN growth is on sapphire substrates. However, this leads to high dislocations, 10^8-10^{10}cm^{-2}, due to the large 16% lattice mismatch and thermal expansion coefficient mismatch between GaN and sapphire. ZnO substrates have

only a 1.8% lattice mismatch and a similar thermal expansion coefficient as GaN. Therefore, ZnO should be a better base for the growth of GaN leading to lower dislocation materials. However, due to the issues mentioned before, many challenges were faced when growing on ZnO.

GaN growth on sapphire substrates was used as the standard for high-quality GaN growth on ZnO substrates because of its accepted use for current commercial LEDs. Typical x-ray diffraction (x-ray) and room-temperature photoluminescence (PL) data for GaN on sapphire are shown in Figure 4.1. These peaks show clearly distinct GaN peaks. The x-ray data shows a (0002) GaN peak with a full width at half maximum (FWHM) of 216arcsec at 17.3 degrees for the omega scan, which correlates to about 34.6 degrees for a 2 theta-omega scan. PL shows a GaN peak at 3.42eV with a FWHM of 0.04eV. A slight yellow emission can be seen on the left. The yellow emission is commonly seen in GaN due to inherent defects in the material. The ratio between the blue and yellow peak intensities is 37.791. These are typical values obtained for high-quaility GaN on sapphire.

The first growths of GaN on ZnO substrates did not show such prominent GaN peaks. In fact, over 150 growth studies were performed before the first distinct GaN PL and x-ray peaks indicated the presence of GaN. All samples showed a distinct ZnO peak at 3.27eV for the main ZnO (0002) peak. GaN should peak at ~3.42eV and most samples observed a PL spectrum with a hint of a shoulder peak between 3.3eV and 3.4eV, but this could have been due to defects in the material. A shoulder between 3.2eV and 3.25eV was attributed to Zn doped GaN, which lowers the ability of GaN to emit. Also, it is more difficult to excite GaN sufficiently to emit stronger than ZnO due to ZnO having a

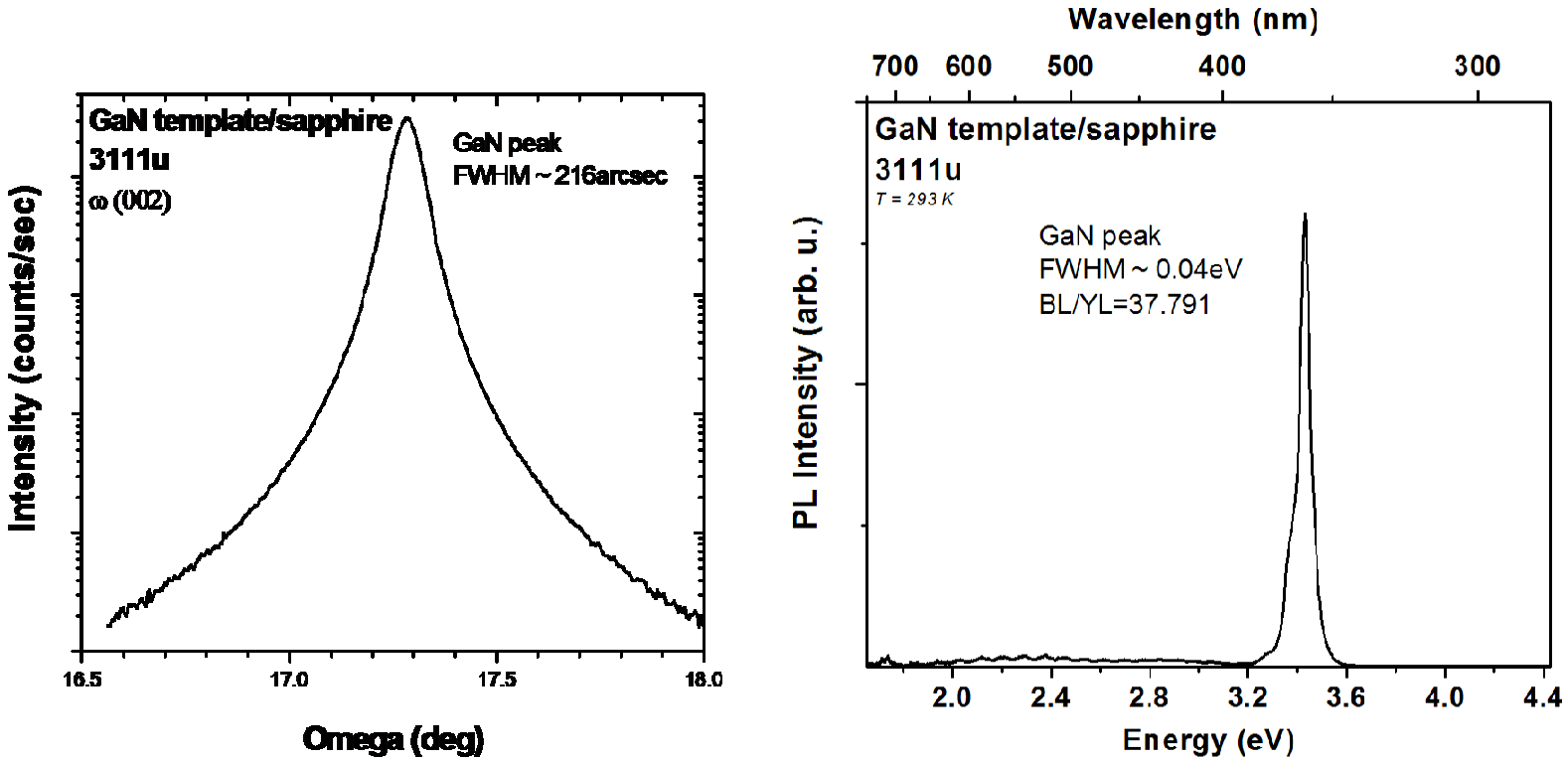

Figure 4.1: (a) HRXRD with FWHM of 216arcsec and (b) PL with FWHM of 50μm of GaN template on sapphire. These are typical results from high-quality GaN on sapphire.

smaller bandgap than GaN and therefore absorbing some of the energy from the GaN emission.

Various buffer layers were attempted to resolve these issues. Different materials such as GaN, AlN, InGaN, InN, or AlGaN were used either as single layers or in combination with each other. However, only GaN and AlN buffer layers proved successful in solving the issues of growing GaN on ZnO. These results are summarized in three generations below covering the steps taken towards the first successful GaN growth on ZnO by MOCVD. The first generation study resulted in multiple cracks in the layers which prevented any useable epilayer or devices to be made. The second generation used multiple buffer layers and solved the cracking issue, but the peeling of the buffer layers became an issue due to pinholes still inherent in the material. The third generation solved both the cracking and the peeling by using multiple buffers and an initial AlN buffer layer instead of GaN. Specific details are presented and discussed below.

4.2 Generation 1a: High Temperature Anneal of Low Temperature GaN on ZnO

The goal of Generation 1a was to grow GaN on ZnO at a temperature high enough to achieve high-quality GaN. Recipes were based on growth on sapphire since there were no successful reports of GaN growth on ZnO reported in the literature.

The goal of the first GaN on ZnO growths was to grow an initial low-temperature GaN buffer layer in order to provide a nucleation surface for grown epitaxial GaN. This buffer layer was then recrystallized at a higher temperature of 1000ºC and then GaN deposited at a temperature over 1000ºC to form a high-quality epilayer GaN. However,

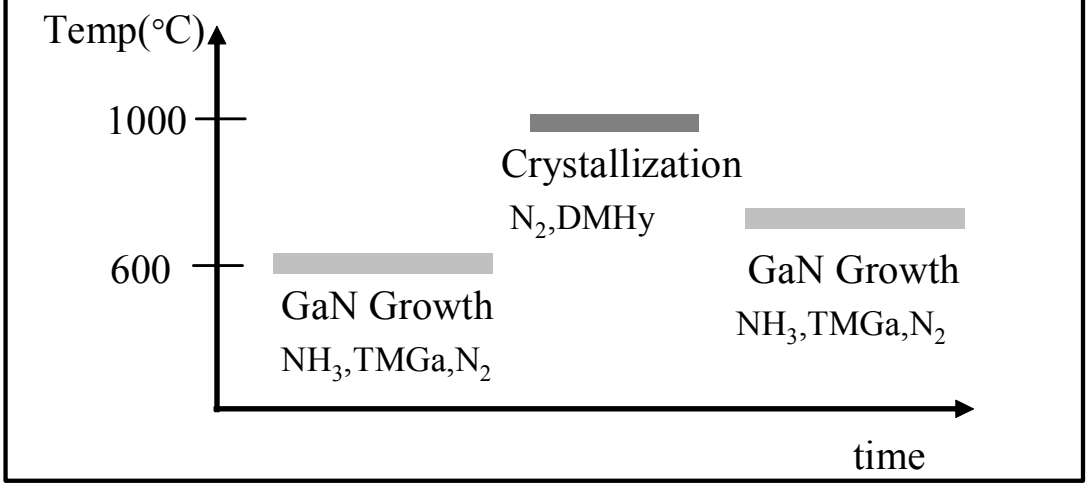

Figure 4.2: Schematic of growth conditions for Generation 1a.

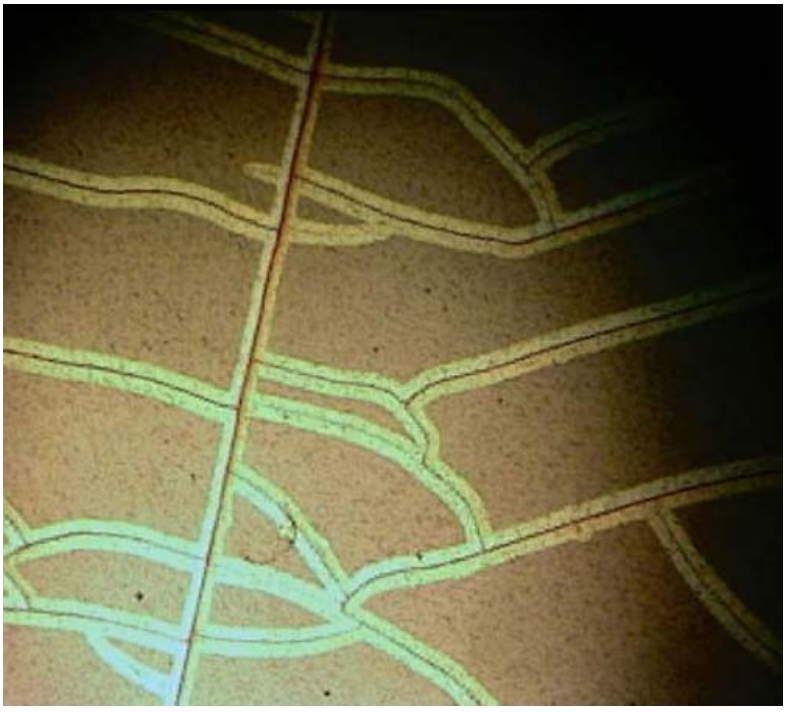

Figure 4.3: Cracking of GaN epilayers grown on GaN buffer/ZnO.

the high temperatures were an issue as discussed below, and these three steps were taken and modified in order to achieve a temperature of 1000°C while maintaining a stable substrate.

The final recipe used in Generation 1a consisted of first covering the ZnO surface with a 150nm thick low temperature (LT) GaN layer deposited at 540ºC. Then, this layer was recrystallized at a higher temperature of 1000°C. A 100nm thick GaN layer was then grown after annealing at around 800°C, see Figure 4.2. The epilayer GaN was not able to reach the desired 1000ºC due to the issues discussed below. The entire growth process was performed in a N_2 atmosphere to prevent H_2 back-etching from the H_2 carrier gas. However, ammonia (NH_3) also introduces unwanted H_2 into the growth process at temperatures greater than 800°C. Consequently, dimethylhydrazine (DMHy) was investigated as a replacement for N_2 in order to overcome unwanted H_2. However, a high concentration of carbon was found in these layers leading to low-quality GaN. Therefore, the use of NH_3 was continued as the nitrogen source, and DMHy was used only during the recrystallization process as a protective gas to prevent GaN decomposition.

The results from this procedure showed serious surface cracking, Figure 4.3. However, the PL and x-ray studies did show peaks attributed to GaN after recrystallization optimization, Figure 4.4. X-ray showed a (0002) GaN peak with a FWHM of 452arcsec. The PL showed peaks at 3.46eV and 3.27eV, which are attributed to GaN and ZnO, respectively. Note that the GaN peak has a lower intensity than the ZnO. This is due to ZnO having a smaller bandgap than GaN and therefore absorbing some of the energy from the GaN emission.

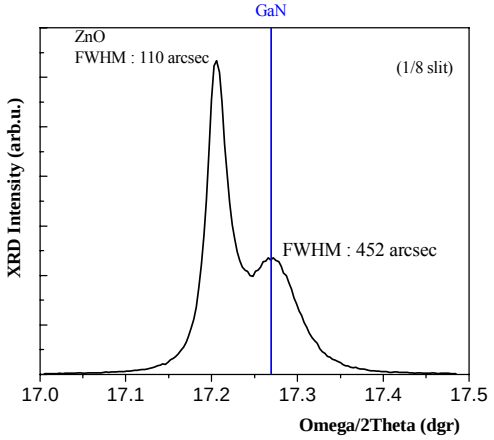

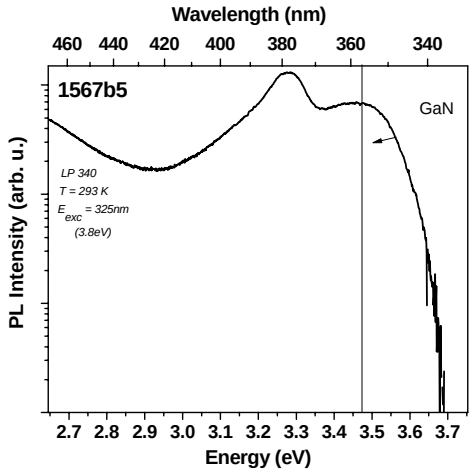

Figure 4.4: HRXRD and PL of GaN on ZnO for Generation 1a growths.

(a)

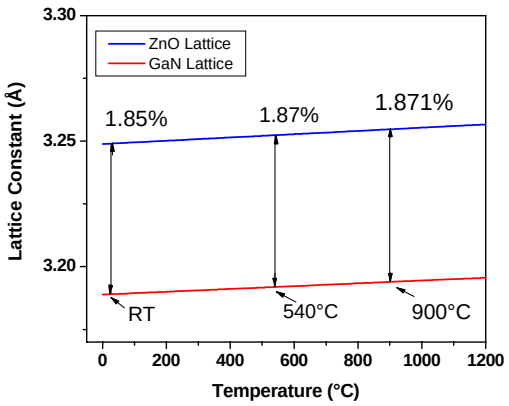

(b)

Figure 4.5: (a) Cracking on surface and (b) temperature dependent lattice constant calculations between GaN and ZnO.

Two checks were performed in order to see if the small lattice mismatch between GaN and ZnO and the difference in thermal expansion coefficients could be the cause of the cracking. GaN was replaced by an InGaN layer containing 18% indium that is perfectly lattice matched to ZnO. However, the InGaN layer also showed many cracks on the surface, and therefore, the lattice mismatch between GaN and ZnO was ruled out as the cause for the cracking, Figure 4.5(a). Calculations were performed to compare the temperature dependence of the thermal expansion difference between GaN and ZnO. The lattice mismatch stayed relatively consistent over the temperature difference, Figure 4.5(b). Therefore, the thermal expansion difference between GaN and ZnO was also ruled out as the cause for the cracks.

Possible origins for the cracking are phase transformation and recrystallization during temperature ramping that would lead to a concentration of stress at the grain boundaries. Additionally, NH_3 can diffuse through the cracks into voids underneath the cracks, degrading the film quality and making high temperature epitaxy impossible.

4.3 Generation 1b: Multi LT-GaN Buffer for Crack Free Growth

The goal of Generation 1b was to solve the cracking problem in Generation 1a. Multiple buffer layers were used to achieve this goal.

The structure grown in Generation 1a was used as the buffer layers for Generation 1b. The 1st buffer layer from Generation 1a was modified by reducing its thickness from 150nm to 80nm for easier phase transformation during the crystallization step and also to minimize stress between the ZnO substrate and the first buffer layer. Crystallization with DMHy was then performed at 1000°C. The 2nd GaN buffer was the GaN epilayer from

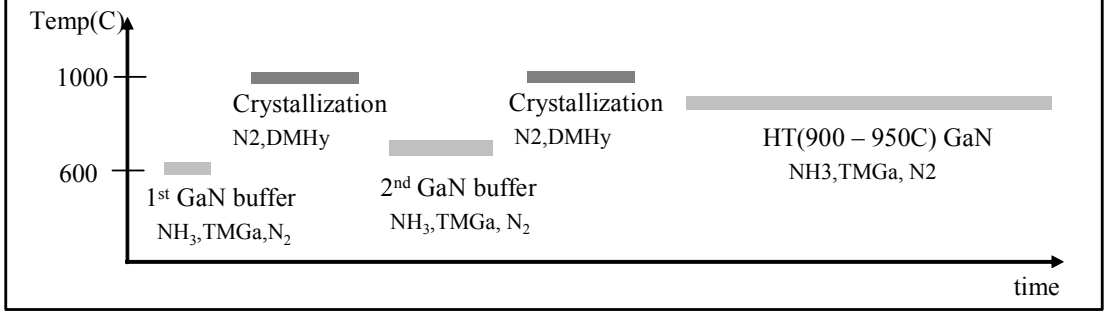

Figure 4.6: Schematic of growth condition for Generation 1b.

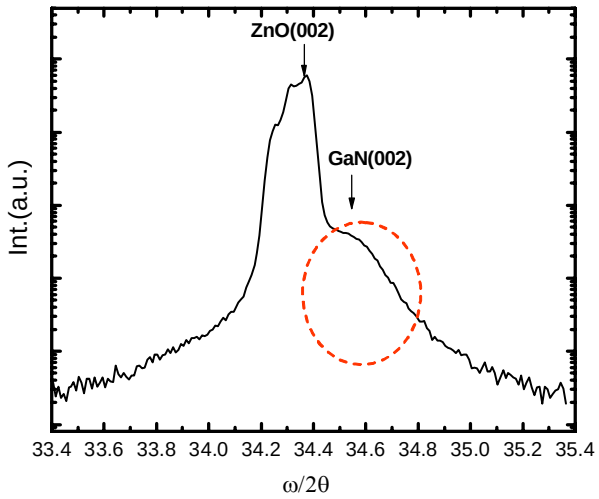

Figure 4.7: HRXRD of GaN on ZnO using a multiple buffer layer approach to ramp up temperature for high-temperature growth of GaN epilayer.

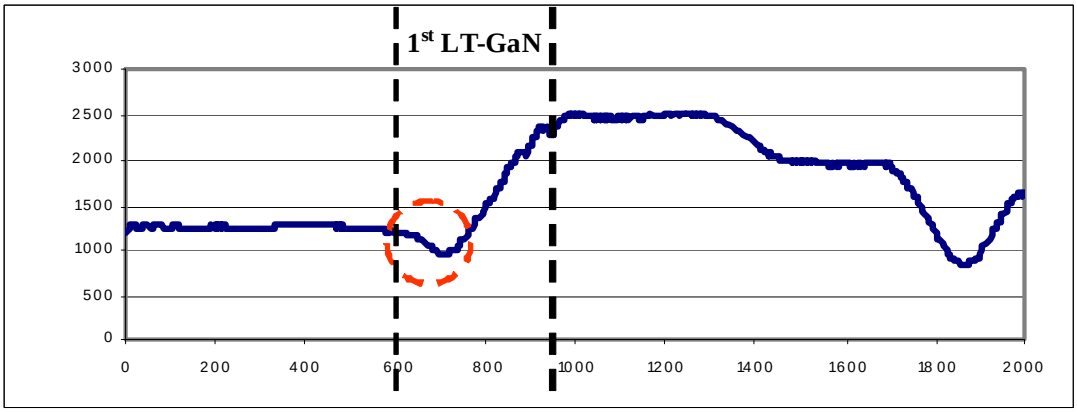

Figure 4.8: Epimetrix showing dip in reflective signal at the initial stage of 1st LT-GaN.

Generation 1a. The 2nd 100nm GaN buffer layer covers the pinholes from the 1st GaN buffer and provides a second layer to ensure the surface is completely and uniformly covered by GaN before high-temperature growth. Crystallization with DMHy was performed for a second time after the 2nd GaN buffer. A 150nm GaN epilayer was then grown at 900ºC. Therefore, Generation 1b used multiple buffer layers in order to gradually ramp up the growth temperature and also to cover the ZnO surface thoroughly, see Figure 4.6.

Results showed that with the two GaN layers it was possible to grow at temperatures as high as 900-950°C, and therefore, subsequently achieve epilayer growth of GaN. X-ray was also able to detect GaN, Figure 4.7. The peak was much weaker than Generation 1a due to peeling of the layers. *In*-situ monitoring of these buffer layers showed the reflective signal dropped at the initial stage of the 1st LT-GaN layer, Figure 4.8. The signal drop could be due to surface roughening at the initial growth stage, but there are two other possibilities to be considered. The two possibilities for the signal drop are the growth of a layer whose refractive index is smaller than ZnO or an alloyed layer of quaternary GaZnNO layer that forms at the initial stage of growth. A comparison performed by atomic force microscopy (AFM) showed a rougher surface for when the signal drops, which is attributed to an intermixing layer, Figure 4.9(a). The signal drop was found to be very sensitive to the growth temperature of the 1st GaN buffer layer. Optimization of the growth temperature resulted in a sweet spot for the transition layer for crack-free growth, Figure 4.10. The sweet spot was located at a growth temperature of about 650ºC. T represented the depth of the signal drop and hence the thickness of the intermixing layer. Temperatures below 650ºC resulted in cracked layers and a thin

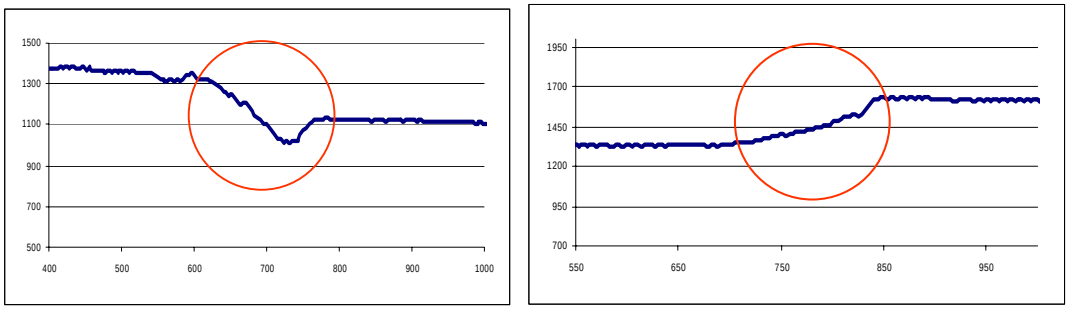

(a)

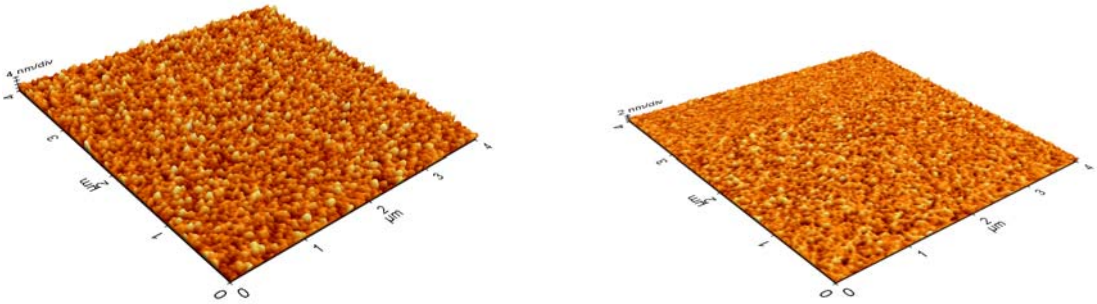

GaZnON layer

RMS = 1.5nm

GaN layer

RMS = 1nm

(b)

Figure 4.9: (a) Epimetrix showing reflective dip at the initial stage of 1st LT-GaN. This corresponds to an intermixing layer of GaZnON which shows a rougher surface. (b) Epimetrix showing reflective signal with no drop in the signal. This corresponds to a smoother surface of GaN.

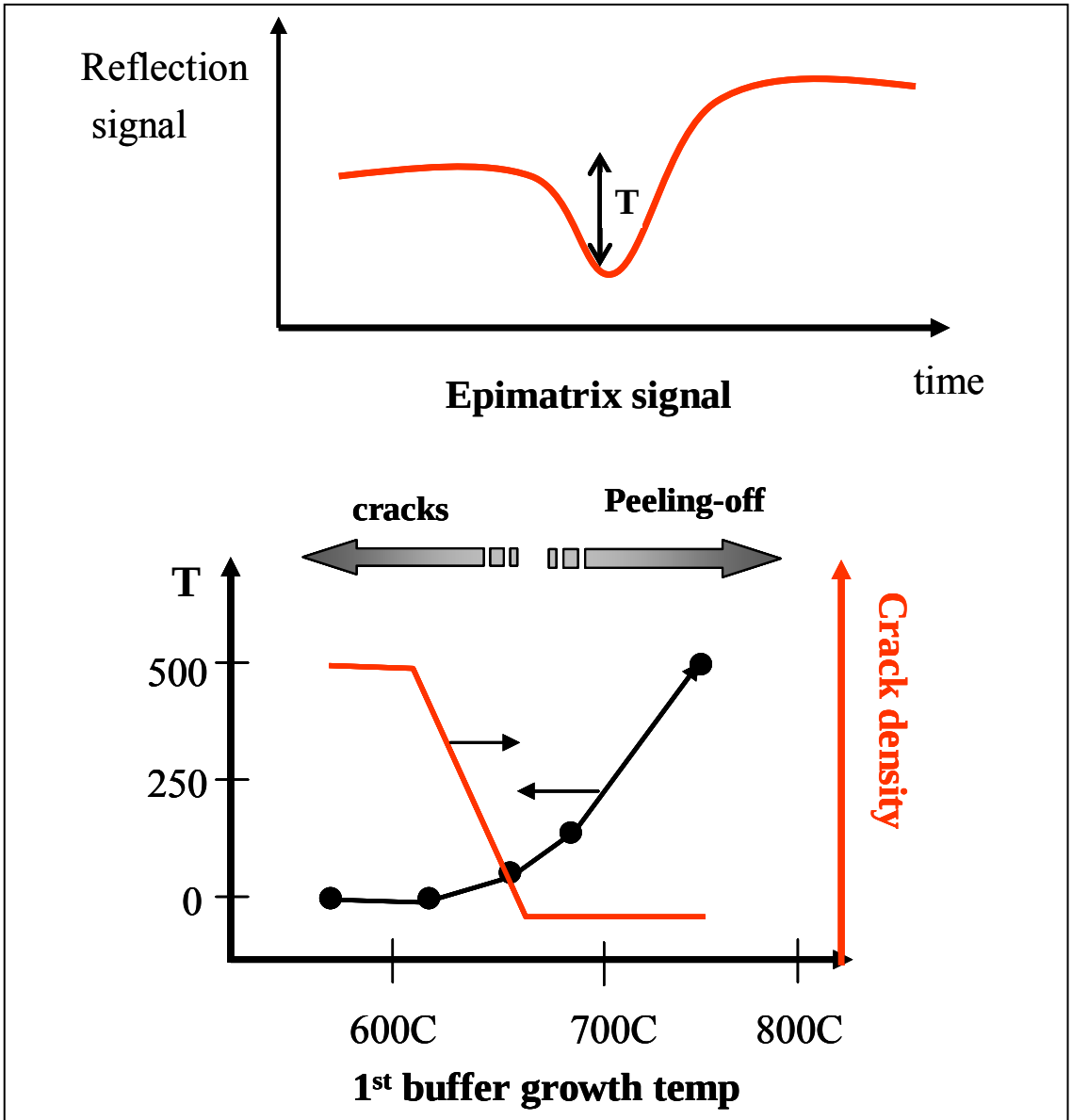

Figure 4.10: Optimization of the growth temperature resulted in an optimized crack-free transition layer. T represented the depth of the signal drop and hence the thickness of the intermixing layer.

Figure 4.11: SEM of (a) peeling-off region and (b) and (c) of point etching of ZnO.

intermixing layer. Temperatures above 650ºC resulted in fewer cracks and a thicker intermixing layer, but peeling of the epilayer appeared. The optimized spot resulted in a transition layer that helps with preventing cracks by absorbing the strain between the GaN and ZnO. However, this transition layer, an intermixing layer of GaZnNO, could still be too thick causing an adhesion problem and resulting in some regions peeling-off entirely. All areas also showed high-density etched pits of the ZnO substrate through GaN pinholes. Scanning electron microscope (SEM) images of peeling-off of the ZnO substrate and pinholes are shown in Figure 4.11.

At the end of Generation 1b the cracking issues were solved, but pinholes still appeared in the samples leading to peel-offs of the layers and etched pits. A possible origin of the peeling-off and etched pits are the pinholes in the LT-GaN multi-buffer layers. NH_3 can attack the ZnO substrate through the pinholes. Therefore, the high-density pinhole regions could be the peeling-off regions. The pinhole density in the LT multi-buffer layer needs to be reduced in order to solve the peeling off issue.

4.4 Generation 2: 1st AlN and 2nd GaN LT-buffer Layers

The goal of Generation 2 is to solve the peeling off issue. The end result was to use an AlN buffer layer to cover the surface more densely before growing the 2nd GaN buffer layer.

Generation 2 was the same structure as Generation 1b for solving the cracking and peeling-off issues. However, the first buffer layer was changed from GaN to AlN, Figure 4.12. The final GaN epilayer had a growth rate of about 1.77μm/hr and was about 80nm thick. AlN was investigated to prevent peel-off due to Al's low surface mobility and high

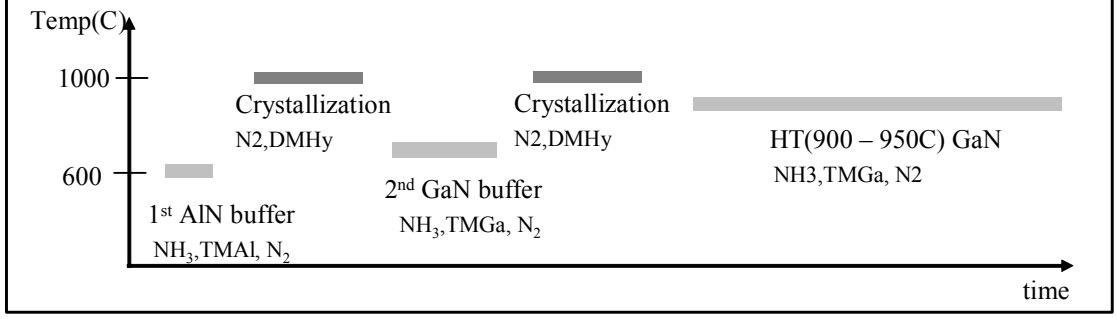

Figure 4.12: Schematic of growth condition for Generation 2.

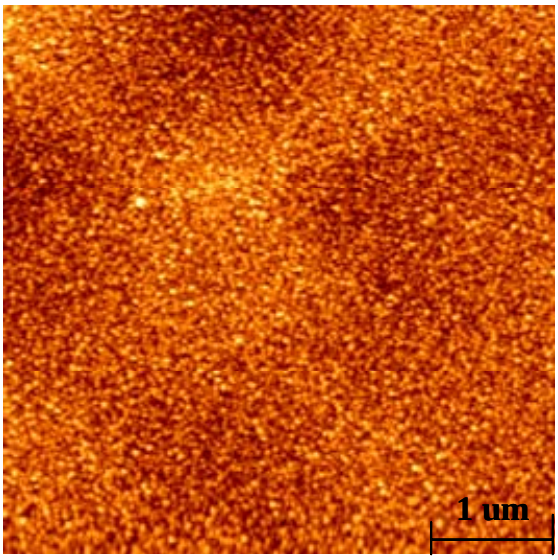

(a)

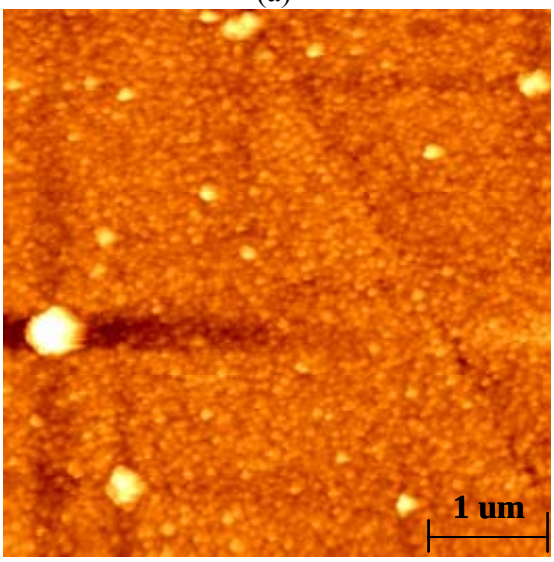

(b)

Figure 4.13: AFM of (a) LT-AlN after annealing with RMS = 4.3nm and (b) LT-GaN after annealing with RMS = 3.7nm.

surface coverage. Al also has a stronger bond to N than Ga potentially resulting in a more stable interfacial layer for high temperature growth. AlN provides a more complete surface coverage on ZnO, allowing for lower surface pinholes during the high temperature crystallization step. AFM images show ALN providing a more densely covered nuclei on top of the ZnO surface compared to GaN, Figure 4.13. The interfacial layer of AlZnNO might also be more suitable for absorbing the strain than GaZnNO.

An optimization study on the final structure found that the final GaN epilayer was sensitive to the growth time of the AlN buffer layer and the thickness of the GaN buffer layer. The optimal time for the AlN buffer layer was about 6.5 minutes where neither cracking nor peeling appeared. Below 6.5 minutes, even at 4 minutes, the surface showed signs of pinholes appearing. Above 6.5 minutes, as close as 8 minutes, pinholes started appearing. Longer times of 15 minutes resulted in whole surfaces peeling off. The optimal thickness for the GaN buffer layer was found between 60nm and 120nm. Layers thinner than 60nm did not provide enough coverage for high-temperature GaN growth and peeling-off of the layers were seen. Layers thicker than 120nm proved hard to crystallize as PL intensities were weak.

Results showed PL emission at 3.46eV and 3.27eV, which are attributed to GaN and ZnO, respectively. These results were very unique as most samples did not show a prominent GaN peak, but they were still not a big improvement from Generation 1a. The PL GaN was lower than the ZnO peak due to the absorption from the ZnO smaller bandgap. X-ray had a GaN peak with a FWHM of 151arcsec, Figure 4.14. However, this peak might be a low angle grain boundary. It was also very weak and not a significant improvement from Generation 1a. Crack free, no peeling-off, and low defect

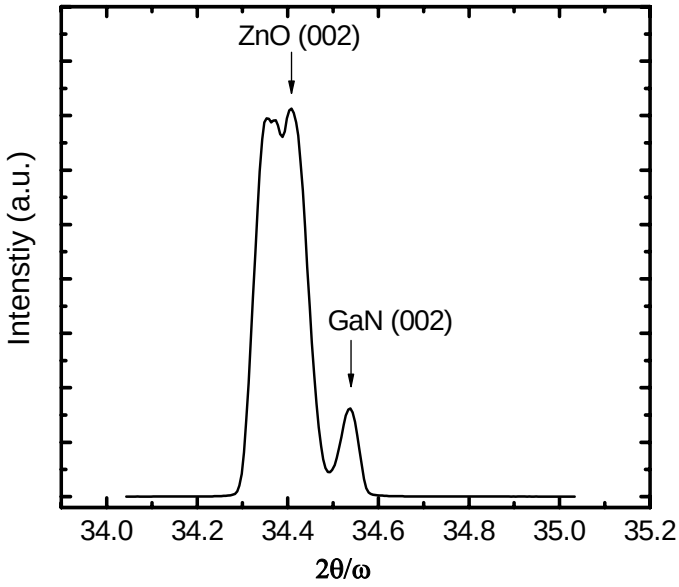

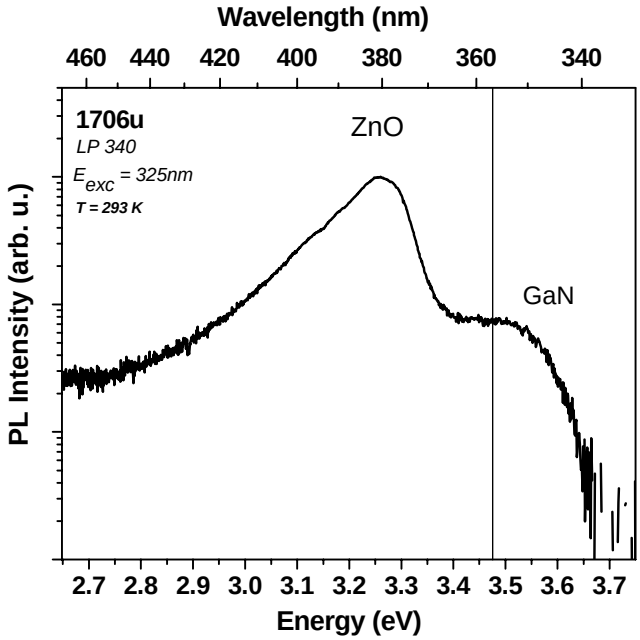

Figure 4.14: PL and x-ray of GaN on ZnO for Generation 2 growths.

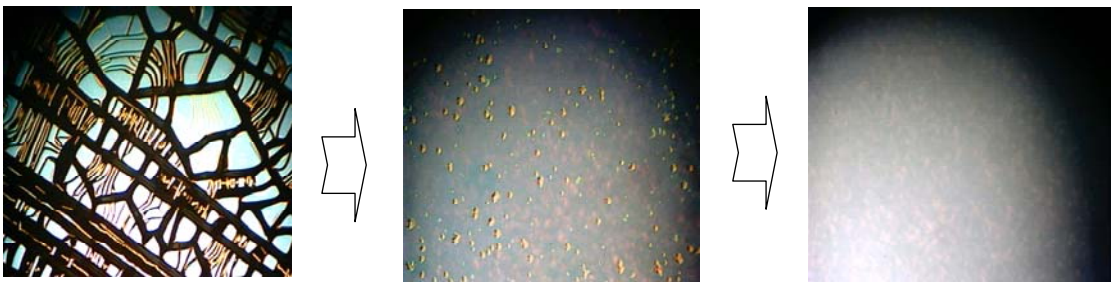

Figure 4.15: Crack free, no peeling-off, and low defect density GaN surfaces have been obtained from optimized buffer layers using AlN as the first buffer layer.

density GaN surfaces were obtained from these optimized buffer layers as seen in Figure 4.15.

The etch pit density (EPD) was performed with 85% H_3PO_4 at 160°C for 90-120 minutes at 160x magnification. Random areas were selected over the entire wafer and all etched pits contained in a fixed area were counted. An EPD for GaN on ZnO was found to be 1.2 $x10^6 cm^{-2}$ by the end of Generation 2, Figure 4.16(a), which was significantly lower than would be achieved on sapphire and SiC. Normal defect densities of GaN on sapphire are around $10^{8-10} cm^{-2}$. Blue emission was also visible to the eye on different areas of $20x20mm^2$ samples, Figure 4.16(b). This emission was excited by a 325nm HeCd laser. Crack free, no peeling-off, and low defect density GaN surfaces have been obtained, however, x-ray and PL still do not show optimal results indicative of high-quality GaN.

4.5 Evidence of Zn and O Diffusion Into GaN Layers

Secondary ion mass spectrometry (SIMS) was performed to measure the concentration of different elements in the GaN/ZnO structures. There was a high concentration of $Zn=5x10^{19}$ and $O=10^{21} atoms/cm^3$ in the GaN layer, which indicates a high rate of Zn and O diffusion from the ZnO into the epilayers, Figure 4.17. However, the results also demonstrated that GaN was successfully grown on ZnO substrates as seen by the high concentration of Ga and N in the epilayer. The high concentration of Zn and O make it more difficult to dope GaN p- and n-type for LED structures.

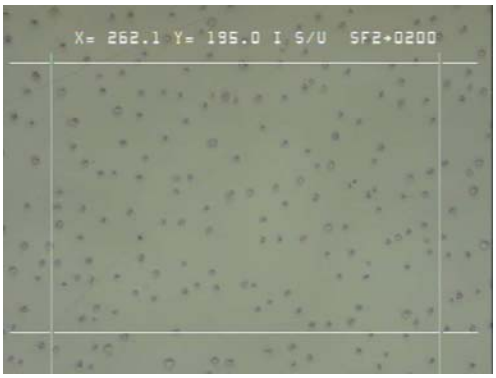

(a)

(b)

Figure 4.16: (a) EPD of 1.2 x$10^{6}$$cm^{-2}$ which is less than GaN grown on sapphire or SiC and (b) blue emission from GaN on ZnO.

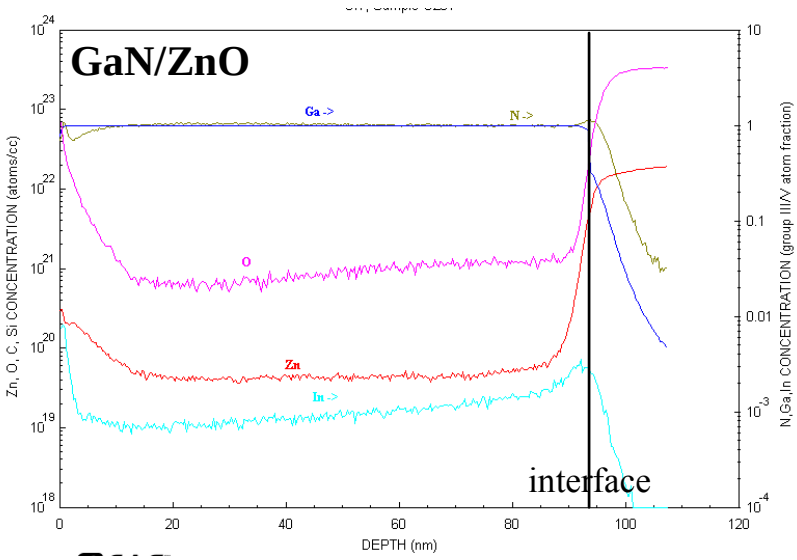

Figure 4.17: SIMS of GaN/ZnO.

Figure 4.18: Schematic of GaN directly grown on ZnO.

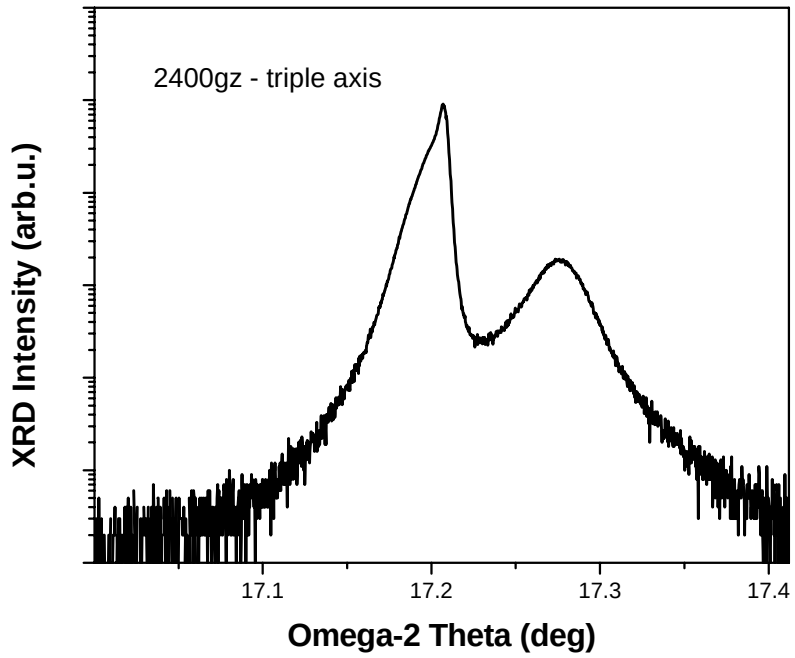

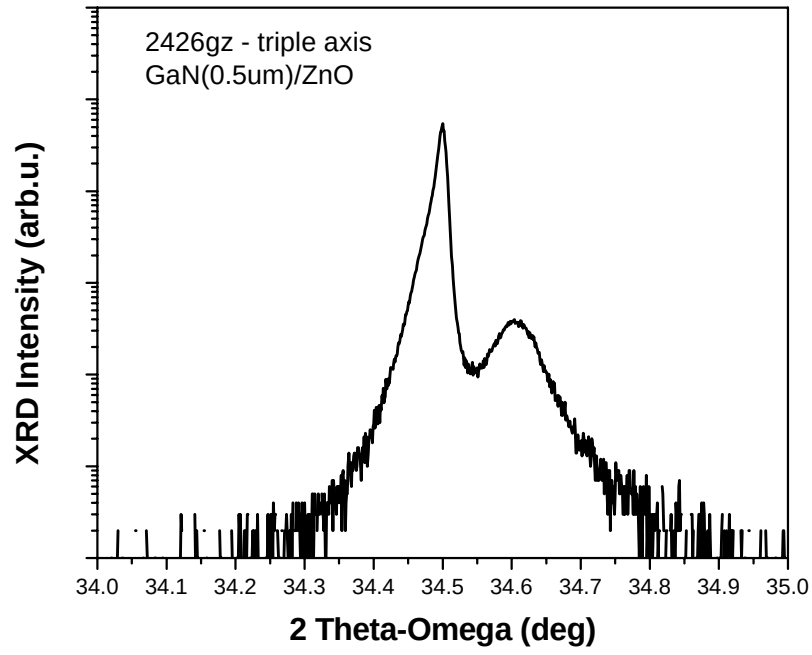

Figure 4.19: X-ray of GaN directly grown on ZnO.

4.6 Direct Growth of GaN on Bare ZnO

The ideal growth process is to grow the desired epilayer directly on the substrate with no buffer or transition layers in between. This was attempted by growing a 500nm thick GaN layer directly on bare ZnO without the aid of a buffer or transition layers, Figure 4.18. X-ray reveals the single crystal diffraction GaN peak on the right of the ZnO peak, Figure 4.19. However, the surface of the GaN was very rough even to the naked eye, and therefore still needs to be improved.

4.7 Summary of GaN Growth on Bare ZnO Substrate

This work has demonstrated the first GaN growth on bare ZnO substrate by MOCVD. Initially, MOCVD growth of GaN on ZnO brought many challenges because of Zn diffusion out of the substrate and H_2 back-etching into the substrate. These problems caused cracking and entire peeling-off of the epilayer while in the chamber. These issues were solved by a three generations study as discussed in this chapter. A multi-buffer layer method of LT-AlN/GaN was found to solve the cracking and peeling-off issues. Characterization by PL and x-ray showed peaks for GaN growth for these generations. However, SIMS studies showed that Zn diffusion is still a big issue for high-quality GaN. The interfacial Zn and O concentration must be reduced to a manageable level in order to successfully dope GaN p- or n-type for LED devices.

CHAPTER 5

INITIAL GROWTH STUDIES OF InGaN ON BARE ZnO SUBSTRATE

This work has demonstrated the first InGaN growth on bare ZnO substrates by metalorganic chemical vapor deposition (MOCVD). GaN growth on ZnO was improved significantly by the studies reported in Chapter 4. However, the optical characteristics indicated that the GaN layers grown were not comparable to high-quality GaN seen on sapphire. Therefore, the goal in the growth of InGaN on bare ZnO was to optimize the optical characteristics of the nitride layers and thereby improving layers for light emitting diodes (LEDs) with a potential for higher indium concentrations than that seen on sapphire for green LEDs.

5.1 Introduction

The optimization of InGaN alloys is important for the development of optical devices operating in the green visible region. InGaN is a direct bandgap material, whereas the other LED material system of interest, AlInGaP, is an indirect bandgap material. Indirect bandgap materials are less efficient due to their inability to emit photons by direct radiative recombination. A two-step process is necessary to return the electron to the valence band in order to emit the photon. However, the current issue for InGaN growth is the inability to incorporate sufficienatly high enough concentrations of indium to shift the wavelength up to 555nm for efficient green emitters.

The large atomic size difference between Ga (atomic radius = 130pm) and indium (atomic radius = 155pm) leads thermodynamics to predict a miscibility gap between GaN and InN [34]. These miscibility gaps explain the phase separation seen at high concentrations of indium. Phase separation leads to less efficient LEDs and is frequently observed in bulk layers as well as in multiple quantum wells (MQW) on GaN template/sapphire. (Note: for the remainder of this thesis, the GaN template/sapphire studies will be referred to simply as sapphire.) These phase separations occur at indium composition >20% due to spinodal decomposition [35-39]. Low luminescence efficiency has been observed for green light emitting InGaN quantum wells (QWs) with submicron-sized small phase separation [40].

The successful growth of InGaN layers on the Zn face of (0001) ZnO substrates by MOCVD are reported in this chapter. These InGaN layers contained indium compositions, in the range of 17-27%, suitable for InGaN MQW LED device applications. The key factor of this success was the use of a low temperature GaN buffer layer. It was found that InGaN composition with 17-27% indium could be obtained on ZnO with no phase separation compared to their identical growths on sapphire. Further details in this chapter will explain the phenomenon behind this occurrence.

5.2 InGaN Growth on Bare ZnO

5.2.1 Experimental Procedures

In place of the AlN/GaN multiple buffer layer, reported in Generation 2, a low temperature GaN buffer layer was grown at 530^{o}C to a thickness of ~30nm, using trimethylgallium (TMGa) and ammonia (NH_3) as the gallium and nitrogen sources,

respectively. GaN has a lower bonding energy than AlN and provides a better quality buffer layer. In addition, the lattice mismatch between ZnO and GaN is only 1.8% compared to 5% for AlN. Following the buffer layer growth, InGaN layers ~70nm thick were grown at temperatures between 680°C and 720°C by introducing trimethylindium (TMIn) and triethylgallium (TEGa) into the reactor. The InGaN films were grown for a shorter time and at a lower temperature than GaN, thus minimizing H_2 etching from NH_3 of the ZnO substrate. A N_2 carrier gas was also used in order to avoid etching of the ZnO surface. Good-quality InGaN films were achieved due to the shorter exposure time and lower temperature growth. The annealing process from Generation 2 was also removed to avoid carbon contamination from dimethylhydrazine (DMHy).

5.2.2 *In-situ* Monitoring

The growth schematic and the *in-situ* reflectance curve of the typical growth procedure are shown, respectively in Figure 5.1(a) and (b). The *in-situ* reflectance curves clearly demonstrate the growth of a LT-GaN buffer followed by the growth of InGaN. The InGaN growth rate increased with decreasing temperature from 0.16 to 0.2μm/h over a temperature range of 680°C to 720°C. This change in reflectance intensity with growth rate was expected for InGaN growth and showed that indium concentrations varied from 17% to 27% with a decrease in temperature from 720°C to 680°C. This correlation was due to higher sticking coefficients, expected as indium composition should increase as the temperature decreases.

5.2.3 Crack Free, No Peeling-Off, and Low Surface Defect Density

The optical microscope image of the InGaN surface is shown in Figure 5.2(a). The image shows a smooth and mirror-like surface. No cracking or peeling can be seen

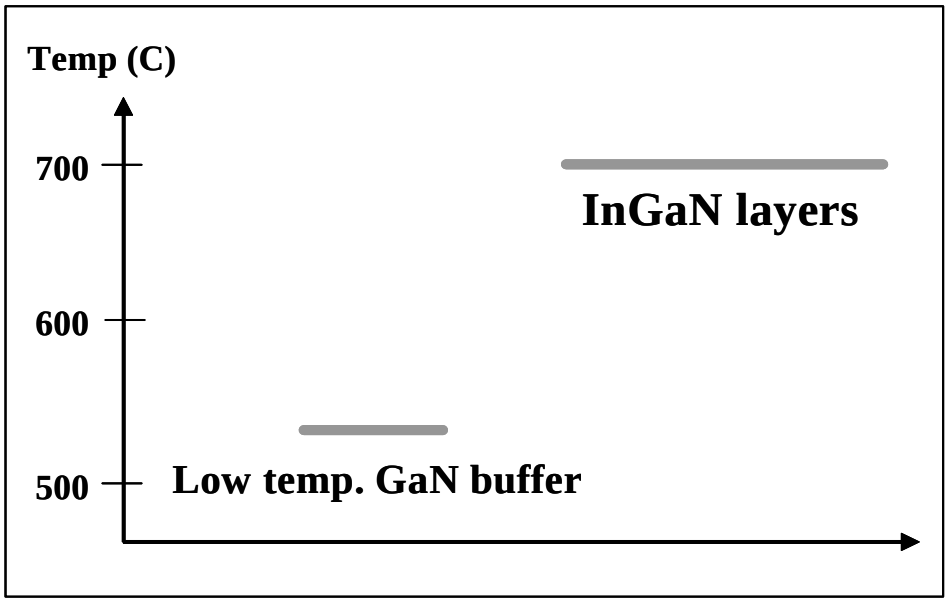

(a)

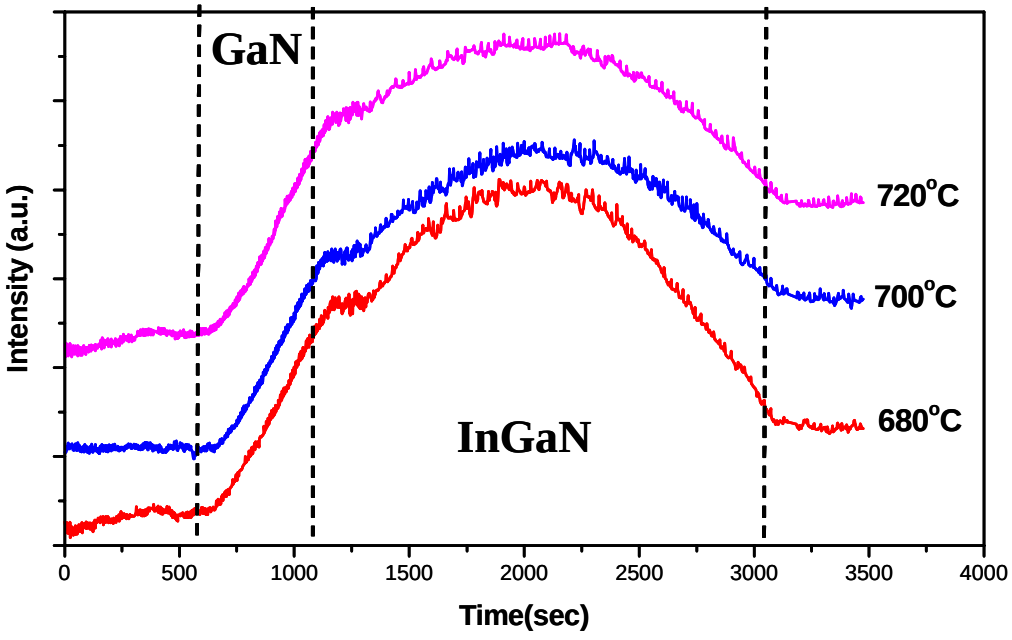

(b)

Figure 5.1: (a) Illustration of the growth procedure for InGaN growth on GaN buffer layer (b) In-situ reflectance curve showing successful GaN and InGaN growth at temperatures ranging from 600°C to 720°C.

compared with previous generations. This can be attributed in part to the shorter time and lower growth temperature, but also because the InGaN layer is more ductile than the GaN layer. Also, the inserted image shows the 20x20mm^2 InGaN film on a bare ZnO substrate. Scanning electron microscope (SEM) was used to study the surface microstructures of the GaN buffer layer and InGaN film, and showed no evidence of indium droplets on the surface, Figure 5.2(b) and (c), respectively. The GaN buffer reveals the presence of quadrilateral grains, and the InGaN layer shows link-strip grains.

5.2.4 Structure and Indium Composition of InGaN Layers

X-ray diffraction (x-ray) (1st order) 2θ/ω scans from three samples show two well-separated peaks from the ZnO substrate and InGaN layers, Figure 5.3. The concentration of indium from the InGaN layer was calculated from the shift of the (0002) InGaN peak position relative to the (0002) ZnO peak position (set at 0 arcsec) via Vegard's law. The degree of indium incorporation in the InGaN layers was adjusted by changing the growth temperature. The InGaN films showed single crystal diffraction peaks corresponding to indium concentrations of 17%, 23%, and 27% for samples grown at 720^{o}C, 700^{o}C, and 680^{o}C, respectively. All x-ray patterns revealed a small shoulder peak on the right of the main ZnO peak, possibly from diffraction of the GaN buffer layer. Remarkably, only InGaN and ZnO peaks appeared in all the samples and no extra peaks were observed even in samples with indium compositions as high as 27%. This showed that no indium droplets or phase separations were present in the InGaN layers.

Phase separation, or spinodal decomposition, has been widely reported for InGaN grown on sapphire [34, 35, 37, 41]. A test was performed by growing InGaN with the same growth parameters on both a sapphire substrate and a ZnO substrate. Neither,

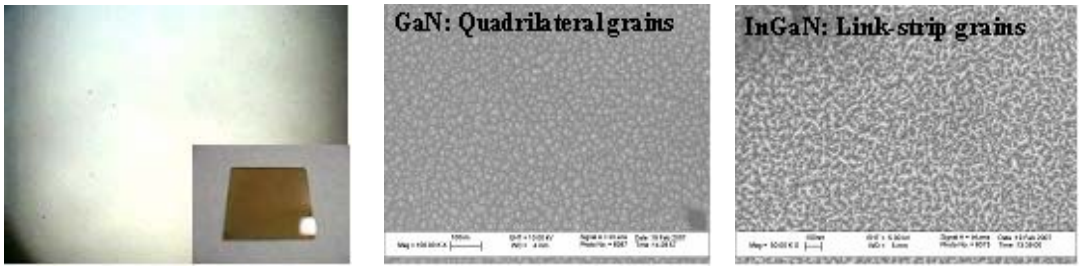

(a) (b) (c)

Figure 5.2: (a) Optical microscope images and SEM pictures of (b) GaN and (c) InGaN surface.

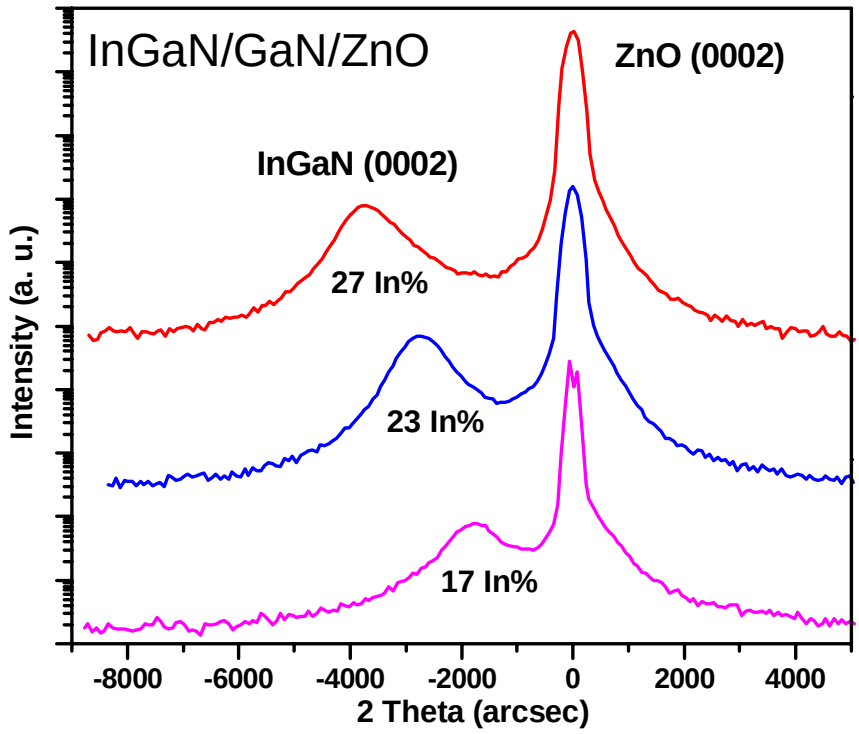

Figure 5.3: X-ray $2\theta/\omega$ scan of InGaN layers with different indium composition grown on ZnO substrates by MOCVD.

indium droplets or phase separation were detected by x-ray for the InGaN films grown on ZnO substrate but were detected for the InGaN film grown on sapphire. Biaxial strain in the epilayer is helpful in suppressing the phase separation in InGaN materials from theoretical calculation and experimental observation [42, 43]. Phase separation easily occurs when the InGaN layer starts to relax due to compressive strain from the sapphire. InGaN has a perfect lattice match to ZnO at an indium concentration of 18% and may stay completely strained, by providing a higher strain state that can retard phase separation compared with layers grown on sapphire. The difference in strain relaxation mechanisms for ZnO versus the sapphire substrate will be discussed in more detail in a later section.

5.2.5 Optical Characteristics of InGaN at Room-Temperature

Room-temperature photoluminescence (PL) spectra of the same three samples examined by x-ray are shown in Figure 5.4. For the samples with indium compositions of 17%, 23%, and 27%, the PL emission peaks were observed at 2.4, 2.1, and 1.9eV, respectively. A calculated band edge can also be calculated by the following equation. Assuming the 70 nm InGaN layers were strained, and employing the reported bandgap expression seen in Equation 5.1 [44]:

$$Eg = 3.42 - (0.65)x - 3.4159x(1-x) \qquad (4.1)$$

where x is the indium composition, the band edge emission energy can be calculated if the indium concentration is known. The calculated PL peak energies of 2.8, 2.6, and 2.5eV are obtained by using the x(In) values of 17%, 23%, and 27% from x-ray measurements in Figure 5.3. The calculated PL results are quite different from the experimental PL results of 2.4, 2.1, and 1.9eV observed from Figure 5.4. For each

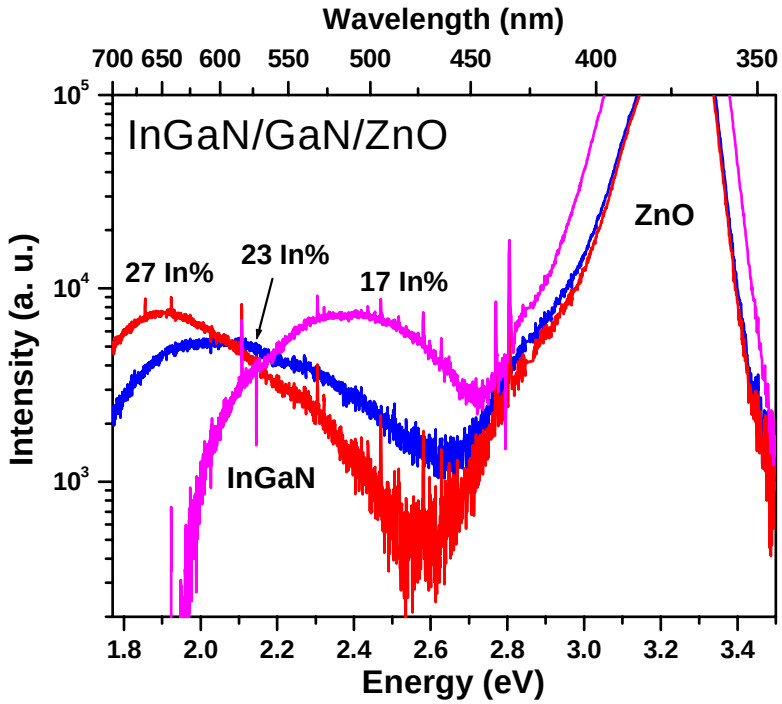

Figure 5.4: Room-temperature PL spectra of InGaN films with different indium composition grown on ZnO substrates by MOCVD.

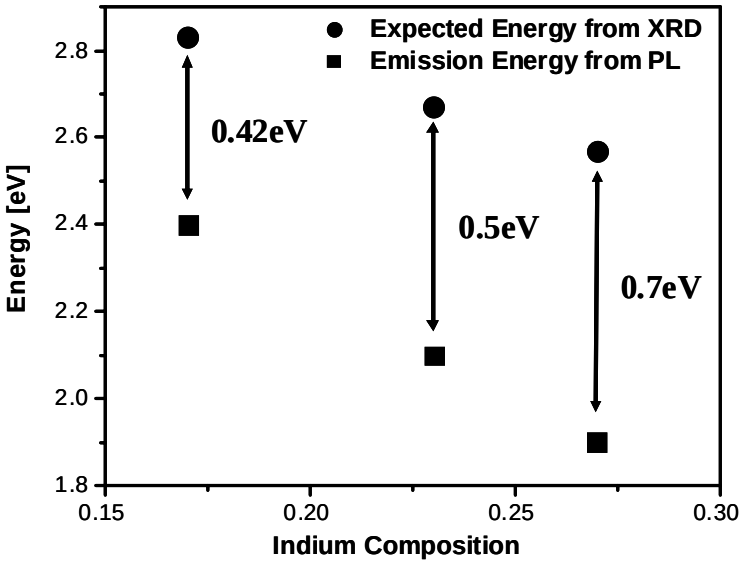

Figure 5.5: PL and x-ray peaks have 0.4~0.7eV shift for InGaN layers.

sample the calculated PL shifts from the experimental spectral PL peak by about 0.4~0.7eV, Figure 5.5. It has also been observed that the position of the PL peak in intentionally Zn doped InGaN occurs at values between 0.4~0.5eV lower than the calculated and experimental band gap energy of $In_xGa_{1-x}N$ [45]. Therefore, the lower energy PL emissions may be due to Zn and O diffusion from ZnO into the InGaN layers, forming impurity levels inside the band gap that can emit light with lower energy than the InGaN energy gap. A high density diffusion of Zn and O impurities into InGaN might also be a contributing factor to the broad full width at half maximum seen in PL.

5.2.6 Optical Characteristics of InGaN at Varying Temperatures

Temperature-dependant PL measurement were taken over a wide range of temperatures from 80K to 673K for InGaN films grown at 700^{o}C, with x(In) of 23%, to further verify the InGaN related PL emission, Figure 5.6. The variation in intensity of InGaN (below 630nm) with temperature is seen in this region. It shows that the PL intensity decreases with an increase in temperature, slowly at the low temperature region of 80-300K but rapidly at the high temperature region of 373-673K. The Arrhenius plot of InGaN-related PL peak intensity versus temperature in the range of 80-673K is shown in Figure 5.7. Best fitting leads to an activation energy, E_a, of about 59meV for InGaN with 23% indium content. Smith et al. reports an E_a=56meV for $In_xGa_{1-x}N$ epilayer with x=0.12 [46] and Teo et al. reports on $In_{0.2}Ga_{0.8}N$ MQWs with an E_a value of 63meV for x=0.20 [47]. The data reported in this paper is close to the above reported values in literature.

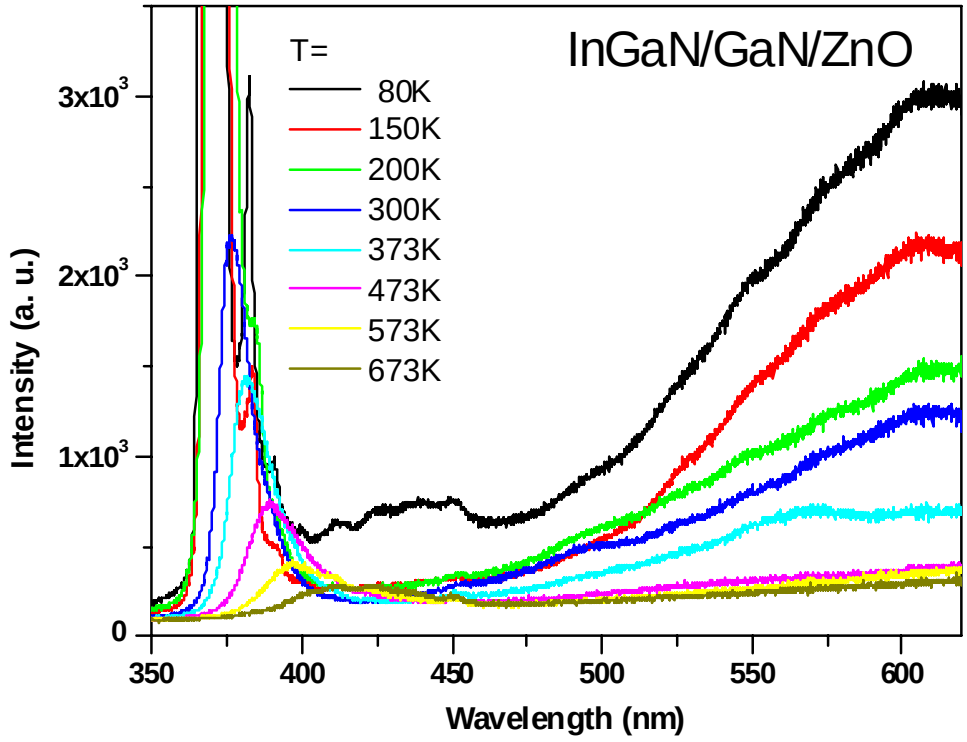

Figure 5.6: Temperature-dependent PL spectra (80-673K) of InGaN film grown on ZnO substrate at 700°C.

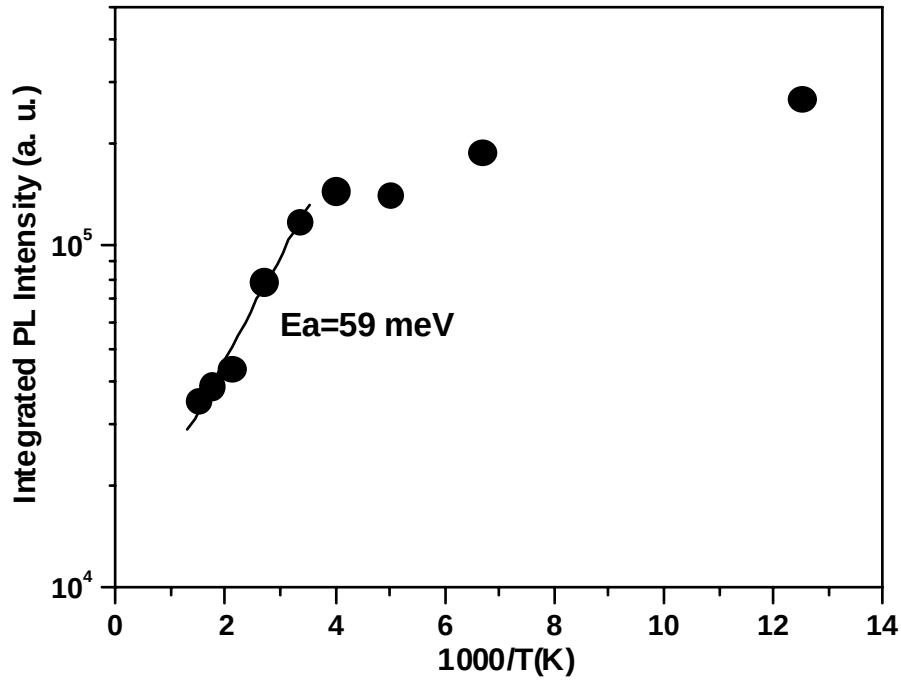

Figure 5.7: PL intensity versus temperature (80-673K) of the InGaN layer.

5.2.7 Evolution of Surface Morphology With Temperature

Surface roughness can be improved by increasing the growth temperature. Increased temperature changes the growth mode from grain to step-flow as seen in the atomic force microscopy (AFM) images shown in Figure 5.8 At low temperature, the roughness had an RMS = 5.73nm, while at high temperature the RMS went down to 2.49nm. The InGaN layer is grown in a step-flow like mode at high temperatures, which is a duplication of the underlying GaN buffer. The InGaN surface is rough at low temperature, depicting initial nucleation of discrete islands and the subsequent coalescence of the islands. This growth mode results in poor quality films because dislocations and other crystalline imperfections will form at the grain boundaries. Therefore, in order to obtain high quality InGaN films, temperatures must be controlled higher than 720^{o}C.

5.2.8 Evidence of Zn and O Diffusion Into InGaN Layers

Secondary ion mass spectrometry (SIMS) was performed to measure the concentration of different elements in the InGaN/GaN/ZnO structures. A high indium content in InGaN was verified by SIMS concentration profile for InGaN/GaN/ZnO showing that InGaN was successfully grown on the ZnO substrate, Figure 5.9. However, the strong diffusion of Zn and O from the ZnO substrate (Zn=10^{20}, O=10^{21} atoms/cm^{3}) into the InGaN layer still occurred showing that further improvement is needed to prevent the out-diffusion of Zn and O.

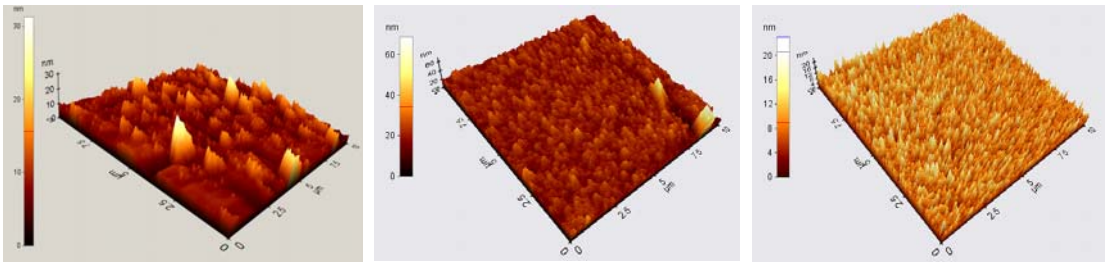

(a) (b) (c)

Figure 5.8: AFM images (10μm×10μm) for InGaN samples grown at (a) 680°C, (b) 700°C, and (c) 720°C. The RMS values were 5.73nm, 4.47nm, and 2.49nm.

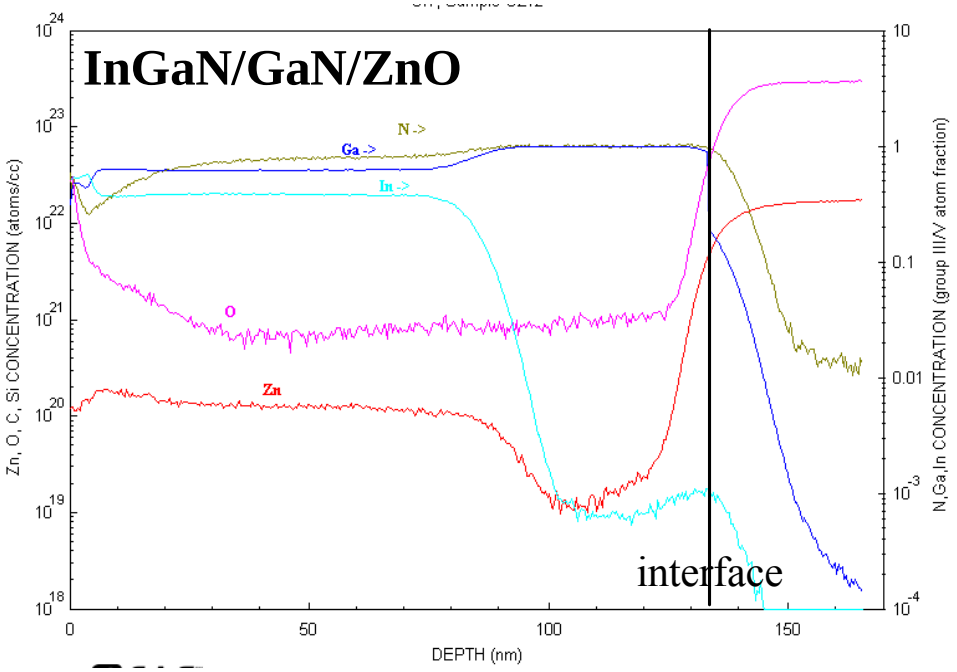

Figure 5.9: SIMS of InGaN/GaN/ZnO.

5.3 Direct Growth of InGaN on Bare ZnO

The ideal growth process is to grow the desired epilayer directly on the substrate with no buffer or transition layers in between. This was attempted by growing a 100nm thick InGaN layer directly on bare ZnO substrates without the aid of buffer or transition layers, Figure 5.10. The diffraction patterns of the InGaN layers grown on ZnO substrates are seen in Figure 5.11. The three samples all show multiple phases of InGaN with growth temperatures from 680^{o}C to 720^{o}C, from left to right. An InN layer might have been grown on the ZnO surface unintentionally. There is a large lattice mismatch between InN and InGaN which could provide a lower strain state for epilayers and induce phase separation. Therefore, further study is needed to understand how to directly grow InGaN without showing any phase separation.

5.4 Phase Separation Study of InGaN on Sapphire and ZnO Substrates

InGaN epilayers were grown on both ZnO and sapphire at the same time. These layers were evaluated by x-ray and found to show phase separation only on sapphire. The growth on ZnO also showed higher indium content compared to on sapphire.

Successful growth of InGaN layers on (0001) ZnO substrates by MOCVD has been reported in the previous section. One of the issues for InGaN growth is phase separation when indium compositions exceed certain levels in the alloys leading to non-homogeneity [48]. The large atomic size difference between Ga and indium atoms leads thermodynamics to predict a miscibility gap between GaN and InN [49]. These miscibility gaps explain the phase separation seen at high concentrations of indium. S. Y.

Figure 5.10: Schematic of InGaN directly grown on ZnO.

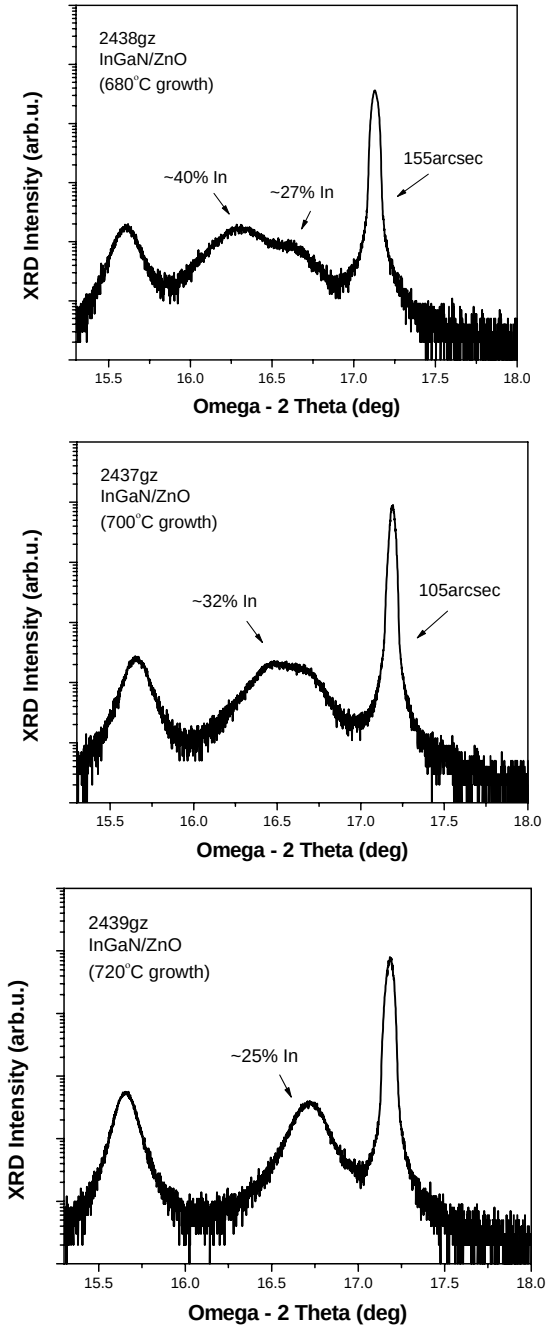

Figure 5.11: X-ray of InGaN directly grown on ZnO at different temperatures from left to right of 680ºC, 700ºC, and 720ºC showing multiple phases of InGaN.

Karpov created a GaN-InN phase diagram from his study on the suppression of InGaN phase separation due to elastic strain. This phase diagram showed that a strained layer allows for higher indium incorporation than if the layer relaxed, Figure 5.12. This section addresses the issues of InGaN phase separation and further studies of ZnO substrate as a growth medium for obtaining indium concentration up to 42% without any detectable phase separation.

5.4.1 Experimental Procedures

InGaN/GaN structures were grown with identical growth conditions on (0002) sapphire substrates as well as on the Zn face of (0001) ZnO substrates by MOCVD. The GaN templates consisted of a 2μm thick GaN grown on (0001) bare sapphire substrates at 1050^{o}C using H_2 carrier gas and TMGa and NH_3 as the gallium and nitrogen sources, respectively. A schematic of the structures grown on sapphire and ZnO substrates are illustrated in Figure 5.13. A low temperature GaN buffer layer was grown at 530^{o}C with a thickness of about 30nm using TMGa and NH_3 as the gallium and nitrogen sources. Following the buffer layer, growth of InGaN films of about 100nm thick were grown at temperatures of 650^{o}C and 700^{o}C by introducing TMIn and TEGa into the reactor. N_2 carrier gas was used during the entire growth process to avoid H_2 etching of the ZnO surface. Si doping was also introduced into the InGaN layers grown on both substrates at temperatures of 700^{o}C and 720^{o}C using similar growth conditions as described above.

5.4.2 X-ray of InGaN Phase Separation

The x-ray (1st order) 2θ/ω scan patterns from the InGaN layers on sapphire and ZnO substrates are shown in Figure 5.14(a) and (b), respectively. The indium composition in the layers was calculated via Vegard's law by the shift of the (0002) InGaN peak position

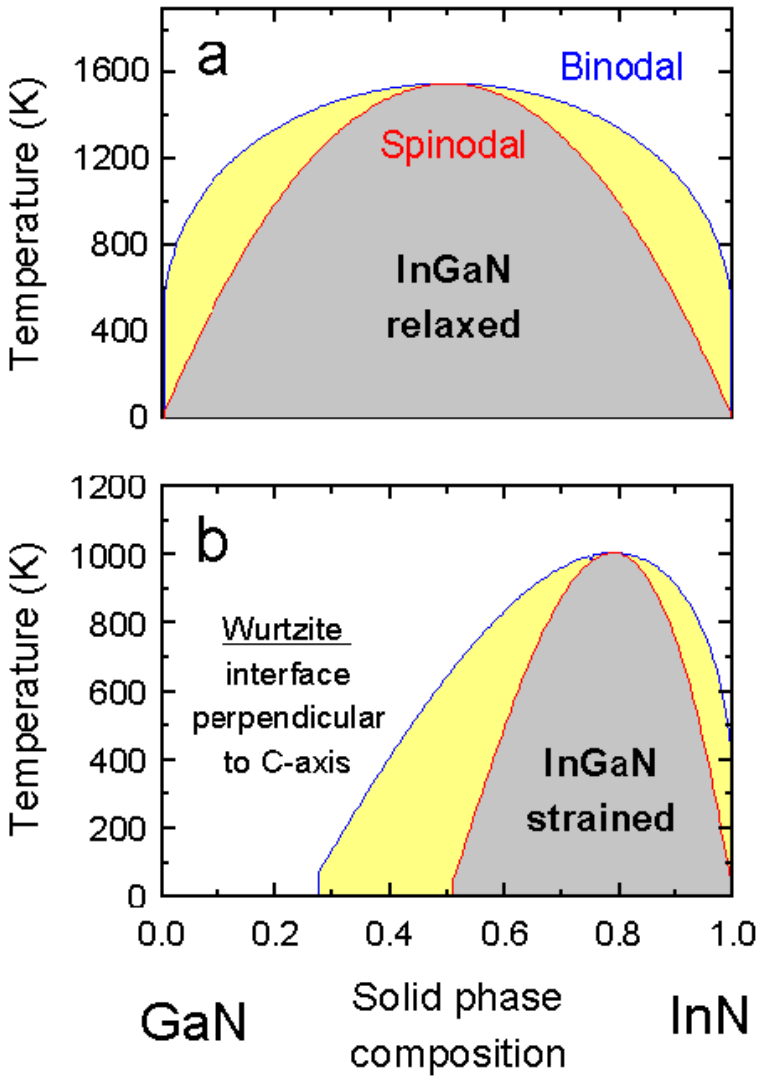

Figure 5.12: GaN-InN phase diagram showing that a strained layer allows for higher miscibility of GaN and InN and therefore higher indium incorporation without phase separation.

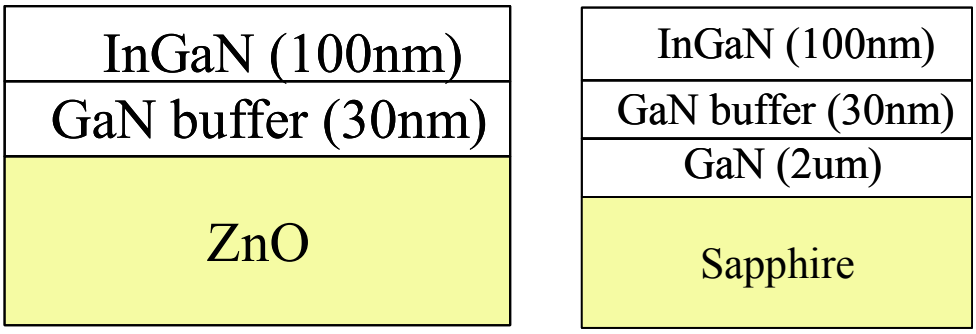

Figure 5.13: Schematic illustration of the sample structures: (a) InGaN/GaN/GaN template/sapphire and (b) InGaN/GaN/ZnO.

relative to the (0002) GaN and (0002) ZnO peak positions (set at 0 arcsec).

The InGaN on sapphire was studied first. A single InGaN phase corresponding to 17% indium content for samples grown at a temperature of 700^{o}C is shown in Figure 5.14(a). However, when the growth temperature was ramped down to 650^{o}C, multiple phases of InGaN appeared with the highest concentration at 32% indium. From thermodynamics, an increase in indium concentration resulting in phase separation is attributed to the growth of InGaN alloys below the critical temperature required for miscibility [34, 43]. In addition, an increase in indium concentration leads to an increase in the lattice mismatch between InGaN and sapphire. The difference in bond lengths leads to internal strain due to crystalline lattice distortion. Therefore, any small amount of group-III element into a ternary compound changes the lattice constant drastically [43]. This increase in lattice mismatch easily generates edge dislocation, which relaxes the compressive strain and thereby inducing phase separation. The compressive strain relaxation is progressive and phase separation occurred at growth temperatures as low as 650^{o}C.

Remarkably, only a single InGaN phase appeared on the ZnO substrate with calculated compositions as high as 28% and 43% indium grown at temperatures of 700^{o}C and 650^{o}C, respectively, Figure 5.14(b). SIMS has confirmed that the 650^{o}C ZnO sample consists of 39% indium, Figure 5.15. All the InGaN growths on ZnO are considered fully strained due to close lattice match. Also, the 100nm InGaN is commonly considered a thin layer and therefore can be safely considered a fully strained layer. From the GaN-InN phase diagram, InGaN with 43% indium is located at a stable region for miscibility in the strained layer case [43]. Biaxial strain in the epilayer assists in suppressing the

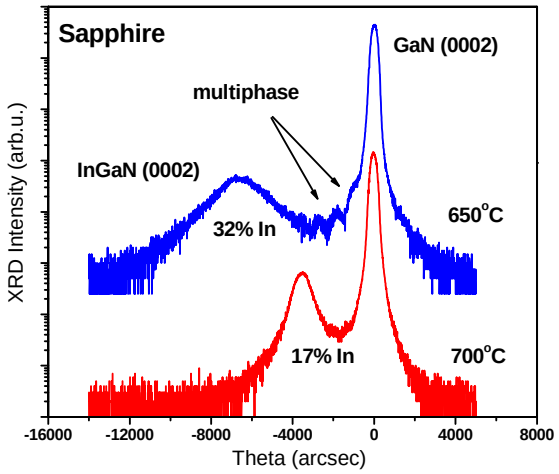

(a)

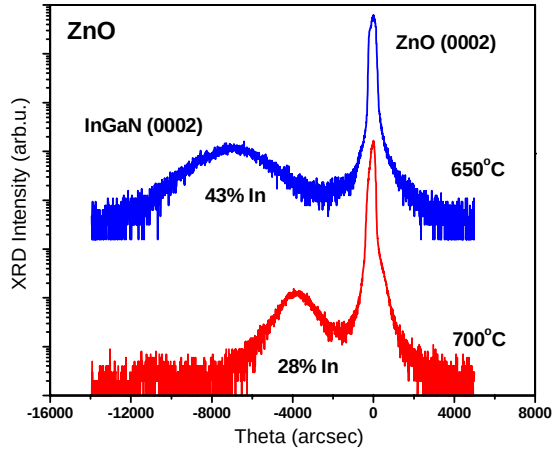

(b)

Figure 5.14: X-ray $2\theta/\omega$ scan of InGaN layers with different indium composition grown on (a) sapphire and (b) ZnO substrates by MOCVD.

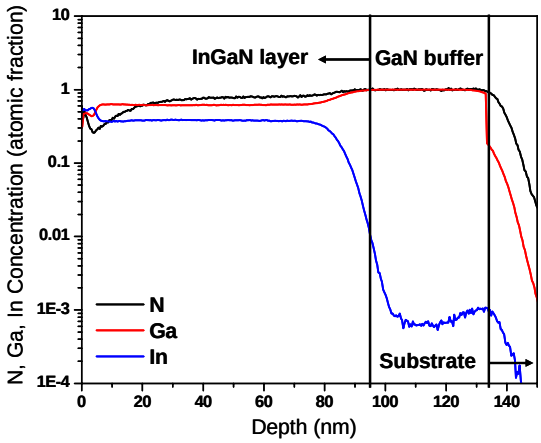

Figure 5.15: SIMS of InGaN/GaN/ZnO showing 39% indium concentration in the InGaN epilayer which coincides with the calculated value from x-ray.

phase separation in InGaN materials based on theoretical calculation and experimental observation [42, 43, 50]. Phase separation easily occurs when the InGaN layer starts to experience compressive strain relaxation from sapphire, usually only greater than 20% indium concentration. It is believed that the InGaN layers grown on ZnO might stay at a higher strain state due to its ability to stay fully strained even after 18% indium concentration, thereby allowing for higher indium incorporation.

5.4.3 X-ray of Si Doped InGaN

A second study was performed on InGaN grown on sapphire and ZnO in order to show that the growths were indeed phase separating on sapphire but not on ZnO. It has been widely reported that compressive strain can be induced by Si doping into the GaN based epilayer [51-53]. I. H. Lee et al., reported that Si doping induced relaxation of compressive strain in the GaN layers [51]. M. K. Chen and co-workers proposed that spinodal decomposition is strongly caused by Si doping as seen in changes in InGaN strain relaxation of InGaN/GaN MQWs [52]. P. Cantu and his group also found that increasing Si doping enhanced the relaxation of compressively strained 200nm-thick $Al_{0.49}Ga_{0.51}N$ layers grown on top of 1μm-thick $Al_{0.62}Ga_{0.38}N$ coated sapphire [53]. The diffraction pattern of InGaN layers with Si doping grown at 700^{o}C and 720^{o}C on sapphire and ZnO substrates are seen in Figure 5.16. Phase separation does not occur for InGaN films grown on sapphire and ZnO substrate at 720^{o}C. However, phase separation is seen in the sapphire growth as the growth temperature decreases to 700^{o}C. InGaN growth on ZnO substrate did not exhibit any phase separation at 700^{o}C. The relaxation of the compressive strain is due to the substitution of larger Ga (atomic radius = 130pm) or indium (atomic radius = 155pm) atoms by smaller Si atoms (atomic radius = 117.6pm) in

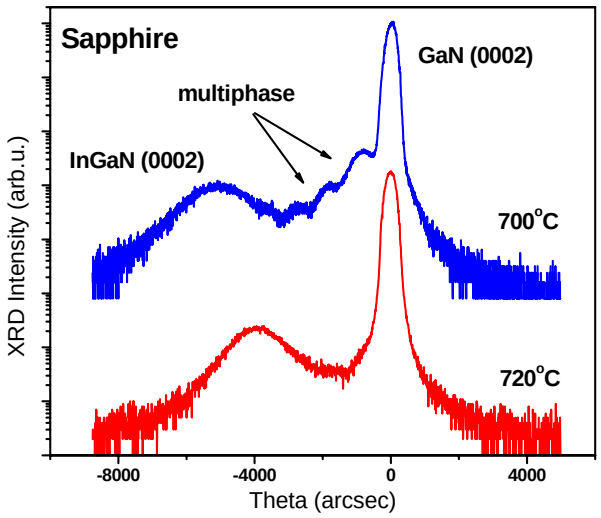

(a)

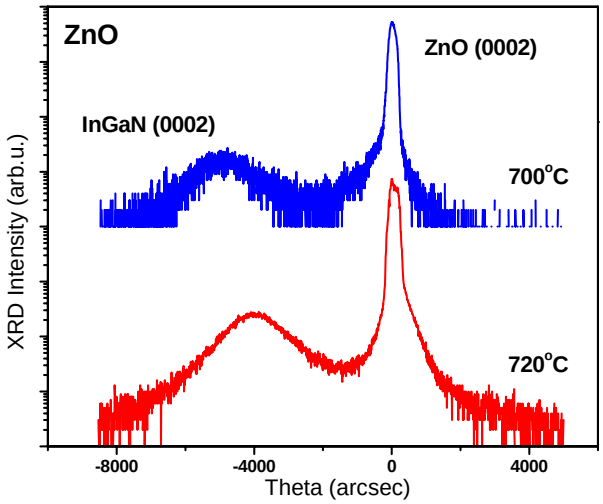

(b)

Figure 5.16: X-ray $2\theta/\omega$ scan of InGaN layers with Si doping grown on (a) sapphire and (b) ZnO substrates by MOCVD.

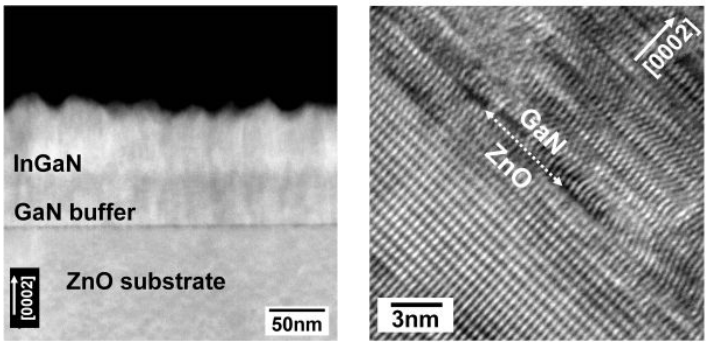

(a) (b)

Figure 5.17: Cross-sectional HAADF-STEM image of (a) InGaN/GaN buffer/ZnO structure and HRTEM image of (b) a coherent interface between GaN buffer and ZnO.

the InGaN films. InGaN on sapphire is able to preserve an initial high strain level with no phase separation for Si doped InGaN on sapphire grown at 720^{o}C due to the smaller lattice mismatch between InGaN and sapphire at low indium concentration. However, an increase in indium content at a lower temperature of 700^{o}C reduced the initial strain level due to a larger lattice mismatch between InGaN and sapphire and thereby showing phase separation. Therefore, Si can further induce phase separation on sapphire compared to Figure 5.14(a) where no phase separation appeared at 700^{o}C. In contrast, the Si doped InGaN grown on ZnO at 700^{o}C did not show multiple phases in x-ray. This result indicates that, compared to sapphire, ZnO can provide a higher strain state in InGaN films to suppress phase separation caused by Si doping.

5.4.4 HAADF-STEM and HRTEM of InGaN Structures

A cross-sectional high angle annular dark field (HAADF) scanning transmission electron microscopy (STEM) image of the InGaN/GaN buffer/ZnO structure grown at 700^{o}C can be seen in Figure 5.17(a). There are no significant threading dislocations to be found because the ZnO has a smaller c-plane lattice mismatch with GaN than sapphire. An enlarged image of the lattices of the GaN buffer and ZnO substrate measured by high-resolution transmission electron microscopy (HRTEM) can be seen in Figure 5.17(b). The two crystals match perfectly. The lattice is continuous across the interface plane, which shows that the interfaces between GaN and ZnO are coherent. A fully coherent interface, with a slight mismatch of 1.8%, leads to coherency strain in the adjoining lattices between the GaN buffer and ZnO. In other words, the larger a-axis lattice constant of GaN on ZnO is preferable for lattice matching to InGaN with high indium concentration. In addition, InGaN consisting of 18% indium content is exactly lattice-

matched with ZnO. As a result, the InGaN layer may stay completely strained on a thin GaN buffer at high indium composition because the GaN buffer is coherently grown on the underlying ZnO substrate, and the InGaN is lattice matched up to a higher indium concentration. In contrast, the large lattice mismatch between InGaN and sapphire will easily generate local dislocation, thereby, relaxing the compressive strain and inducing phase separation when indium composition is at a high level. Therefore, a higher strain state in InGaN films with high indium concentration (28%~43%) will be provided by ZnO compared with those (17%~32%) grown on sapphire.

5.4.5 Case Study of Phase Separation in InGaN Grown on Sapphire

The phase separation phenomena between both the ZnO and sapphire case can be addressed by previous studies on thick InGaN layers grown on sapphire substrates. A plot of a- and c-lattice constant versus indium composition is shown in Figure 5.18. Data showed that indium concentration less than 20% in InGaN layers are coherently strained on the GaN templates. The layers start to gradually relax the strain for indium composition between 20% and 30%, and InGaN films appear to be fully relaxed for composition over 30%. The different strain relaxation appears to be the reason that phase separation is observed for InGaN grown on sapphire compared with ZnO.

The lattice constant has been shown as a function of indium composition, i.e. the strain state will change with indium composition, which is demonstrated by reciprocal space mapping (RSM), as shown in Figure 5.19. From it, two lines are drawn: the line to the origin, which is the zero strain line where InGaN is fully relaxed, and the perpendicular line, where InGaN is fully strained on GaN. The InGaN layer with x=0.14 is coherently grown on the GaN template, whereas the InGaN layer with x=0.31 is fully

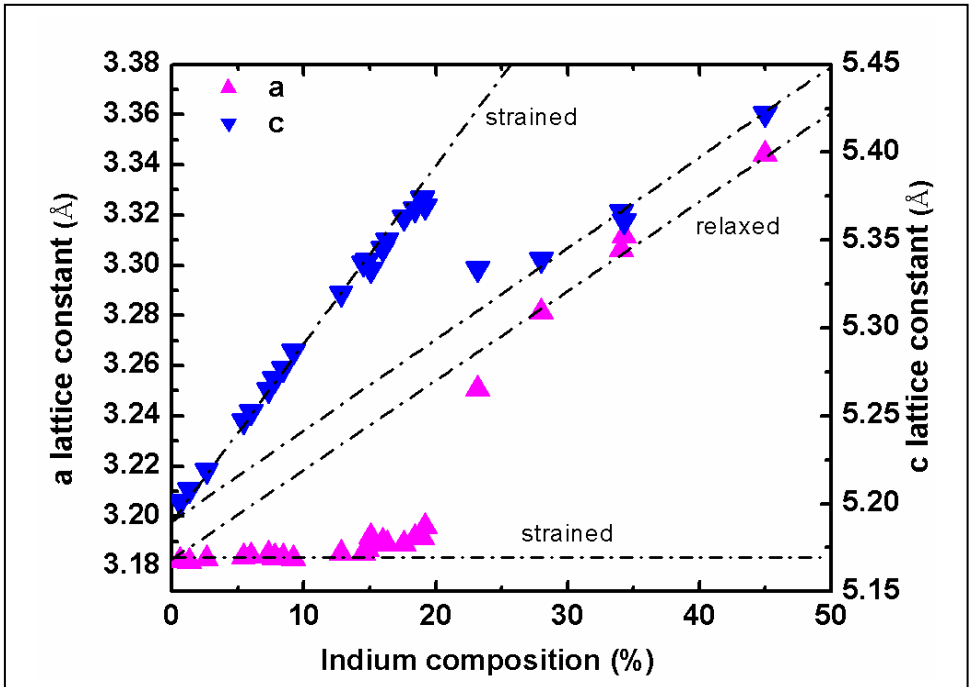

Figure 5.18: Plot of a and c lattice constant versus indium composition.

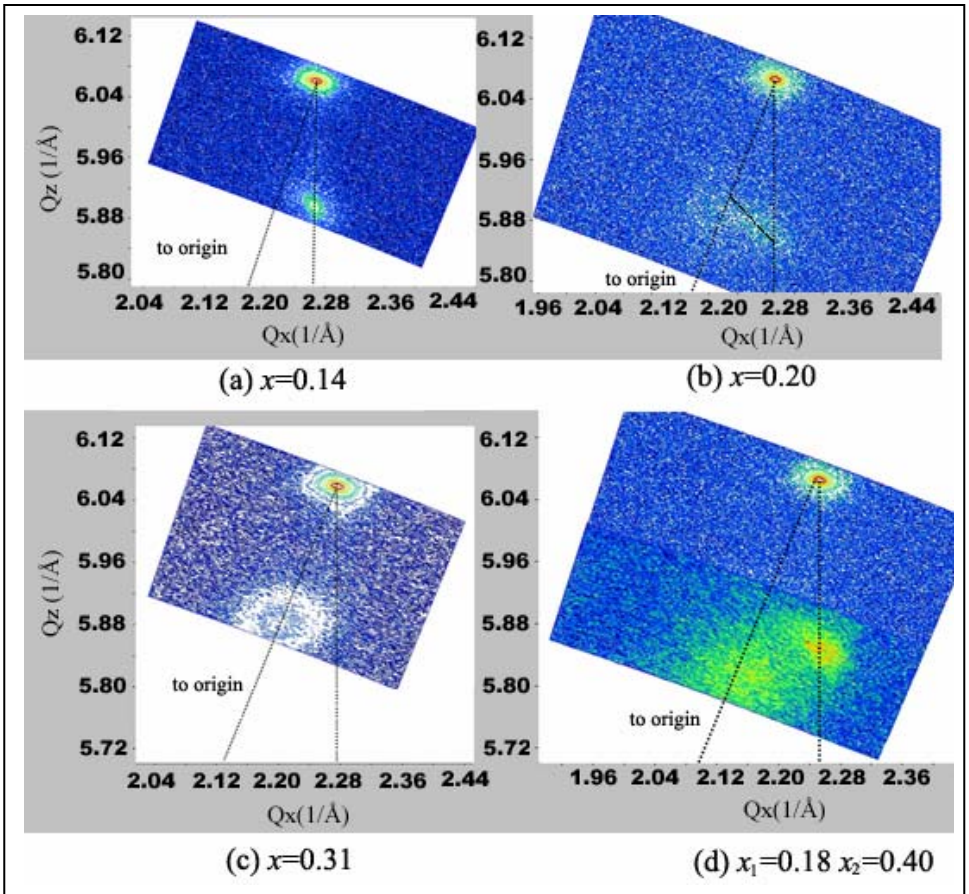

Figure 5.19: Reciprocal space mapping of InGaN on sapphire.

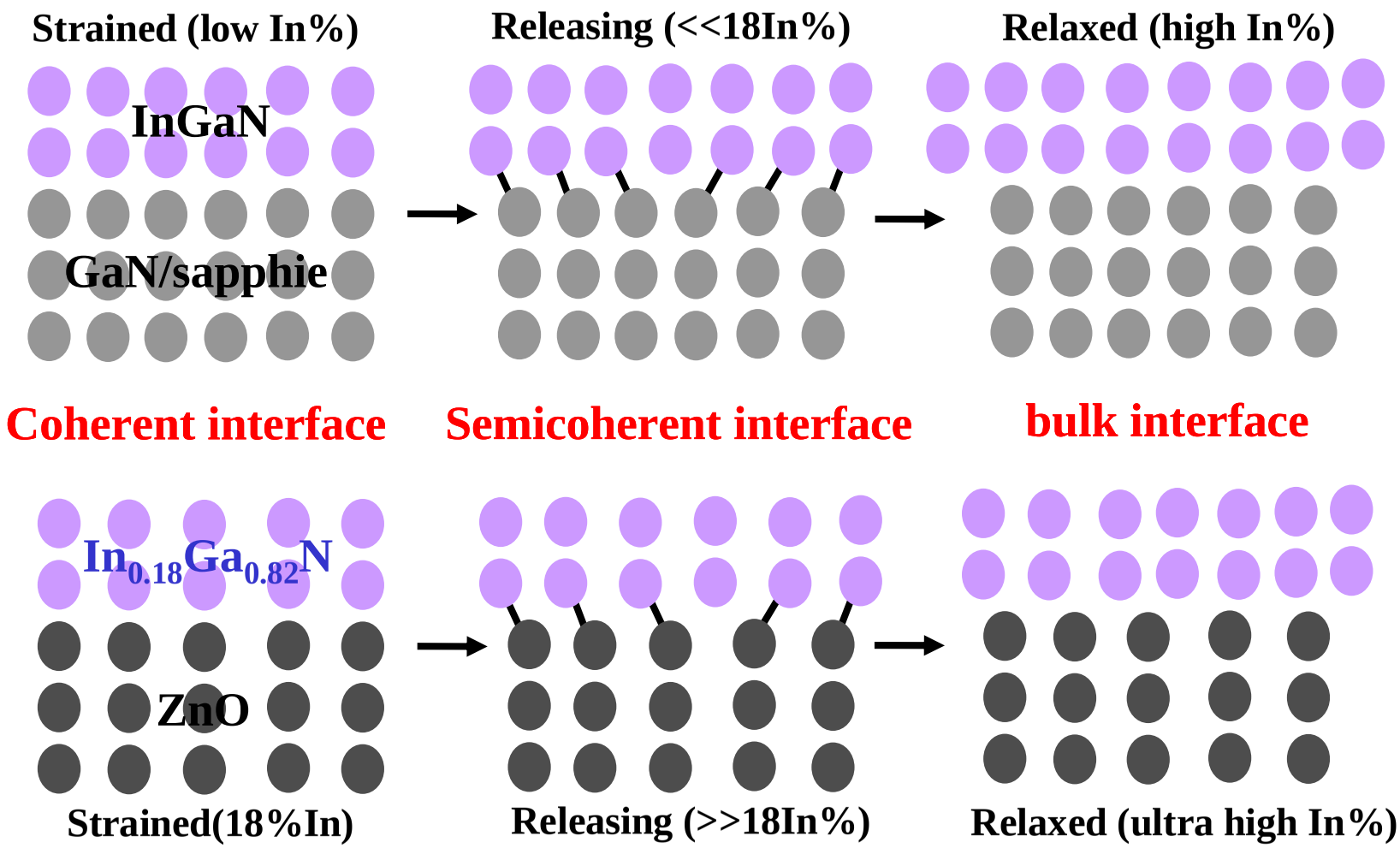

Figure 5.20: Summary of InGaN layer strained on GaN template/sapphire and on ZnO substrate. Results are based on experimental data showing ZnO's ability to contain higher indium concentration because of its higher strain state.

relaxed. The InGaN layer with 20% indium is believed to undergo the strain relaxation process. A 20%-isocomposition line connecting the fully strained to fully relaxed regions is drawn in Figure 5.19(b) for comparison. It is observed that the InGaN layer has strain states that continuously change from fully strained to fully relaxed, while the composition remains almost unvarying. Therefore, the strain relaxation is progressive and may take place either along the growth direction or across the heterointerface.

5.4.6 Summary of Phase Separation Study

From theoretical calculation and experimental observation, biaxial strain in the epilayer is helpful in suppressing the phase separation in InGaN materials. Phase separation easily occurs when the InGaN layer starts to relax due to compressive strain from sapphire. The observed suppression of phase separation in the InGaN growth on ZnO is believed to be due to a higher strain state for InGaN on ZnO compared to InGaN on sapphire. An InGaN layer may stay completely strained on a thin GaN buffer coherently grown on ZnO at high indium composition since InGaN consisting of 18% indium is exactly lattice-matched with ZnO. InGaN does not start to relax or become fully relaxed even at indium percentages as high as 43%. As a result, a higher strain state in InGaN films with high indium concentration will be provided by ZnO to retard the phase separation. This discrepancy is possibly caused from the different strain relaxation mechanisms in ZnO and sapphire substrate. In other words, the large lattice mismatch between InGaN and sapphire will easily generate the local dislocation for relaxing the compressive strain to induce phase separation. A summary of indium composition with strain limitations is illustrated in Figure 5.20.

5.5 Summary of InGaN Growth on Bare ZnO substrate

The successful growth of InGaN layers on the Zn face of (0001) ZnO substrates by MOCVD are reported in this chapter. GaN growth on ZnO improved significantly as seen in Chapter 4. However, the optical characteristics of the GaN did not reach high-quality GaN. Therefore, the goal in the growth of InGaN on bare ZnO was not only to provide a better substrate for green LEDs, but also to optimize the characteristics of the nitride layers. The key factor of this success is the use of a low temperature (530^{o}C) GaN buffer layer. Good quality InGaN films, with a range of high indium composition of 17-27%, have been obtained with growth temperatures of 680-720^{o}C. The InGaN films show no indium droplets or phase separation, which can be attributed to the strain relaxation in InGaN epilayers grown on ZnO substrates. PL data for all InGaN films show a strong emission band from ZnO and broad InGaN-related emissions, with the peak energy varying with indium composition. Peak energy values of the broad emissions are measured to be less than the calculated InGaN band gap by 0.5$\pm$0.1eV. These InGaN-related emissions may be due to recombination involving Zn-/O-impurities in InGaN due to the Zn/O diffusion from the ZnO substrate. Temperature-dependent PL measurements, 80-673K, obtained an activation energy of 59meV for the InGaN epilayer.

InGaN layers were grown on ZnO and sapphire substrates under the same conditions showing two distinct results for phase separation in the InGaN layers. InGaN films with 32% indium content exhibited phase separation when grown on sapphire. For InGaN layers grown on ZnO, there was no observation of phase separation with indium content as high as 43%. In addition, phase separation is strongly induced by Si doping InGaN films grown on sapphire compared with that on ZnO. InGaN layers with high indium

composition grown on ZnO might exhibit a higher strain state than that grown on sapphire, suppressing phase separation caused by Si doping. HAADF-STEM and HRTEM results revealed reduction of threading dislocation and perfectly matched crystals at the GaN buffer/ZnO interface. Therefore, InGaN can stay completely strained on a thin GaN buffer due to the larger a-axis lattice constant of GaN on ZnO, which is also preferable for lattice matching to strained InGaN with high indium concentration.

CHAPTER 6

GaN GROWTH ON ZnO USING AN Al_2O_3 TRANSITION LAYER

Al_2O_3 was deposited on ZnO substrates as a transition layer by atomic layer deposition (ALD). The transition layer is being added based on the previous results obtained from GaN and InGaN growth on ZnO. GaN growths on ZnO were optimized so that the final GaN sample showed mirror-like surfaces with no crack, pinholes, or peel-offs of the layers. InGaN growths on ZnO substrates exhibited well defined GaN buffer and InGaN epilayer photoluminescence (PL) and x-ray diffraction (x-ray) peaks. The InGaN samples also showed the ability to incorporate high indium content of up to 43% (compared to InGaN growth on sapphire of 32%) without phase separation. This was attributed to the perfect lattice matching of InGaN and ZnO at 18% indium, which allows for higher indium incorporation before strain relaxation compared to growth on sapphire. However, high Zn diffusion was observed by secondary ion mass spectrometry (SIMS) even after optimization of both GaN and InGaN on ZnO. Therefore, a transition layer of Al_2O_3 by ALD was proposed in order to minimize Zn diffusion and promote nitride growth of GaN on ZnO by metalorganic chemical vapor deposition (MOCVD).

6.1 Introduction

Successful growth of GaN and InGaN on ZnO has been demonstrated in this work. ZnO offers many advantages as a substrate for GaN and InGaN epitaxial growth because of its closely matched lattice constant and similar thermal expansion coefficients. However, previous results showed H_2 etching of the ZnO substrate and Zn diffusion out of the substrate, which resulted in low-quality GaN layers and prevented proper doping of, multiple quantum wells (MQWs), and p-GaN for LED structures. Hence, a transition layer was grown on the substrate before MOCVD growth to prevent Zn diffusion, protect the ZnO substrate from H_2 back etching, and promote high-quality nitride growth.

Al_2O_3 was chosen as the transition material because of its transparency, excellent thermal stability (in contrast to ZnO), and because it is a readily available material that can be deposited by ALD [54]. Another positive attribute of Al_2O_3 is its ability to form the $ZnAl_2O_4$ phase if it reacts with ZnO. $ZnAl_2O_4$ has been shown to be a good buffer layer for the growth of GaN on sapphire by hydride vapor phase epitaxy (HVPE) [55]. S. Gu et al. reported that ZnO reacted with the sapphire producing $ZnAl_2O_4$, which in turn enhanced the initial nucleation of GaN and improved the quality of the layer. The new $ZnAl_2O_4$ layer provided an improved lattice match to GaN as well as modifying the surface energy to enhance the nucleation of the initial GaN phase [55].

6.2 Growth of Al_2O_3

Two techniques were attempted for the deposition of Al_2O_3. Electron beam (e-beam) was the first attempted method because it was a readily available tool that is commonly used for Al_2O_3 deposition. The second approach was to use ALD which provided a

smooth surface and more accurate thickness control on ZnO. After comparison of initial results all Al_2O_3 deposition were performed using ALD.

6.2.1 E-beam Deposition

A 100nm thick film was deposited on a ZnO substrate by e-beam deposition. The pre-deposited Al_2O_3 was transformed into a spinel structure of $ZnAl_2O_4$ through high-temperature annealing in a ZnO box at 900ºC. An O_2 atmosphere was used to promote the reaction with the ZnO substrate. A ZnO box was used in order to prevent the ZnO substrate from diffusing. This annealing technique will be described in more detail in a later section. The presence of $ZnAl_2O_4$ has been found to enhance GaN nucleation, as well as retard Zn diffusion [56, 57]. Scanning electron microscope (SEM) showed the formation of a $ZnAl_2O_4$ layer after annealing but also the presence of a thicker Al_2O_3 on top with voids appearing in the ZnO substrate, Figure 6.1. The is undesirable and might have been due to continuous reaction of the Al_2O_3 source material with oxygen. The voids in the substrate reveal rapid diffusion or different plane dissolution rate of Zn occurring at the ZnO/Al_2O_3 interface. Altogether, the films achieved by e-beam deposition were not ideal for the desired transition layer for high-quality GaN growth. In addition, it has been reported that thinner Al_2O_3 layers provide better crystallinity because of their ability to anneal the entire layer faster and more uniformly [32, 58]. Therefore, a more controllable deposition technique was required to obtain thinner layers.

6.2.2 Atomic Layer Deposition

ALD is an excellent deposition method for applications that require smooth, uniform coverage and controllability of thickness. The ALD process is a cycle in which, individual atomic precursors are pulsed into the reactor followed by a purging N_2 or

evacuation period. This method allows for a self-limited layer-by-layer growth mode where the thickness is accurately controlled solely by the number of growth cycles rather than by temperature, etc. Additionally, precursor fluxes do not need to be uniform across the substrate surface: the flux only has to be large enough that the chemisorption layer on the substrate is saturated. This results in each cycle depositing the same amount of material, with any excess taken away during purging [32, 33]. This method allows for smooth layer deposition with low pinhole density and good uniformity over large-area substrates.

Al_2O_3 films were grown on the Zn face of ZnO (0001) substrates at a temperature of 100^{o}C inside a quartz tube with trimethylaluminum (TMAl) and H_2O (water vapor) as the precursors. The film growth took place in a cyclic manner at a base pressure of 500mTorr. One growth cycle consisted of four consecutive steps: (1) exposure to the metal precursor TMAl, (2) N_2 purge, (3) exposure to H_2O, and (4) another N_2 purge. Initially, Al_2O_3 was deposited to a thickness of 200nm at 100ºC. Cross-section SEM showed a smooth and uniform interface on the substrate for the 200nm Al_2O_3 transition layer, Figure 6.2. However, previous findings from e-beam showed that thinner layers would provide better crystallinity. Therefore, thinner layers ranging between 2nm to 100nm were used going forward [59]. A variety of temperatures were attempted ranging from 100ºC to 600ºC to try to anneal the ALD material during growth. A summary of the various thicknesses and temperatures used are shown in Table 6.1.

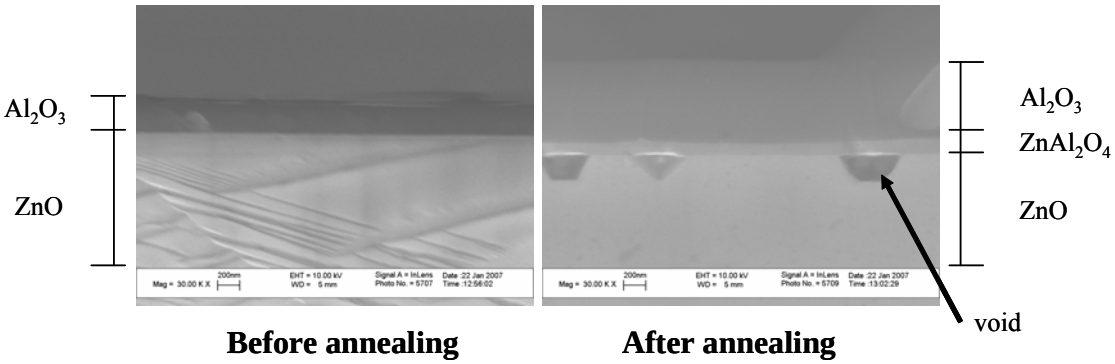

Figure 6.1: SEM of before and after annealing of Al_2O_3 on ZnO.

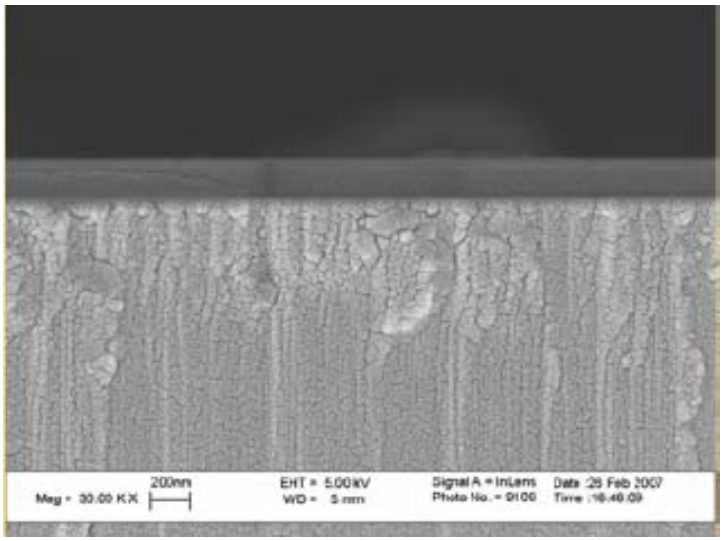

Figure 6.2: Cross-section SEM of ALD 200nm Al_xO_{1-x} on ZnO before annealing.

Table 6.1: All ALD growths.

ALD Al_2O_3/ZnO	100ºC	350ºC	600ºC
2nm	x	x	
5nm	x	x	
10nm	x	x	
20nm	x		
30nm	x		
50nm	x		
60nm	x		
90nm	x	x	x

6.3 Initial Annealing of ALD Al_2O_3 to Crystallize Layer

ALD layers are initially amorphous when grown. Therefore, annealing studies were performed at various times and temperatures in order to study the crystallization effects of the transition layers. Four types of annealing equipment were used: rapid thermal annealing (RTA), in-situ annealing in the MOCVD growth chamber, in-situ annealing in the ALD growth chamber, and annealing in a tube furnace. Results for each of the annealing equipment are described below.

6.3.1 RTA Annealing

The first method of annealing was performed by RTA. It is a readily available annealing method commonly used for activation of Mg dopants in p-GaN layers. The annealing for this study was performed on 5nm and 10nm ALD Al_2O_3 growths for 1 [32], 3, 5, and 10 minutes [57]. These short annealing times did not show a significant difference in crystallinity un-annealed samples. Therefore, the annealing time was increased to 25 and 40 minutes. However, RTA is designed for quick annealing and not long durations at high temperature (900ºC in these cases). For this reason annealing in the RTA was limited to 5 minute increments. The schematic for RTA ramping is shown in Figure 6.3. X-ray measurements of the layers grown on these annealed samples are shown in Figure 6.4. The data does not show optimal InGaN peaks. InGaN grown on Al_2O_3/ZnO layers that were annealed for 25 minutes showed an InGaN peak with 32% indium concentration but also a separate peak at a lower angle. InGaN grown on layers annealed for 40 minutes showed an InGaN peak with about 35% indium concentration within a broader peak and also a separate peak to the at a lower angle. This is possibly due to the cooling down and ramping up before and after each 5min increment which

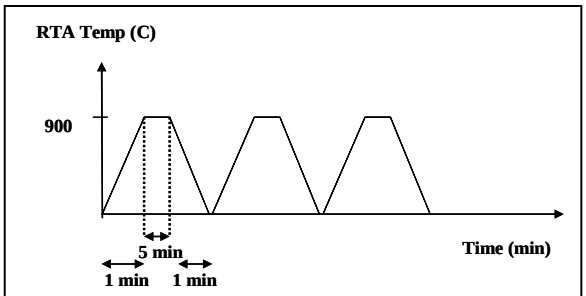

Figure 6.3: RTA ramping schematic.

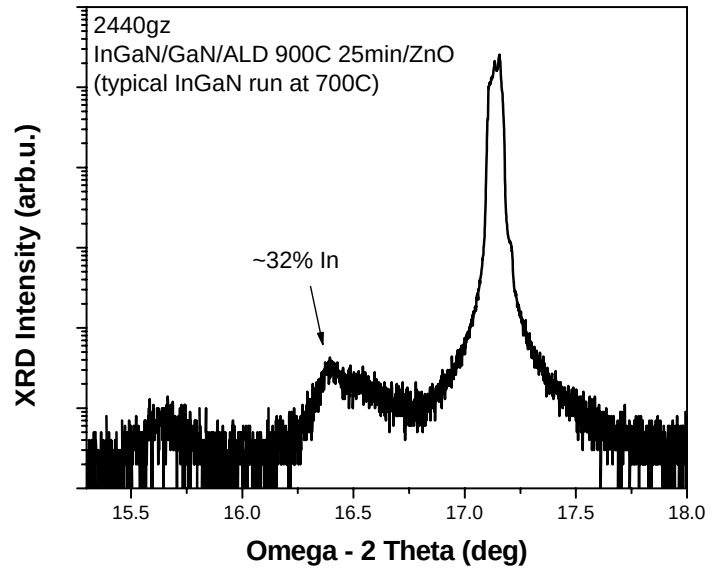

(a)

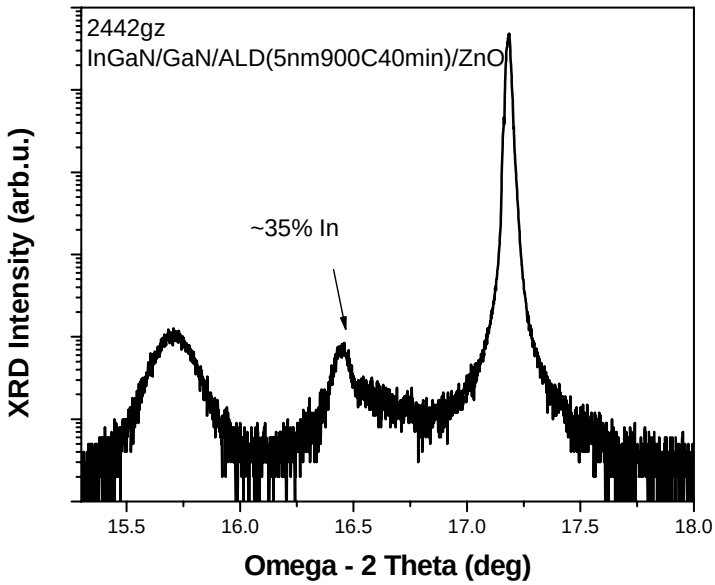

(b)

Figure 6.4: X-ray of RTA annealing of Al_2O_3 ALD at (a) 25 minutes and (b) 40 minutes.

could have caused warping of the material consequently non-uniform epilayers during MOCVD growth of GaN or InGaN.

6.3.2 *In-situ* Annealing in MOCVD Chamber

The second method of annealing attempted was in-situ annealing in the MOCVD chamber directly prior to growth of GaN and InGaN. The growth chamber sllowed continuous annealing as seen in Figure 6.5. The continuous annealing improved the quality of the epilayers over that achieved with incremental annealing required by the RTA, Figure 6.6. X-ray measurement of InGaN grown on an Al_2O_3/ZnO layer annealed for 20 minutes showed an InGaN peak with 32% indium concentration with no additional peaks. The full width at half maximum (FWHM) was 478arcsec, which met the first gate metric in the project, which was for a FWHM of ≤500arcsec. InGaN grown on an Al_2O_3/ZnO layer annealed for 30 minutes also showed an InGaN peak with 32% indium concentration but with a separate broad peak to the at a lower angle. Thus, the 20 minute annealing time showed promise for InGaN growth on Al_2O_3/ZnO. However, contamination from the growth chamber, due to prior doping experiments performed, could be contributing to unwanted defects during the annealing phase. Therefore, an MXI tube furnace was purchased to be used for the remainder of the annealing studies, as this would be able to provide a controllable environment.

6.3.3 *In-situ* Annealing in ALD Chamber

In addition to post-deposition annealing, high temperature ALD at 350ºC and 600ºC was investigated as a possible method of annealing the samples during growth in the ALD system. Si is a commonly used substrate for ALD growths and therefore was used as a control in conjunction with the ZnO growths for this *in-situ* annealing study. As a

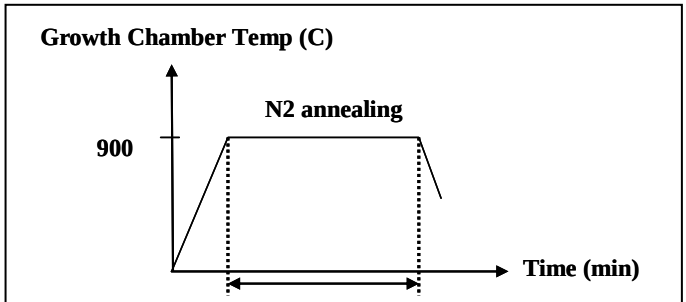

Figure 6.5: Growth chamber ramping schematic.

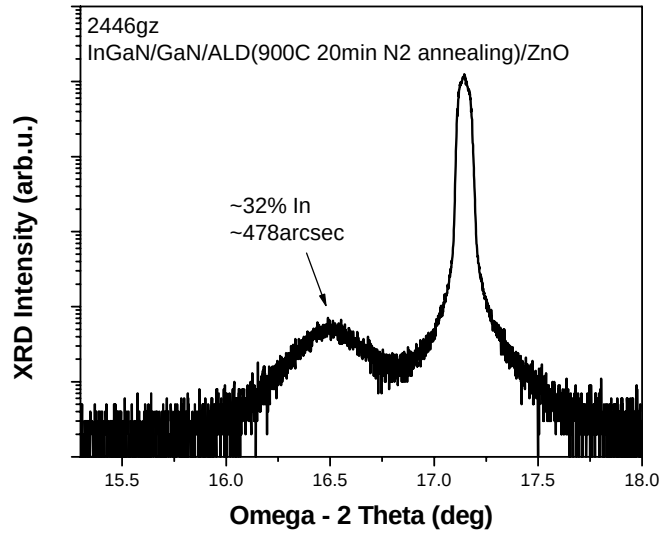

(a)

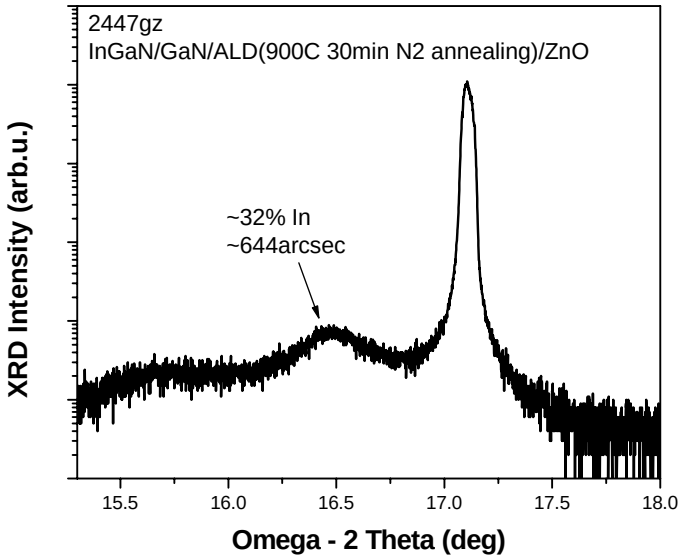

(b)

Figure 6.6: X-ray of Al_2O_3 annealed in chamber for (a) 20 minutes and (b) 30 minutes directly before InGaN growth.

starting point, 90nm layers were grown at each of the growth temperatures in order to perform material characterization and subsequently optimize growth parameters. Growths by MOCVD were based on the InGaN growth that showed a FWHM of 478arcsec. This MOCVD growth consisted of a 20 minute anneal at 900ºC in the chamber before growing a GaN buffer layer followed by an InGaN layer at 700ºC.

X-ray measurements showed Al_2O_3 phases in samples deposited at all three temperatures investigated, Figure 6.7. Peaks were observed at 38 and 82 degrees, which correspond to Al_2O_3 (110) and (306) phases. The (110) peak decreased when the temperature was increased from 100ºC to 350ºC and increased when the temperature was increased to 600ºC. The (306) phase was significantly more intense in the 600ºC sample than in the other two. The $ZnAl_2O_4$ phases of (311) and (400) at 36 and 44 degrees were very weak, almost unidentifiable, for the 100C and 350ºC samples. However, they were very prominent in the 600ºC sample. The (311) was unique because it only shows up again for the 50nm anneal discussed later. These results indicated that polycrystalline phases of Al_2O_3 were formed and better crystallinity can be obtained by employing a higher growth temperature. A summary of the phases of Al_2O_3 and $ZnAl_2O_4$ for *in-situ* ALD annealing can be seen in Table 6.2. The highlighted column denotes the chosen best time for crystallization of the material.

Cross-section SEM was performed on the 350ºC growth and 100ºC growth. The 100ºC showed a much rougher, more uneven surface than the 350ºC growth, Figure 6.8. The cross-section image showed a CVD like growth for the 100ºC sample. The deposited layer was as high as 400nm in places. The self limiting growth reaction no longer occurred after only a few high temperature growths. SEM of the surface of the

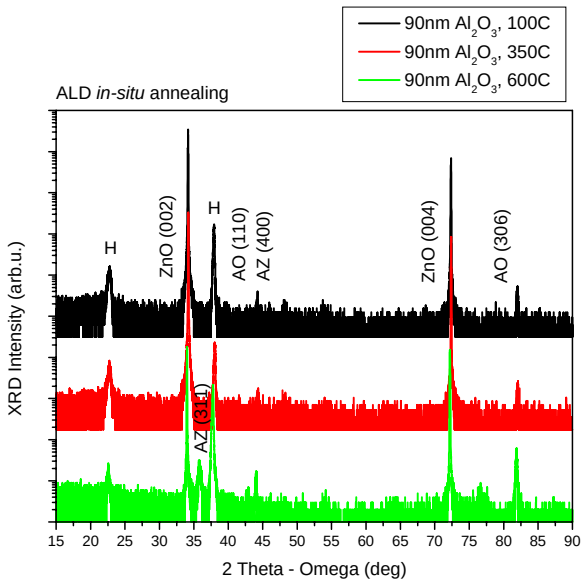

Figure 6.7: X-ray of high temperature annealing in ALD on ZnO substrates.

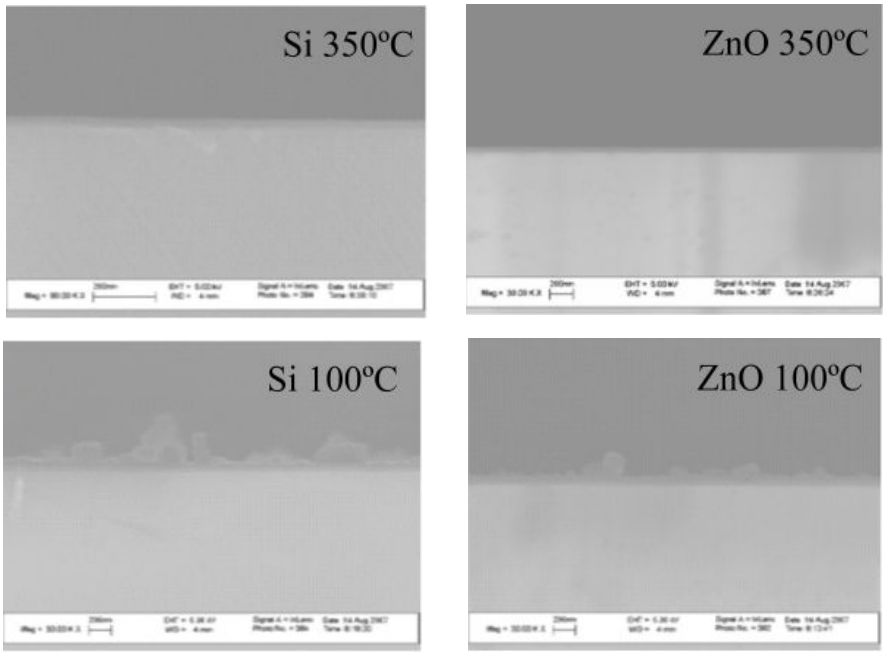

Figure 6.8: SEM cross-section of 350ºC and 100ºC ALD growth.

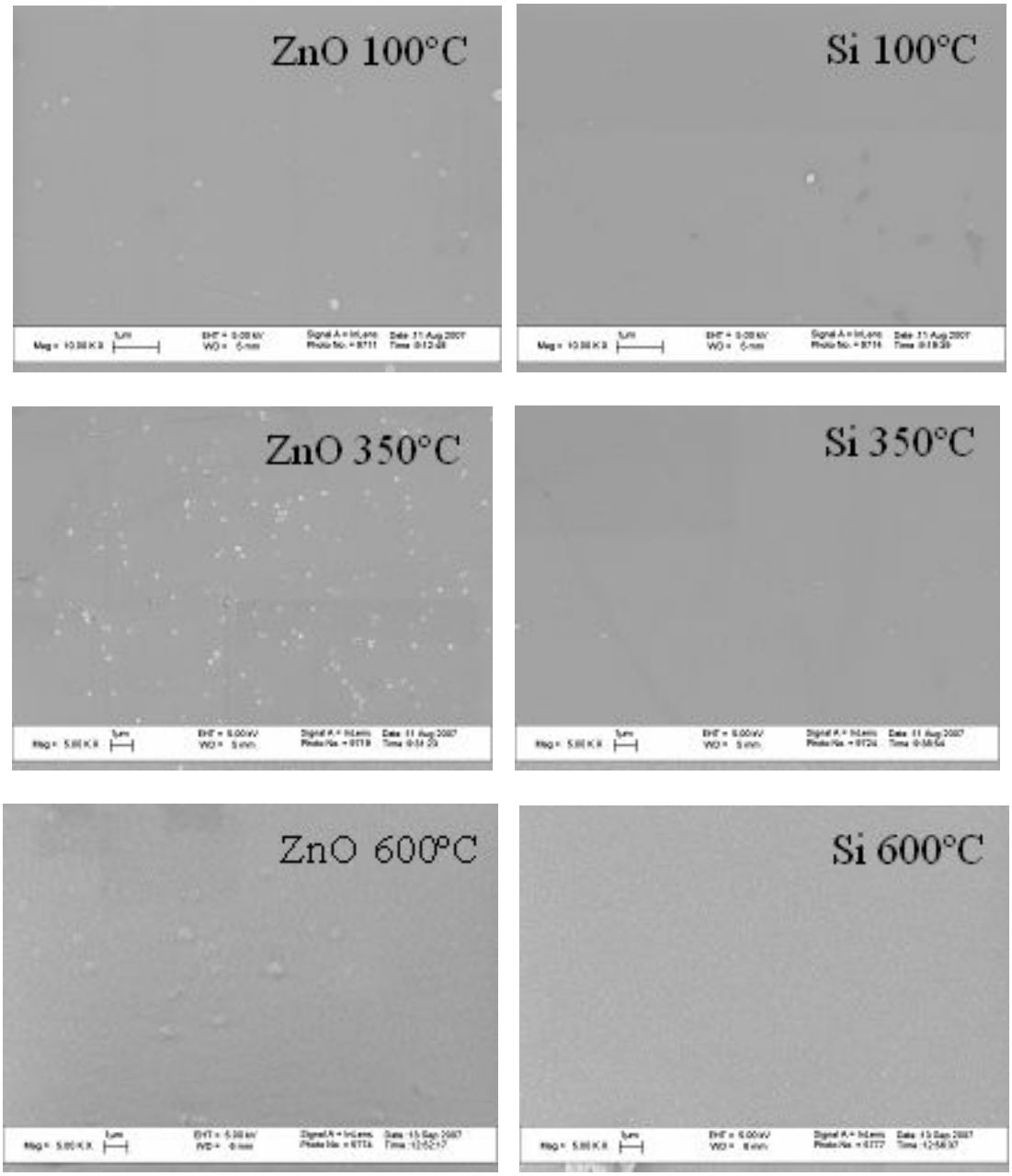

Figure 6.9: SEM surface analysis of ALD grown Al_2O_3 on ZnO and Si at 100ºC, 350ºC, and 600ºC.

Table 6.2: Summary of high growth temperature in ALD, x = showed peaks.

ALD Al_2O_3/ZnO	**High Growth Temperature**			
Phases	degree	100ºC	350ºC	600ºC
H	23	x	x	x
(012) Al_2O_3	25			
(311) $ZnAl_2O_4$	36			x
(110) Al_2O_3, H	38	x	x	x
(400) $ZnAl_2O_4$	44			x
(533) $ZnAl_2O_4$	48			
(024) Al_2O_3	53			
(306) Al_2O_3	82	x	x	x

600ºC growth was also taken and compared with 350ºC and 100ºC, Figure 6.9. It showed a grainer surface compared to the other growths. Layers deposited on ZnO showed more grains than those on the Si substrate. The reason for this is not clear. From these findings, high temperature ALD was not pursued further due to complications with the available ALD tool. All further annealing studies were performed using a tube furnace to anneal after ALD growth and before GaN buffer/InGaN growth.

6.4 Furnace Annealing of Al_2O_3/ZnO

A systematic growth of ALD layers on ZnO has been investigated. The approach is to obtain enough empirical data to further optimize material growth and hence LED structures. These ALD layers are initially amorphous and therefore the samples need to be annealed in order to form crystalline structures. An MXI furnace was used moving forward for the annealing studies. The furnace provides a clean controllable environment for the studying the annealing affects on Al_2O_3/ZnO. N_2 was the primary gas used for annealing, but air and O_2 were also investigated. Ideally, a single crystal of Al_2O_3 would be obtained. However, all the annealing results showed polycrystalline material including the non-annealed samples. Therefore, the only way to choose the best criteria was to look for the annealing condition that showed the highest intensities among all the peaks.

6.4.1 Introduction

The studies shown in the previous sections of annealing in RTA, in the MOCVD reactor, and in an ALD system all showed promise. However, all of these techniques

have limitations that make them unsuitable for use in a reliable, systematic study. These limitations included the short annealing times required for the RTA, contamination in the MOCVD chamber, and difficult to control parameters in the ALD system. Therefore, a furnace was used for the bulk of this thesis work. The furnace allowed for high temperature annealing of above 1000ºC as well as a clean environment for annealing studies. Samples were annealed at various temperatures ranging from 1100ºC to 1300ºC for times ranging from 5 to 120 minutes. These annealing studies were performed in order to understand the best crystallization conditions for the amorphous ALD layer in order to produce high-quality GaN epilayers by MOCVD. X-ray was used for the study of crystallization. X-ray measurements included scans from 25-90 degrees in order to encompass as many Al_2O_3 phases as possible since the crystalline phase of the annealed samples were unknown.

6.4.2 Preliminary Study

Initially 200nm thick layers were grown and studied as discussed in a previous section. However, as SEM showed in Figure 6.1, undesired layers were achieved after annealing of the amorphous Al_2O_3 layer. Therefore, a 5nm layer, a 50nm layer, and a stacked layer of Al_2O_3 and TiO_2 were attempted. TiO_2 was chosen because it was the other available source on the oxide ALD system. These layers were all annealed at 900ºC, which was the same temperature used for RTA annealing. Peaks were identified by using the x-ray JCPDS database. Si samples were used in conjunction with ZnO growths as calibration samples because Si is a commonly used material for ALD deposition.

The layers were annealed for 30 and 60 minutes. The 34 and 72 degrees peaks were attributed to the (0002) and (0004) ZnO peak. Possible Al_2O_3 (AO) and $ZnAl_2O_4$ (AZ) peaks were seen after the (0002) ZnO peak. The following phases were identified: Al_2O_3 peaks at 38 degrees for (110) phase, $ZnAl_2O_4$ peaks at 44, 48, and 82 degrees for (440), (311), and (444) phases, and unidentified phases at 23 and 53 degrees. Also, the (110) phase is the same peak that is seen for the x-ray stage, which is marked as H in the figures. However, the peak intensity at 38 degrees shifts with annealing temperature and time and therefore is likely a mixture of both the x-ray stage peak and an Al_2O_3 (110) emission.

For the 50nm layer, the sample annealed for 30 minutes showed the (110) and the (444) peak, Figure 6.10. No significant change was observed when the annealing time was increased to 60 minutes. The (440), (311), and 53 degree peaks were so weak that they were difficult to identify. The annealing time was then increased to 120 minutes to see if a longer time was required for further crystallization to occur. The (110) and (444) phases were similar to those observed after 30 minutes of annealing with the addition of a peak at 48 degrees for the $ZnAl_2O_4$ (311) peak. Overall, the 120 minutes annealing time was found to be the best case for the 50nm sample. SEM was performed and can be seen in Figure 6.11 and Figure 6.12. Cracking of the layers appeared for both the 30 and 60 minutes annealing time. However, the layers annealed for 60 minutes also showed separation from the ZnO, Figure 6.11. It was assumed that the layers annealed for 120 minutes would also show separation from the ZnO. In addition, SEM surface analysis showed a smoother surface for after 30 minutes of annealing than after 60 minutes, Figure 6.12. There might have been too much stress in the layers leading to cracks and

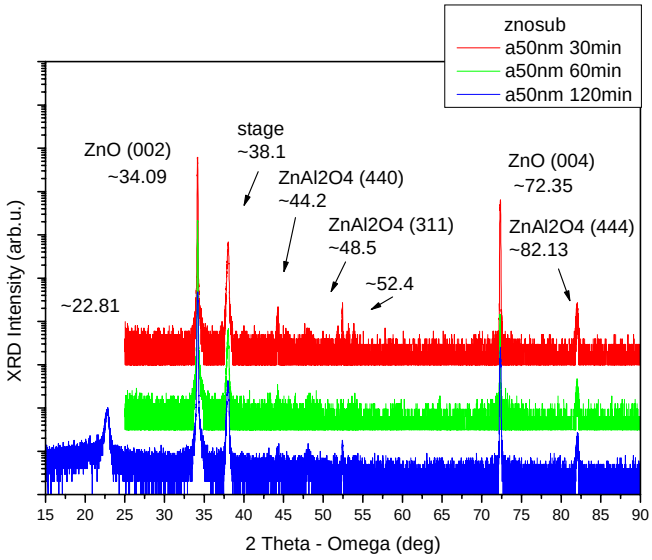

Figure 6.10: 50nm Al_2O_3 grown on ZnO substrate annealed for 30, 60, and 120 minutes at 900ºC.

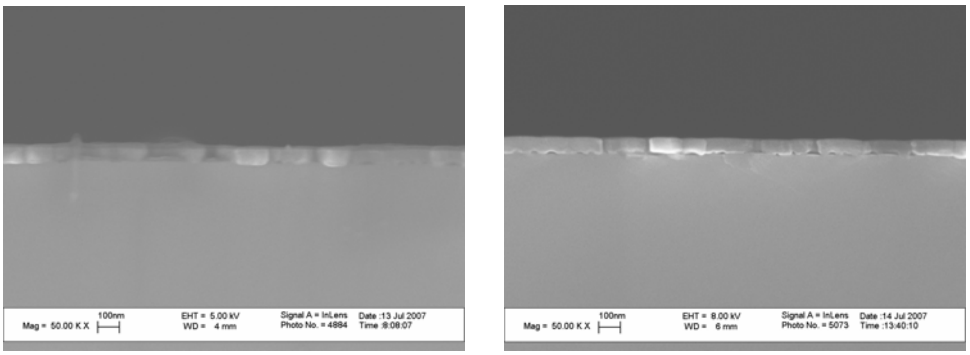

(a) (b)

Figure 6.11: SEM cross-section of 50nm Al_2O_3 on ZnO by ALD annealed in (a) 30 minutes and (b) 60 minutes increments in a furnace of N_2 ambient at 900ºC.

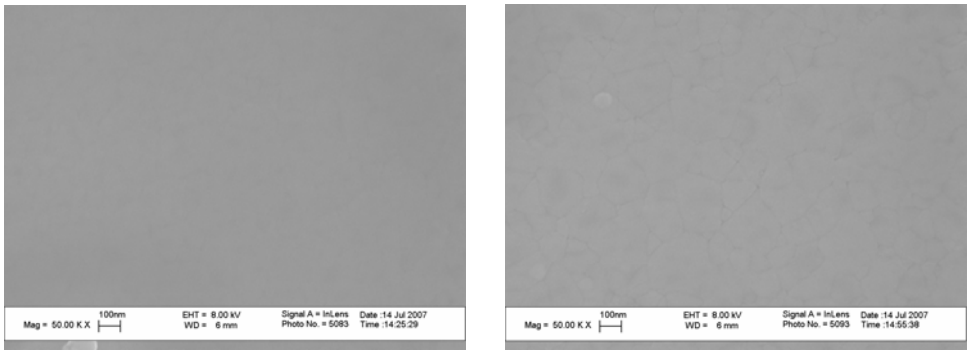

(a) (b)

Figure 6.12: SEM surface of 50nm Al_2O_3 on ZnO by ALD annealed in (a) 30 minutes and (b) 60 minutes increments in a furnace of N_2 ambient at 900ºC.

hence separation from the substrate. This led to growth of thinner layers at 5nm thickness.

The 5nm Al_2O_3 sample was thinner than the 50nm and therefore was thought to require a shorter annealing time. However, annealing for 15 minutes showed weaker peaks than the 30 and 60 minutes anneal time, Figure 6.13. The 60 minutes anneal showed the most x-ray peaks and the highest intensities of the three annealing times studied. The 15 minutes anneal showed all the peaks, but (440), (311), and (444) were very weak. The 30 minutes annealing showed an increase in intensity of the (440) and (444) $ZnAl_2O_4$ peaks, and the 60 minutes annealing showed the highest intensity and most distinct of all the peaks. However, the 5nm layers were too thin for structural analysis, such as SEM, and therefore further studies were not pursued.

A stacked layer of $Al_2O_3/TiO_2/Al_2O_3/TiO_2/AL_2O_3$ was grown on ZnO with Al_2O_3 at 5nm and TiO_2 at 2.5nm for a total of 20nm. The stacked layer was grown in order to see if the multi-layer would prevent Zn diffusion. The annealing times were the same as for the 5nm sample of 15, 30, and 60 minutes. Here, the 15 minutes annealing time showed all the phases of Al_2O_3 and $ZnAl_2O_4$ at higher intensities than seen for 30 minutes and 60 minutes annealing, Figure 6.14. The 53 degrees peak disappeared for the layer annealed for 30 minutes. Increasing the annealing time to 60 minutes made the (311) phase disappear, and the ZnO peaks were no longer visible. No peaks were identified as TiO_2 peaks or mixtures of the two materials. However, due to the addition of TiO_2, the identification of the peaks were not definite compared to the XRD JCPDS database. SEM was also performed for 30 minutes annealing at 900ºC for Al_2O_3 on bare ZnO, Al_2O_3 on Si, and Al_2O_3/TiO_2 stacks on ZnO substrates, are shown in Figure 6.15(a), (b),

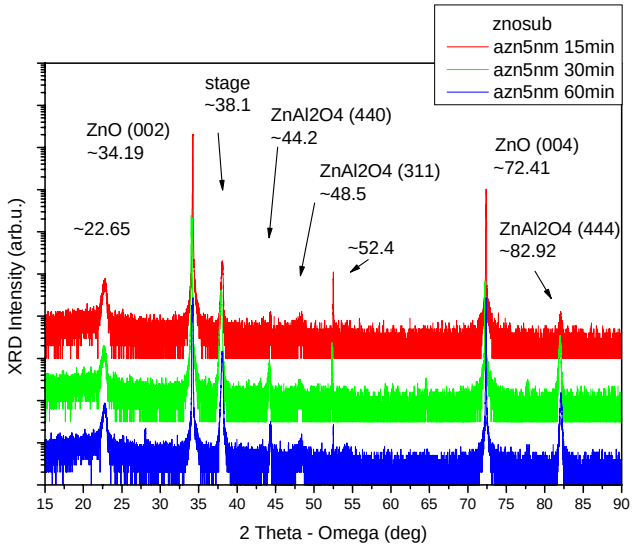

Figure 6.13: 5nm Al_2O_3 grown on ZnO substrate annealed for 15, 30, and 60 minutes at 900ºC.

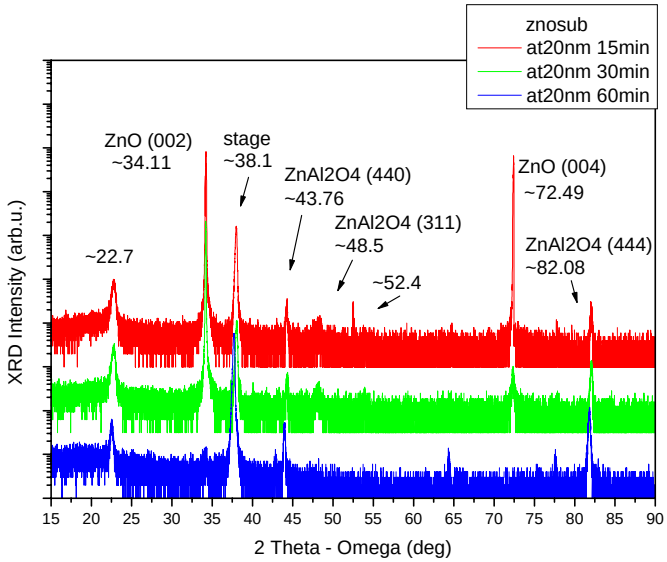

Figure 6.14: Al_2O_3 at 5nm and TiO_2 at 2.5nm grown on ZnO substrate in the following configuration: $Al_2O_3/TiO_2/Al_2O_3/TiO_2/Al_2O_3$, annealed for 15, 30, and 60 minutes at 900ºC.

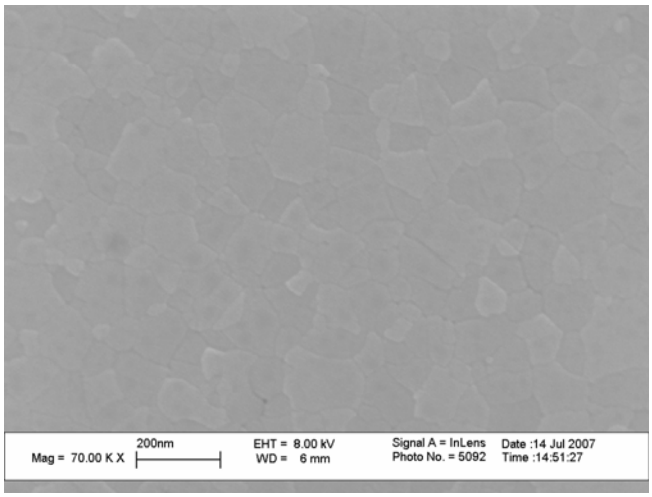

(a)

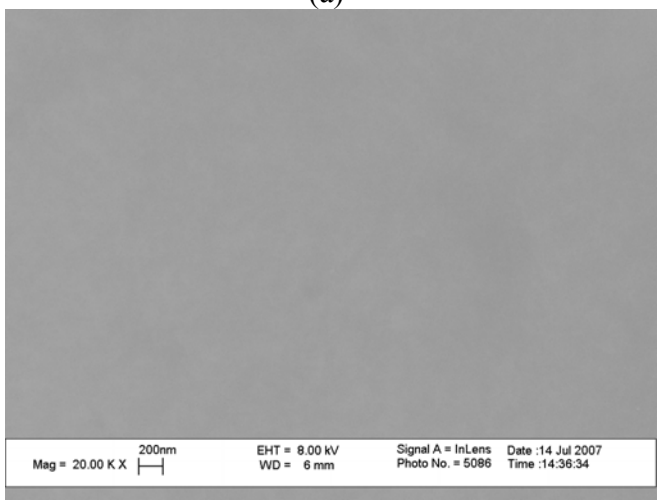

(b)

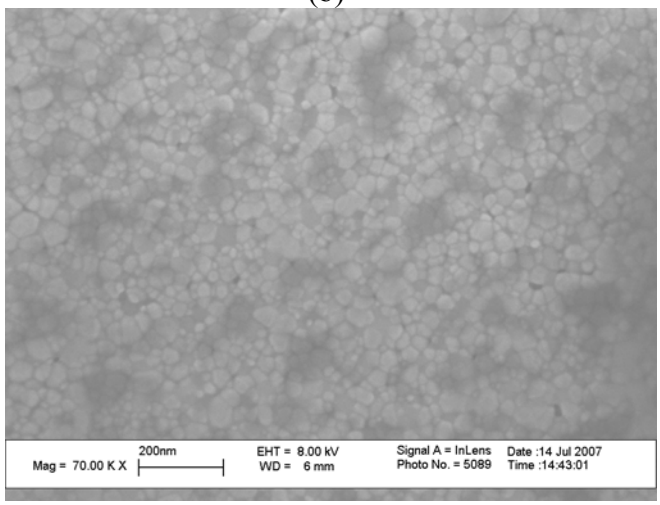

(c)

Figure 6.15: SEM of 30 minutes annealed 5nm Al_2O_3 on (a) ZnO and (b) Si. (c) SEM of 30 minutes annealed Al_2O_3/TiO_2 stack on ZnO.

Table 6.3: Summary of phases seen in preliminary study, x = showed peaks.

ALD Al_2O_3/ZnO	**Preliminary Study**									
Phases	degree	50nm Al_2O_3			5nm Al_2O_3			stacked Al_2O_3/TiO_2		
		30min	60min	120min	15min	30min	60min	15min	30min	60min
unidentified	23	x	x	x	x	x	x	x	x	x
(110) Al_2O_3	38	x	x	x	x	x	x	x	x	x
(440) $ZnAl_2O_4$	44					x	x	x	x	x
(311) $ZnAl_2O_4$	48			x	x	x	x	x	x	
unidentified	53	x		x	x	x	x	x		
(444) $ZnAl_2O_4$	82	x	x	x	x	x	x	x	x	x

and (c). The Al_2O_3 grown on ZnO exhibits more grains than that grown on Si after the same annealing time. In addition, the stack layer is less crystalline than the single Al_2O_3 layer on ZnO. Although the stacked layers showed promising results, due to time constraints they were not pursued, because they did not show a significant improvement compared to single layer Al_2O_3 on ZnO. A summary of the phases of Al_2O_3 and $ZnAl_2O_4$ observed in the preliminary studies can be seen in Table 6.3. The highlighted columns denote the chosen best time for crystallization of each material thickness. The 50nm layer showed promise due to its higher crystallinity and ability to be easily studied by SEM and x-ray. Therefore, the 50nm Al_2O_3 layer was carried forward into further annealing studies.

6.4.3 Increase in Annealing Temperature to 1100ºC

The next series of annealing studies investigated increased temperatures between 1100-1300ºC. These high temperatures also correlate to the high temperatures seen in MOCVD growths. The layers were annealed at various times (90 and 180 seconds). The results showed that only the 1100ºC showed multiple peaks pertaining to 38 and 82 degrees of Al_2O_3 and 36 and 48 degrees of $ZnAl_2O_4$, Figure 6.16. The 38 degrees peak showed up for all the samples but is probably from the stage holder. The 1200ºC sample did show the rare (311) $ZnAl_2O_4$ phase, but it did not show any of the other peaks. Therefore, 1100ºC was carried forward for the annealing study of 10, 20, and 50nm Al_2O_3/ZnO. An additional study was also performed on 10nm 350ºC grown ALD Al_2O_3/ZnO. The bare ZnO substrate showed no peaks, meaning the peaks seen on the annealing studies were phases from Al_2O_3 and/or $ZnAl_2O_4$ from ALD Al_2O_3 growth. The

34 and 72 degrees peaks of the (0002) and (0004) phases of ZnO appeared. The following phases were also identified: Al_2O_3 peaks at 25, 38, 53, and 82 degrees for (012), (110), (024), and (306) phases, $ZnAl_2O_4$ peaks at 36, 44 and 48 degrees for (311), (400), and (533) phases, and x-ray stage holder peaks at 23 and 38 degrees. The unidentified peaks at 23 and 53 degrees from the preliminary study have been assigned to the x-ray stage holder and the (024) Al_2O_3 phase, respectively. The 23 degrees peak was consistent and did not change in intensity through all the measurements and also showed up on the bare ZnO substrate. Therefore, it was attributed to the x-ray stage holder. New peaks at 25 and 36 degrees for the (012) and (311) phases of Al_2O_3 and $ZnAl_2O_4$, respectively, only appeared in the 50nm sample. The 50nm sample showed more promise than the other thicknesses and therefore was studied for a wider variety of annealing times than the 10nm and 20nm sample. The (311) $ZnAl_2O_4$ phase was originally assigned to the 48 degrees peak, and was reassigned to the (533) $ZnAl_2O_4$ phase. The 44 degrees peak originally assigned to the (440) $ZnAl_2O_4$ phase was reassigned to the (400) $ZnAl_2O_4$ phase. Also, the 82 degrees peak originally for the (444) $ZnAl_2O_4$ phase was reassigned to be the (306) Al_2O_3 phase. These changes were made after further studies in comparison between measured x-ray degrees and the x-ray JCPDS database. Another detail to notice is the un-annealed samples. X-ray showed that the phases seen for Al_2O_3 and $ZnAl_2O_4$ were also seen for the un-annealed samples, which led to the theory that the un-annealed samples were not amorphous but polycrystalline. The annealing studies were still important as changes in the polycrystalline structure can affect the subsequent MOCVD GaN layers.

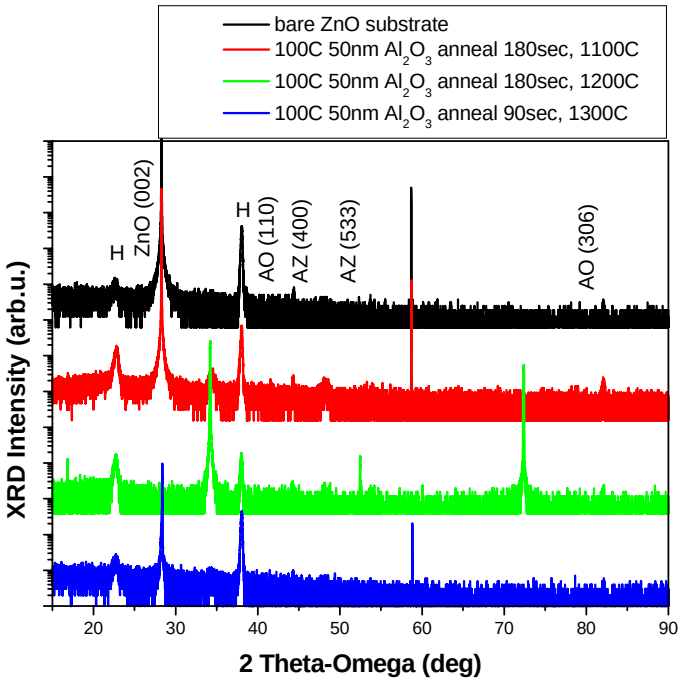

Figure 6.16: X-ray on bare ZnO substrate and 50nm ALD Al_2O_3/ZnO annealed at various temperatures of 1100ºC, 1200ºC, and 1300ºC.

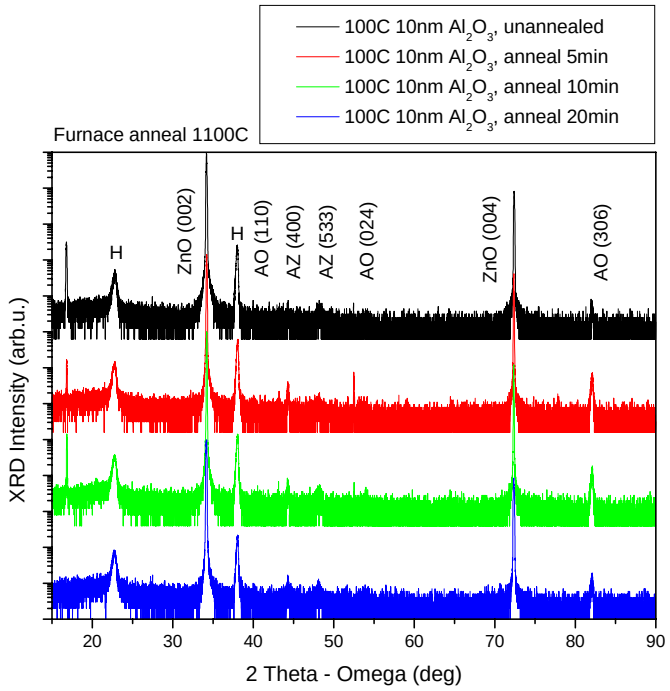

Figure 6.17: X-ray on a non-annealed 10nm Al_2O_3, and 1100ºC annealed samples at 5, 10, and 20 minutes.

The first study was on 10nm ALD Al_2O_3/ZnO samples annealed for 5, 10, and 20 minutes, Figure 6.17. An un-annealed 10nm Al_2O_3/ZnO was used for comparison and was also grown on by MOCVD, discussed in a later section. The (110) and (306) planes of Al_2O_3 (AO) can be observed for all the annealing times, including the un-annealed sample. The intensity of the (110) plane was constant for all annealing times, and hence was assumed to be all from the sample holder. The sample annealed for 5 minutes had the highest intensity (306) phase peak. Also, the strongest peaks for (024), (400), and (533) phases all appeared in this sample. Each of these peaks decreased in intensity as the annealing time was increased. Therefore, is was concluded that the sample annealed for 5 minutes contained higher-quality polycrystalline Al_2O_3 phases. A quick study was performed on 10nm 350ºC *in-situ* annealed ALD Al_2O_3/ZnO. The samples were further annealed in a furnace for 5, 10, and 20 minutes. The results do not show any prominent peaks except for an increase in Al_2O_3 (110) and (306) phases for 10 minutes annealing, Figure 6.18. However, the best InGaN results from this study were grown on these samples, as will be shown in a later section. Due to unforeseen issues with high temperature ALD growths, discusses in the previous section, these annealing studies were not carried forward.

The next study was on 20nm ALD Al_2O_3/ZnO annealed for 10, 20, and 40 minutes, Figure 6.19. An un-annealed 20nm Al_2O_3/ZnO was used for comparison and was also grown on by MOCVD, discussed in a later section. The (110) and (306) phases of Al_2O_3 and the $ZnAl_2O_4$ (533) phase can be observed for all the annealing times including the un-annealed sample, as seen in the study of 10nm films. The highest intensities of the (110) and (306) planes were observed for the un-annealed, 10, and 40 minute annealing

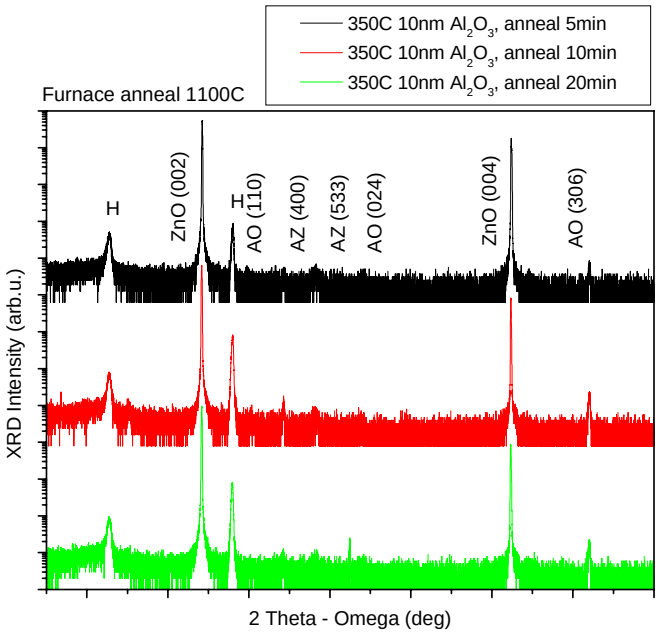

Figure 6.18: 10nm 350ºC *in-situ* annealed ALD Al_2O_3/ZnO further annealed in furnace at 1100ºC for 5, 10, and 20 minutes.

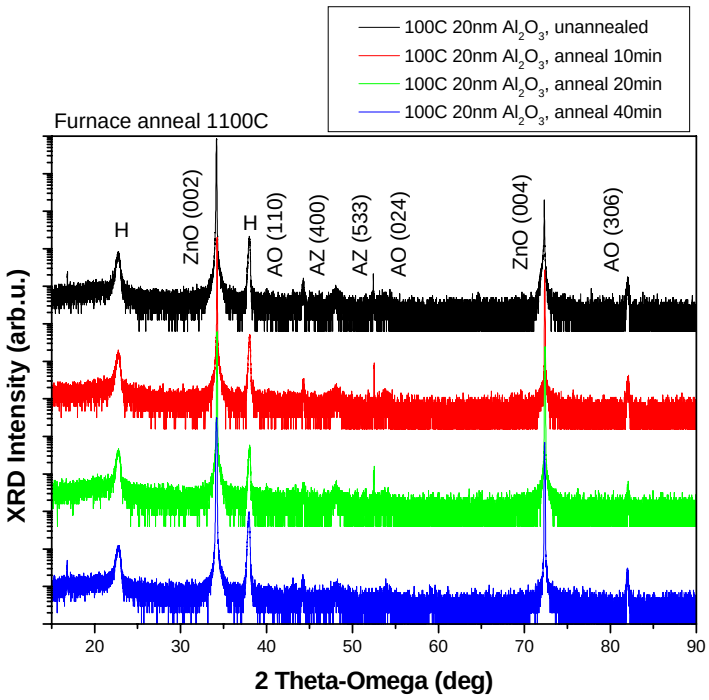

Figure 6.19: X-ray on a non-annealed 20nm Al_2O_3, and 1100ºC annealed samples at 10, 20, and 40 minutes.

times. The strongest $ZnAl_2O_4$ (533) phase appeared for the un-annealed, 10, and 20 minute annealing times. The $ZnAl_2O_4$ (400) phase appeared on the un-annealed and the 10 minutes annealed sample, and the Al_2O_3 (024) phase only appeared on the 10 and 20 minute annealing. Through the process of elimination, the 10 minute annealing was chosen as the best annealing time for improving crystalline quality for 20nm Al_2O_3/ZnO. An additional observation from this study was that the $ZnAl_2O_4$ phases were more clearly present in x-ray measurements than in the 10nm Al_2O_3 layer. This phenomenon could be due to the detection limitation on a thinner layer.

The third study was on 50nm Al_2O_3/ZnO. The first set of anneals were performed at 50 and 100 minutes, below the two high times used in the preliminary study, Figure 6.20. An un-annealed 50nm Al_2O_3/ZnO was used for comparison. The two annealing times showed only weak Al_2O_3 (110) and (306) phases compared to the intensities seen for the un-annealed sample. The un-annealed sample also showed Al_2O_3 (024) and $ZnAl_2O_4$ (400) phase. For the next set of samples the annealing times used were the same as for the 20nm Al_2O_3 layers (10, 20, and 40 minutes), Figure 6.21. The (110) peak appeared for all of these samples but decreased noticeably in the samples annealed for 40 minutes. The optimal annealing time for 50nm was found to be at 20 minutes, which was determined because this sample showed all of the reported peaks of (012), (110), (024), and (306) for Al_2O_3 and (400) and (533) for $ZnAl_2O_4$. Also, each peak was distinct, which was not the case for the un-annealed, 10 minute, or 40 minute annealed samples. A decrease in annealing time to 10 minutes made all the phases decrease in intensity. The (400), (533), and (024) phases were nearly undistinguishable, and the (012) phase was not observed. An increase in time to 40 minutes caused all of the peaks disappear

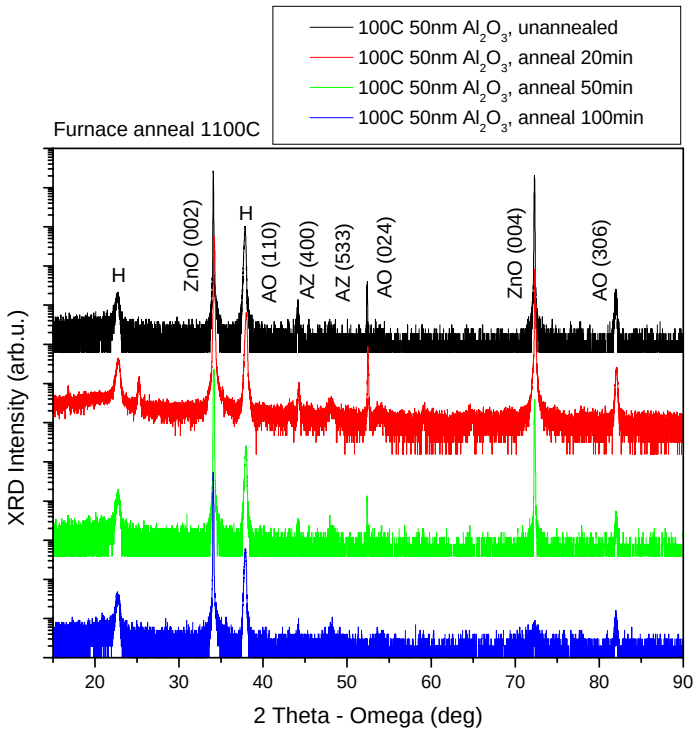

Figure 6.20: X-ray on a non-annealed 50nm Al_2O_3, and 1100ºC annealed samples at 20, 50, and 100 minutes.

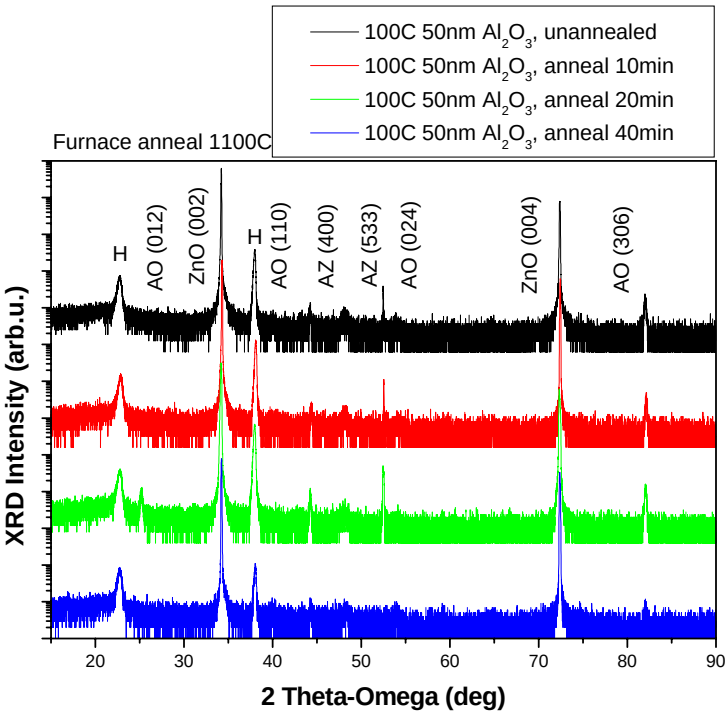

Figure 6.21: X-ray on a non-annealed 50nm Al_2O_3, and 1100ºC annealed samples at 10, 20, and 40 minutes.

except for the (110) peak, which was assumed to be from the XRD sample holder. The un-annealed case only showed the $ZnAl_2O_4$ (400) phase and the Al_2O_3 (024) and (306) phases, which were weaker than the peaks seen for the 20 minute annealed sample. Therefore, 20 minutes was chosen as the optimal annealing time for improving the crystallinity of 50nm Al_2O_3/ZnO. The sample annealed for 20 minutes was able to show distinct peaks for all of the observed phases, including (012) and (533), which were the least prominent in all the annealing studies.

A two-step annealing process was also attempted on 50nm Al_2O_3/ZnO. The 50nm samples were annealed at 1100ºC for 180 seconds followed by a 1000ºC anneal for 0, 20, 40, and 60 minutes. This annealing condition (1100ºC, 180 seconds) was chosen for obtaining better crystallinity of Al_2O_3, based on x-ray results of ALD on Si. However, according to literature the temperature for $ZnAl_2O_4$ formation at 640ºC, which meant the investigated temperature of 1100ºC might be too high for annealing [60]. Therefore, the annealing temperature was cooled down to 1000ºC after the 1100ºC for various annealing times of 0, 20, 40, and 60 minutes to achieve the proper annealing temperature, Figure 6.22. Al_2O_3 peaks at 38, 53, and 82 degrees for (110), (024), and (306) phases, $ZnAl_2O_4$ peaks at 44 and 48 degrees for (400) and (533) phases, and x-ray stage holder peaks at 23 and 38 degrees were seen in all the samples. However, the intensity of the peaks did not show any increase or decrease relative to each other. Two extra peaks were observed at 25 and 36 degrees, corresponding to the (012) and (311) peaks of Al_2O_3 and $ZnAl_2O_4$, respectively. These two peaks only appeared for annealing at 1100ºC for 180 seconds with no ramp down to 1000ºC. This showed that the higher temperature was actually ideal for the 50nm layer, contrary to prediction. The (012) peak was only seen in one

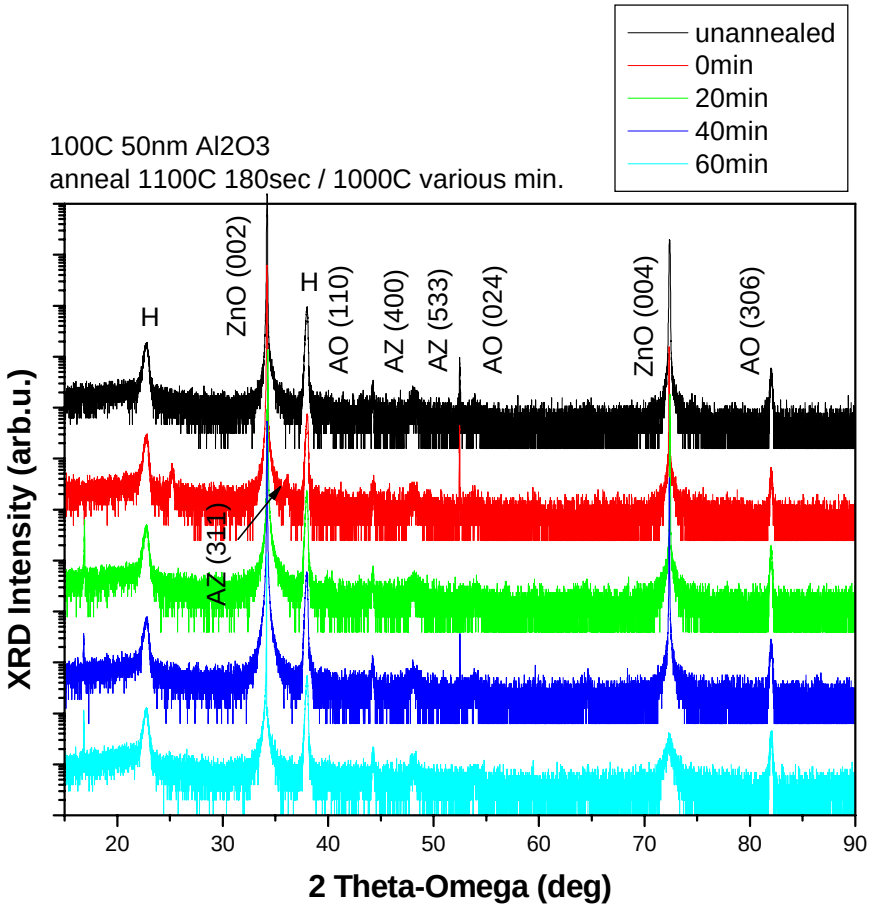

Figure 6.22: ALD 100ºC 50nm Al_2O_3/ZnO annealed in furnace 1100ºC 180sec/1000ºC (0, 20, 40, and 60 minutes).

Table 6.4: Summary of 1100ºC annealed samples in furnace, x = showed peaks.

ALD Al_2O_3/Zn		**1100ºC Annealing in Furnace**														
Phases	degree		50nm Al_2O_3			10nm Al_2O_3				10nm 350ºC Al_2O_3			20nm Al_2O_3			
		bare ZnO	1100ºC	1200ºC	1300ºC	0min	5min	10min	20min	5min	10min	20min	0min	10min	20min	40min
H	23	x	x	x	x	x	x	x	x	x	x	x	x	x	x	x
(012) Al_2O_3	25															
(311) $ZnAl_2O_4$	36		x	x												
(110) Al_2O_3, H	38	x	x	x	x	x	x	x	x	x	x	x	x	x		x
(400) $ZnAl_2O_4$	44						x	x	x		x		x	x		
(533) $ZnAl_2O_4$	48			x			x	x	x				x	x	x	x
(024) Al_2O_3	53						x							x	x	
(306) Al_2O_3	82			x			x	x	x	x	x	x	x	x	x	x

ALD Al_2O_3/ZnO		**1100ºC Annealing in Furnace**										
Phases	degree	50nm Al_2O_3 annealed 1100ºC						50nm Al_2O_3(1000ºC 180sec/1000ºC)				
		0min	10min	20min	40min	50min	100min	no ann	0min	20min	40min	60min
H	23	x	x	x	x	x	x	x	x	x	x	x
(012) Al_2O_3	25			x					x			
(311) $ZnAl_2O_4$	36								x			
(110) Al_2O_3, H	38	x	x	x	x	x	x	x	x	x	x	x
(400) $ZnAl_2O_4$	44	x		x				x	x	x	x	x
(533) $ZnAl_2O_4$	48		x	x				x	x	x	x	x
(024) Al_2O_3	53	x		x		x		x	x	x	x	x
(306) Al_2O_3	82	x	x	x	x	x	x	x	x	x	x	x

Table 6.5: Reanalysis of Al_2O_3 phases on 20 and 50nm Al_2O_3/ZnO.

ALD Al_2O_3/ZnO		**1100°C Annealing in Furnace**														
Phases	degree	20nm Al_2O_3				50nm Al_2O_3 annealed 1100°C						50nm Al_2O_3(1000°C 180sec/1000°C)				
		0min	10min	20min	40min	0min	10min	20min	40min	50min	100min	no ann	0min	20min	40min	60min
H	23	x	x	x	x	x	x	x	x	x	x	x	x	x	x	x
(012) Al_2O_3	25							x					x			
(110) Al_2O_3, H	38	x	x		x	x	x	x	x	x	x	x	x	x	x	x
(400) Al_2O_3	44	x	x			x		x				x	x	x	x	x
(024) Al_2O_3	53		x	x		x		x		x		x	x	x	x	x
(306) Al_2O_3	82	x	x	x	x	x	x	x	x	x	x	x	x	x	x	x

other case: 50nm annealing at 1100ºC for 20 minutes. The (311) peak was only seen in one other case: *in-situ* ALD annealing at 600ºC. A summary of the phases of Al_2O_3 and $ZnAl_2O_4$ for the 1100ºC anneals can be seen in Table 6.4.

6.4.4 Reevaluation of 20nm and 50nm Al_2O_3/ZnO

A third round was performed for the comparison of x-ray experimental peak values to the x-ray JCPDS database. The peak at 44 degrees, which was initially attributed to the $ZnAl_2O_4$ (400) phase, was reassigned again to become the (113) phase of Al_2O_3. This left only one peak at 48 degrees for the $ZnAl_2O_4$ (533) phase. One peak is not enough for a conclusive study of $ZnAl_2O_4$ phases. Therefore, only the Al_2O_3 peaks were taken into consideration. The Al_2O_3 peaks were at 25, 38, 44, 53, and 82 degrees for (012), (110), (113), (024), and (306) phases. Substituting the (113) phase into the 20nm and 50nm studies discussed in the previous section did not change the conclusions made. Therefore, the best annealing times were still 10 minutes for 20nm and 20 minutes for 50nm Al_2O_3/ZnO. A summary of the results can be seen in Table 6.5.

The surface morphology of the as-deposited and post-annealed 20nm Al_2O_3 film was measured by atomic force microscopy (AFM) as seen in Figure 6.23. The surface of the as-deposited Al_2O_3 film has a terrace-like feature and excellent conformity, Figure 6.23(a). The root mean square (RMS) roughness of the as-deposited film was about 1.6nm, which increased to 3.5nm after 10 minutes annealing, Figure 6.23(b). The grains coalesced and the roughness increased after thermal annealing. The roughness could lead to a better nucleation layer for the GaN epilayer because of the multiple nucleation sites.

6.4.5 Evaluating the Use of a ZnO Box During Annealing

The surface damage on ZnO from chemical mechanical polishing (CMP) must be removed prior to use as a substrate in order to achieve growth of high quality GaN. This can be done by annealing the substrate prior to ALD or MOCVD growth. However, the equilibrium vapor pressure of oxygen in ZnO is lower than zinc. One method is to use a ZnO MOCVD tool to produce a Zn ambient during high temperature annealing. However, this leads to the same issue of unknown contaminant levels in the growth chamber discussed previously. Unwanted precursors could affect the annealing of the substrate. Therefore, a ZnO box was used in conjunction with a tube furnace to supply a Zn ambient during annealing. Annealing in a ceramic ZnO box increases the Zn partial pressure in the atmosphere and can suppress desorption of Zn atoms from the ZnO surface thereby maintaining the surface stoichiometry [30]. This in turn affects the polarity of the ZnO material and consequently the GaN growth. Zn-face (Zn-polar) ZnO, such as the substrates used in this study, result in Ga-polar GaN. Ga-polar GaN growths yield better crystal quality compared with N-polar GaN.

Samples for this study were annealed with and without a box. Both bare ZnO substrates and Al_2O_3/ZnO substrates were annealed. AFM was performed on these samples. A bare non-annealed ZnO substrate showed an RMS value of 0.271nm, Figure 6.24(a). The substrate was then annealed for 3 hours at 1100°C in an air environment inside a ZnO box and showed an RMS value of 1.547nm, Figure 6.24(b). The sample became rougher showing terrace like steps. The long annealing time and high temperature were performed in an attempt to anneal out substrate defects prior to subsequent growths. MOCVD MQWs were attempted on these substrates. However, no

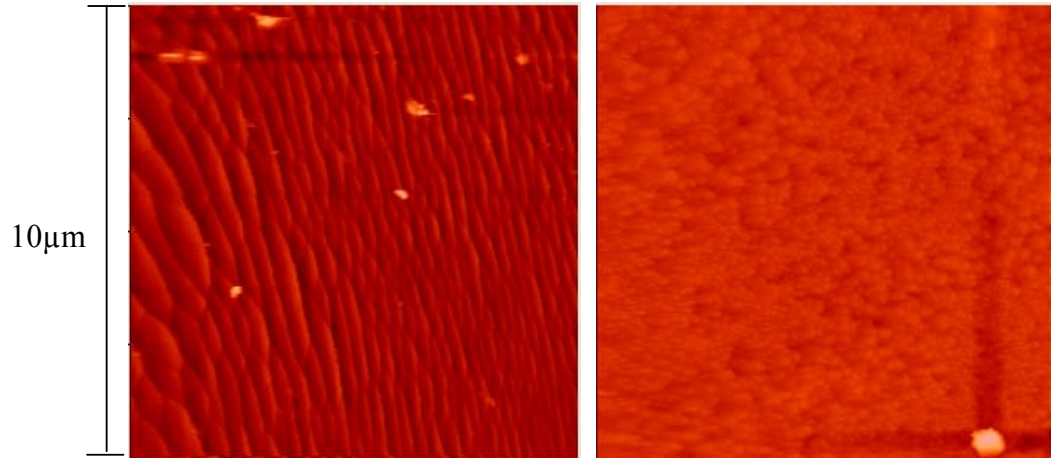

(a) (b)

Figure 6.23: Atomic force microscopy scans (10x10µm) of 20nm Al_2O_3 films deposited on ZnO substrates for (a) as-deposited and (b) after 10 minutes, 1100ºC annealing.

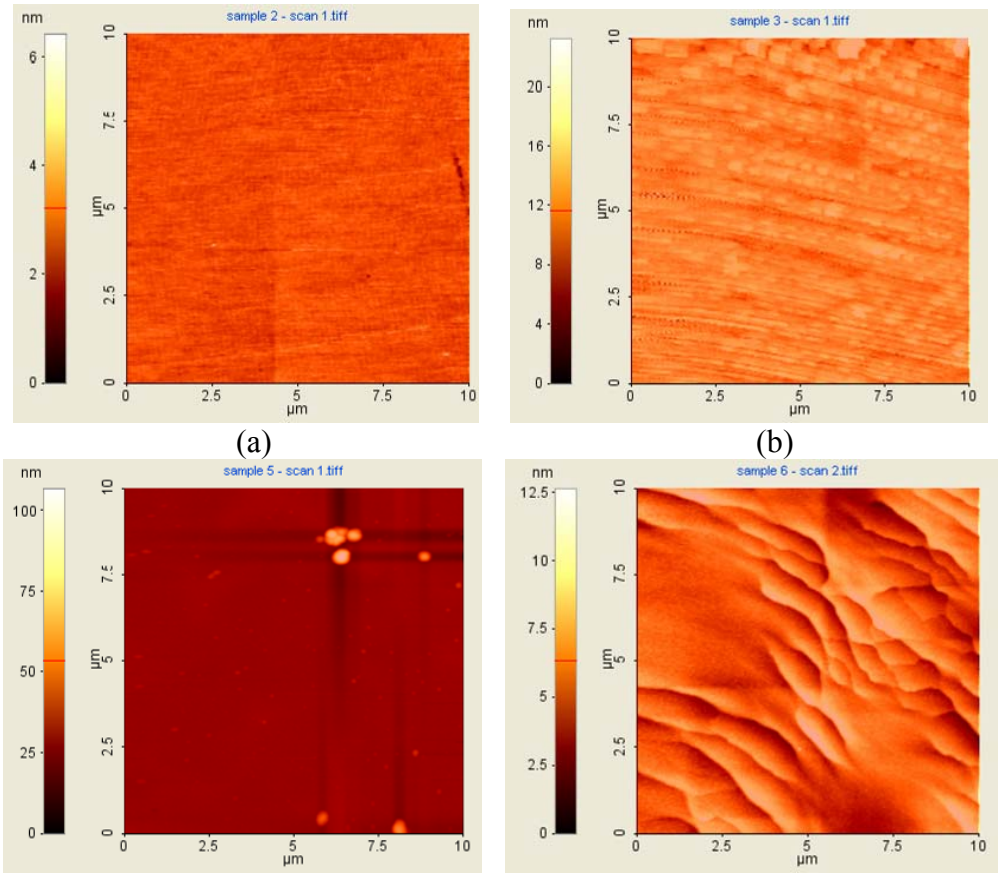

(a) (b)

(c) (d)

Figure 6.24: (a) Pre-annealing bare ZnO substrate with RMS = 0.271nm, (b) post-annealing bare ZnO substrate in a ZnO box for 3 hours in air with RMS = 1.547nm, (c) 200nm Al_2O_3/ZnO annealed without a ZnO box with RMS = 4.916nm, and (d) 200nm Al_2O_3/ZnO annealed with a ZnO box with RMS = 1.814nm.

significant growths were reported, and therefore, this study was not pursued. The 200nm ALD Al_2O_3 was annealed without and with a ZnO box and showed a decrease in RMS values from 4.916nm to 1.814nm, Figure 6.24(c) and (d), respectively. The pre-annealed sample appears to be smoother but with a high spike only in one spot, and hence the high RMS value. The post-annealed sample leveled the surface and displayed a terrace like surface with a lower RMS value.

6.4.6 Summary of Annealing Study

An Al_2O_3 ALD layer was proposed as a transition layer on ZnO substrates in order to block Zn diffusion, promote GaN growth, and prevent H_2 etching into the substrate. The ALD layer was said to be initially amorphous, and therefore annealing studies were performed on the ALD layers using a furnace. X-ray measurements showed a number of crystalline phases including Al_2O_3 peaks at 25, 38, 53, and 82 degrees corresponding to (012), (110), (024), and (306) phases as well as $ZnAl_2O_4$ peaks at 36, 44 and 48 degrees for (311), (400), and (533) phases, and x-ray stage holder peaks at 23 and 38 degrees. The appearance and intensity of the phases were dependent on the time and temperature of the annealing. Un-annealed samples also displayed smiliar Al_2O_3 and $ZnAl_2O_4$ phase and therefore showed that the un-annealed samples might actually be polycrystalline. Reanalysis of the phases was a continuous process, and in the end only the Al_2O_3 phases were kept: 38, 44, 53, and 82 degrees for (110), (113), (024), and (306) phases. Annealing for 5, 10, or 20 minutes at 1100ºC were found to be the best annealing parameters for 10, 20, and 50nm Al_2O_3 thicknesses, respectively. An additional annealing study was performed to assess the effectiveness of annealing the ZnO substrates and Al_2O_3/ZnO samples in a ZnO box in order to create a Zn ambient to help

suppress the desorption of Zn atoms from the ZnO surface. AFM characterization showed terrace like surfaces for post-annealing of a bare ZnO substrate and a 200nm Al_2O_3/ZnO. The bare ZnO had a RMS value of 1.547nm, and the 200nm Al_2O_3/ZnO had a RMS value of 1.814nm.

6.5 MOCVD Growth of GaN on Al_2O_3/ZnO

In previous chapters, an extensive study of GaN growth on bare ZnO was completed and it was proposed to use ALD films as a means to solve the issues arising from growth on ZnO. For example, growth of GaN on bare ZnO showed cracks and peeling of the epilayer due to Zn diffusion from ZnO and H_2 etching from (ammonia) NH_3. These issues were solved, but Zn diffusion did not allow for high-quality GaN growth. A transition layer of Al_2O_3 was deposited before the MOCVD growth in order to provide a protective layer and promote GaN growth. This layer also acts as a stabilizing layer when the sacrificial substrate is etched off. A series of annealing studies for the Al_2O_3 ALD layer were performed, and GaN was grown by MOCVD on these layers.

6.5.1 Experimental Setup

The GaN layers (buffer plus main layer) were grown with identical growth conditions on annealed 20 and 50nm Al_2O_3/ZnO substrates using a 1 step growth method for GaN directly on Al_2O_3/ZnO. Annealing was performed at 10 and 20 minutes, respectively. The GaN buffer layer for GaN eptiaxial growth was grown at 770^{o}C with a thickness of 30nm using trimethylgallium (TMGa) and NH_3 as the gallium and nitrogen sources, respectively. The GaN epilayer was then grown at a thickness of 200nm at 800^{o}C at a

growth rate of 0.25μm/h. N_2 carrier gas was used throughout the growth process. The structures were characterized by x-ray and Raman scattering spectroscopy (Raman). Optical properties were performed using room-temperature PL. Surface and structure analysis was measured by SEM.

6.5.2 Preliminary Study

20nm and 50nm were the selected thicknesses for ALD Al_2O_3 deposited on ZnO substrates. The optimal annealing conditions were at 1100°C for 10 and 20 minutes for 20 and 50nm, respectively. Two growth conditions were attempted on Al_2O_3/ZnO substrates as an initial study for GaN growth on Al_2O_3/ZnO.

Two-Step Growth of GaN Using LT-GaN on Al_2O_3/ZnO

A low temperature (LT) GaN buffer at 540°C was initially grown on Al_2O_3 coated ZnO substrates. A high temperature (HT) GaN buffer was grown at 800°C following the LT-GaN buffer in order to prevent Zn/O diffusion. X-ray and PL results can be seen in Figure 6.25. The 20nm Al_2O_3 layer, after 1100°C annealing, resulted in superior GaN growth compared to the 50nm layer. A significant GaN x-ray diffraction peak as well as a weak PL emission was observed from the 20nm sample. However, there was no indication of crystalline GaN in the x-ray measurement of the 50nm sample, nor was there bandedge emission observed in PL. This indicates that the thinner 20nm Al_2O_3 could provide higher crystalline quality after annealing and offer a better GaN nucleation site.

One-Step Growth of GaN Directly on Al_2O_3/ZnO

In this series of growths the HT-GaN buffer was grown directly on the 20nm and 50nm ALD Al_2O_3 coated ZnO substrate. A thin GaN buffer was first deposited at 770°C

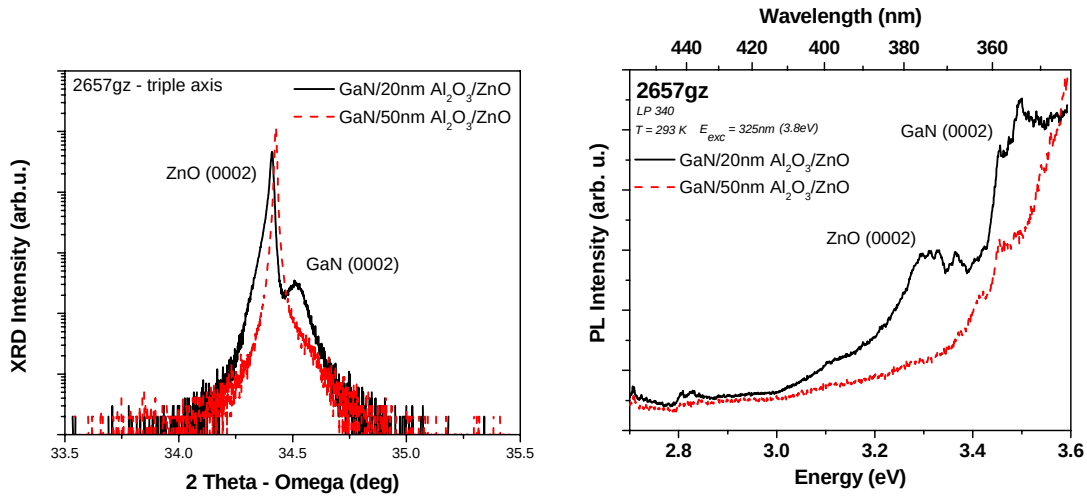

(a) (b)

Figure 6.25: (a) X-ray $2\theta/\omega$ scan and (b) RT-PL spectra of two-step GaN layers grown on 20 and 50nm annealed Al_2O_3/ZnO substrates by MOCVD.

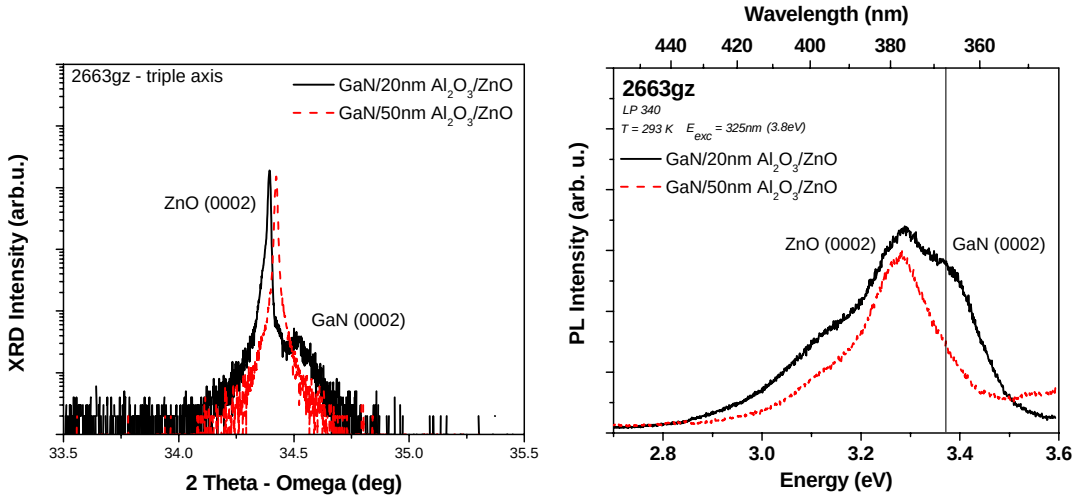

(a) (b)

Figure 6.26: (a) X-ray $2\theta/\omega$ scan and (b) RT-PL spectra of one-step GaN layer grown at 800ºC on 20 and 50nm annealed Al_2O_3/ZnO substrates by MOCVD.

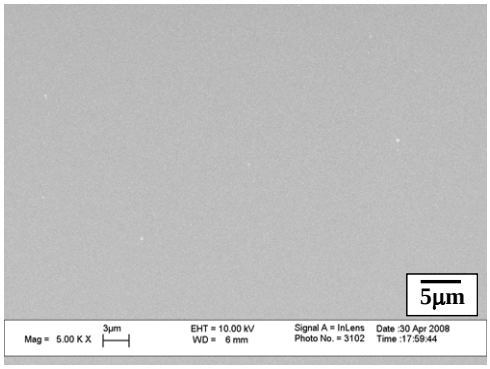

Figure 6.27: SEM image of GaN surface grown on 20nm annealed Al_2O_3/ZnO.

and then the temperature was increased to 800°C to grow the main GaN layer by using a low NH_3 flow rate. Both the ZnO and GaN x-ray diffraction peaks and PL emission peaks can be seen in Figure 6.26. The results from these growth were similar to the first approach in that the annealed 20nm ALD layers produced superior characterization results compared to 50nm ALD layers that were annealed in the same conditions. Overall, the epitaxial GaN produced without the LT-GaN buffer yielded a more distinct GaN PL emission. Therefore, all subsequent GaN growth studies used only the HT-GaN buffer between the ALD films and the primary epilayers.

6.5.3 Structural Analysis

A $2\theta/\omega$ x-ray scan was performed on the epitaxial GaN layers grown at 800ºC on 20 and 50nm Al_2O_3/ZnO substrates, Figure 6.26(a). The peaks with the highest intensity were the diffraction from the ZnO (0002) plane of ZnO bulk materials. The only sample that showed a second peak was the Gan on 20nm Al_2O_3/ZnO substrate, which showed that the (0002) plane of the wurtzite GaN was successfully grown. However, there was no evidence growth of a GaN layer on the 50nm Al_2O_3/ZnO substrate. It is possible that the thicker Al_2O_3 film has a weaker structural relationship with the underlying ZnO substrate after crystallization. Therefore, the polycrystalline 20nm α-Al_2O_3 may possess a more highly textured orientation with hexagonal ZnO compared to the 50nm sample, which could assist the nucleation of the GaN layer in the initial stage of growth. In addition, SEM showed a mirror-like GaN surface with no observation of etched pits or peeling off from the 20 nm sample, Figure 6.27.

Raman scattering is a well known straightforward method for distinguishing wurtzite GaN [61]. Here, Raman spectroscopy has been carried out on a bare ZnO substrate and a

GaN layer grown at 800ºC on a 20nm Al_2O_3/ZnO substrate, Figure 6.28. These studies were recorded at room temperature in back scattering Z(x,x)$\underline{Z}$ geometry, with the Z-direction along the c-axis using a laser with λ_{exc} = 488nm. The prominent characteristics of the bare ZnO substrate are observed at 437cm^{-1}, which corresponds to the E_2(high) mode, and at 332cm^{-1}, which corresponds to a 2-phonon line. Moreover, the E_2(high) and A_1(LO) modes of GaN phonon peaks were clearly identified in the spectra at 569 and 735cm^{-1}, respectively. These results indicate the presence of a well-crystallized wurtzite GaN layer on 20nm Al_2O_3/ZnO substrates.

6.5.4 Optical Characteristics of GaN at Room-Temperature

Room-temperature PL was performed using a HeCd laser emitting at 325nm as the excitation source. The GaN layers grown at 800ºC on 20 and 50nm Al_2O_3/ZnO substrates are shown in Figure 6.26(b). The ZnO substrate emission can be seen at 3.28eV, which is consistent with the emission seen for bare ZnO substrate. A shoulder was visible at 3.39eV in the 20nm sample, which was attributed to the near-edge emission of GaN. This emission has a 30meV red-shift from the typical band-edge emission of GaN at 3.42eV. Moreover, a clear near-edge GaN emission was observed from a sample grown at 850ºC growth on a 20nm Al_2O_3/ZnO substrate. This emission occurred at approximately 3.36eV with a red-shift of 60meV. The 50 nm sample grown at 850ºC did not show any GaN peak, Figure 6.29. It has been reported that zinc doping in GaN or InGaN forms a deep level, which induces a red-shift of ~0.4~0.5eV [45, 62, 63]. Thus zinc diffusion from the ZnO substrate could still be occurring. An alternate explanation is that oxygen could be diffusing into the GaN and substituting for nitrogen. Oxygen substitution for nitrogen in GaN acts as a shallow donor in unintentionally doped

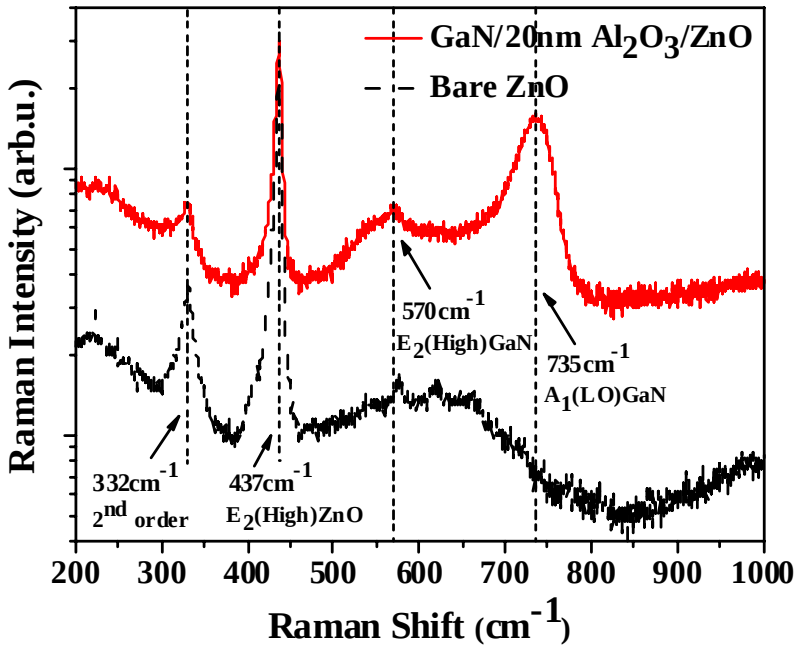

Figure 6.28: Raman spectroscopy of GaN/20 nm Al_2O_3/ZnO structure and bare ZnO substrate.

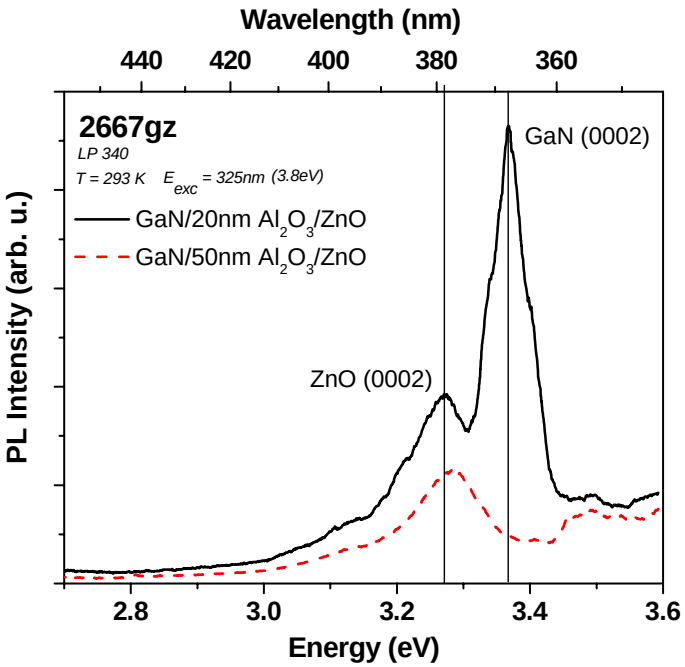

Figure 6.29: RT-PL spectra of GaN layers grown at 850ºC on 20 and 50nm annealed Al_2O_3/ZnO substrates.

GaN [64]. As a result, the oxygen diffusion into the GaN could form an oxygen-related level as a shallow donor below the conduction band that induces the red-shift. Therefore, these slight red-shifts may be caused by oxygen contamination in the GaN layers instead of zinc. In addition, the oxygen concentrations in GaN could vary with growth temperature and could thus explain the difference in red-shift observed in the two 20nm Al_2O_3/ZnO samples.

6.5.5 Summary of GaN Growth on Al_2O_3/ZnO Substrate

This study presented the MOCVD growth of GaN layers on annealed 20 and 50nm Al_2O_3/ZnO substrates by using NH_3 as a nitrogen source at high growth temperature. Wurtzite GaN was only seen on the 20nm Al_2O_3/ZnO substrate but not the 50nm Al_2O_3/ZnO substrate. The SEM image revealed a mirror-like GaN surface without etched pits or film peeling. Room-temperature PL showed the near band-edge emission of GaN red-shifted, which may be caused by oxygen diffusion into the GaN layer forming an oxygen-related level, which acts as a shallow donor. Raman scattering confirmed a good quality wurtzite GaN layer grown on the 20nm Al_2O_3/ZnO substrate. These studies have shown that a 20nm ALD film is a promising transition layer for the heteroepitaxial growth of GaN.

6.6 MOCVD Growth of InGaN on Al_2O_3/ZnO

A series of InGaN growths were performed on annealed Al_2O_3 ALD layers. InGaN was the main focus of the whole study due to its perfect lattice match with ZnO at 18% and its ability to be grown at a lower temperature than GaN. Three different MOCVD chambers were attempted for the InGaN growths. However,

due to time constraints, the study was narrowed to only one chamber to eliminate the significant variability in growth conditions introduced by different chambers.

6.6.1 Experimental Setup

InGaN layers were grown by MOCVD on 5, 10, 20, and 50nm Al_2O_3/ZnO substrates with various annealing times. The GaN buffer layer for InGaN epitaxy was grown at 530^{o}C with a thickness of 30nm using TMGa and NH_3 as the gallium and nitrogen sources, respectively. InGaN layers were grown to a thickness of 100nm at 700^{o}C with a growth rate of 0.18μm/h by introducing trimethylindium (TMIn) and triethylgallium (TEGa) into the reactor. N_2 carrier gas was used throughout the growth process. The structures were characterized by x-ray. Optical properties were examined using optical transmission measurement (OT). Depth profile and surface analysis were measured by Rutherford backscattering spectroscopy (RBS), atomic emission spectroscopy (AES), and x-ray photoelectron spectroscopy (XPS).

6.6.2 Preliminary Study

Growths were performed in three different MOCVD reactors. The CERMET MOCVD chamber was a home-built MOCVD system built by CERMET. Our lab consisted of a modified MOCVD system that consisted of two interchangeable reactors. One was the device chamber, which flowed known III-Nitride sources and dopants. The seoncd reactor was the materials chamber, which flowed unknown gases, such as ZnO. ZnO studies from Chapter 4 and 5 and GaN/Al_2O_3/ZnO growths were all initially performed in the materials chamber. However, techinial difficulties with the materials chamber resulted in the preliminary study of growing InGaN on Al_2O_3/ZnO substrates in the CERMET and device chamber.

Growth Runs in the CERMET MOCVD Tool

Growths were started in the CERMET MOCVD tool in order to understand the operational characteristics of this tool to increase the number of future growth runs. InGaN was grown on three samples of 5, 10, and 50nm ALD Al_2O_3. The annealing for this study was based on early *in-situ* annealing in the MOCVD chamber for 20 minutes at 900ºC. No intermediate GaN buffer was used and InGaN was grown directly on the Al_2O_3/ZnO at 700ºC. The direct growth was the growth process developed by CERMET for InGaN deposition in their MOCVD tool. X-ray measurements of these epilayers showed very weak InGaN peaks, Figure 6.30. This could be due to the use of a different reactor and changes in InGaN growth parameters. Since this was the initial growth in this system, further optimization needed to be performed.

Growth Runs in the MOCVD Device Chamber

One of the two nitride growth chambers in our lab is specified as the device chamber. The device chamber is typically reserved for growths using only standard III-Nitride precursurors and dopants to decrease the likelihood of contamination by experimental materials, including ZnO. Therefore, ZnO growths were performed in the device chamber at the end of the chamber's growth duration. In-chamber annealing was employed for 5 and 10nm ALD Al_2O_3 layers at 900ºC prior to InGaN growth. Both thicknesses of 5 and 10nm showed different diffraction patterns by x-ray measurement, Figure 6.31(a) and (b). The diffraction pattern shows an inhomogeneous phase in the InGaN layer for both the 5 and 10nm transition layers, Figure 6.31(a). The cause might be multiple nucleation sites affecting the surface diffusion or nucleation of Ga and nitrogen sources. A possible reason might also be that the Al_2O_3 layer was too thin and

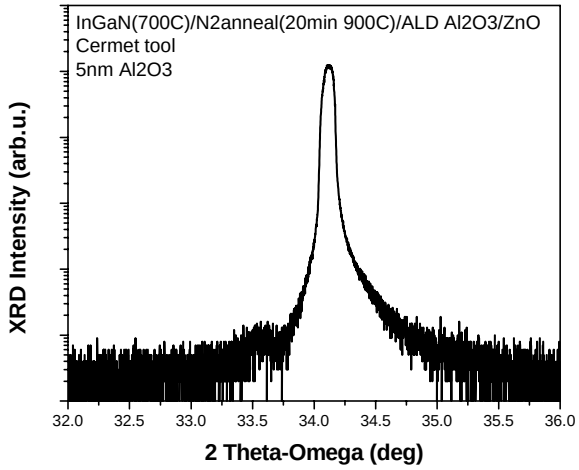

(a)

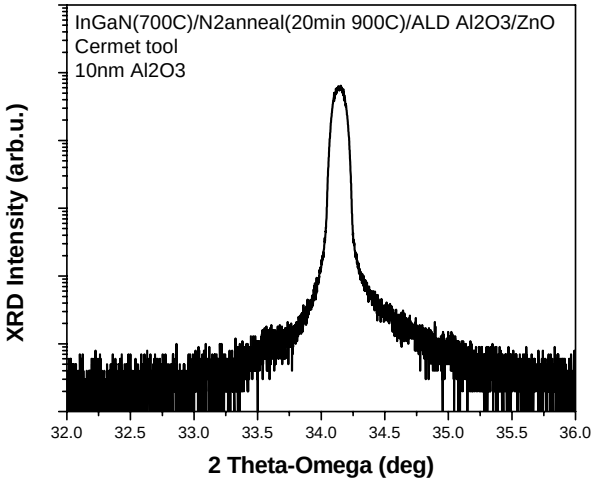

(b)

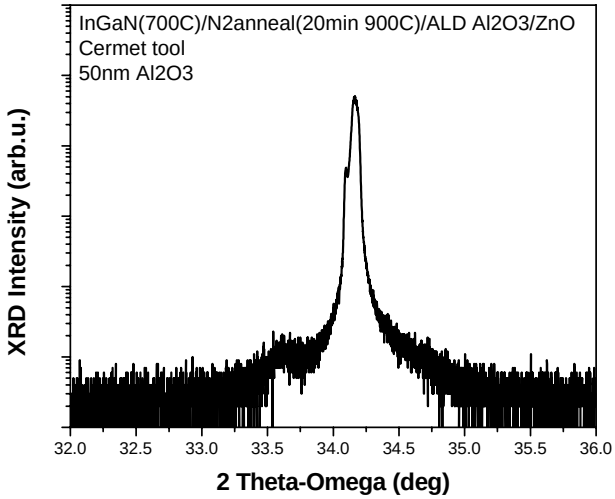

(c)

Figure 6.30: X-ray of MOCVD InGaN grown in Cermet tool on annealed ALD of (a) 5nm Al_2O_3, (b) 10nm Al_2O_3, and (c) 50nm Al_2O_3.

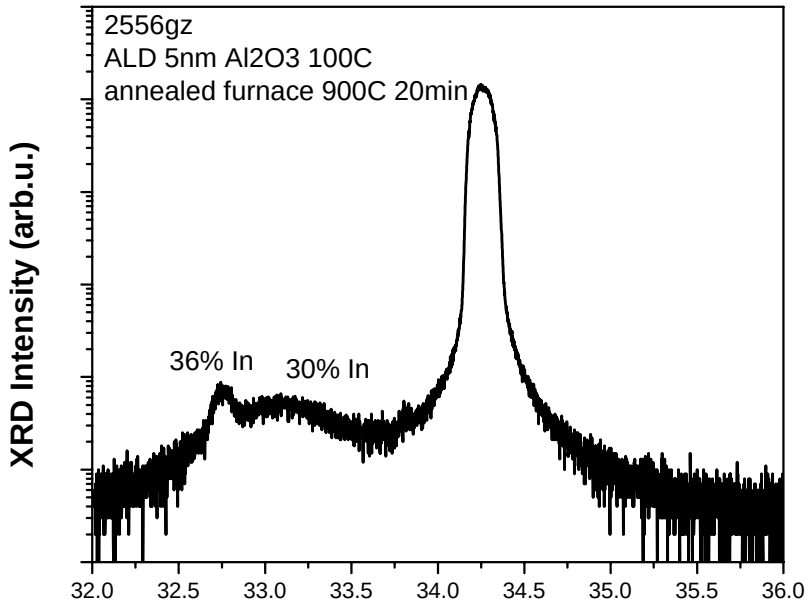

(a)

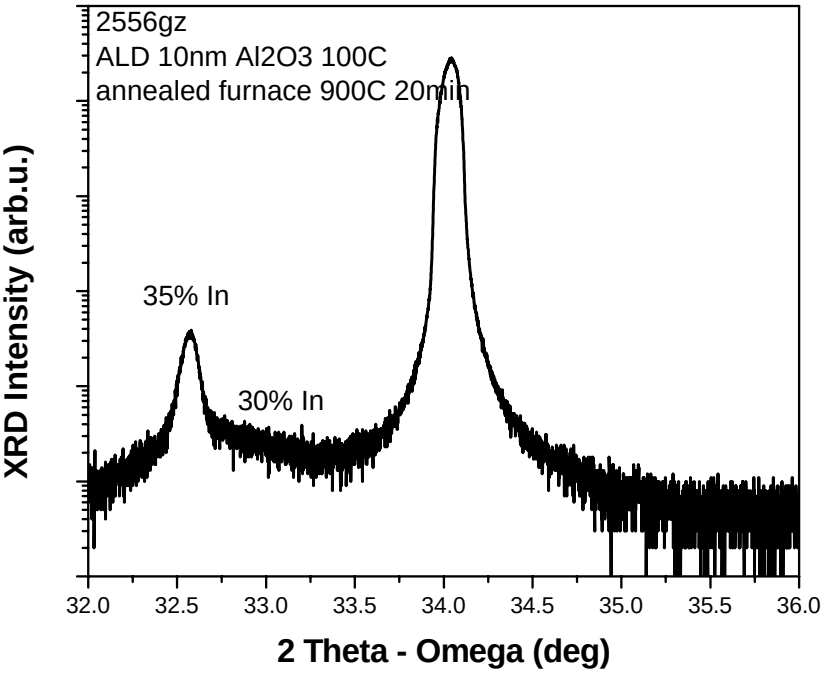

(b)

Figure 6.31: X-ray of InGaN on 900ºC annealed in furnace for 20 minutes of (a) 5nm Al_2O_3 and (b) 10nm Al_2O_3.

easily decomposed in some areas during annealing. This would result in exposing the ZnO surface thereby creating multiple nucleation sites for the GaN buffer growth. These runs, including CERMET tool runs, were based off of previous studies performed in the materials chamber. The materials chamber is a materials research reactor where experimental dopants, alloys, and substrates can be investigated. Despite using the same growth recipe (developed in the materials chamber), the variability of the results from InGaN grown in the CERMET and device chambers indicated that extensive optimization for the individual tools would be required. Therefore, due to time constraints, the materials chamber was continued for all subsequent MOCVD growth studies.

Initial Growth of InGaN on Bare ZnO

The first series of InGaN growths were 100nm thick layers were grown on bare ZnO substrates with the 30nm GaN buffer layer. These growths were used to find optimal growth conditions which would then be used for later growths on annealed Al_2O_3/ZnO substrates. Random RBS measurements were performed on the InGaN/GaN/ZnO structures in order to confirm the indium composition as well as the thickness of each individual layer, Figure 6.32. The energy for backscattering of both gallium and indium at the surface has been labeled. A simulation of the random spectrum reveals that the good-quality InGaN layer has an indium composition as high as 35% and a thickness of about 80nm. Moreover, the thickness of the GaN buffer layer was estimated from a random spectrum as 35nm. The values of composition and thickness were close to those measured by x-ray and in-situ reflectance curve.

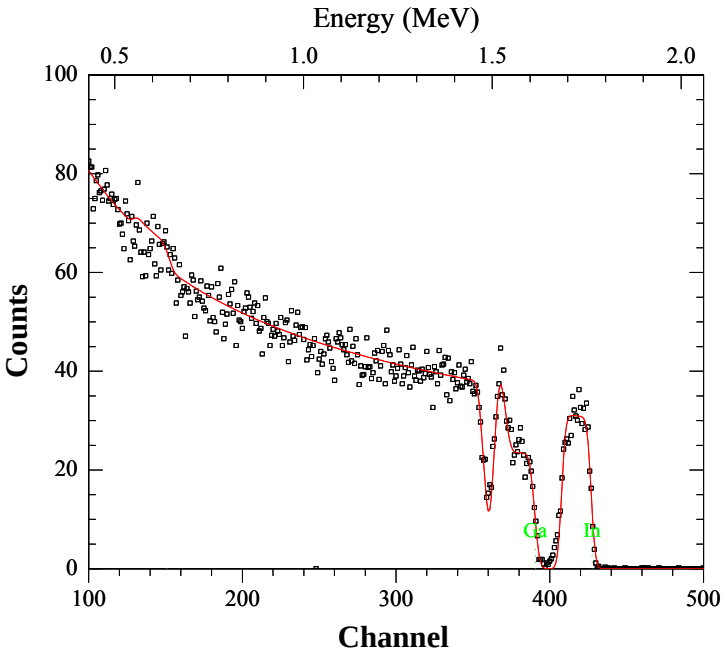

Figure 6.32: Random (square) and simulated (solid line) RBS spectra of an InGaN/GaN/ZnO sample.

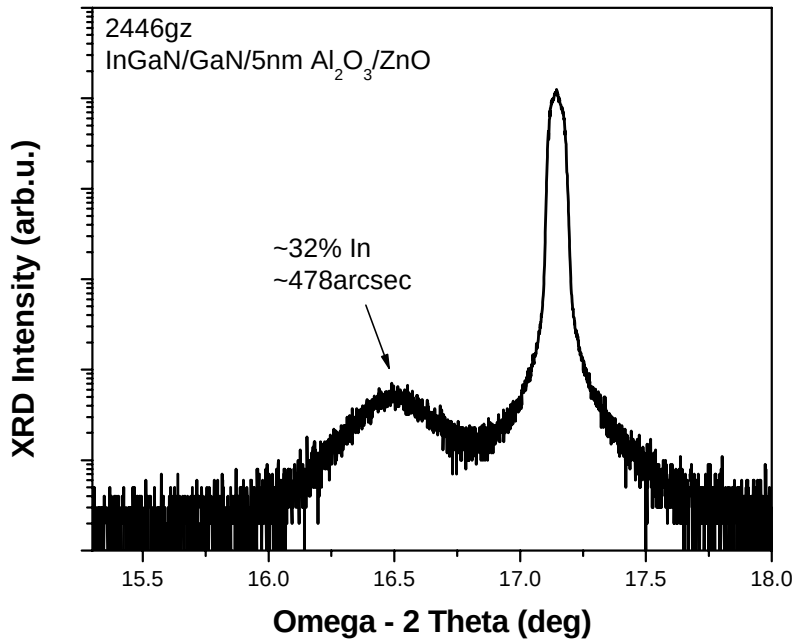

Figure 6.33: X-ray $2\theta/\omega$ scan of InGaN layers grown on annealed 5nm Al_2O_3/ZnO substrates.

6.6.3 Structure Analysis on Different ALD Al_2O_3 Thicknesses

One of the first InGaN growths on an ALD layer was on 5nm Al_2O_3/ZnO that was *in-situ* annealed in the MOCVD chamber. Thin ALD layers were used in the beginning of the study. *In-situ* annealing of a 5nm Al_2O_3/ZnO substrate at 900°C for 20 minutes in N_2 ambient was attempted in the MOCVD chamber directly before growth of the InGaN layer. X-ray measured a successful growth of a single phase InGaN on 5nm annealed Al_2O_3/ZnO, as can be seen in Figure 6.33. The concentration of indium from the InGaN layer was calculated by the shift of the (0002) InGaN peak position relative to the (0002) ZnO peak position via Vegard's law. This yielded an indium concentration of 32% for this sample.

The next growth series was performed on 10nm Al_2O_3/ZnO *in-situ* annealed in the ALD chamber at 350°C. The 10nm ALD Al_2O_3/ZnO was additionally annealed at 1100°C at 5, 10, and 20 minutes in the tube furnace to investigate the annealing effect on *in-situ* ALD-Al_2O_3 layers for the InGaN growth. A 350°C Al_2O_3/ZnO sample without annealing was also used for comparison. X-ray results of (002) InGaN diffraction peaks are shown in Figure 6.34. The unannealed sample did not show any InGaN peaks whereas InGaN peaks were visible on all the annealed substrates, regardless of annealing time. The annealing time did affect the indium incorporation in InGaN. Higher indium content was observed for shorter annealing time. This result was attributed to the different nucleation sites of InGaN provided by the Al_2O_3 layer under various annealing times. This series of InGaN growth showed the best InGaN results for all annealing times, but due to ALD *in-situ* annealing limitations these studies were not carried forward.

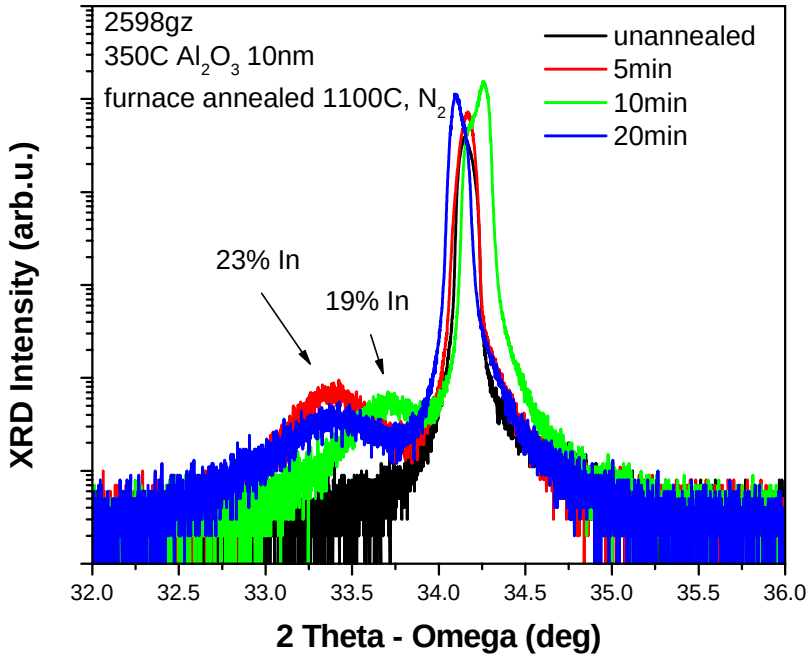

Figure 6.34: X-ray of InGaN grown on 10nm 350ºC ALD Al_2O_3/ZnO annealed at various times.

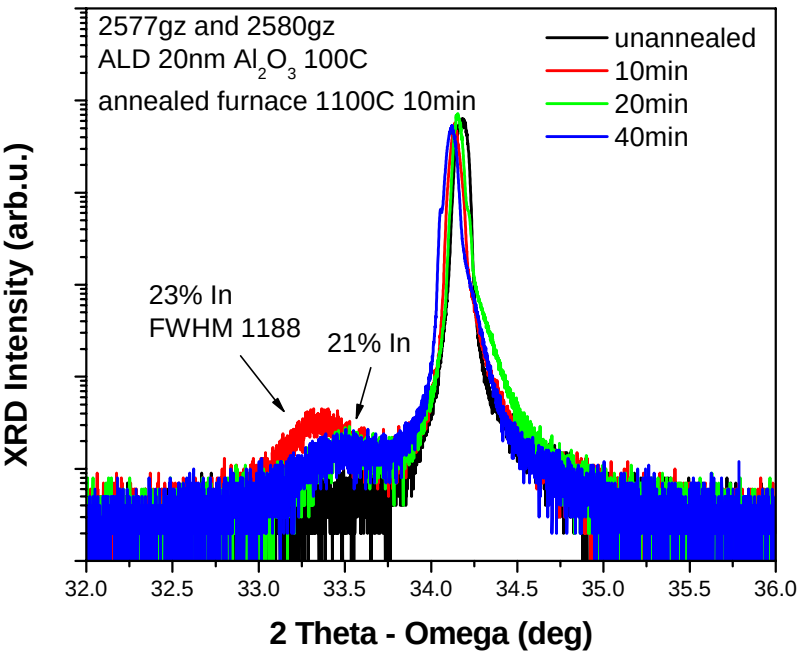

Figure 6.35: X-ray $2\theta/\omega$ scan of InGaN layers grown on annealed 20nm Al_2O_3/ZnO substrates.

InGaN on 20nm Al_2O_3/ZnO showed successful growth after annealing. The $2\theta/\omega$ x-ray scan showed two well-separated peaks from the ZnO substrate and InGaN layers, as seen in Figure 6.35. InGaN (0002) diffraction peaks were obtained on 20nm Al_2O_3/ZnO substrates, which were annealed at 1100ºC for times of 0, 10, 20, and 40 minutes. The intensity of the InGaN peaks decreased with increasing annealing time indicating an effect on the quality of the InGaN layer. Only one significant InGaN peak can be observed for 10 minutes annealing while very weak InGaN peaks were found for the rest of the annealed samples. This result agrees with the annealing studies of the ALD layers, which indicated that 10 minutes was the optimal annealing time for 20nm ALD Al_2O_3 layers. Moreover, no InGaN (0002) peak was seen on the un-annealed sample. Shifts seen in the InGaN peaks denote different indium incorporation. This could be due to differences in surface properties of the various samples, which would change the nucleation density as well as the growth mode of the subsequent GaN and InGaN epilayers. This would in turn cause variation in indium incorporation.

The 50nm ALD Al_2O_3/ZnO was annealed in the furnace at 1100ºC for 20 minutes under N_2 ambient. Annealing studies had shown that 20 minutes was ideal for 50nm ALD Al_2O_3 layers. InGaN with 33% indium was successfully grown on Al_2O_3/ZnO substrate as seen in Figure 6.36. The FWHM of the InGaN (0002) diffraction was broader compared with previous growths. Therefore, InGaN growth was attempted using the two-step annealing process discussed in the annealing section to see if this would improve the InGaN quality.

The 50 nm ALD transition layer was annealed at 1100ºC for 180 seconds and then ramped down to 1000ºC for 0, 20, 40, and 60 minutes. InGaN peaks were observed for

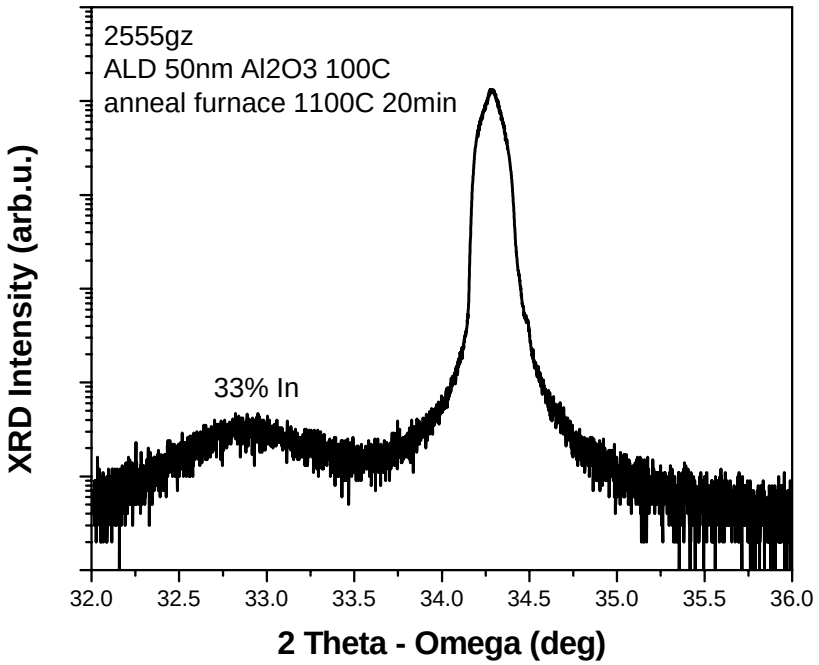

Figure 6.36: X-ray of InGaN grown on 1100ºC furnace annealed for 20min of 50nm Al_2O_3.

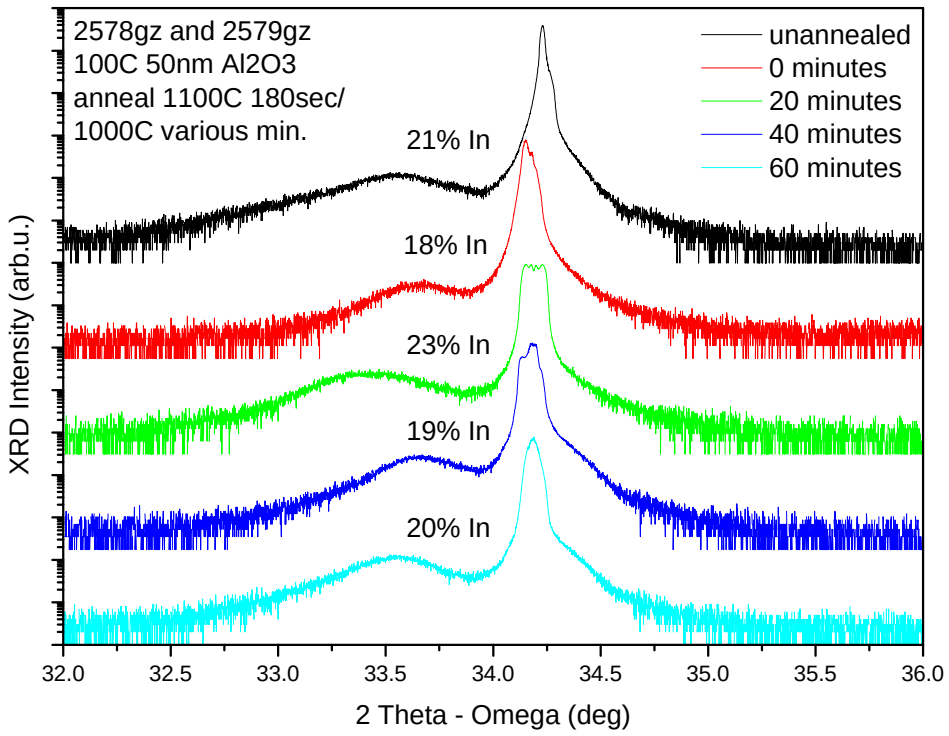

Figure 6.37: GaN/InGaN growth on 1100ºC/1000ºC furnace annealing for 50nm ALD Al_2O_3/ZnO.

each of these samples, Figure 6.37. These showed some improvement from the one-step annealing process. It was found that longer annealing improved the InGaN film quality as indicated by a smaller FWHM for x-ray peaks from the InGaN layer, Figure 6.38. It is believed that the thicker ALD film requires a longer annealing time to become crystalline. There are two possibilities for the different results of InGaN growth between 50 and 20nm. One is the higher annealing temperature 1100ºC used for the 20nm thickness while the 50nm only used 1000ºC for its primary annealing temperature. Second, the thickness difference may cause a change in epitaxial growth of InGaN. The non-annealed 50nm ALD film also showed an InGaN peak, though with a broad FWHM.

6.6.4 Optical Characteristics of InGaN by Optical Transmission

OT measurements were performed on an InGaN layer grown on bare ZnO and on 5nm Al_2O_3/ZnO, Figure 6.39. Two obvious steps appear in each curve, corresponding to the absorption edge of ZnO and InGaN. Both spectra exhibit a sharp and transmission wavelength edge at 387nm, which was attributed to the underlying ZnO substrates. Moreover, the InGaN optical absorption edge can be determined by the sigmoidal fitting seen in Equation 6.1 [65, 66]:

$$T(E) = \frac{T_0}{1 + \exp\left(\frac{E_g - E}{\Delta E}\right)} \tag{6.1}$$

where T is the transmission, E_g is the bandgap of the alloy, and ΔE is the broadening parameter, which is equivalent to the Urbach tailing energy. The bandgaps for InGaN grown on bare ZnO and on annealed Al_2O_3/ZnO substrates were calculated to be approximately 2.43 and 2.51eV, respectively. The bandgap energy of InGaN was not altered significantly when grown on annealed Al_2O_3/ZnO substrates. Inserting the

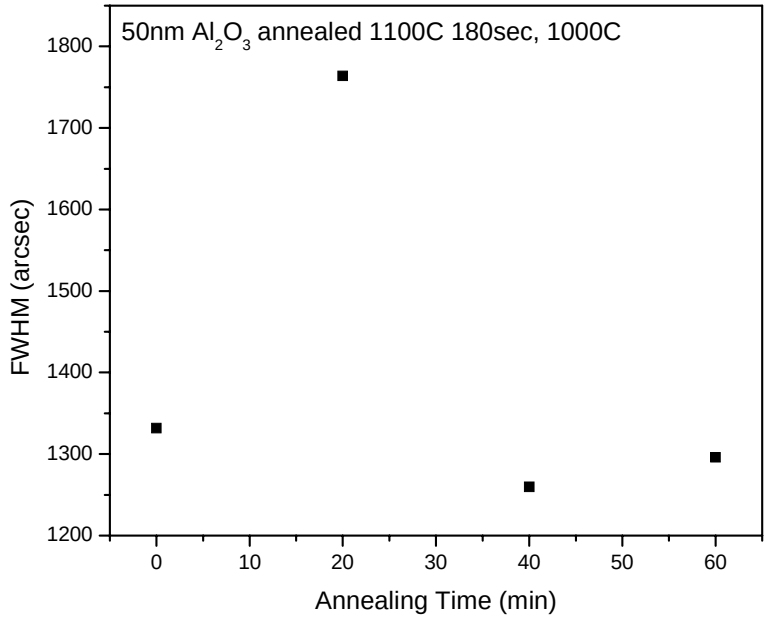

Figure 6.38: The FWHM of InGaN versus annealing time for 1100ºC/1000ºC anneal.

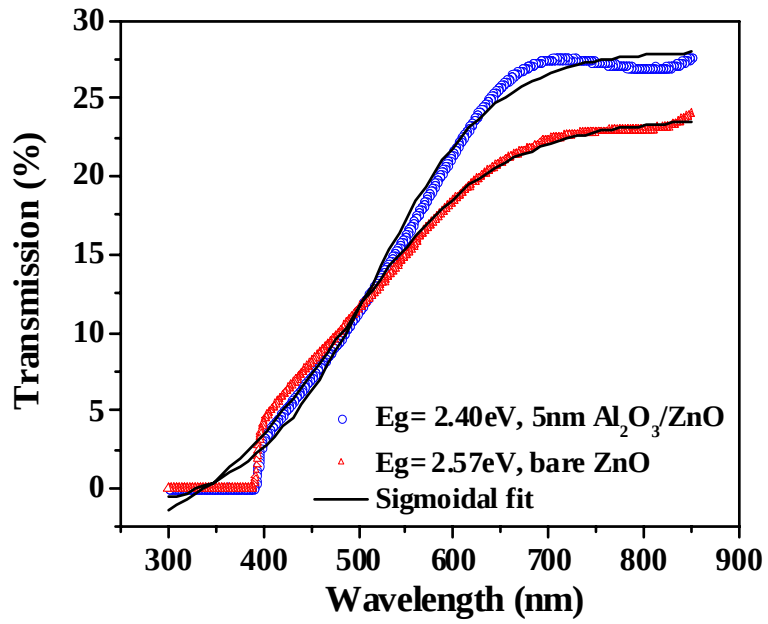

Figure 6.39: Optical transmission spectra of InGaN layers grown on bare ZnO and annealed 5nm Al_2O_3/ZnO substrates.

bandgap of InGaN on 5nm Al_2O_3/ZnO into the following equation: E_g(strained) = 3.42 – 0.65x – 3.4159x(1-x) where E_g = 2.43eV gives 34% indium concentration, which is close to the value obtained by the x-ray measurement mentioned in the previous section of 32% [67].

6.6.5 Depth Profile and Surface Analysis

An important issue that was investigated was the prevention of Zn/O diffusion during growth. An extensive study of GaN growth on bare ZnO was completed and in this work it was proposed to use ALD layers as a means to solve the issues arising from growth on ZnO. An ALD transition layer was grown before MOCVD layers to minimize Zn diffusion and promote nitride growth of GaN on ZnO by MOCVD. The ALD layers were shown in previous sections to have helped promote GaN and InGaN growths. The depth profiles were measured to check if the ALD layers did help minimize the Zn and O diffusion into the epilayers.

AES was measured for atomic depth profiles of InGaN layers grown on bare ZnO and 5nm annealed Al_2O_3/ZnO substrates, Figure 6.40(a) and (b). The diffusion of Zn from the ZnO substrate into the InGaN layer is clearly visible for both cases, as seen in Figure 6.40(a). The concentration of Zn in the InGaN layer grown on bare ZnO substrate is around 0.7at.%. Moreover, the concentration of Zn is reduced to 0.3at.% when grown on annealed Al_2O_3/ZnO substrate, Figure 6.40(b). The 5nm Al_2O_3 succeeded in retarding the Zn diffusion, but the Zn-content still needed to be further reduced. The Zn diffusivity was also evaluated in the case of bare ZnO substrates. The schematic diagram of the InGaN/GaN/ZnO structure can be seen in Figure 6.41. The Zn atomic flux from the ZnO substrate into the InGaN layer can be calculated by Equation 6.2 [68]:

$$J_{Zn} = \frac{T \bullet A \bullet \rho \bullet f_{zn} \bullet N_0}{M_{Zn} \bullet t \bullet A} \tag{6.2}$$

where T is the InGaN thickness; A is the epilayer area; ρ is the density of InGaN with 32% indium, (6.3g/cm^3); f_{Zn} is the Zn weight fraction in InGaN (0.01); N_o is Avogadro's number; t represents the growth time (30 minutes); and M_{Zn} is the atomic weight of Zn. Substitution of all the values above yields J_{Zn}= 2.75x10^{12} (atom/cm^{2}s). The Zn atomic flux in the GaN buffer layer, J_{Zn}, also can be expressed by Fick's second law, assuming the Zn concentration gradient is linear. With this approximation the diffusivity of Zn in the GaN can be obtained by Equation 6.3 [69]:

$$J_{Zn} = D_{Zn} \frac{C_{Zn,2} - C_{Zn,1}}{\chi_{GaN}} \tag{6.3}$$

where D_{Zn} is the Zn diffusivity in the GaN, χ_{GaN} is the thickness of the GaN layer, $C_{Zn,1}$ is the theoretical Zn concentration in ZnO, (2x10^{22}atoms/cm^3), and $C_{Zn,2}$ is the Zn concentration in InGaN, (6.12x10^{20}atoms/cm^3), which can be obtained from the AES atomic depth profile. Therefore, D_{Zn} is calculated to be about 2.37x10^{-16}cm^2/sec. This diffusivity of Zn in GaN at 700^{o}C is in the same order as the Zn diffusivity in GaN at 930^{o}C (1x10^{-16}cm^2/sec) [70]. The concentration of O in the InGaN layer was at a consistent value of 0.1% with and without the Al_2O_3 film deposited. The thicknesses marked in Figure 6.40 are only observations. Figure 6.40(a) might have different thicknesses due to etching of the ZnO substrate during growth, which induces the non-uniformed interface of each individual layer. The Al_2O_3 spreading in Figure 6.40(b) could be caused by post-annealing and diffusion during epilayer growth. Therefore, its thickness during atomic depth profile measuring could seem bigger.

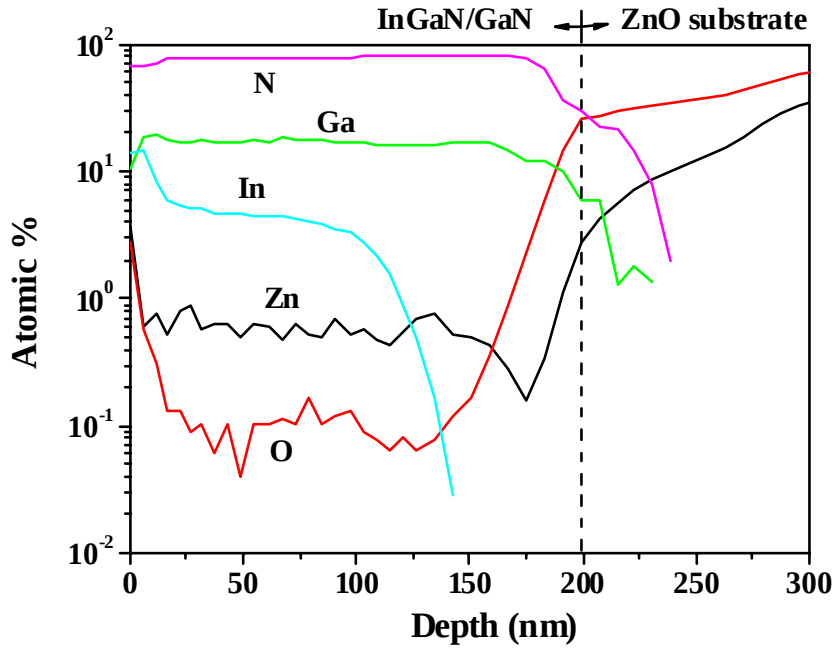

(a)

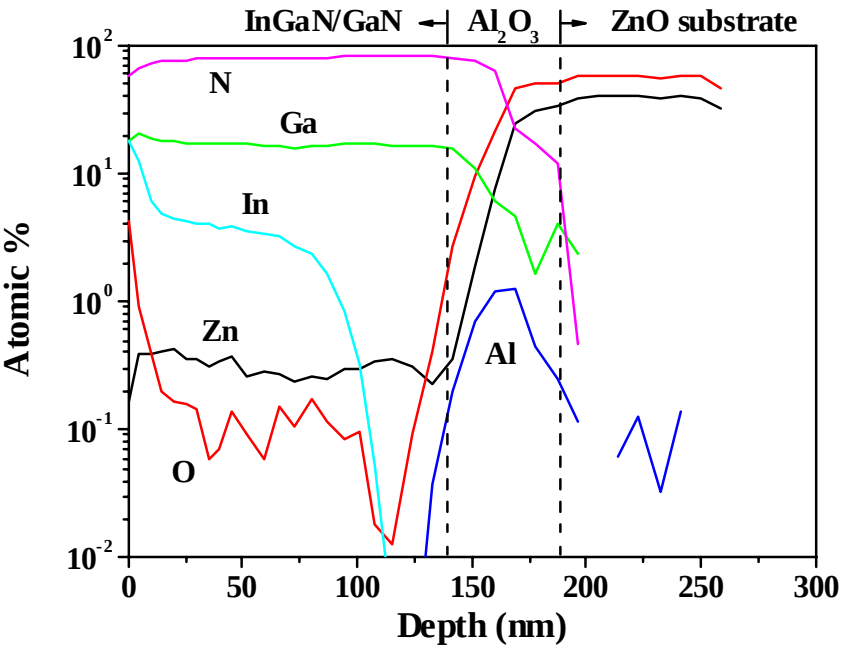

(b)

Figure 6.40: AES atomic depth profile of InGaN layers grown on (a) bare ZnO and (b) annealed 5nm Al_2O_3/ZnO substrate.

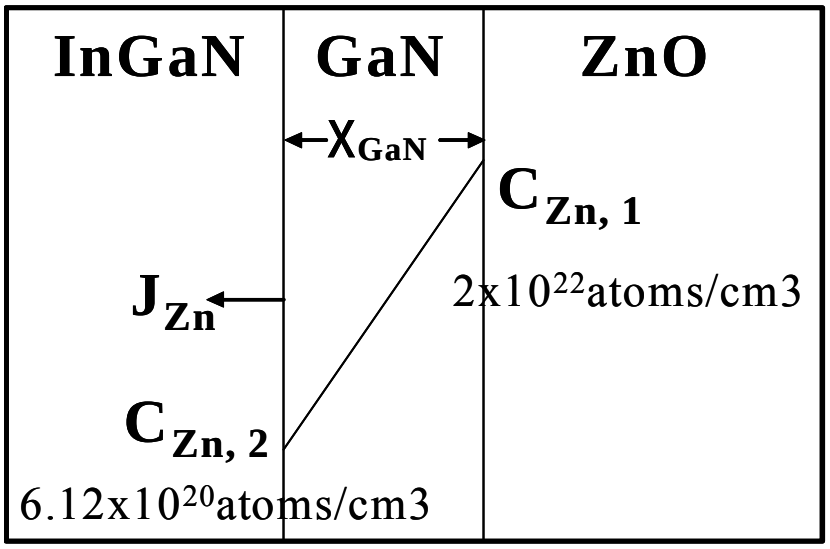

Figure 6.41: Schematic drawing of the interfaces for Zn atomic flux calculation from the bare ZnO substrate into the InGaN layer.

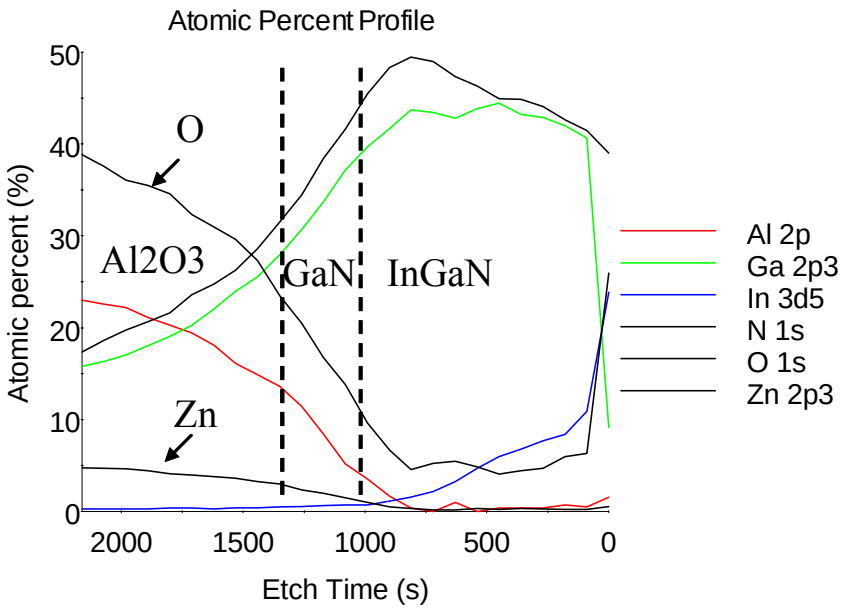

Figure 6.42: Concentration profile of InGaN(100nm)/GaN(30nm)/ALDAl_2O_3 (50nm)/ZnO.

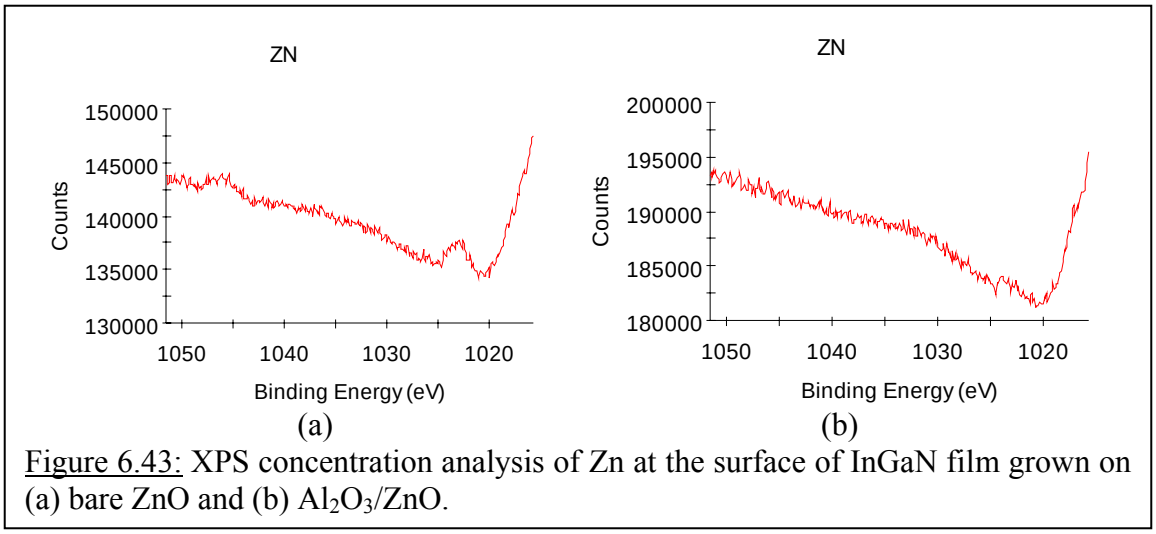

Figure 6.43: XPS concentration analysis of Zn at the surface of InGaN film grown on (a) bare ZnO and (b) Al_2O_3/ZnO.

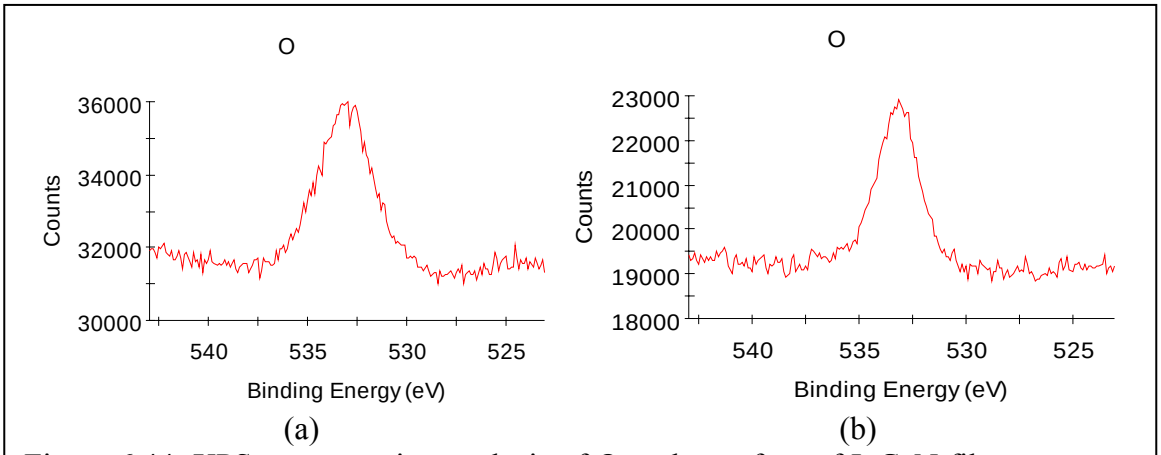

Figure 6.44: XPS concentration analysis of O at the surface of InGaN film grown on (a) bare ZnO and (b) Al_2O_3/ZnO.

Table 6.6: Zn and O concentration at the surface of the InGaN layer.

InGaN	Elements	At. %
on bare ZnO	Zn2p	5.6
	O1s	9.59
on Al_2O_3/ZnO	Zn2p	Detection limitation
	O1s	5.44

XPS measurement was performed on a sample consisting of the following layer, InGaN(100nm)/GaN(30nm)/ALD Al_2O_3(50nm)/ZnO, Figure 6.42. This sample had shown an x-ray InGaN (0002) diffraction peak. The ALD Al_2O_3 layer was shown to have prevented Zn atoms from diffusing out of the ZnO substrate. The Zn concentration went down to 0.2at.% = $1.5x10^{20}$atom/cm^3 from 0.7at.%, which indicates that the Al_2O_3 can retard much of the Zn diffusion though further reduction in Zn concentration is required. O atoms continued to diffuse into the InGaN layer resulting in a consistent value of 6at.%, though this could have been sourced by the Al_2O_3 layer rather than the ZnO substrate.

XPS was also used to analyze the Zn and O concentration at the surface of the InGaN layer. This measurement was performed in order to compare the Zn and O diffusion into the InGaN epilayer grown on both bare ZnO and Al_2O_3 deposited ZnO, Figure 6.43(a) and (b) and Figure 6.44(a) and (b). The Zn 2p and O 1s binding energies in the case of the bare ZnO are at 1023eV and 532.5eV, respectively, which shows intensities higher than that of Al_2O_3/ZnO. InGaN films exhibited higher Zn and O incorporation when grown on bare ZnO. Samples were compared with corresponding growths on thin Al_2O_3 layer coated ZnO substrate which shows the reduction of the Zn diffusion from the ZnO substrate. The concentration of Zn and O are summarized in Table 6.6. The limitation detection showed that the Zn concentration at the surface was below the detection limit of the system.

6.6.6 Summary of InGaN Growth on Al_2O_3/ZnO Substrate

X-ray measurements showed successful InGaN growth on 5, 10, 20 and 50nm Al_2O_3/ZnO with the ability to incorporate different indium concentrations. Growth on *in-situ* ALD annealed Al_2O_3/ZnO showed the best results with InGaN peaks of smaller

FWHM and greater intensity, but due to unavailability of the *in-situ* ALD material these growths were not continued. OT indicated that the bandgap energy of InGaN was not altered significantly when grown on annealed Al_2O_3/ZnO substrates and an indium concentration of 34% was calculated, which was close to the x-ray measurement of 32%. Furthermore, AES atomic depth profiling showed the Zn concentration in the InGaN layer dropped from 0.7at.% to 0.3at.% with the use of the 5nm Al_2O_3 transition layer. XPS also showed a decrease in Zn concentration in the surface of the InGaN epilayer compared to InGaN on bare ZnO. The transition layer has shown that it is a promising method for reducing Zn diffusion from the ZnO substrate into the InGaN layer.

6.7 Multiple Quantum Wells and Superlattices Growth by MOCVD on Al_2O_3/ZnO

Multiple quantum wells (MQWs) and superlattices (SLs) were utilized in this work for unconventional purposes. They were used to help minimize Zn diffusion into the epilayer and damage to the film quality. Proper growths of these layers were needed for them to be successful and therefore a systematic study was performed in order to verify their feasibility. These MQWs and SLs layers can later be utilized in the active region for LED structures.

6.7.1 MQWs Growth on ALD Al_2O_3/ZnO

Baseline of MQWs Growth on Sapphire Substrate

The purpose of using a MQW structure in this work was for the enhancement of band emission and to help minimize Zn diffusion into the epilayer and damage to the film quality. Optimization of the MQWs can later be used for the LED structures on Al_2O_3/ZnO substrates. The baseline structure consisting of InGaN/GaN 5MQWs was

grown on a GaN template and optimized before transitioning to growth on Al_2O_3/ZnO substrates. X-ray and PL for 5MQWs structures on a GaN template grown at 740ºC can be seen in Figure 6.45(a) and (b). The figure shows clear satellite peaks and a PL emission at 2.70eV with a FWHM of about 30meV.

Baseline of MQWs Growth on Bare ZnO Substrate

The optimized MQWs structure was grown on a bare ZnO substrate**.** X-ray and PL results can be seen in Figure 6.46(a) and (b). The only InGaN x-ray peak that appeared was from the diffraction of the underlying InGaN layer. No satellite peaks could be seen from the MQWs structure. Two possible causes of this were the rough surface of the underlying InGaN layer and the thickness of the well not being detected by x-ray. This indicated that lower temperature growth at 740ºC for InGaN layers is not as useful for the MQWs on ZnO as it was for growth on a GaN template. No MQW emission was observed in the PL results; only the ZnO band emission was visible. These characterization results indicated that a different structure would be needed for growth on ZnO.

MQWs Growth on "GaN Template" on Bare ZnO Substrate

The optimized InGaN structure from the previous section was utilized as the "GaN template" on bare ZnO substrate. A low temperature GaN buffer layer was grown at 530^{o}C on ZnO substrate with a thickness of about 30nm. Following the buffer, an InGaN film of approximately 5nm thick was grown at a temperature of 760^{o}C. Ten periods of MQWs (GaN(12nm)/InGaN(3nm)) were grown on top of the InGaN thin film, and a 50nm GaN cap completed the structure. In addition, the GaN barriers were doped with Si to obtain abrupt transitions between the barriers and the wells and to minimize

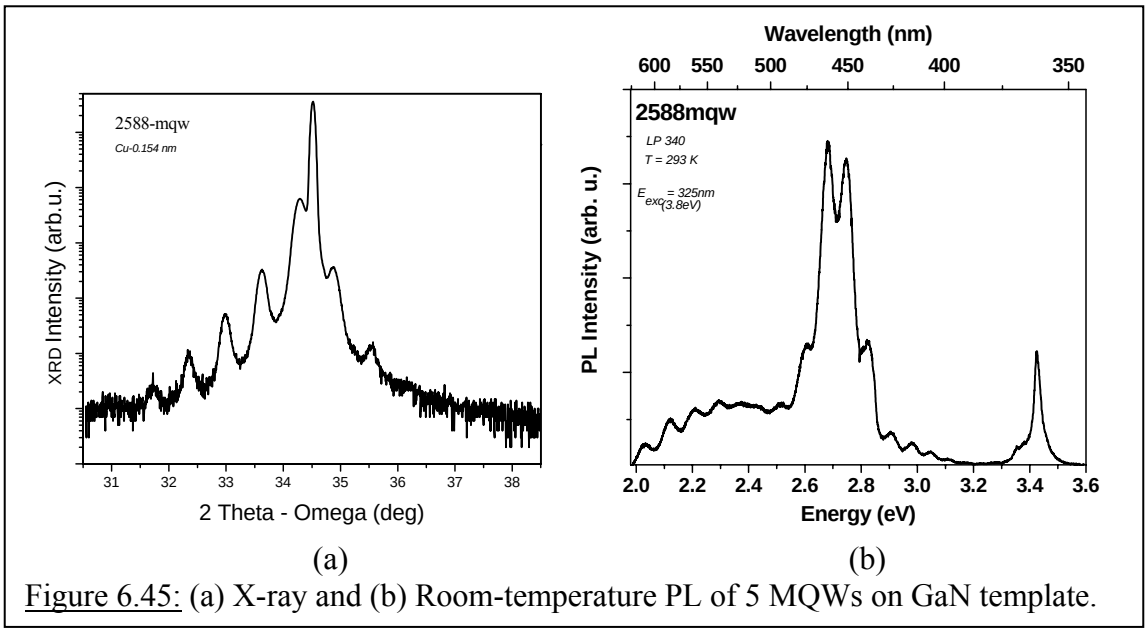

(a) (b)

Figure 6.45: (a) X-ray and (b) Room-temperature PL of 5 MQWs on GaN template.

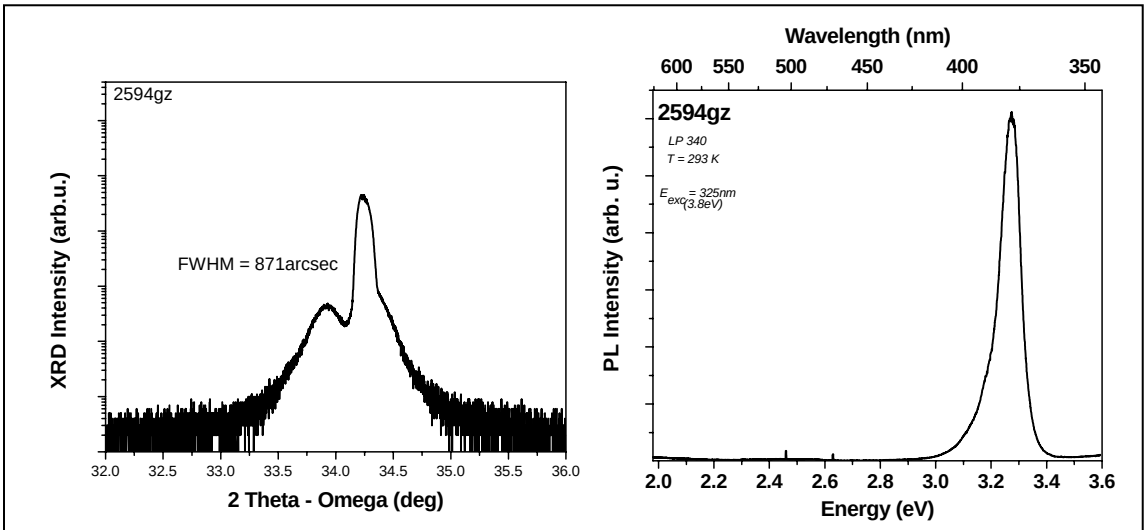

(a) (b)

Figure 6.46: (a) X-ray and (b) PL for 5 MQWs structures on a bare ZnO substrate.

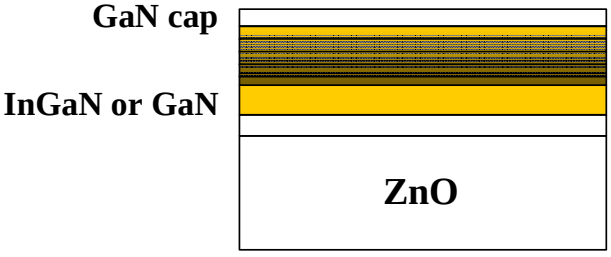

Figure 6.47: Schematic of the basic MQW structure grown on ZnO substrate.

intermixing. This structure will be known as the "basic structure" in this study, Figure 6.47. X-ray results showed the zero order for the MQWs and an InGaN well of 8% indium composition, Figure 6.48. X-ray also showed a shoulder at a higher angle from the ZnO peak, which was due to the GaN barriers. However, there were no significant satellite peaks visible, which meant that the interface quality of the MQWs needed to be improved. Interface roughness and intermixing between barriers and wells might have caused a degradation of the MQWs. It is also possible that the underlying layers of LT-GaN and InGaN could not provide a smooth surface for subsequent MQWs growth. Several other approaches were performed in order to obtain MQWs on ZnO such as: ramping up the growth temperature of the barrier, growth interruption, and N_2 or N_2/ dimethylhydrazine (DMHy) annealing after LT-GaN buffer growth. However, these studies did not result in any significant improvement.

Therefore, a higher temperature GaN buffer layer was grown, in place of the LT-GaN, at 770^{o}C on bare ZnO. The basic structure was then grown on top. X-ray results showed the zero order for the MQWs, Figure 6.49. X-ray also showed two shoulders on both sides of the ZnO peak, which were attributed to the first order. However, the satellite peaks still did not show up significantly, which meant the interface quality of the MQWs did not improve significantly. Results from the basic structure and initial GaN growth on ALD-Al_2O_3/ZnO are discussed below.

MQWs Growth on ALD Al_2O_3/ZnO Substrate

The ALD Al_2O_3 transition layer was added to see if it would improve the basic structure properties as it had for individual GaN and InGaN epilayers. The previously

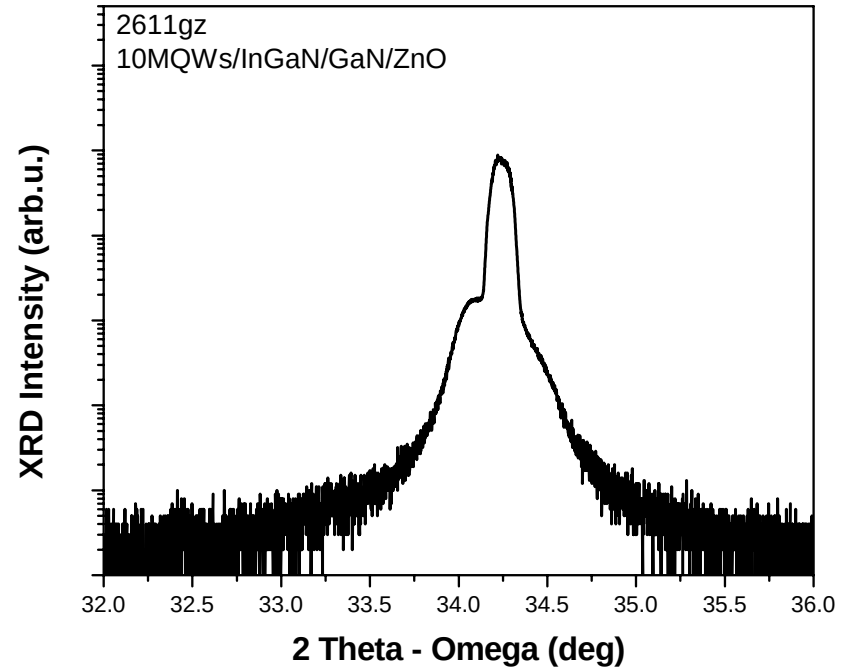

Figure 6.48: X-ray of 10MQWs on ZnO substrate with a LT-GaN as the "GaN template" for ZnO.

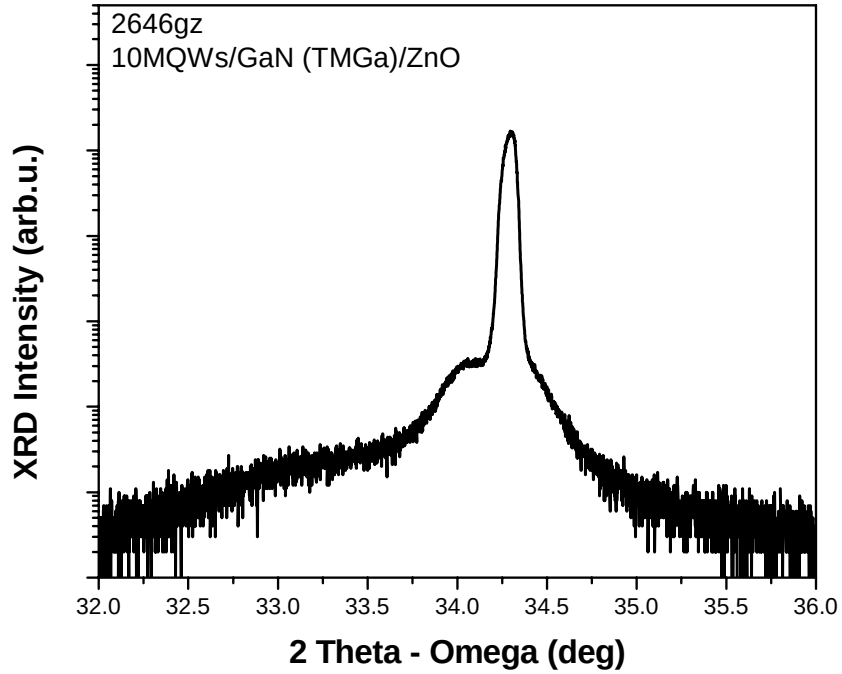

Figure 6.49: X-ray of 10MQWs on ZnO substrate with a HT-GaN as the "GaN template" for ZnO.

discussed results from the GaN growth study utilizing the one-step buffer layer formed the basis for this study of MQW growth on ALD Al_2O_3 layers.

The MQW recipe with the one-step GaN buffer growth was executed on a 20 and 50nm ALD-Al_2O_3/ZnO substrates. The first order satellite peaks for MQWs showed up on the 20nm sample, Figure 6.50. This peak was much stronger than what was observed from the bare ZnO substrate discussed above. However, there were no significant satellite peaks observed from the 50nm sample. It is believed that the 20nm ALD Al_2O_3 after 10 minutes annealing can provide the proper nucleation surface for subsequent MOCVD growth. This correlates with the GaN epilayer study discussed before that the 20nm layers exhibited better results than the 50nm layers. The MQWs showed promise on the 20nm ALD layer but still required improvement. Therefore a different interlacing structure was proposed moving forward: AlGaN/GaN superlattices.

6.7.2 AlGaN/GaN Superlattice Structure Grown on ALD Al_2O_3/ZnO

The AlGaN/(Al)GaN SLs structure is important for III-Nitride optoelectronic devices because it is reported that the SLs structure can help to decrease threading dislocation density and relax the in-plane strain in the heterostructure. Moreover, it has been demonstrated that the average hole concentration of the Mg-doped SLs layer at room temperature is enhanced more than a factor of 10 over that achieved in bulk GaN films [71]. Here, the purpose of AlGaN/GaN SLs structure growth was for the improvement of material quality and to help block Zn/O diffusion from the substrate to the epilayer.

Normally, Al-containing III-Nitride epilayers are grown at a high temperature (>1000°C) under H_2 ambient, which can enhance the Al atom movement on the surface of the epilayer. However, III-Nitride growth on a ZnO substrate must be performed at a

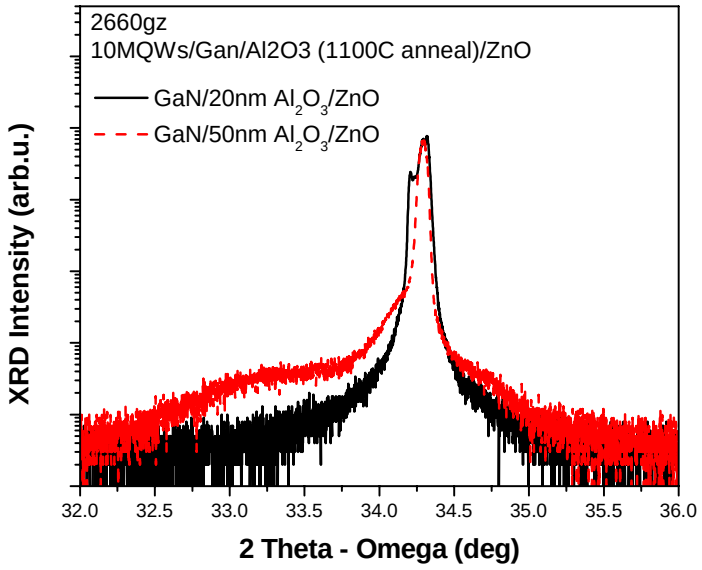

Figure 6.50: MQWs grown on 20 and 50nm ALD Al_2O_3/ZnO.

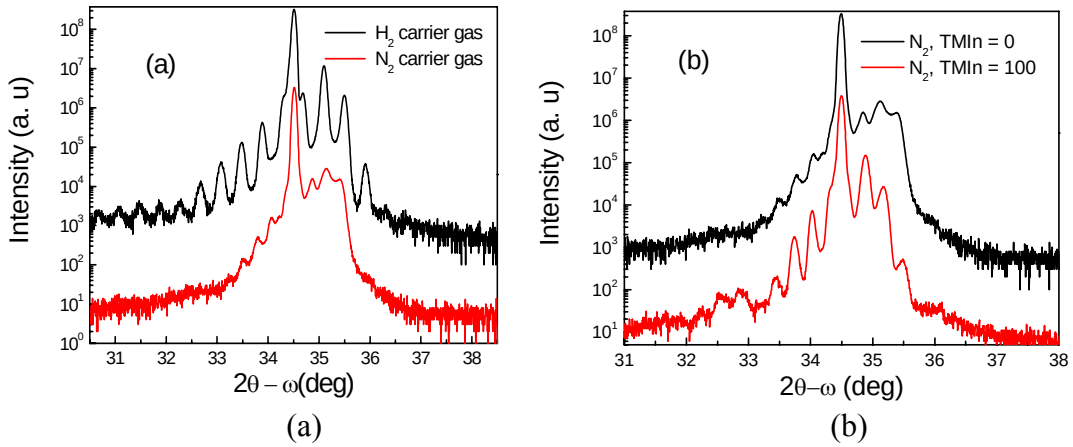

(a) (b)

Figure 6.51: X-ray of 5 AlGaN/GaN SLs grown on GaN template (a) in different carrier gases and (b) using different TMIn flow rate.

relatively low temperature under N_2 ambient due to the high reactivity of oxygen with H_2 at high temperatures.

Baseline of SLs Growth on Sapphire Substrate

Samples with five periods of AlGaN/GaN SLs were grown on a GaN template at a relatively low growth temperature (790°C) before transferring to growth on ZnO substrates in order to optimize the growth conditions. X-ray results of two samples which were grown with H_2 and N_2 as carrier gases are shown in Figure 6.51(a). X-ray measurement of the sample grown under H_2 displayed much higher order and stronger SLs related satellite peaks in comparison with that of the sample grown under N_2. This indicated a higher interfacial quality between AlGaN and GaN and was attributed to the growth surface where the motion length of the atoms in H_2 ambient is longer than that in N_2 ambient and can improve the interfacial sharpness.

TMIn was used as a surfactant (100sccm) during AlGaN growth to improve the structural quality of the AlGaN/GaN SLs grown in a N_2 ambient. Clearer and stronger SL satellite peaks with higher orders were observed from the sample with TMIn flow compared to that without TMIn, Figure 6.51(b). The results verified experimentally that high quality AlGaN/GaN SLs can be achieved even at low growth temperatures and with a N_2 ambient by calibrating the growth conditions, which provides a promising structure for growth on ZnO substrates.

Baseline of SLs Growth on Bare ZnO Substrate

The process was transferred to the ZnO substrate with a GaN buffer layer after optimization was completed on the GaN template. However, x-ray measurement of the sample did not show any SL related peaks, Figure 6.52. It was suspected that the crystal

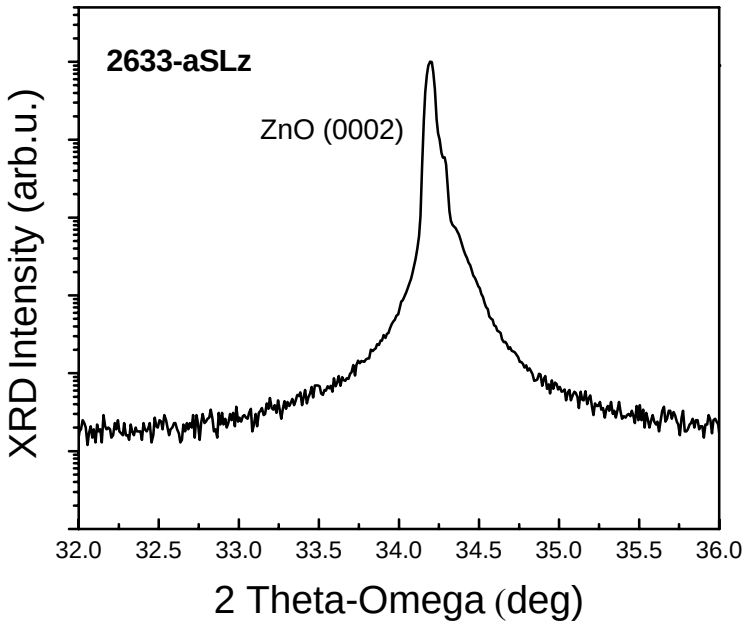

Figure 6.52: X-ray of AlGaN/GaN SLs on normal GaN buffer/ZnO substrate, no SLs related peaks.

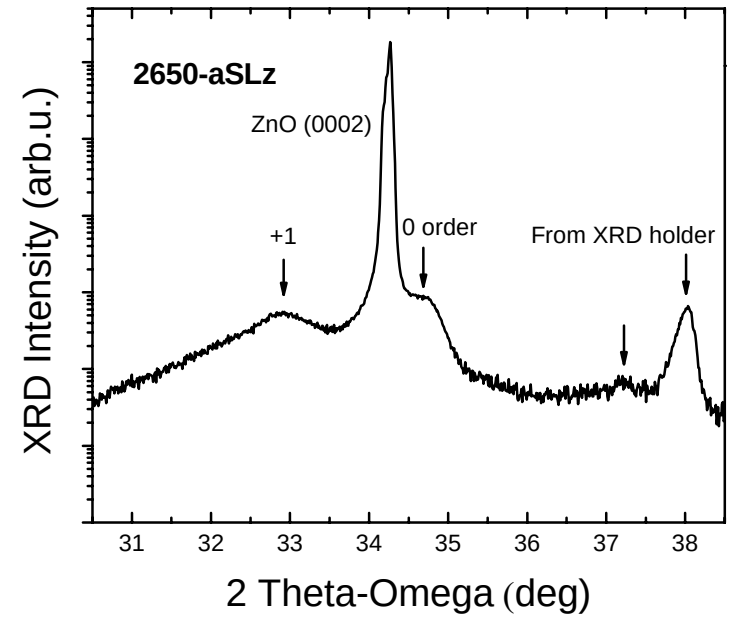

Figure 6.53: X-ray of AlGaN/GaN SLs on improved GaN buffer/ZnO substrate, with clear SLs related peaks.

quality of the GaN buffer layer on ZnO was relatively poor compared to GaN on a sapphire substrate. This could be due to the low temperature (530°C) nucleation layer that was deposited on the ZnO substrate to avoid the reaction between the ZnO substrate and NH_3.

Therefore, the low temperature nucleation layer was removed, and a GaN buffer layer was grown on ZnO at 770°C directly, the one-step growth method. However, this resulted in the surface of the GaN layer being etched and some regions were peeling from the ZnO substrate. Further optimization achieved a successful smooth GaN buffer without low temperature nucleation. The AlGaN/GaN SLs grown on this kind of GaN buffer displayed clear satellite peaks as shown in Figure 6.53. However, the structural quality of the SLs could still be improved by further optimizing the growth process.

Optimization of SLs Structural Design on Bare ZnO Substrate

Further optimization was performed on the layer thickness and period numbers to improve the quality of AlGaN/GaN SLs. First, the thickness of the AlGaN layers in the SLs was calibrated by changing the growth time from 1.8 minutes (10nm) to 1.5 minutes (8nm), while keeping the thickness of the GaN layers constant. The intensities of the SLs related peaks from the sample with a thinner AlGaN layer were much stronger, Figure 6.54(a). A higher order of satellite peaks was observed compared to the SLs with thicker AlGaN layers. This was because the interfacial quality between the AlGaN and GaN was improved. Also, the period number of the SLs was increased from five to eight while keeping other growth parameters constant. X-ray of the two samples with different periods are shown in Figure 6.54(b). The sample with eight periods of AlGaN/GaN SLs shows a better x-ray characterisatic.

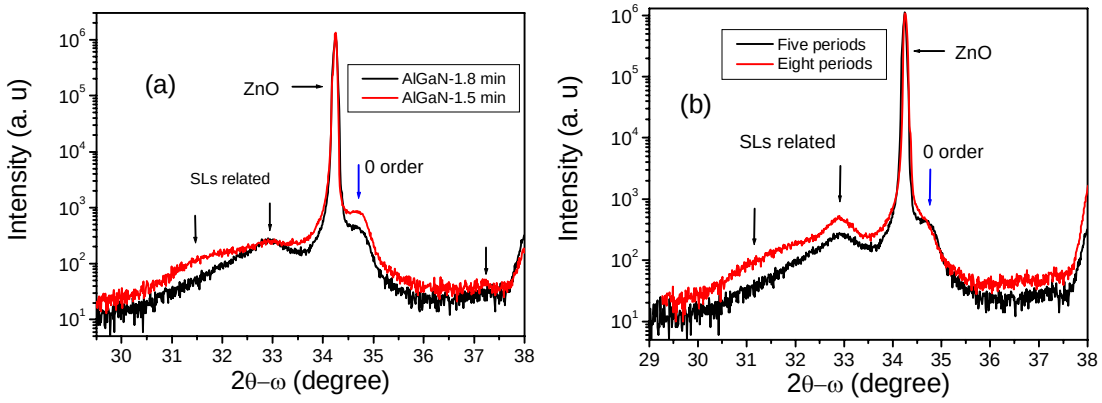

(a) (b)

Figure 6.54: X-ray of AlGaN/GaN SLs with different AlGaN (a) thicknesses (b) and periods.

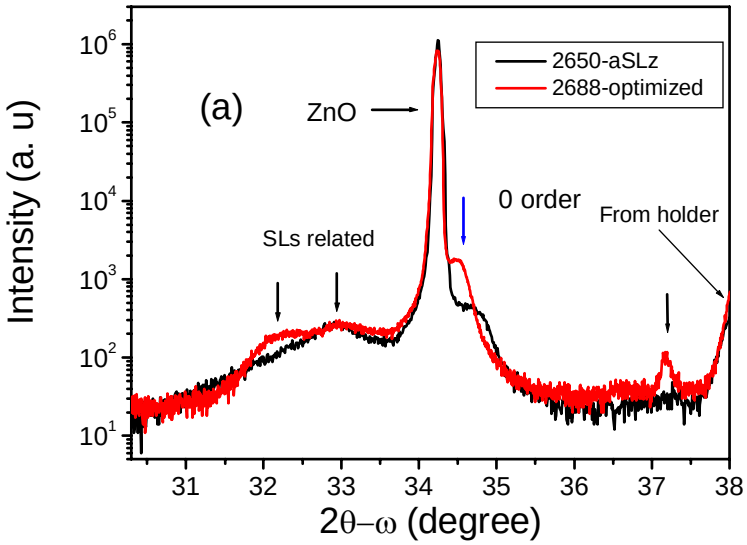

Figure 6.55: X-ray of AlGaN/GaN SLs before and after optimization.

The optimized growth conditions were combined in one recipe, which used a relatively higher growth temperature, thinner AlGaN layers, and SL eight periods. The x-ray results are shown in Figure 6.55. X-ray displayed clear and strong SLs satellite peaks with higher orders compared to previous SLs growths.

SLs Growth on ALD Al_2O_3/ZnO Substrate

The optimized growth process was transferred to the ALD Al_2O_3/ZnO substrate with 20 and 50nm ALD Al_2O_3 layers after optimization of the growth conditions. As a comparison the pre-optimized SL growth condition was also used on the 20 and 50nm ALD Al_2O_3 layers. X-ray results from these samples are shown in Figure 6.56. The sample used for after optimization showed SL satellite peaks, though the intensities of these peaks were much weaker than those from the structure grown on a bare ZnO substrate. The material quality of AlGaN/GaN SLs has been influenced by the ALD Al_2O_3 layer. However, further studies must be done in order to understand its full impact. These findings show that it is possible to grow on the ALD layers but further study must be done to see if the ALD really benefits the SLs growth process. The SLs as a whole showed more promise than the MQWs on ALD/ZnO.

6.7.3 Summary of MQWs and SLs Growth on Al_2O_3/ZnO Substrate

MQWs and SLs were used to help minimize Zn diffusion into the epilayer and damage to the film quality. A systematic study was performed in order to verify their feasibility. Growths were all performed initially on GaN templates on sapphire before being transferred to bare ZnO and then to ALD Al_2O_3/ZnO. The one-step growth method was utilized for the MQWs and was more successful for the 20nm Al_2O_3/ZnO layer than the 50nm layer, as was the case for GaN epilayers. However, this one-step growth

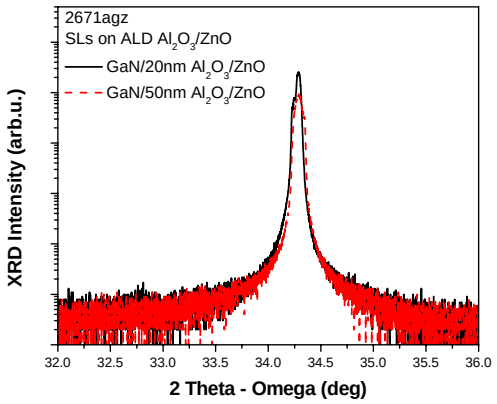

(a)

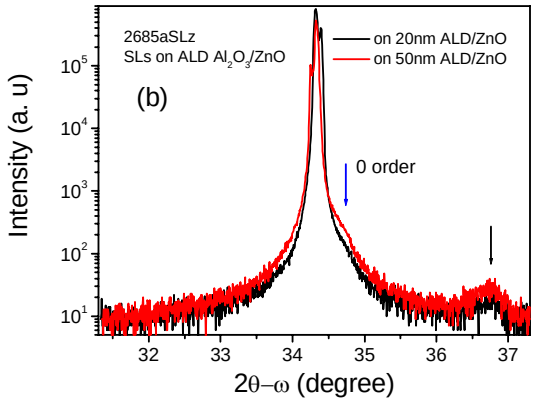

(b)

Figure 6.56: X-ray of AlGaN/GaN SLs grown on 20nm and 50nm ALD Al_2O_3/ZnO substrate (a) pre-optimization and (b) post-optimization.

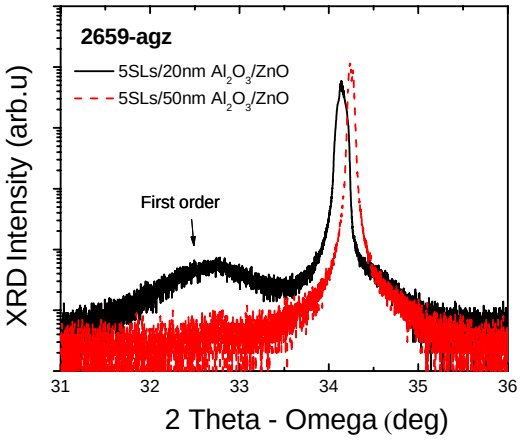

(a)

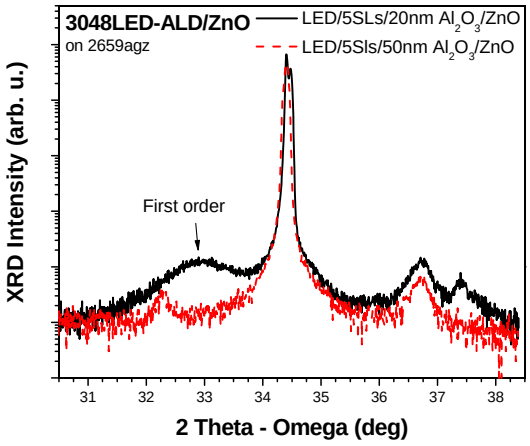

(b)

Figure 6.57: LED structure grown on 5 superlattices on 20nm and 50nm Al_2O_3/ZnO. (a) X-ray of 5 superlattices showing AlGaN/GaN first order peak. (b) LED structure showing first order AlGaN/GaN supperlatice peak as well as additional unidentified peaks for both the 20nm and 50nm sample.

method was not possible for SLs. The SLs were optimized by changing their thicknesses and number of periods until they showed promising peaks on bare ZnO. SLs were then grown on 20 and 50nm Al_2O_3/ZnO. Both samples showed peaks in x-ray, however, the 20nm Al_2O_3/ZnO sample showed better results than the 50nm. Even with the weak peaks, the results showed that the optimized steps for SLs did show promising results compared to pre-optimized growth conditions, and hence showed promise for future SLs growth on Al_2O_3/ZnO.

6.8 LED Growth on Al_2O_3/ZnO

LED structures were attempted on MQW and SL structures grown on Al_2O_3/ZnO substrates. MQWs and SLs were selected as the base structure to help minimize Zn diffusion into the LED. X-ray measurement of the initial 5 superlattices alone showed an AlGaN/GaN first order peak on the 20nm Al_2O_3/ZnO but not the 50nm Al_2O_3/ZnO, Figure 6.57(a). The LED structure was grown on this 5 superlattices structure on 20nm and 50nm Al_2O_3/ZnO. The LED structure showed the first order peak as well as additional unidentified peaks for both the 20nm and 50nm samples, Figure 6.57(b). This was the only LED structure grown that showed any satellite peaks. I-V measurements were performed, but all of the LEDs were highly resistive, probably due to Zn diffusion into the epilayers.

6.9 Gate Metrics for DOE Project

The study of ALD Al_2O_3 as a transition focused on three areas: improving the crystalline quality of the ALD transition layer, improving the GaN and InGaN optical and

crystalline qualities, and minimizing Zn diffusion into the nitride layer. These tasks coincided with the gate metrics mentioned in Chapter 2, which are described below. Achieving these goals allowed for the growth of higher quality epilayers, which can then be used to grow LEDs.

6.9.1 X-ray Diffraction

An InGaN peak on 5nm Al_2O_3/ZnO was obtained with an indium concentration of 32% and a FWHM of 478arcsec, which met the x-ray gate metric for the first year of a FWHM ≤ 500arcsec, Figure 6.58(b). A GaN peak of 385arcsec on 20nm Al_2O_3/ZnO also met the goal, Figure 6.58(a). This GaN sample also met the x-ray gate metric for the second year, which required a FWHM ≤ 450arcsec.

6.9.2 Photoluminescence

PL results from two samples show a GaN peak and an InGaN peak with FWHM of 0.02eV and 0.40eV in Figures 6.59(a) and (b), respectively. The GaN sample was a 200nm GaN layer on 20nm Al_2O_3/ZnO. The InGaN sample consisted of a 100nm InGaN layer grown on a 30nm GaN buffer on 5nm Al_2O_3/ZnO. The Al_2O_3 for Figure 6.59(b) was annealed for 20 minutes at 900ºC. Both samples met the gate metrics for PL, which required a FWHM ≤ 0.4eV.

6.9.3 Carrier Concentration and Mobility

Carrier concentration and mobility gate metrics for Year 1 were both met with $7.86 \times 10^{17} cm^{-3}$ and $397 cm^2 V^{-1} s^{-1}$. This was achieved by etching the ZnO substrate with HCl. The calculated etch rate of HCl on ZnO is shown in Figure 6.60(b). The epilayer was covered in wax to protect the GaN from the HCl. The ZnO substrate was etched from 480μm to 240μm. The carrier concentration and mobility were measured after each

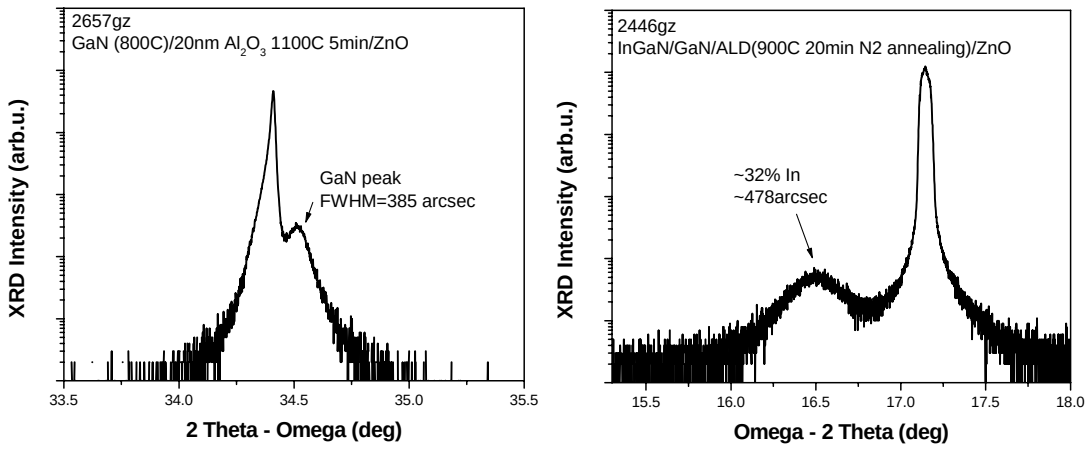

(a) (b)

Figure 6.58: X-ray of (a) GaN and (b) InGaN grown on top of annealed Al_2O_3, which met the gate metric for x-ray FWHM ≤ 500arcsec.

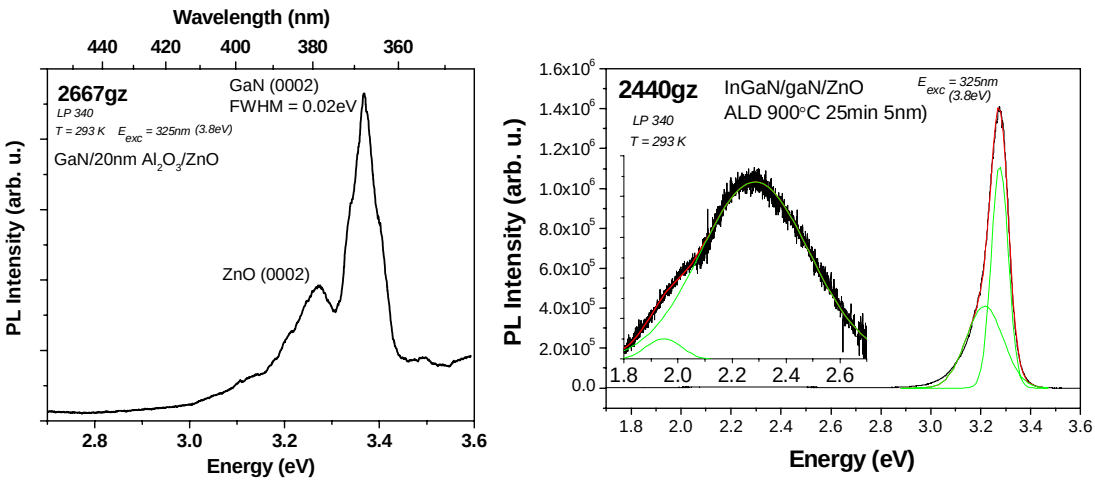

(a) (b)

Figure 6.59: PL of (a) GaN and (b) InGaN on ALD/ZnO with GaN and InGaN FWHM ≤ 0.4eV.

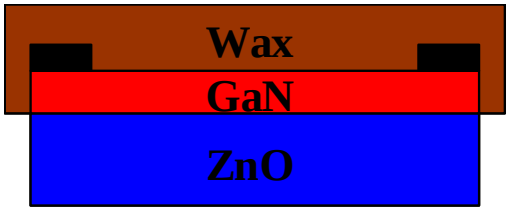

(a)

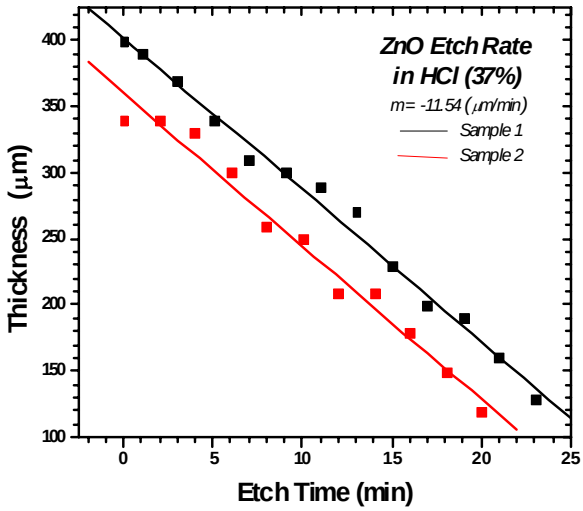

(b)

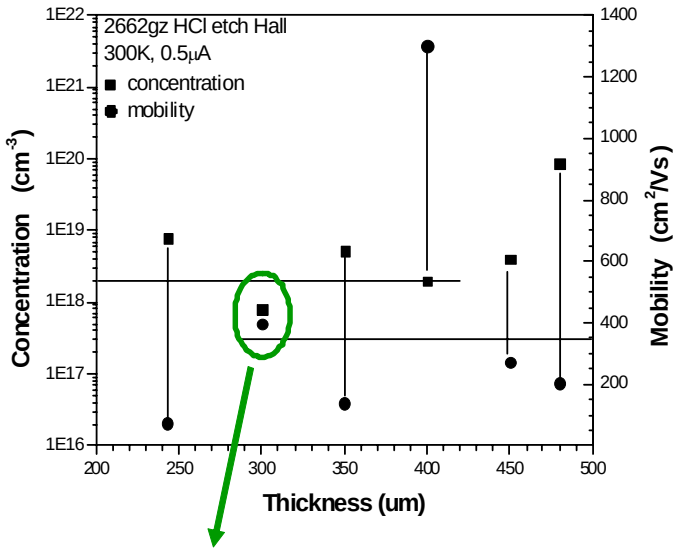

Carrier Concentration = 7.86×10^{17} cm^{-3}

Mobility = 397 $cm^2V^{-1}s^{-1}$

(c)

Figure 6.60: (a) Schematic, (b) ZnO Etch Rate in 37% HCl, and (c) Hall concentration and mobility results after sequential etching of GaN/20nm Al_2O_3/ZnO in HCl.

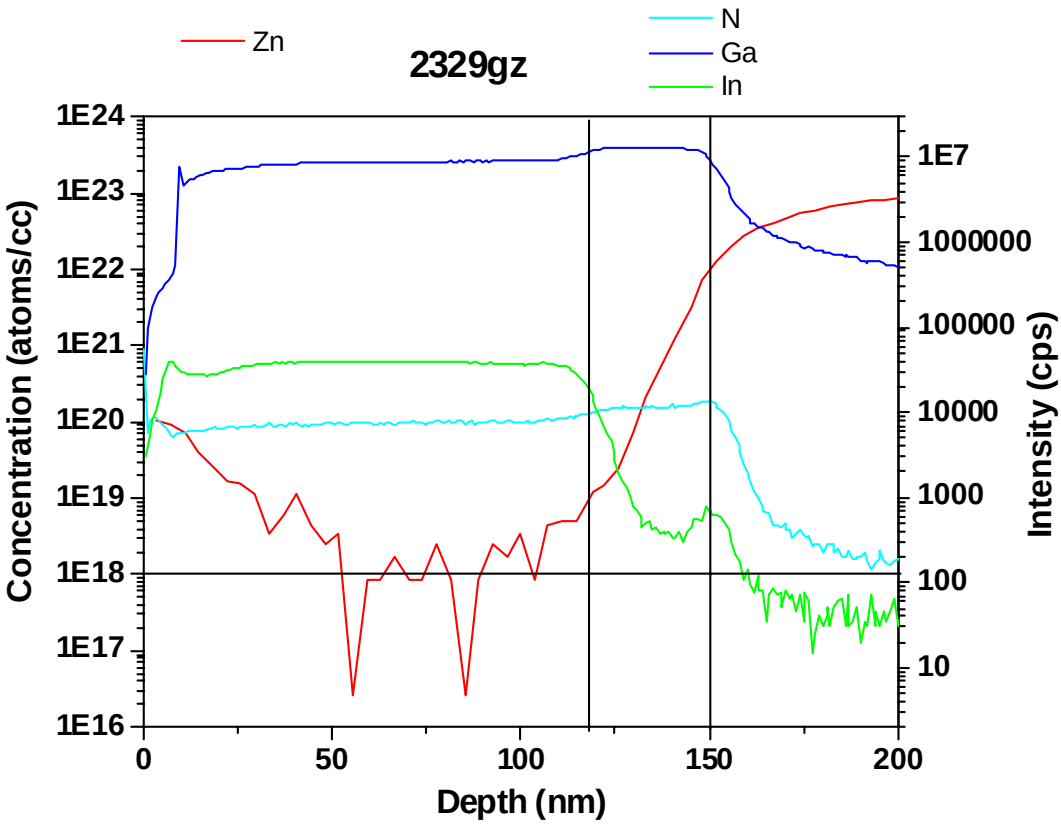

Figure 6.61: SIMS of InGaN on ZnO showing a Zn concentration of about $1x10^{18}cm^{-3}$.

50μm etching as shown in Figure 6.60(c). The etching helped the measurement by physically taking out the background concentration contributed by the ZnO substrate.

6.9.4 Concentration Impurity

The SIMS gate metric for Year 1 was also met with a Zn impurity concentration of $\leq 10^{18} cm^{-3}$, Figure 6.61. Very few samples met this requirement, indicating that minimizing Zn diffusion required highly optimized growth conditions.

6.10 Summary of GaN and InGaN Growth on ZnO Using an Al_2O_3 Transition Layer

An Al_2O_3 ALD layer was proposed as a transition layer on ZnO substrates in order to block Zn diffusion, promote GaN growth, and prevent H_2 etching into the substrate. Al_2O_3 was chosen as the transition material for its optical transparency, excellent thermal stability (in contrast to ZnO), and ease of deposition by ALD. ALD allows for a self-limited, layer-by-layer growth mode. Therefore, the thickness is accurately controlled just by the number of growth cycles rather than by temperature, etc. The ALD layer is initially amorphous, and therefore annealing studies were performed on the ALD layers using a furnace. X-ray measurements showed a number of Al_2O_3 phases including: Al_2O_3 peaks at 25, 38, 53, and 82 degrees for (012), (110), (024), and (306) phases, $ZnAl_2O_4$ peaks at 36, 44 and 48 degrees for (311), (400), and (533) phases, and x-ray stage holder peaks at 23 and 38 degrees. The appearance and intensity of the phases were dependent on the time and temperature of the annealing. Reanalysis of the phases was a continuous process, and in the end only the Al_2O_3 phases were kept: 38, 44, 53, and 82 degrees for (110), (113), (024), and (306) phases. Annealing for 5, 10, and 20 minutes at 1100ºC were found to be the best annealing parameters for 10, 20, and 50nm Al_2O_3

thicknesses, respectively. An additional annealing study was performed to investigate annealing the ZnO substrates and Al_2O_3/ZnO samples in a ZnO box in order to create a Zn ambient to help suppress the desorption of Zn atoms from the ZnO surface. AFM characterization showed terrace like surfaces after annealing of a bare ZnO substrate and a 200nm Al_2O_3/ZnO. The bare ZnO had a RMS value of 1.547nm, and the 200nm Al_2O_3/ZnO had a RMS value of 1.814nm.

GaN showed promising growths on Al_2O_3/ZnO. X-ray and PL showed distinct GaN peaks on 20nm Al_2O_3/ZnO whereas no peaks were seen on 50nm Al_2O_3/ZnO. A one-step growth process was used. A thin GaN buffer was first deposited at 770^{o}C and then the temperature was increased to 800^{o}C to grow the main GaN layer. Raman scattering also showed the distinct peaks of wurtzite GaN. The peaks were more prominent on Al_2O_3/ZnO than on bare ZnO. Single phase InGaN layers were also successfully grown on Al_2O_3/ZnO with a x-ray FWHM $\leq$ 500arcsec. InGaN peaks shifted with growth temperature verifying the ability to control indium incorporation. OT measurements showed that the bandgap energy of InGaN was not altered significantly when grown on annealed Al_2O_3/ZnO substrates. The bandgaps of the InGaN films were calculated to be 2.43 and 2.51eV for bare ZnO and Al_2O_3/ZnO. The concentration of Zn in the InGaN layer on bare ZnO substrate was approximately 0.7at.% whereas growth on Al_2O_3/ZnO showed a concentration of 0.3at.%. XPS also showed a higher concentration of Zn on the surface of InGaN growno n bare ZnO compared to that grown on Al_2O_3/ZnO. The Zn concentration was so low on the Al_2O_3/ZnO substrate that it could not be detected for a quantitative at.%. This showed that the Al_2O_3 transition layer did help in the reduction of Zn diffusion into the epilayer.

MQWs and SLs were used to help minimize Zn diffusion into the epilayer and damage to the film quality. A systematic study was performed in order to verify their feasibility. Growths were all performed initially on GaN templates before being transferred to bare ZnO and then to ALD Al_2O_3/ZnO. The one-step growth method was utilized for the MQWs and was more successful for the 20nm Al_2O_3/ZnO layer than the 50nm as was the case for GaN epilayers. However, this one-step growth method was not possible for SLs. The SLs were optimized by changing their thicknesses and number of periods until they showed multiple satellite peaks in x-ray on bare ZnO. SLs were then grown on 20 and 50nm Al_2O_3/ZnO. Both samples showed peaks in x-ray. However, the 20nm Al_2O_3/ZnO sample still showed better results than the 50nm. Even though the peaks were weak, the results showed that the optimized steps for SLs did show promising results compared to pre-optimized growth conditions, and hence showed promise for future SLs growth on Al_2O_3/ZnO. These studies were also carried through to the first growth of LEDs on Al_2O_3/ZnO substrates. One satellite peak appeared, but IV curves showed the device to be highly resistive.

CHAPTER 7

CONCLUSIONS AND FUTURE WORK

The purpose of this thesis work was to develop high quality GaN epitaxial growth on alternative substrates resulting in higher external quantum efficiency devices through metalorganic chemical vapor deposition (MOCVD) growth on ZnO substrates. This work demonstrated the first successful growth of GaN on ZnO by MOCVD on both bare ZnO and Al_2O_3/ZnO substrates. Over 450 GaN on ZnO samples and over 240 atomic layer deposition (ALD) Al_2O_3 layers on ZnO were grown to achieve the results discussed in this thesis. A number of papers and presentations came out of this work [72-94].

7.1 Conclusion

Current GaN-based LEDs are grown on foreign substrates such as sapphire and SiC. These substrates have proved viable for the current technology and have produced LEDs with optical outputs exceeding 100 lumens. However, there is a limit to the efficiency achievable by LEDs grown on foreign substrates due to the internal defects (10^8-10^{10}cm^{-2}) caused by mismatches in lattice size and thermal expansion coefficient. Sapphire substrates also require a GaN template to be grown prior to any epitaxial growth. This growth step increases device cost as it uses up expensive metalorganic precursors, adds to the growth time, and reduces the epitaxy tool's lifetime. GaN substrates have been successfully used by some companies (such as Cree and Kyma) but are still too expensive

for research or for mass production of commercial LED. Therefore, ZnO substrates were proposed in this project as an alternative substrate for GaN growth. ZnO has a small lattice mismatch with GaN of only 1.8% and has a similar thermal expansion coefficient. ZnO is also perfectly lattice matched to InGaN at 18% indium concentration. Thus, the defect densities seen in current LEDs on sapphire or SiC can be decreased by using ZnO. Also, ZnO has shown that it has the ability to incorporate higher indium concentration into InGaN, which will allow for more efficient green LEDs.

The main growth process investigated in this work was MOCVD, which is the industry accepted method for LED production. High quality MOCVD GaN growth on ZnO is difficult to achieve due to the thermal stability of the ZnO substrate, out-diffusion of Zn from the substrate, and H_2 back etching into the sample. A solution to these problems was developed by utilizing a transition layer technique based on atomic layer deposition (ALD) of Al_2O_3. The ALD Al_2O_3 layers were amorphous after growth; therefore, an annealing study was performed in order to obtain the optimal annealing parameters for subsequent MOCVD growth of GaN. Characterizations by destructive and non-destructive methods provided a close analysis of the materials grown and led to the results discussed below.

The initial attempts to grow GaN on ZnO by MOCVD resulted in cracking and peeling of the epilayer due to the previously mentioned problems of Zn out-diffusion and H_2 back-etching into the ZnO substrates. To solve this, a series of growths were performed using a variety of buffer layers such as GaN, AlN, InGaN, InN, or AlGaN. One successful technique was discovered, which utilized a multi-buffer layer of low temperature AlN/GaN. These samples were characterized by photoluminescence (PL), x-

ray diffraction (XRD or x-ray), and secondary ion mass spectrometry (SIMS). PL and x-ray both showed peaks which indicated successful GaN growth for these generations. However, the films were not high-quality GaN, and SIMS showed that Zn diffusion was still occurring, with a concentration of $5x10^{19}$atoms/cm^3 observed in the GaN films. The interfacial Zn and O concentration have to be reduced in order to successfully dope GaN p- or n-type for LED devices.

In addition, InGaN growth on bare ZnO substrate was investigated due to its ability to be grown at lower temperatures and its perfect lattice match to ZnO at 18% indium concentration. The goal was not only to provide a better substrate for green LEDs but also to optimize the material characteristics of the nitride layers. Good quality InGaN films, with high indium composition of 17-27%, were obtained with growth temperatures of 680-720°C. The key factor of this success is the use of a low temperature (530°C) GaN buffer layer. The InGaN films showed no indium droplets or phase separation, which can be attributed to the strain relaxation in the InGaN epilayers grown on ZnO substrates. PL data for all of the InGaN films show a strong emission band from ZnO and broad InGaN-related emissions, with the peak energy varying with indium composition. Peak energy values of the broad PL emissions were measured to be less than the calculated InGaN bandgap by 0.4-0.6eV. These emission shifts may be due to recombination involving Zn- or O-impurities in the InGaN films due to Zn/O diffusion from the ZnO substrate. Temperature-dependent PL measurements, 80-673K, revealed an activation energy of 59meV for the 23% indium InGaN epilayer, which correlated to literature findings for similar indium doping concentrations.

A case study was performed on InGaN layers grown on ZnO and sapphire substrates under the same conditions. The samples showed two distinct results for phase separation in the InGaN layers. InGaN films with 32% indium content exhibited phase separation when grown on sapphire. For InGaN layers grown on ZnO, there was no observation of phase separation with indium content as high as 43%. In addition, Si-doping induced much stronger phase separation in InGaN films grown on sapphire than in those grown on ZnO. A possible explanation for this is that InGaN layers with high indium composition grown on ZnO might exhibit a higher strain state than those grown on sapphire, which could suppress phase separation caused by Si doping. Previous studies reported clear phase separation for InGaN films grown on sapphire with indium concentrations below 20%. Research has also shown that strain in the InGaN layer helps in suppressing phase separation, which correlates with the ZnO characteristics. ZnO is perfectly lattice matched with InGaN at 18% and therefore should not exhibit relaxation until after 20% indium incorporation. Cross-sectional high angle annular dark field (HAADF) scanning transmission electron microscopy (STEM) and high-resolution transmission electron microscopy (HRTEM) analysis of these films revealed reduction of threading dislocation and perfectly matched crystals at the GaN buffer/ZnO interface. Therefore, InGaN can stay completely strained on a thin GaN buffer due to the larger a-axis lattice constant of GaN on ZnO, which is also preferable for lattice matching to strained InGaN with high indium concentration.

An Al_2O_3 ALD layer was proposed as a transition layer on ZnO substrates in order to block Zn diffusion, promote GaN growth, and prevent H_2 etching into the substrate. Al_2O_3 was chosen as the transition material for its optical transparency, excellent thermal

stability (in contrast to ZnO), and ease of deposition by ALD. ALD allows for a self-limited, layer-by-layer growth mode. Therefore, the thickness is accurately controlled just by the number of growth cycles rather than by temperature, etc. The ALD layer is initially amorphous, and therefore annealing studies were performed on the ALD layers using a furnace. The X-ray showed a number of Al_2O_3 phases including: Al_2O_3 peaks at 25, 38, 53, and 82 degrees for (012), (110), (024), and (306) phases, $ZnAl_2O_4$ peaks at 36, 44 and 48 degrees for (311), (400), and (533) phases, and x-ray stage holder peaks at 23 and 38 degrees. The appearance and intensity of the phases were dependent on the time and temperature of the annealing. Reanalysis of the phases was a continuous process, and in the end only the Al_2O_3 phases were kept: 38, 44, 53, and 82 degrees for (110), (113), (024), and (306) phases. Annealing for 5, 10, or 20 minutes at 1100ºC were found to be the best annealing parameters for 10, 20, and 50nm Al_2O_3 thicknesses, respectively. An additional annealing study was to anneal the ZnO substrates and Al2O3/ZnO samples in a ZnO box in order to create a Zn ambient to help suppress the desorption of Zn atoms from the ZnO surface. AFM characterization showed terrace like surfaces for post-annealing of a bare ZnO substrate and a 200nm Al_2O_3/ZnO. The bare ZnO had a RMS value of 1.547nm, and the 200nm Al_2O_3/ZnO had a RMS value of 1.814nm.

GaN showed promising growths on Al_2O_3/ZnO. X-ray and PL showed distinct GaN peaks on 20nm Al_2O_3/ZnO whereas no peaks were seen on 50nm Al_2O_3/ZnO. A one-step growth process was used. A thin GaN buffer was first deposited at 770°C, and then the temperature was increased to 800°C to grow the main GaN layer. Raman spectroscopy also showed the distinct peaks of wurtzite GaN. The peaks were more prominent on Al_2O_3/ZnO than on bare ZnO. Single phase InGaN layers were also successfully seen on

Al_2O_3/ZnO with FWHM ≤ 500arcsec. InGaN peaks shifted with growth temperature indicating that temperature could be used to control indium incorporation, which is consistent with growth on sapphire. Optical transmission (OT) measurements showed that the bandgap energy of InGaN was not altered significantly when grown on annealed Al_2O_3/ZnO substrates. The bandgaps were calculated to be 2.43eV and 2.51eV for bare ZnO and Al_2O_3/ZnO, respectively. X-ray photoelectron spectroscopy (XPS) showed that the concentration of Zn in the InGaN layer on bare ZnO substrate was around 0.7at.% whereas growth on Al_2O_3/ZnO showed a concentration of 0.3at.%. XPS also showed a higher concentration of Zn on the surface of InGaN on bare ZnO compared to growth on Al_2O_3/ZnO. The Zn concentration was so low on the Al_2O_3/ZnO substrate that it could not be detected for a quantitative at.%. These results show that the Al_2O_3 transition layer successfully reduced Zn diffusion into the epilayer.

Multiple quantum well (MQW) and superlattice (SL) structures were investigated as another technique for minimizing Zn diffusion into the epilayer and the corresponding damage to the film quality. A systematic study was performed to examine the effectiveness of these structures. Calibration growths were performed on GaN templates before being attempted on bare ZnO and then ALD Al_2O_3/ZnO. The one-step growth method was utilized for the MQWs and proved to be more successful on the 20nm Al_2O_3/ZnO layers than on the 50nm layers; this was also the case for the GaN epilayers. However, this one-step growth method was not possible for SLs as peeling of the epilayers occured. The SLs were optimized by changing their thicknesses and number of periods until they showed multiple satellite peaks in x-ray on bare ZnO. SLs were then grown on 20nm and 50nm Al_2O_3/ZnO. Both samples showed satellite peaks in x-ray.

However, the 20nm Al_2O_3/ZnO showed higher intensity peaks than the 50nm, which was consistent with GaN and InGaN results. Although the peaks were weak, characterization results of the optimized SLs were superior to those from pre-optimized growth runs, and hence showed promise for future SL growths on Al_2O_3/ZnO. These studies were also carried through to the first growth of LEDs on Al_2O_3/ZnO substrates. One satellite peak appeared, but IV curves showed the device to be highly resistive.

7.2 Future Direction

There is a great deal of continuing work in this area. Light extraction techniques such as roughening of the surface are still to be performed, as well as successful growth of LED structures, removal of the ZnO substrate, and fabrication studies. Two studies extending from this thesis work have begun and are discussed below. These studies include an early prototype of an emissivity correcting pyrometer device and modeling of opal layers for better light extraction.

7.2.1 Real Time Monitoring of Surface Roughening for Increase in Light Extraction

During fabrication of a LED, in order to increase the light extraction, surface roughening of the surface of the LED will be performed using metallic nano-particle deposition, for which in-situ two color long wavelength emissivity correcting pyrometer (ECP) techniques will be utilized in order to provide real time monitoring of surface roughness.

The majority of mechanical parts for the construction of the ECP are commercially available, with a small number of custom built parts. While the use of these commercially available parts increases the device size and decreases aesthetics, it provides fast prototyping, minimizes cost, and will enable the early clarification of technical issues. A

rendering of the main detector, the beamsplitter cube, and the interface to the tool is shown in Figure 7.1. The optical design was simulated using a commercially available ray tracing program, OSLO. A narrowband radiometer with emissivity compensation has been designed. The detector is a Mercury Cadmium Telluride device. The lens and detector components are specified at wavelengths of 10μm. Critical parameters, (detector performance, refractive indices, etc.) were taken at 8μm. The ray tracing results of the optical design are shown in Figure 7.2. The final choice of the operating wavelength of the device was chosen in order to collect the quantitative absorption spectra from process gases used in the MOCVD production of GaN-based LED structures. A summary of these absorption spectra is shown in Figure 7.3.

One challenge in the design has been a light source for the reflectometer with sufficient brightness. A thermal source and tuning fork chopper was the planned approach. Simulations showed functionality of this approach. However, the intensity on the detector is just sufficient (approximately 100X detector train noise). Therefore, light source brightness is a concern. Due to this concern, the following light source for the prototype was selected. This is the CH-20s thermal source with incorporated tuning fork optical chopper. In order to fully design the prototype and required mounts, this light source was rendered in to the *SOLIDEDGE* CAD system and is shown in Figure 7.4. This choice represents the best options for brightness and compact design, both of which are required for successful operation of the prototype. The thermal source is operating at 5W power output while the tuning fork has been designed for 600Hz modulation. This design also allows for very compact reference intensity monitoring of the thermal source which does not require expensive, fast detector schemes.

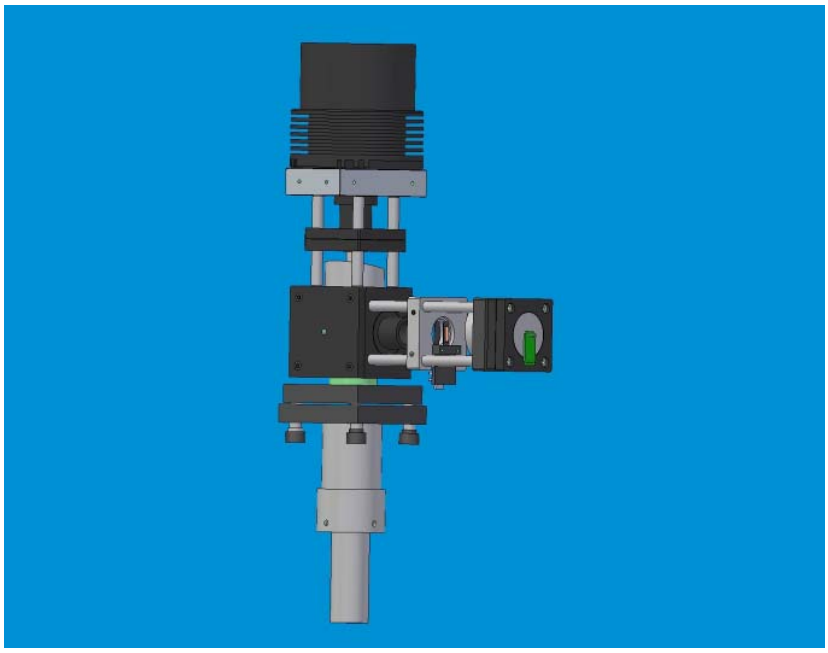

Figure 7.1: Rendering of the main detector mechanical arrangement. The top assembly is the detector while the bottom corresponds to the interface to the GaN tool.

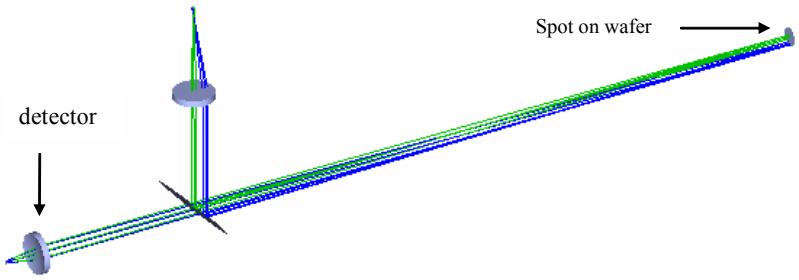

Figure 7.2: Raytrace of optical elements in the design of an ECP pyrometer for white LED manufacturing process control.

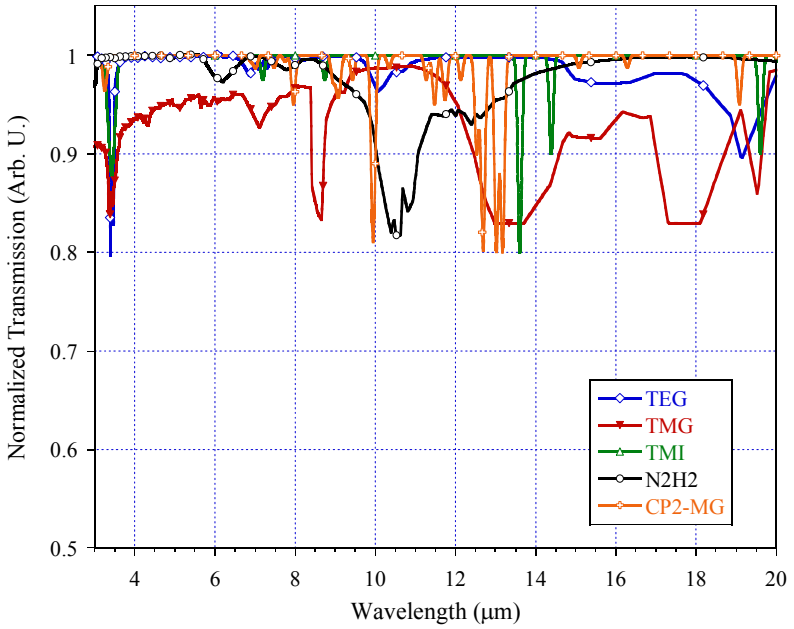

Figure 7.3: Infrared absorption spectra for precursor gases utilized in the MOCVD growth of GaN based LED structures. These spectra were used in establishing the final choice of pyrometer wavelength.

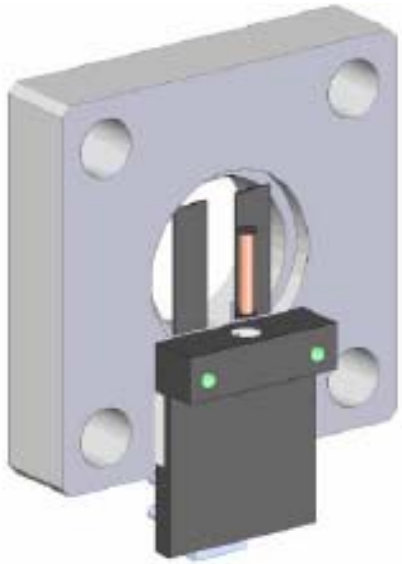

Figure 7.4: CH20-s light source with built in tuning fork chopper. Also shown is the custom mount required to incorporate the light source into the compact ECP prototype.

7.2.2 Enhancement of LED Light Extraction Using Opals Layer

Introduction

Initial theoretical and modeling studies of LEDs using an opals layer have been proposed as an extension to the present work of ALD passivation layers. The opals will assist in better light extraction efficiency for LEDs. Like other conventional semiconductor LEDs, the external efficiency is blocked by total internal reflection which is caused by index mismatch between GaN (n=2.46) and its surroundings. For most GaN-based LEDs, the ratio of the total flux reaching the capping layer, filled with epoxy-ester, (n=1.4) is only 8%.

To overcome the poor extraction efficiency of LEDs, three different schemes have been attempted by various research groups, see Figure 7.5(a), (b), and (c). One is to place a metal reflection layer near the active layer to build a microcavity. The drawback with this design is that only the light normal to the surface is enhanced [95-97]. The second method involves roughening the surface or implementing photonic crystals in the LEDs to enhance the extraction efficiency [96]. The roughened surface enhances the scattering property of the LED and changes the micro-area to avoid total internal reflection. However, this method is difficult to control. The third method used surface plasmons in LEDs to enhance the efficiency by coupling photons to surface polaritons [98]. Among these methods, a number of attempts have been performed on incorporating photonic crystals (PC) into LEDs. These devices have reported up to 30% external efficiency. But the effect of non pillar and hole type nano-particle shapes on the light extraction was not investigated thoroughly.

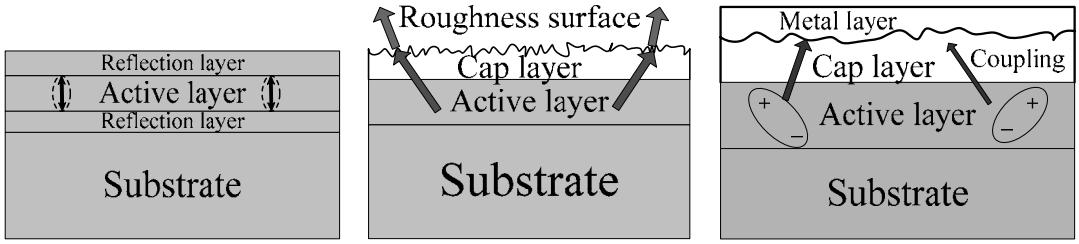

(a) (b) (c)

Figure 7.5: (a) Microcavity LED, (b) LED with roughness surface, and(c) LED with surface plasmons.

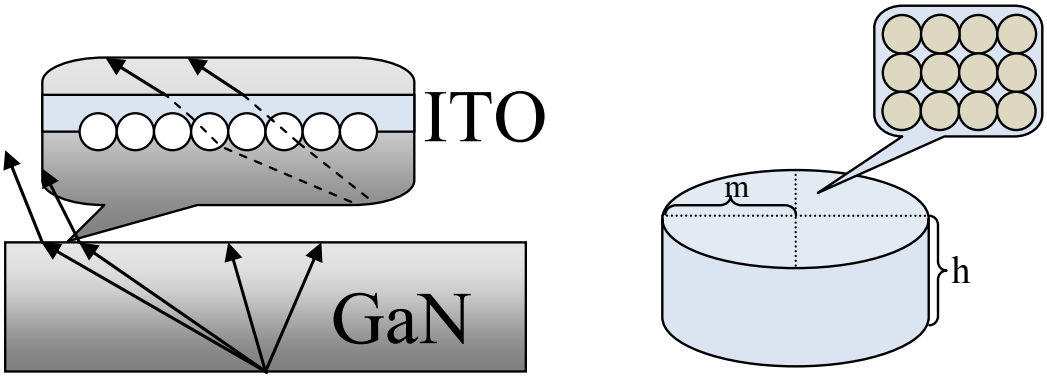

(a) (b)

Figure 7.6: Sketch map for GaN-based LEDs with opals layer. (a) Cross section view of the structure; (b) Top view of the structure.

Here, a new kind of LED structure is theoretically demonstrated with an opals layer on the surface, Figure 7.6. These structures can be prepared as an extension to the ALD growths reported in this thesis. Synthetic opals produce wide gap omnidirectional PCs and when inverted with high refractive index materials - using conformal infiltration techniques such as ALD - produce complete photonic bandgaps [99]. ALD yields highly conformal growth and nanometer-scale film thickness control, and has proven to be an ideal route for opal infiltration [100]. In this work, an infiltrated opals layer with ITO on the surface was placed as a light extraction layer, which combines the merits of a rough surface and photonic crystals. This method displayed a significant improvement in the light extraction angle.

Theory

Photons generated in the active region, unless they are absorbed internally, will be incident upon the LED's surface and side walls. The reflection coefficients Γ_{TE} and Γ_{TM} for transverse electric (TE) and transverse magnetic (TM) modes, as shown in Figure 7.7, are given by Equations 7.1 and 7.2

$$\Gamma_{TE} = \frac{n_1 \cos\varphi_1 - n_2 \cos\varphi_2}{n_1 \cos\varphi_1 + n_2 \cos\varphi_2} \tag{7.1}$$

$$\Gamma_{TM} = \frac{n_1 \cos\varphi_2 - n_2 \cos\varphi_1}{n_1 \cos\varphi_2 + n_2 \cos\varphi_1} \tag{7.2}$$

where n_1 and n_2 are the refractive indices of the materials on either side of the interface. The magnitude of both Γ_{TE} and Γ_{TM} becomes unity, implying so-called total internal reflection. The photon transmittances T_{TE} and T_{TM} for TE and TM photons will then be given by Equations 7.3 and 7.4.

$$T_{TE} = 1 - R_{TE} = 1 - \left|\Gamma_{TE}\right|^2 \tag{7.3}$$

$$T_{TM} = 1 - R_{TM} = 1 - \left|\Gamma_{TM}\right|^2 \tag{7.4}$$

The transmission ratio for TM polarization is always greater than that for TE polarization because of the Brewster angle phenomenon [101]. Figure 7.7(b) shows the transmission ratio of TE and TM mode at the interface between GaN and epoxy-ester. For TE mode, the transmission decreases linearly with an increase in angle. For TM mode, the transmission first increases with the incident angle and then decreases dramatically to zero. For a MQW LED, emitted photons between two dielectric layers always have TE-like polarization [102]. An average is considered in this work, unlike other simulations which may focus on TE polarization.

Equation 7.5 gives the total internal reflection angle as dictated by Snell's law:

$$\varphi_{total} = \sin^{-1}(n_2 / n_1) \tag{7.5}$$

where n_1 and n_2 are the refractive index of the incident and exit side. The light escape angle can be expressed by Equation 7.6.

$$\begin{aligned} \Omega &= \int_{\theta=0}^{2\pi} \int_{\varphi=0}^{\varphi_{total}} \sin\varphi d\varphi d\theta \\ &= 2\pi(1 - \sqrt{1 - \sin^2\varphi_{total}}) \\ &\approx 2\pi\left[1 - (1 - \frac{1}{2}\sin^2\varphi_{total})\right] = \pi\sin^2\varphi_{total} \end{aligned} \tag{7.6}$$

This leads to the light extraction efficiency which is equal to Equation 7.7.

$$\eta = \frac{\Omega}{4\pi} = \frac{1}{4}\sin^2\varphi_{total} \tag{7.7}$$

The extraction efficiency is less than 4% for light incident from GaN to air. Most of the light is trapped in the LEDs as guided light which is eventually absorbed by the material. A large part of the energy is converted to heat which has a negative impact on the

performance and lifetime of the LEDs.

Experimental Setup

Opals can be made from many kinds of materials, and silica is chosen because it is a low cost material. Monte Carlo ray tracing is used to simulate the refraction and reflection of light. This method allows for ray directions to be chosen randomly and a reliable answer is obtained by tracing a very large number of rays. This takes into account the ability of light to go in all directions.

The sphere surface is the key characteristic in helping light extraction. For example, when the sphere is made of a low index material with a Brewster angle equal to θ/2, the incident light can have a dramatically large incident angle φ compared to planar surface LEDs as shown in Figure 7.8. However, only the line crossing the center of the sphere will be emitted out for a small incident angle while others are reflected back. Some will inject to the next sphere surface. This could be overcome by optimizing the refractive index and the radius of the spheres.

In the process of simulation the micro local surface, d*s*, is assumed to be large enough compared with the light line. Lambert's law is used to define the absorption of the material, Equation 7.8.

$$\Phi_{\mathrm{t}rans} = \Phi_{in} e^{-\alpha l} \tag{7.8}$$

Where Φ_{trans} and Φ_{in} are transmitted and incident flux, α is the absorption coefficient, and *l* is the length the light ray travels. A threshold, Φ_t, is defined to determine whether one light ray is live or being absorbed. The length from the source to the surface is defined as h, the radius of the LEDs surface as m, and the radius of the opals sphere as r.

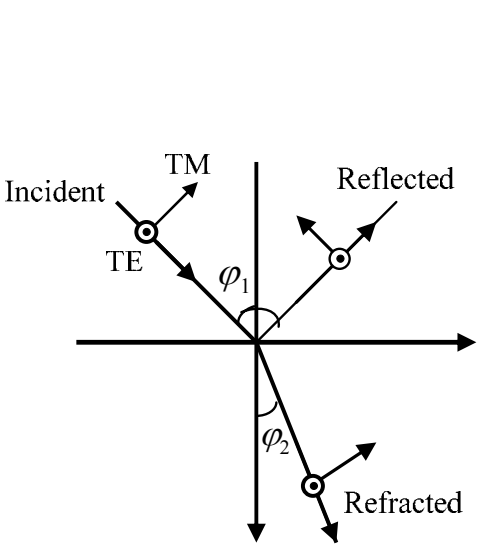

(a)

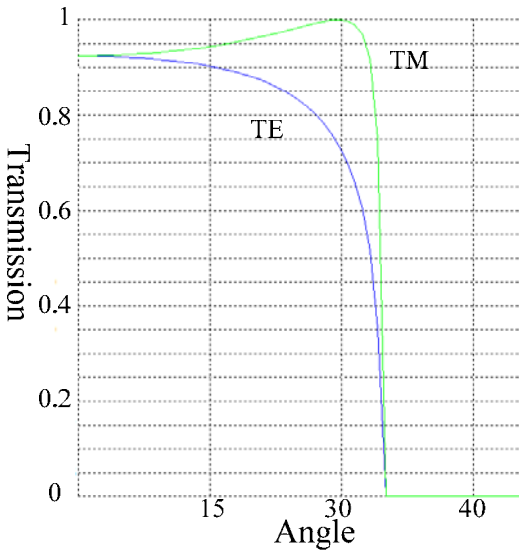

(b)

Figure 7.7: (a) Light reflective and refractive relationship. (b) Transmission relationship for TM and TE mode.

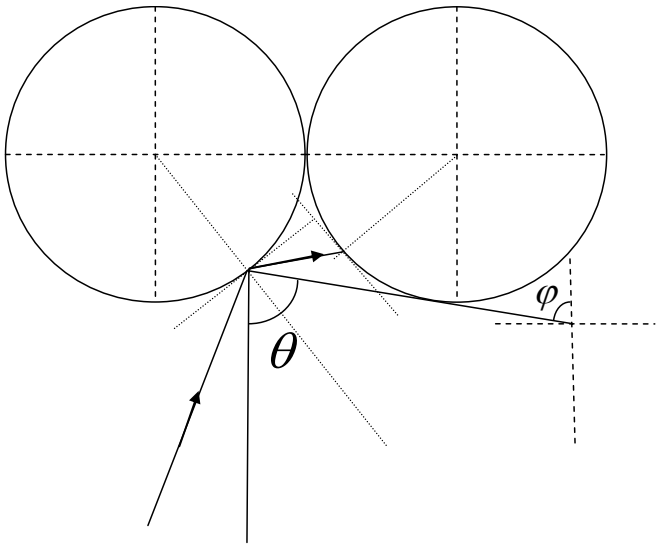

Figure 7.8: Microcosmic structure of the opals layer for modeling.

A semi-sphere is put in the chips as a point source with emitted rays normal to the surface and being emitted randomly.

Modeling

The simulation results of the examples analyzed by the Monte Carlo method are shown in Figure 7.9. A point source with 2W of optical power was put in the center under the surface. Comparison was done on the irradiation map of the LED chips with and without the opal layer when h/m = 0.3. Fifty thousand rays were applied in the simulation to calculate the photon intensity distribution on the LED surface. The X and Y axes are the length scale of the emitted light projected on a plane. The white circle is the boundary of the surface of the chip and colors stand for the different photon intensities with a unit of W/m^2. The light escape corner is very small, only a small part of the surface has light emission and the corresponding light escape angle is less than 30 degrees, Figure 7.9(a). The light intensity distribution map spreads over the entire surface when an opal layer is grown on the surface, which means the light escape corner is enlarged significantly to over 70 degrees. The total power extraction efficiency is also strongly enhanced. The efficiency was only 6% in a conventional LED and increased to 60% with the opals layer.

When the opals layer is used without proper optimization, the power extraction efficiency will decrease. For comparison, opal spheres were deposited only on half of the surface with a large radius, as is shown in Figure 7.10(b). In this example, the power extraction efficiency is only 10%. Most of the light is emitted from the center of each sphere, looking like micro-lens array. This is because only incident rays with a small incident angle through the center of the sphere could be emitted, while others are

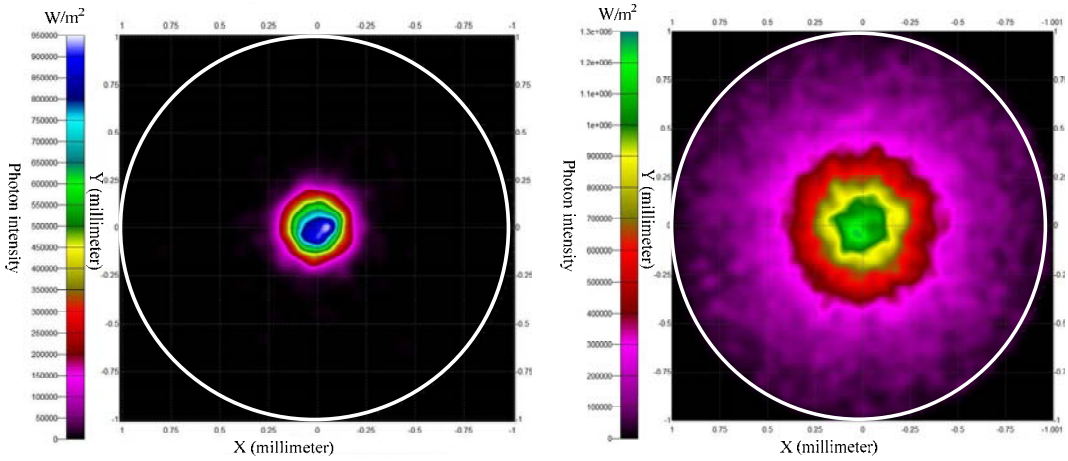

(a) (b)

Figure 7.9: Light intensity distribution on the emission surface of an LED. (a) Map for conventional LEDs (b) Map for LEDs with an opals layer on the surface.

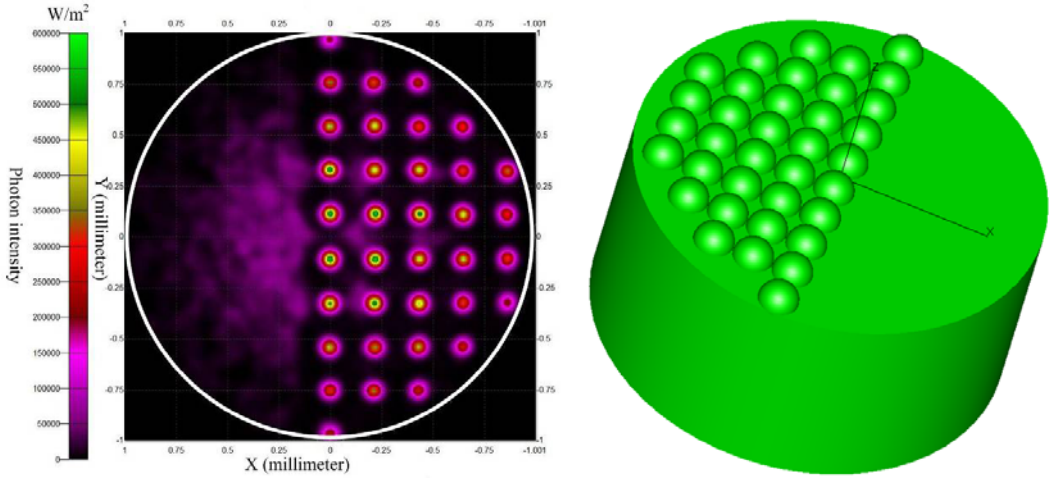

(a) (b)

Figure 7.10: (a) Photon intensity map. (b) Sketch map of the LEDs structure with only half of the opals sphere.

reflected back due to the large incident angle. For the spheres lying far away from the source center the incident angle will become large again and rays can be emitted through the center. This can be overcome by changing the structural parameters, including sphere radius, index of refraction, and thickness of the cladding layer. When the radius of the opal sphere is decreased, the multi-point phenomena will disappear and the light extraction efficiency will increase dramatically.

Opals layer with a different lattice structure was also simulated. Previous photon intensity was calculated for a square lattice and shows a light extraction efficiency of more than 60%, Figure 7.9(b). A triangular lattice, on the other hand, is more common for opals. The simulated result of LEDs with the triangular lattice structure is shown in Figure 7.11. It shows a light extraction efficiency of 58% which is slightly lower than that of the square lattice. The opals take into account the advantage of the refractive index difference and the sphere structure to enhance the efficiency. Consequently, the refractive index and radius are the most crucial. The photonic crystal phenomena might appear when smaller spheres with radius less than 1 μm are used. Under this condition, the lattice structure would have a greater influence on the extraction efficiency.

The effects of changing the refractive index of the opal spheres and changing the distance between the source and the surface were also analyzed. The light extraction efficiency will decrease with an increase in the index of refraction as seen in Figure 7.12(a). This means that rays traveling from the opals to the ITO layer may play an important role in the efficiency enhancement. With a smaller refractive index, it would be easier for light lines to be injected into the ITO layer because there will be a larger total reflection angle between the opals and ITO. The simulation result when the normalized

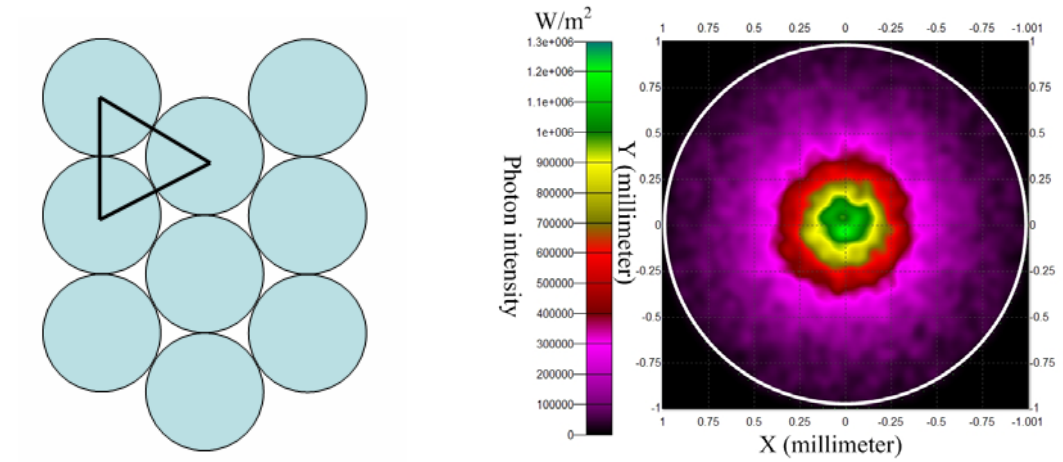

(a) (b)

Figure 7.11: (a) Illustration of triangular lattice structure. (b) Photon intensity map of the triangular lattice structure.

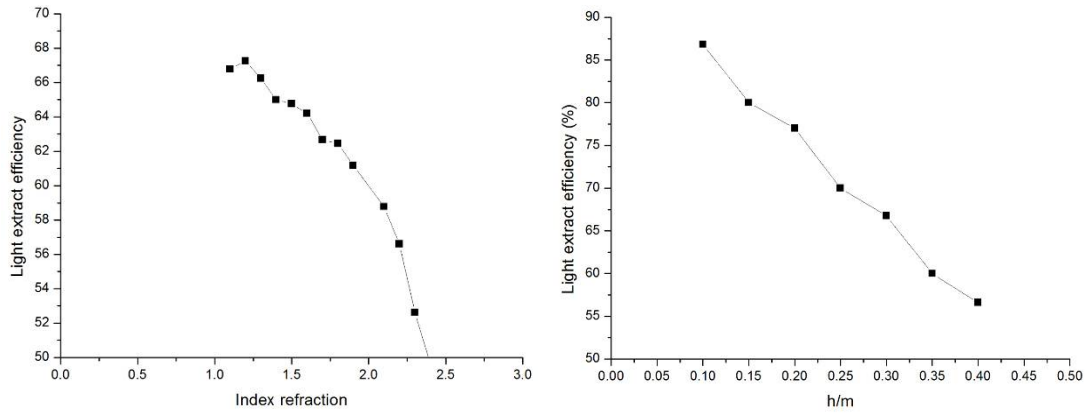

(a) (b)

Figure 7.12: (a) Light extract efficiency as a function of index refraction of the opals spheres (b) light extract efficiency as a function of the distance between the source and the surface.

distance h/m changes is shown in Figure 7.12(b). The efficiency increases with a decrease in the distance and goes up to almost 90% when h/m is about 0.1.

The opal layer can increase the total reflection angle and therefore will adequately release the performance from the opal layer when the distance is very small and more rays can be extracted out. The sidewalls are a perfect absorber during the simulation. Rays with a large incident angle that are incident on the sidewall of the LEDs will travel to the surface and get a chance to be emitted out.

It would not be suitable to use the Monte Carlo method when the radius of the opal sphere is smaller than 1μm because the micro-scale phenomena of diffraction and photonic bands will appear. The plane wave expansion (PWE), finite difference time domain (FDTD), and rigorous coupled wave analysis (RCWA) methods are used to calculate the energy band structures and the extraction efficiency of the infiltrated opal layer, respectively. When the radius is smaller than 1μm it will be very hard to fabricate the LED opal layer. No forbidden bandgap appears as seen in Figure 7.13. It is hard to enhance the extraction efficiency by using traditional photonic crystal bandgap phenomena. The simulation result of light extraction efficiency is not very high by FDTD. Only rigorously designed opals with exact radius and index of refraction will have very high light extraction efficiency. The simulated result of light extraction efficiency as a function of opal sphere radius is seen in Figure 7.14. A number below 1μm was chosen and resulted in lower efficiency.

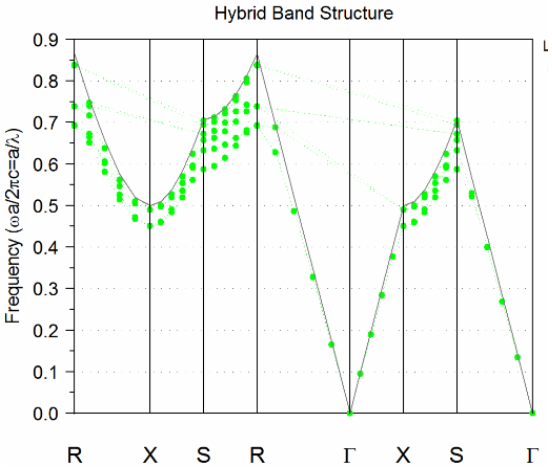

(a)

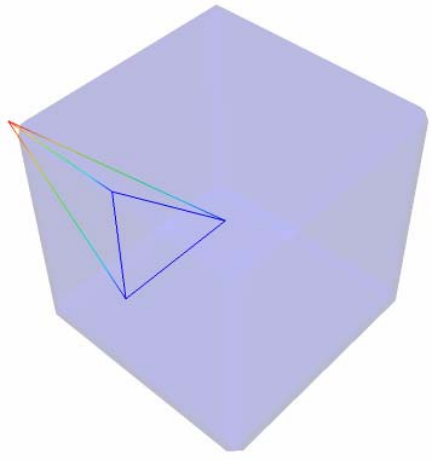

(b)

Figure 7.13: (a) Simulated Hybrid Band Structure (b) First Brillouin zone.

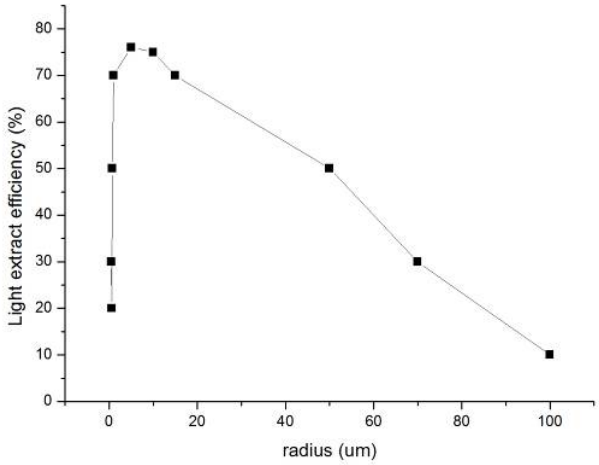

Figure 7.14: Light extraction efficiency as a function of radius of the opals sphere.

7.3 Closing Statement

LEDs have come a long way and are currently seen in everyday appliances such as cell phones and laptops. However, in order for LEDs to make a huge breakthrough into the general lighting market and for higher efficiency in the green wavelength region, there must be a new design process in growing LEDs. LEDs grown on currently used foreign substrates have a limited achievable efficiency. A new substrate, such as ZnO, is needed to decrease the internal defect density and allow for higher external light extraction. The first GaN and InGaN growth on ZnO by MOCVD was reported in this thesis and show a possible new direction for higher-quality LEDs.

REFERENCES

1. F. Hamdani, M.Y., D. Smith, H. Tang, W. Kim, A. Salvador, A. Botchkarev, J. Gibson, A. Polyakov, M. Skowronski, and H. Morkoc, "Microstructure and optical properties of epitaxial GaN on ZnO (0001) grown by reactive molecular beam epitaxy", *Journal of Applied Physics*, 83 (1998) 2.

2. Navigant Consulting, I., "Energy Savings Potential of Solid State Lighting in General Illumination Applications", *Department of Energy*, (2003).

3. David Nicol, *Chapters: Introduction, Issues and Solutions, Motivation and Understanding, State of the Art*. Pending Book on Solid State Lighting.

4. Tekla S. Perry, "Red Hot", *IEEE Spectrum*, 40 (2003) 6.

5. Daniel A. Steigerwald, "Illumination with Solid State Lighting Technology", *IEEE Journal on Selected Topics in Quantum Electronics*, 8 (2002) 2.

6. Solid State Lighting Industry Trade Association (SSLITA), "LED Market Glows: The HB LED market is growing", *SPIE Professional*, (2008) July.

7. Gallium Nitride, in *2000 – Technology Status, Applications, and Market Forecast, Strategies Unlimited*. 2000: Mountain View, CA.

8. Glenn Zorpette, "Let There Be Light", *IEEE Spectrum*, 39 (2002) 9.

9. Kendall, M. and M. Sholand, "Energy savings potential of solid state lighting in general lighting applications," *Department of Energy*, (2001).

10. "Bright Future for Solid State Lighting", *IEE Review*, 50 (2004) 9.

11. Peter Fairley, "Lighting Up The Andes", *IEEE Spectrum*, 41 (2004) 12.

12. I. T. Ferguson, A.M., N. Li, D. Nicol, E. Park, and G. Tosini, *Imitating Broadband Diurnal Light Variations Using Solid State Light Sources*, in *1st International Conference on White LEDs and Solid State Lighting*. 2007: Japan.

13. Tsuguo Fukuda, D.E., "Prospects for the ammonothermal growth of large GaN crystal", *Journal of Crystal Growth*, 305 (2007).

14. Wataru Utsum, H.S., Hiroshi Kaneko, Tetsu Watanuki, Katsutoshi Aoki, and Osamu Shimomura, "Congruent melting of gallium nitride at 6 GPa and its application to single-crystal growth", *Nature Materials*, 2 (2003).

15. Cree, *GaN Substrates Technology*. 2008.

16. Kyma, *Gallium Nitride (GaN) Substrates*. 2008.

17. Richard Stevenson, *GaN substrates offer high performance at a price* in *Compound Semiconductor* 2004.

18. Hitachi Cable, *Hitachi confirms 3-inch GaN substrate, eyes 4-inch*, in *Compound Semiconductor* 2007.

19. Panasonic, *Panasonic claims GaN substrate LED breakthrough*, in *Compound Semiconductor*. 2007.

20. CERMET, *Crystal growth technology*. 2008: Atlanta.

21. Nause, J. and B. Nemeth, "Pressurized melt growth of ZnO boules", *Semiconductor Science and Technology*, 20 (2005) 4.

22. D.C. Reynolds, e.a., "High-quality, melt-grown ZnO single crystals", *Journal of Applied Physics*, 95 (2004) 9.

23. TokyoDenpa, *New material department*. 2008.

24. E. Hellman, D.B., D. Wiesmann, and I. Brener, "Growth of Ga-face and N-face GaN films using ZnO Substrates", *MRS Internet Journal of Nitride Semiconductor Research*, 1 (1996).

25. X. Gu, M.R., A. Teke, D. Johnstone, H. Morkoc, B. Nemeth, and J. Nause, "GaN epitaxy on thermally treated c-plane bulk ZnO substrates with O and Zn faces", *Applied Physics Letters*, 84 (2004) 13.

26. Paszkiewicz, R., et al., "MOVPE GaN Grown on Alternative Substrates", *Crystal Research and Technology*, 36 (2001).

27. Nola Li, E.-H.P., Yong Huang, Adriana Valencia, Bill Nemeth, Jeff Nause, and Ian Ferguson, "Growth of GaN on ZnO for Solid State Lighting Applications", *Proceedings of SPIE*, 6337 (2006).

28. G. Namkoong, S.B., K. Lee, E. Trybus, W. Doolittle, and et. al., "III-nitrides on oxygen- and zinc-face Zn) substrates", *Applied Physics Letters*, 87 (2005) 18.

29. Suzuki, T., et al., "Relation between interdiffusion and polarity for MBE growth of GaN epilayers on ZnO substrates", *Current Applied Physics*, 4 (2004) 6.

30. A. Kobayashi, et al., "Room Temperature Layer by Layer Growth of GaN on Atomically Flat ZnO", *Japanese Journal of Applied Physics*, 43 (2004).

31. A. Kobayashi, J.O., and H. Fujioka, "Low temperature epitaxial growth of In0.25Ga0.75N on lattice-matched ZnO by pulsed laser deposition", *Journal of Applied Physics*, 99 (2006).

32. Jakschik, S.a.e.a., "Crystallization behavior of thin ALD-Al2O3 films", *Thin Solid Films*, 425 (2003).

33. Ritala, M.a.M.L., *Handbook of Thin Film Materials - Deposition and Processing of Thin Films. Atomic Layer Deposition*, ed. H.S. Nalwa. Vol. 1. 2002: Academic Press.

34. Ho, I. and G.B. Stringfellow, *Applied Physics Letters*, 69 (1996) 2701.

35. D. Doppalapudi, S.N.B., K. F. Ludwig Jr., and T. D. Moustakas, *Journal of Applied Physics*, 84 (1998) 1389.

36. M. D. McCluskey, L.T.R., B. S. Krusor, D. P. Bour, N. M. Johnson, and S. Brennan, *Applied Physics Letters*, 72 (1998) 1730.

37. N. A. EI-Masry, E.L.P., S. X. Liu, and S. M. Bedair, *Applied Physics Letters*, 72 (1998) 40.

38. Steckl, A.J. and R.H. Birkhahn, *Applied Physics Letters*, 73 (1998) 1700.

39. Y. Narukawa, Y.K., M. Funato, S. Fujita, S. Nakamura, *Applied Physics Letters*, 70 (1997) 981.

40. Grabmaier, G.B.a.B.C. Luminescent Materials. 1994, Berlin, Germany: Springer-Verlag.

41. Z. C. Feng, T.R.Y., R. Liu, and T. S. A. Wee, *Mater. Sci. in Semi. Proce*, 5 (2002) 39.

42. A. Tabata, L.K.T., L. M. R. Scolfaro, J. R. Leite, A. Kharchenko, T. Frey, D. J. and D.S. As, K.Lischka, J. Furthmüller, and F. Bechstedt, *Applied Physics Letters*, 80 (2002) 769.

43. S.Y. Karpov, *MRS Internet J. Nitride Semicond. Res.*, 3 (1998) 16.

44. C. A. Parker, J.C.R., S. M. Bedair, M. J. Reed, S. X. Liu, and N. A. El-Masry, and L.H. Robins, *Applied Physics Letters*, 75 2566.

45. S. Nakamura, *Journal of Crystal Growth*, 145 (1994) 911.

46. M. Smith, G.D.C., J. Y. Lin, H. X. Jiang, M. Asif Khan, Q. Chen, *Applied Physics Letters*, 69 (1996) 2837.

47. K. L. Teo, J.S.C., P. Y. Yu, E. R. Weber, M. F. Li, W. Liu, K. Uchida, H. and N.A. Tokunaga, K. Matsumoto, *Applied Physics Letters*, 73 (1998) 1697.

48. Liu, W., et al., "Effect of high temperature and interface treatments on photoluminescence from InGaN/GaN multiple quantum wells with green light emissions", *Applied Physics Letters*, 83 (2003) 5.

49. Ho, I. and G.B. Stringfellow, *Appl. Phys. Lett.*, 69 (1996) 2701.

50. A. Zunger, *Handbook of Crystal Growth*, ed. D.T.J. Hurle. Vol. 3. 1994, New York: Elsevier. 998.

51. I. H. Lee, I.H.C., C. R. Lee, E. J. Shin, D. Kim, S. K. Noh, S. J. Son, K. Y. Lim, and H. J. Lee, *Journal of Applied Physics*, 83 (1998) 5787.

52. M. K. Chen, Y.C.C., J. Y. Chen, C. M. Wub, C. C. Yang, K. J. Mad, J. R. Yange, and A. Rosenauerf, *Journal of Crystal Growth*, 279 (2005) 55.

53. P. Cantu, F.W., P. Waltereit, S. Keller, A. E. Romanov, U. K. Mishra, S. P. DenBaars, and J. S. Speck, *Applied Physics Letters*, 83 (2003) 674.

54. L Zhang, H.C.J., C Liu, J W Dong, and P Chow, "Annealing of Al2O3 thin films perpared by atomic layer deposition", *Journal of Physics D: Applied Physics*, 40 (2007).

55. Shulin Gu, R.Z., Jingxi Sun, Ling Zhang, and T. F. Kuech, "Role of interfacial compound formation associated with the use of ZnO buffers layers in the hydride vapor phase epitaxy of GaN", *Applied Physics Letters*, 76 (2000) 23.

56. Bi, Z.X.a.e.a., "Prepare of ZnAl2O4/alpha-Al2O3 complex substrates and growth of GaN films", *MRS Symp. Proc.*, 693 (2002).

57. C.R. Gorla, "Structure and interface-controlled growth kinetics of ZnAl2O4 formed at the (112bar0) ZnO/(011bar2) Al2O3 interface", *Journal of Applied Physics*, 87 (2000) 8.

58. S. Gu, *J. of Nitride Semi. Res.*, (2000).

59. T. Ueda, T.F.H., S. Spruytte, H. Lee, M. Yuri, K. Itoh, T. Baba, J.S. Harris Jr., "Vapor phase epitaxy growth of GaN on pulsed laser deposited ZnO buffer layer", *Journal of Crystal Growth*, 187 (1998).

60. Th. EI-Nabarawy, A.A.A., and M. N. Alaya, *Mater. Lett.*, 24 (1995) 319.

61. Z.C. Feng, *Opt. Eng.*, 41 (2002) 2022.

62. N. Nepal, M.L.N., H.U. Jang, J.Y. Lin, and H.X. Jiang, *Appl. Phys. Lett.*, 89 (2006) 192111.

63. S.J. Wang, N.L., E. H. Park, S.C. Lien, Z.C. Feng, A. Valencia, J. Nause, and I. Ferguson, *J. Appl. Phys.*, 102 (2007) 106105.

64. Neugebauer, J. and C.G.V.d. Walle, *Phys. Rev. B*, 50 (1994) 8067.

65. F.B. Naranjo, M.A.S.-G., F. Calle, E. Calleja, B. Jenichen, and K.H. Ploog, "Strong localization in InGaN layers with high In content grown by moleculer-beam epitaxy", *Appl. Phys. Lett.*, 80 (2002) 2.

66. S. Pereira, M.R.C., T. Monteiro, E. Pereira, M.R. Soares, and E. Alves, "Indium content determination related with structural and optical properties of InGaN layers", *J. Cyrst. Growth*, 230 (2001) 3-4.

67. Parker, C.A., et al., "Optical band gap dependence on composition and thickness of InxGa1-xN (0<x<0.25) grown on GaN", *Appl. Phys. Lett.*, 75 (1999) 17.

68. Wang, S.J. and C.Y. Liu, "Study of Interaction between Cu-Sn and Ni-Sn Interfacial Reactions by Ni-Sn3.5Ag-Cu Sandwich Structure", *J. Elect. Materials*, 32 (2003) 11.

69. Wang, S.J. and C.Y. Liu, "Kinetic Analysis of the Interfacial Reactions in Ni/Sn/Cu Sandwich Structures", *J. of Elec. Materials*, 35 (2006) 11.

70. Haneda, H., et al., "SIMS analysis of impurities and nitrogen isotopes in gallium nitride thin films", *Appl. Surface Science*, 252 (2006) 19.

71. P. Kozodoy, Y.P.S., Monica Hansen, Huili Xing, Steven P. DenBaars, Umesh K. Mishra, A. W. Saxler, R. Perrin, and W. C. Mitchel, "Polarization-enhanced Mg doping of AlGaN/GaN superlattices", *Appl. Phys. Lett.*, 75 (1999) 16.

72. William Fenwick, H.Y., Shenjie Wang, Nola Li, Andrew Melton, Benjamin Klein, and Ian Ferguson, "Metalorganic Chemical Vapor Deposition of III-Nitride Epilayers on ZnO Substrates for Green Emitter Applications", *Proc. of SPIE*, 7058 (2008).

73. William E. Fenwick, H.Y., Nola Li, Shen-Jie Wang, Adriana Valencia, Jeff Nause, Benjamin Klein, and Ian T. Ferguson, "MOCVD Growth of GaN and InGaN on ZnO (0001) Substrates for Green Emitter Applications", *Submitted to Journal of Vacuum Science and Technology B, June 2009 issue*, (2008).

74. W.E. Fenwick, H.Y., S. Wang, N. Li, M. Jamil, and I. Ferguson, "MOCVD growth of GaN on ZnO (0001) substrates using different buffer layers", *To be submitted*, (2008).

75. William E. Fenwick, H.Y., Shen-Jie Wang, Nola Li, Andrew Melton, Jeff Nause, and Ian T. Ferguson, "MOCVD Growth of GaN-based Materials on ZnO and Si Substrates", *MRS Symposium Proceedings, 2009*, (2008).

76. C.L. Huang, Y.Z.H., Z.C. Feng, Y.L. Shen, N. Li, S.J. Wang, and I. Ferguson, *Optical and structure properties of MOCVD-grown InGaN/GaN on ZnO substrate with Al2O3 transition layer by atomic layer deposition*, in *Taiwan Display Conference*. 2008: Taipei, Taiwan. p. 383-386.

77. Nola Li, S.-J.W., Chung-Lung Huang, Zhe Chuan Feng, Adriana Valencia, Bill Nemeth, Jeff Nause, Christopher Summers, and Ian Ferguson, *Al2O3 as a Transition Layer for MOCVD Growth of GaN and InGaN on ZnO Substrates*, in *UK Semiconductors*. 2008: University of Sheffield.

78. Nola Li, S.-J.W., Chung-Lung Huang, Zhe Chuan Feng, Adriana Valencia, Bill Nemeth, Jeff Nause, Christopher Summers, and Ian Ferguson, "Effect of an Al2O3 Transition Layer on InGaN on ZnO Substrates by Organometallic Vapor Phase Epitaxy", *Special issue of Journal of Crystal Growth, In Press, Accepted Manuscript (14th International Conference of Metalorganic Vapor Phase Epitaxy)*, (2008).

79. Nola Li, S.-J.W., Andrew Melton, Chung-Lung Huang, Zhe Chuan Feng, Adriana Valencia, Jeff Nause, Christopher Summers, and Ian Ferguson, "Al2O3 as a Transition Layer for GaN and InGaN Growth on ZnO by MOCVD", *Submitted to Journal of Vacuum Science and Technology B, June 2009 issue*, (2009).

80. Nola Li, S.-J.W., Eun-Hyun Park, Zhe Chuan Feng, Hung-Lin Tsai, Jer-Ren Yang, Adriana Valencia, Jeff Nause, and Ian Ferguson, "Suppression of phase separation in InGaN growth on ZnO substrates compared to growth on sapphire", *Submitted to JCG, in review process*, (2008).

81. Nola Li, S.-J.W., Eun-Hyun Park, Zhe Chuan Feng, Adriana Valencia, Jeff Nause, and Ian Ferguson, "InGaN layers grown on passivated Al2O3/ZnO substrates prepared by atomic layer deposition", *MRS Symposium Proceedings*, 1035E (2008) 1035-L11-23.

82. Nola Li, S.-J.W., Eun-Hyun Park, Zhe Chuan Feng, Adriana Valencia, Jeff Nause, Christopher Summers, and Ian Ferguson, *Influence of High Indium Composition InGaN on Lattice Matched ZnO Sacrificial Substrates* in *1st International Conference on White LEDs and Solid State Lighting*. 2007: Minato-ku, Tokyo, Japan.

83. Nola Li, S.-J.W., Eun-Hyun Park, Zhe Chuan Feng, Adriana Valencia, Jeff Nause, Christopher Summers, and Ian Ferguson, "Growth of InGaN with High In Content on ZnO Substrates by Metalorganic Chemical Vapor Deposition", *Proc. of SPIE*, 6669 (2007) 66690X.

84. Nola Li, S.-J.W., Eun-Hyun Park, Zhe Chuan Feng, Adriana Valencia, Jeff Nause, Christopher Summers, and Ian Ferguson, "Influence of High Indium Composition InGaN on Lattice Matched ZnO Sacrificial Substrates", *Journal of Light & Visual Environment*, 32 (2008) 2.

85. Nola Li, S.-J.W., Adriana Valencia, Jeff Nause, Christopher Summers, and Ian Ferguson, "Metalorganic Vapor Deposition of GaN and InGaN on ZnO Substrate using Al2O3 as a Transition Layer", *Proc. of SPIE* 7058 (2008).

86. Nola Li, S.-J.W., Hongbo Yu, Christopher Summers, and Ian Ferguson, *InGaN Growth on ZnO Substrate by MOCVD*, in *GT Graduate Student Symposium*. 2008.

87. Nola Li, S.-J.W., Hongbo Yu, Vincent Woods, Christopher Summers, and Ian Ferguson, *Epitaxial Growth of GaN Based LEDs on Simple Sacrificial Substrates*, in *DOE Workshop*. 2008.

88. Shen-Jie Wang, N.L., Eun-Hyun Park, Zhe Chuan Feng, Adriana Valencia, Jeff Nause, Matthew Kane, Christopher Summers, and Ian Ferguson, *MOCVD growth of GaN-based materials on ZnO substrates*, in *7th Int'l Conference of Nitride Semiconductors*. 2007: Las Vegas, Nevada.

89. Shen-Jie Wang, N.L., Eun-Hyun Park, Zhe Chuan Feng, Adriana Valencia, Jeff Nause, Matthew Kane, Christopher Summers, and Ian Ferguson, "MOCVD growth of GaN-based materials on ZnO substrates", *Phys. Stat. Sol. (c)*, 5 (2008) 6.

90. Shen-Jie Wang, N.L., Eun-Hyun Park, Siou-Cheng Lien, Zhe Chuan Feng, Adriana Valencia, Jeff Nause, and Ian Ferguson, "Metalorganic Chemical Vapor Deposition of InGaN Layers on ZnO Substrates", *Journal of Applied Physics*, 102 (2007) 106105.

91. Shen-Jie Wang, N.L., Hong bo Yu, Zhe Chuan, Adriana Valencia, Jeff Nause, Christopher Summers, and Ian Ferguson, "Metalorganic Chemical Vapor Deposition of GaN Layers on ZnO Substrates using α-Al2O3 as a Transition Layer", *To be submitted*, (2008).

92. Hongbo Yu, S.W., Nola Li, William Fenwick, Andrew Melton, B. Klein, and Ian Ferguson, "MOVPE Growth of AlGaN/GaN Superlattices on ZnO Substrates for Green Emitter Applications", *Special issue of Journal of Crystal Growth, In Press, Accepted Manuscript (14th International Conference of Metalorganic Vapor Phase Epitaxy)*, (2008).

93. Hongbo Yu, S.W., Nola Li, William Fenwick, Andrew Melton, B. Klein, and Ian Ferguson, *MOVPE Growth of AlGaN/GaN Superlattices on ZnO Substrates for Green Emitter Applications*, in *14th International Conference of Metalorganic Vapor Phase Epitaxy*. 2008: Metz, France.

94. Bin Zhang, Z.Z., Nola Li, and Ian T. Ferguson, "Enhancement of light extraction of GaN light-emitting diode using opals layer", *Proc. of SPIE*, 6669 (2007) 66691K.

95. D. Delbeke, R.B., P. Bienstman, R. Baets and H. Benisty, "High-efficiency semiconductor resonant-cavity light-emitting diodes: a review", *IEEE Journal of Selected Topics in Quantum Electronics*, 8 (2002).

96. M. Rattier, H.B., R.P. Stanley, J.F. Carlin, R. Houdre, U. Oesterle, C.J.M. Smith, C. Weisbuch and T.F. Krauss, "Toward ultrahigh-efficiency aluminum oxide microcavity light-emitting diodes: guided mode extraction by photonic crystals", *IEEE Journal of Selected Topics in Quantum Electronics*, 8 (2002).

97. P. Royo, R.P.S., and M. Ilegems, "Planar dielectric microcavity light-emitting diodes: Analytical analysis of the extraction efficiency", *Journal of Applied Physics*, 90 (2001).

98. J. Vuckovic, M.L., and A. Scherer, "Surface plasmon enhanced light-emitting diode", *IEEE Journal of Quantum Electronics*, 36 (2000).

99. Summers, D.P.G.a.C.J., "Photonic band gaps in non-close-packed inverse opals", *Journal of Applied Physics*, 100 (2006) 113118.

100. Jeffrey S. King, E.G., and Christopher J. Summers, "Photoluminescence modification by high-order photonic bands in TiO2 /ZnS:Mn multilayer inverse opals", *Applied Physics Letters*, 88 (2006) 081109.

101. Song Jae Lee, "Analysis of light-emitting diodes by Monte Carlo photon simulation", *Applied Optics*, 40 (2001) 9.

102. Shanhui Fan, P.R.V., and J. D. Joannopoulos, "High Extraction Efficiency of Spontaneous Emission from Slabs of Photonic Crystals", *Physical Review Letters*, 87 (1997) 17.